AMBIENT IONIZATION MASS SPECTROMETRY FOR INTRAOPERATIVE AND HIGH-THROUGHPUT BRAIN CANCER DIAGNOSTICS

by

Hannah Marie Brown

A Dissertation

Submitted to the Faculty of Purdue University

In Partial Fulfillment of the Requirements for the degree of

Doctor of Philosophy

Department of Chemistry

West Lafayette, Indiana

May 2022

THE PURDUE UNIVERSITY GRADUATE SCHOOL
STATEMENT OF COMMITTEE APPROVAL

Dr. R. Graham Cooks, Chair

Department of Chemistry

Dr. Hilkka Kenttämma

Department of Chemistry

Dr. Julia Laskin

Department of Chemistry

Dr. Uzay Emir

School of Health Sciences

Approved by:

Dr. Christine A. Hrycyna

Dedicated to the patients and their families.

ACKNOWLEDGMENTS

I am where I am today thanks to the support and influence of a great multitude of people. Reflecting on my Ph.D. experience, there are many individuals I would like to thank.

To the team at Indian University School of Medicine: Heather Cero, Lauren Snyder, Dr. Scott Shapiro, Dr. Mahua Dey, Dr. Aaron Cohen-Gadol, Dr. Eyas Hattab. Your enthusiasm and support for this project directly contributed to its success in particular and the continued acceptance of ambient ionization mass spectrometry methods in general.

To the team at Mayo Clinic – Jacksonville: Aleeshba Basil, Diogo Garcia, Dr. Erik Middlebrooks, Dr. Mark Jentoft, Dr. Kaisorn Chaichana, Dr. Alfredo Quiñones-Hinojosa. It has been a joy and an honor to collaborate with you all for the past two years. You have opened my eyes to the significant impact the technology can have on patient lives and we have laid the groundwork for the continued successful translation of ambient ionization mass spectrometry to clinical applications.

To my committee members: Dr. Hilkka Kenttämma, Dr. Julia Laskin, Dr. Uzay Emir. Thank you for your time and support throughout my Ph.D. experience. You each brought a unique perspective and expertise to our discussions and I am grateful for the investment you have made in me.

To the Astonites. Aston Labs truly does have one of the best collection of people I have ever met. Whether I had the pleasure of working with you all five years or a few months, each of you have made an impact on my life and have taught me valuable lessons I will refer to often in the future. I look forward to seeing the amazing accomplishments you all will no doubt achieve.

To Vale. You were the first Astonite I met and are a significant reason I elected to make Purdue my home for the past five years. I have learned an incredible amount of about how to conduct great science from you, lessons I will carry with me as I begin my professional career.

To Clint. From day one, you held me to a high standard. I am thankful to you for pushing me to be the best I could be. I did not understand it at the time, but I see now that it is the natural consequence of caring intimately for a project's success. I find myself doing the same now.

To Fan. You are the definition of a great lab partner. Your expertise in instrumentation and my clinical knowledge made for a unique and dynamic partnership. I cannot say I miss the early winter morning drives to Indianapolis, but I certainly miss spending time with you.

To Rob. Thank you for teaching me the art of 3D printing and why printing with nylon is a nightmare. Also, thank you for a shared love of Broadway musicals and Bon Appetit.

To Lucas. Thank you partaking in the crazy road trip to Florida and keeping me awake through the winding hills of West Virginia. Thank you also for always answering my panicked calls for instrumentation help in the OR (even if the answer is just a glove stuck in the syringe pump).

To Nick. I have never met someone who so effortlessly balances such a great multitude of responsibilities with such grace as you. Your dedication to mass spectrometry and your unwavering positive attitude were always a welcome sight in DLR. #droplets4lyfe.

To Lillian. To say that you have made a profound impact on my life would be an understatement. Working with you on the Mayo project over the past three years has been nothing short of a great partnership. You have taught me so much: how to be a good communicator and an even better listener, how to maintain a level-head when faced with unanticipated difficulties, and, above all, how to be a great friend. Thank you for never saying no to my adventurous weekend travels. I promise we will make it to Disney World before the end of the project.

To my siblings, Wesley and Meghan. Thank you for always asking about my research and pretending to understand when I explain. I am very blessed to have you both to walk through the journey of life with.

To my family: grandparents, aunts, uncles, cousins. Thank you for believing in me and checking in on me throughout this process. Your support means the world.

To Stefan. You challenge me to be better today than I was yesterday and not to settle until I am as good as I will be tomorrow. I have learned that the best partnerships are those with "people whose strengths compensate[d] for my weaknesses." I am very grateful to have you as a partner. OaOoN.

To Pebbles. You have affectionately gained the nickname of "DESI dog" and have made yourself a valuable member of the brain cancer research team. Both Lillian and I can attest to this. I look forward to celebrating your Ph.D. (Pet honorary Doctorate) too.

To my mom. No matter how technical the writing may get, you are and always will be my most cherished editor. Your lifetime of selflessness and investment in me shaped me into who I am today. You are a shining example of the woman I strive to be and I am beyond proud to be your daughter.

To my dad. I am always humbled when people tell me that I am like you, whether it be our shared love of travel, political events, or fine dining. However, from this day forward, I think my favorite shared quality will be the moniker, “Dr. Brown”, although, in my mind, that title will always be reserved for you.

To Graham. You are an incredible scientist and one of the most effective leaders I know. Thank you for believing me and for giving me the space to grow into an independent scientist. When I first started my Ph.D., my dad emphasized the importance of mentorship. I consider myself blessed to have had your support and mentorship during my Ph.D. As I prepare to embark on my own career, I will never forget the lessons you have taught me and will strive to make you proud.

To Purdue. I have grown so much here in the past five years. I am grateful for every tear, smile, challenge overcome, and dream made reality. I have always believed that you leave a place changed. Hopefully you leave something good behind too.

TABLE OF CONTENTS

LIST OF TABLES

LIST OF FIGURES

LIST OF ABBREVIATIONS

2HG:	2-Hydroxyglutarate
A:	Adequate
ACN:	Acetonitrile
A.I.:	Asian Indian
AUC:	Area under curve
B:	Black
BMA:	Barely marginally adequate
CT:	Computed tomography
DESI:	Desorption electrospray ionization
DESI-MS/MS:	Desorption electrospray ionization tandem mass spectrometry
DESI-MS:	Desorption electrospray ionization mass spectrometry
DMF:	Dimethylformamide
EtOH:	Ethanol
F:	Female
FWHM:	Full width at half maximum
G:	Glioma
GBM:	Glioblastoma
Glu:	Glutamate

GM:	Grey matter
H:	Hispanic
H&E:	Hematoxylin & eosin
HT-DESI	High-throughput desorption electrospray ionization
HT-DESI-MS	High-throughput desorption electrospray ionization mass spectrometry
I:	Inadequate
IDH:	Isocitrate dehydrogenase
IDH-mut:	IDH mutant
IDH-wt:	IDH wild type
IHC:	Immunohistochemistry
IM:	Infiltrative margin
M:	Male
***m/z*:**	Mass/charge ratio
MALDI:	Matrix-assisted laser desorption ionization
MRI:	Magnetic resonance imaging
MRM:	Multiple reaction monitoring
MRS:	Magnetic resonance spectroscopy
MS^3	Second-generation product ion mass spectrometry
MS/MS:	Tandem mass spectrometry

MS:	Mass spectrometry
Mut:	Mutant
N.H.:	Not Hispanic
NAA:	N-Acetylaspartic acid
nESI:	Nanoelectrospray
OR:	Operating room
P:	Primary
PCA:	Principal component analysis
PCA-LDA:	Principal component analysis-linear discriminant analysis
POC:	Point-of-care
PTFE:	Polytetrafluroethylene
R:	Recurrent
ROC:	Receiver operating curve
SNV:	Standard normal variate
TCP:	Tumor cell percentage
TIC:	Total ion count
TMA:	Tissue microarray
TSQ:	Triple-stage quadrupole
W:	White
WM:	White matter

WT:	Wild type

ABSTRACT

My research has focused on the development and translation of ambient ionization mass spectrometry (MS)-based platforms in clinical and surgical settings, specifically in the area of brain cancer diagnostics and surgical decision making. Ambient ionization MS methods, such as those described herein, generate and analyze gas phase ions with high sensitivity and specificity from minimally prepared samples in near-real-time, on the order of seconds to minutes, rendering them well suited to point-of-care applications. We used ambient ionization MS methods, specifically desorption electrospray ionization mass spectrometry (DESI-MS) and extraction nanoelectrospray ionization mass spectrometry (nESI-MS) to molecularly characterize brain cancer biopsies. The characterization was made using diagnostic compounds identified as markers of disease state, tissue composition, tumor type, and genotype in human brain tissue. Methods were developed and validated offline in the laboratory and translated to clinical and surgical settings, thereby generating chemical information on prognostic features intraoperatively and providing valuable information that would be otherwise unavailable. We believe that, with approval, the methodologies described can assist physicians and improve patient outcomes by providing analytical tools and molecular information that can inform surgical decision making and adjuvant treatment strategies, complementing and not interfering with standard of care protocols.

We have successfully demonstrated the use of desorption electrospray ionization mass spectrometry (DESI-MS) for the expedient molecular assessment of human glioma tissue biopsies based on lipid profiles and prognostic metabolites, both at the tumor core and near surgical margins, in two small-scale, clinical studies. Maximal surgical resection of gliomas that avoids non-infiltrated tissue is associated with survival benefit in patients with glioma. The infiltrative nature of gliomas, as well as their morphological and genetic diversity, renders treatment difficult and demands an integrated imaging and diagnostic approach during surgery to guide clinicians in achieving maximal tumor resection. Further, the estimation of tumor cell percentage (TCP), a measure of tumor infiltration at surgical margins, is not routinely assessed intraoperatively. We have previously shown that rapid, offline molecular assessment of tumor infiltration in tissue biopsies is possible and believe that the same assessment performed intraoperatively in biopsied tissue near surgical margins could improve resection and better inform patient management strategies, including postoperative radiotherapy. Using a DESI-MS spectral library of normal brain

tissue and glioma biopsies to generate a statistical model to classify brain tissue biopsies intraoperatively, multivariate statistical approaches were used to predict the disease state and tumor cell percentage (TCP) of each biopsy, thereby providing a measure of tumor infiltration at surgical margins via molecular indicators. In addition to assessment of tumor infiltration, we have developed DESI-MS assays for detecting the oncometabolite 2-Hydroxyglutarate (2HG) to detect isocitrate dehydrogenase (IDH) mutations in gliomas intraoperatively. Knowledge of IDH genotypes at the time of surgical resection could improve patient outcomes, as more aggressive tumor resection of IDH-mutated gliomas is associated with increased survival. While assessments of IDH genotype are typically not available until days after surgery, we have demonstrated the ability to provide this information is less than five minutes. The intraoperative DESI-MS system consists of a minimally modified linear trap quadrupole (LTQ) placed on a custom-machined, stainless-steel cart that houses all necessary hardware for the operation of the instrument and allows for the system to be wheeled into and out of neurosurgical operating rooms (ORs). This system was used in the ORs at Indiana University (IU) School of Medicine in a cohort of 49 patients undergoing craniotomies with tumor resection for suspected diffuse glioma. Small tissue biopsies from the tumor core and surgical margins were analyzed by DESI-MS in the OR in less than five minutes. The results of this preliminary study are discussed in detail in Chapter 2. Ongoing validation of this platform is being performed at Mayo Clinic-Jacksonville, where we are assessing a modification to the DESI-MS assay to measure 2HG. Product ion scans capturing 2HG and glutamate (Glu), an endogenous internal standard, are collected. The ratio between the two product ion fragments is indicative of IDH genotype. The preliminary results from this ongoing study are discussed in Chapter 5, as well as strengths, weaknesses, and areas of improvement for upcoming future iterations of the research.

Point-of-care applications necessitate the adaptation of MS methodologies to smaller devices. Miniature mass spectrometers (Mini MS) boast small footprints, simple operation, and low power consumption, noise levels, and cost, making them attractive candidates for point-of-care use. To this end, in collaboration with PurSpec and IU School of Medicine, the aforementioned DESI-MS assay to detect 2HG in human glioma biopsies was translated to a Mini MS for the intraoperative determination of IDH genotypes intraoperatively. A modification to traditional nanoelectrospray ionization (nESI), was developed to allow for the detection of 2HG from tissue biopsies with minimal sample preparation. The tandem MS approach used intraoperatively at IU School of

Medicine was not suitable for translation to the miniature instrument due to low signal intensity. Consequently, as previously alluded to, a ratiometric approach was adopted; tandem MS (MS/MS) was performed on 2HG and a reference metabolite, glutamate (Glu), an abundant metabolite in the brain not associated with the IDH mutations. The results of this small, 13-patient study are described in detail in Chapter 3. This study was the first application of a miniature mass spectrometer to the assessment of IDH genotypes intraoperative and paves a path forward for the application of Mini MS in the OR. With its small footprint and low power consumption and noise level, this application of miniature mass spectrometers represents a simple and cost-effective platform for an important intraoperative measurement.

While MS-based methods of tissue analysis can detect molecular features of interest and rapidly produce large quantities of data, their inherent speed is rarely utilized because they are traditionally coupled with time-consuming separation techniques (e.g., chromatography). Ambient ionization MS, specifically DESI-MS, is well suited for high-throughput applications due to its lack of sample preparation and purification techniques. A high-throughput DESI-MS (HT-DESI-MS) system was previously developed and successfully used to screen organic reactions and bioassays. In an attempt to rapidly characterize microarrays of tissue biopsies, we developed a HT-DESI-MS method for the rapid characterization of disease state, human brain tumor type, glioma classification, and detection of IDH mutations in tissue microarrays (TMA) of banked and fresh human brain tissue biopsies. The results of this preliminary study are described in Chapter 4. We anticipate that this method could become a standard tool for the generation of spectral libraries for sample classification, the identification of biomarkers through large-scale studies, the correlation of molecular features with anatomical features when coupled to digital pathology, and the assessment of drug efficacy.

Over the past five years, we have developed ambient ionization MS systems that can rapidly and accurately detect molecular aberrations in cancer tissues and successfully translated these systems for intraoperative use at two clinical institutions. None of this research would be possible without the contributions of the patients and their families and their belief in the potential that this technology has to make a real difference in cancer diagnostics and provide otherwise unavailable information to inform diagnosis, prognosis, and treatment approach intraoperatively. I am optimistic of the impact this technology will have in improving the lives of cancer patients and

their families and feel incredibly grateful and honored to have contributed to the research described herein.

CHAPTER 1. INTRODUCTION

1.1 The Role of Molecular Features in Brain Cancer Diagnostics

The accurate diagnosis of brain cancer and prediction of prognosis increasingly relies on molecular features assessed from tumor core biopsies.(1-3) It is well established that the pathway of genetic information to phenotype begins with DNA, a directional relationship referred to as the central dogma of molecular biology. (4) DNA is transcribed into RNA and said RNA is translated into proteins. These proteins, specifically enzymes, catalyze a variety of chemical transformations crucial to a variety of biological processes. In the same manner, mutations in DNA generate downstream effects due to altered RNA transcripts that can generate altered proteins that can produce altered metabolic pathway intermediates, amongst other effects. This approach has increasingly been used to characterize cancer, with the belief that approaches centered on the analysis of metabolites and lipids can provide unique insights into oncogenesis, disease progression, accurate diagnostics, prognosis, and treatment response.(5-8) In particular, the increased energic demands and hypoxic nature of cancer cells results in genetic mutations that are reflected in alterations in metabolic pathways. Additionally, lipidic species such as phospholipids, ceramides, and cholesterol are rapidly synthesized in cancer cells to meet the demand of rapidly proliferating cells. In this way, the analysis of downstream metabolites can be informative of upstream prognostic genetic mutations.(9, 10)

Clinically, the importance of these molecular features on patient prognosis and clinician decision making, both intraoperative and postoperatively, cannot be overstated. The genetic subtyping of cancers, including gliomas, has improved the ability of surgeons to predict patient prognosis, specifically response to treatments and survival, much better than other factors such as cellular morphology or age.(11-13) Personalized medicine approaches emphasize the implementation of treatment protocols that are mostly likely to be effective in treating a patient's specific tumor and maximizing survival benefit, rather than applying a "one size fits all" approach.(14) This desire to tailor treatment to the molecular features of a patient's specific tumor require the ability to assess molecular features at the time of surgery.

Despite knowledge of the diagnostic value of molecular features, the intraoperative assessment of molecular features in brain tissue biopsies is rarely performed. Medical imaging

methods, including magnetic resonance imaging (MRI) and computed tomography (CT), while informing surgical approach and extent of resection, do not allow for the direct analysis of molecular features.(15) Magnetic resonance spectroscopy (MRS), an emerging method capable of detecting unique signals from molecules of interest, holds promise as a noninvasive method for the detection and quantification of clinically relevant biomarkers, although widespread implementation has yet to be realized.(16) The principal source of intraoperative diagnostics remains the microscopic review of tissue. Frozen section histopathology is used intraoperatively only to diagnose core tissue biopsies, confirm the nature of the brain lesion, and the need of its surgical resection.(17, 18) Consequently, the diagnostic consultation is incomplete, and at times inconclusive, since the accurate diagnosis of brain tumors relies heavily on the assessment of molecular features that are currently only performed intraoperatively, with results available days to weeks after surgery.

Ambient ionization mass spectrometry (MS) methods, such as those described herein, are unique approaches to providing this molecular information to clinicians intraoperatively. In particular, the estimation of tumor infiltration can be made using reliable molecular signatures in the metabolic and lipid profiles of brain tumor tissue obtained at the tumor core and surgical margins using multivariate statistical approaches developed offline.(19-22) Additionally, isocitrate dehydrogenase (IDH) mutations, prognostic mutations in human gliomas, can be detected by measuring the relative concentration of the oncometabolite 2-Hydroxyglutarate (2HG).(23) The widespread use of these methods as complementary, intraoperative diagnostic modalities could enable the tailoring of treatment strategies to the molecular features of a patient's individual tumor and have a profound impact on patient prognosis.

1.2 Clinical Applications of Ambient Ionization Mass Spectrometry

In order for an intraoperatively molecular technique to be widely used, the technique must be capable of providing reliable molecular data very rapidly from unprocessed samples. MS is a highly sensitive and powerful analytical technique capable of detecting and quantifying molecules in complex samples. In MS, ions are generated from molecules present in the sample, transferred to the gas phase, and directed towards low-pressure regions of a mass analyzer that detects ion mass-to-charge ratios (m/z). MS is capable of rapidly (milliseconds per scan) generating large amounts of information-rich data with dynamic ranges between 10^3 and 10^6 and the ability to detect

hundreds of molecules from complex biological samples with limits of detection in the sub-parts-per-billion. For these reasons, MS methods of tissue analysis may be able to provide clinically relevant diagnostic information on biological specimens at the time of surgery. However, the intraoperative use of MS has historically faced barrier to implementation due to the time required for sample preparation and, in some cases, the use of time-consuming online chemical separation techniques such as gas chromatography.

Ambient ionization MS methods generate gas-phase ions for detection by MS under conditions of ambient pressure and temperature, eliminating the typical requirement for ionization to be performed under vacuum or for prior sample pretreatment or purification to be performed.(24) For these reasons, ambient ionization MS methods are well suited for point-of-care (POC) and surgical applications. Ambient ionization MS methods have been used to assess the molecular features of cancers, as well analyze surgical margins for residual tumor. The first tissue measurement completed with ambient ionization, reported in 2005 by Dr. Cooks' group at Purdue University, showed that phospholipid distributions served to demarcate tissue type and disease state.(25) The method used in that work was desorption electrospray ionization (DESI), a label-free method in which a spray of charged (~5 kV) solvent microdroplets impact a surface, in this case a tissue surface, and perform a microscopic-scale extraction of compounds into secondary droplets. Analytes of interest are desorbed into these secondary microdroplets and directed to the mass spectrometer for analysis. The desolvation of these ions occurs in a method analogous to electrospray ionization. An inherent benefit of DESI, a solution-based ionization method, is the ability to tailor the chemistry of the experiment by choice of spray solvent to favor the ionization of certain groups of molecules. Evidence of this advantage is demonstrated in the use of different DESI spray solvents for the analysis of lipids as opposed to small metabolites, such as 2HG, as discussed in Chapters 2 and 5.(26) When coupled with a precision moving stage, DESI has been used to chemically image samples, including tissue sections and smears, by rastering the specimen underneath the DESI spray. By correlating the raster speed with the MS acquisition time, unique mass spectra from specific sample positions can be collected and interpreted. When combined into an image, the MS data, consisting of spatial coordinates (x, y) and mass spectra consisting of *m/z* variables and corresponding ion intensities, can provide information as to the spatial distribution of diagnostic molecular features, including metabolites and lipids, in a biological sample.(27) A

modification of this technique also allows for the high-throughput analysis of an array of samples, including tissue microarrays (TMAs), as described in Chapter 4.

DESI-MS has been used in many laboratories for biological applications, including the distinction between cancerous and normal tissues in a variety of human organs.(28-31) In some studies, as those described in Chapters 2 and 5, DESI is not used as an imaging modality, but as diagnostic method.(22, 23, 26) Using unmodified, flash-frozen banked tissue, previous work in Dr. Cooks' group has demonstrated the ability to differentiate different types of brain tumors (i.e. gliomas, meningiomas, and pituitary tumors),(21) different glioma classifications (e.g. astrocytoma, oligodendroglioma),(19) and normal and diseased brain parenchyma.(20, 22, 32) It is the translation of these methodologies to clinical and surgical settings that is the topic of this dissertation.

Extraction nanoelectrospray (nESI) ionization is another ambient ionization technique used in the research described herein to overcome some of the challenges inherent to the translation of diagnostic assays to miniature mass spectrometers (Mini MS), specifically a reduction in sensitivity. In this method, the tissue specimen is touched with a thin strip of Whatman 1 filter paper (ca. 0.5 mm wide and 15 mm long) that was then inserted into a nanotip (i.d. 0.86 mm, length ~4 cm) pre-filled with 20 µL of solvent.(33) The nanotip is subsequently placed in a custom 3D printed sample holder for MS analysis. Extraction of analytes occurs online during nESI. Similar to DESI, the chemistry of the solvent can be modified to favor the ionization of different analytes of interest.

In addition to the aforementioned DESI and nESI, there are a plethora of other ambient ionization methods that have been evaluated as intraoperative diagnostic modalities. In particular, probe-based ambient ionization methods, such as probe electrospray ionization(34) and touch spray ionization(35), have produced pathologically relevant results on fresh tissue samples. Rapid evaporative ionization MS has been used intraoperatively to characterize a variety of cancer types.(36, 37) Several laser ablation systems, based on picosecond-infrared and other optical regimes, have generated diagnostic MS signals with little to no tissue damage.(38, 39) Lastly, the MasSpec Pen has been used *in vivo* to assess residual tumor in a minimally-invasive, non-destructive manner, most recently in human ovarian cancer.(40, 41)

1.3 Applications of Ambient Ionization Mass Spectrometry in Point-of-Care Diagnostics

Considerable attention has been given to point-of-care (POC) diagnostics due to their ability to rapidly analyze samples onsite, in sharp contrast to conventional diagnostic modalities that require the shipment of a patient sample to a centralized laboratory for analysis with turnarounds on the order of hours to days. POC devices are particularly attractive due to their ease of operation, speed of analysis, and, in many cases, low cost. Further, POC testing can be used to personalize patient treatment strategies, increase throughputs of centralized lab by diverting testing efforts, and perform of *in vivo* diagnostics. With an increasingly personalized approach to medicine, the demand for the development of POC diagnostic methods is likely to continue.

Despite the obvious clinical desire for POC diagnostics, a significant limitation of current POC devices is the loss of analytical (e.g., detection limits) and clinical (e.g., sensitivity and specificity) performance compared to conventional laboratory tests. Ambient ionization MS methods, such those described, are apt for POC applications due to the inherent speed, accuracy, and lack of sample pretreatment and purification.(42) The implementation of these methods in clinical and surgical settings has the ability to inform clinical decision making, both intraoperatively and postoperatively, and enhance patient care by improving surgical outcome, maximizing extent of resection, reducing operation length, and increasing treatment efficacy.

This dissertation contains descriptions of three clinical studies aimed at the development, optimization, translation, and validation of ambient ionization MS-based methods for use in intraoperatively for the assessment of tumor infiltration at surgical margins and the detection of prognostic genetic mutations. Two of the clinical studies, described in Chapters 2 and 5, were performed using a minimally modified, commercially available benchtop mass spectrometer measuring 4.25 feet tall and weighing approximately 300 pounds.(22, 23, 26) The instrument is placed on a mobile cart with all required axillary equipment enclosed, better suiting it to POC application. That said, by nature, POC applications demand the adaptation of MS methodologies to smaller devices. Recent advances in the development of Mini MS are of considerable interest and could ease barriers to translation.(43) Specifically, Mini MS boast small footprints, simple operation, and low power consumption, noise levels, and cost, making them attractive candidates for point-of-care use. While adequate analytical and clinical performance remain a challenge, modifications to sampling and ionization methods, like those described in Chapter 3, may assist in the increased use of Mini MS intraoperatively.(44)

1.4 Applications of High-Throughput Ambient Ionization Mass Spectrometry Screening of Biological Specimens

In addition to POC applications, ambient ionization, in particular DESI-MS, is well-suited for high-throughput applications. The high-throughput analysis of tissue specimens, specifically arrays of up to 1000 tissue core biopsies known as tissue microarrays (TMAs), is routinely performed as an effective means of tissue-based biomarker analysis, specifically the standardized screening of biomarkers and biomarker expression, using immunohistochemistry and fluorescent in situ hybridization in a variety of cancers.(45) The use of TMA for simultaneous processing of hundreds of samples using identical conditions, conserving of reagents, saving time, and decreasing the amount of tissue required for study. However, the molecular analysis of TMAs requires the processing and staining of hundreds to thousands of slides, a labor-intensive and time-consuming task when many tumors are analyzed, as well as the development and/or modification of unique IHC and fluorescent-based methods for each biomarker investigated, precluding the ability to identify biomarkers for which a suitable staining protocol does not already exist.

MS-based methods of tissue analysis have proven successful at detecting these molecular features and rapidly generating a large amount of spectral data.(46) Further, when using ambient ionization methods, including DESI-MS, the time limiting steps of sample pretreatment and purification are eliminated, allowing for the ability to perform high-throughput characterization of molecular features(47) including the screening of organic reactions(48-50), generation of spectral libraries(51), and characterization of biological assays(52-54) and bacteria(55). In Chapter 4, we report an application an existing high-throughput DESI-MS system for the rapid characterization of arrays of unmodified, flash frozen tissue biopsies of up to 6,144 samples/array and with throughputs greater than one sample per second. If the analytical and clinical performance is maintained, the method could become a standard tool in the generation of spectral libraries for sample classification, the identification of biomarkers through large-scale studies, and the ability to assess the effectiveness of drug candidates.

1.5 Research Objectives

My dissertation has focused on the development, application, and translation of ambient ionization MS-based platforms in clinical and surgical settings, specifically in brain cancer diagnostics and surgical decision making. The objective was to develop and optimize ambient

ionization methods offline and translate and validate said methods intraoperatively with the overarching goal of the acceptance of ambient ionization MS methods (e.g. DESI-MS and nESI-MS) as a complementary intraoperative diagnostic modality to standard of care methods (e.g. intraoperative histopathological examination of tissue biopsies) capable of providing additional, prognostic molecular information that can improve patient care and outcome, applied specifically to the topic of human brain cancer. To that end, I have participated in research studying the distinct molecular signatures of healthy and diseased brain parenchyma, multiple different types of human brain cancers and glioma classifications, and prognostic genetic mutations, specifically IDH mutations. Additionally, I have made contributions to improved DESI-MS assays for IDH genotyping, the adaptation of the methodology to a Mini MS, and the development of a novel HT-DESI-MS method for the rapid characterization of TMAs.

Chapter 2 describes the results of an initial 49-patient intraoperative study with the goal of successfully translating a DESI-MS system and methodology for assessing IDH genotype, tumor infiltration, and disease state developed offline to an intraoperative setting. The intraoperative DESI-MS system consists of a minimally modified linear trap quadrupole (LTQ) placed on a custom-machined, stainless-steel cart that houses all necessary hardware for the operation of the instrument and allows for the system to be wheeled into and out of neurosurgical operating rooms (ORs). This system was used in ORs at Indiana University (IU) School of Medicine in a cohort of 49 human patients undergoing craniotomy with tumor resection for suspected diffuse glioma in collaboration with a team of enthusiastic neurosurgeons including Dr. Mahua Dey and Dr. Aaron A. Cohen-Gadol and a neuropathologist, Dr. Eyas Hattab. Small tissue biopsies from the tumor core and surgical margins were smeared and analyzed by DESI-MS in the OR in less than five minutes. Validation of the DESI-MS results were made via comparison with, in the case of IDH mutations, IHC and genetic testing and, in the case of tumor infiltration and disease state, pathological review of tissue smears. Assessment of IDH mutations status using DESI tandem MS (DESI-MS/MS) to measure 2HG ion intensities from 71 core biopsies yielded a sensitivity, specifically, and accuracy of 89, 100, and 94%, respectively. Assessment of tumor infiltration, classified as low or high TCP, in 203 tumor and core biopsies by measurement of the signal intensity from the metabolite N-Acetylaspartic acid (NAA) intensity yielded a sensitivity, specificity, and accuracy of 91, 76, and 83%, respectively, while TCP assessment using lipid profile deconvolution yielded a sensitivity, specificity, and accuracy of 76, 85, and 81%,

respectively. Assessment of disease state (defined as glioma (G) or infiltrative margin (IM) by combining metabolite and lipid profiles and using PCA-LDA predictions to generate predictions of disease state yield a sensitivity, specificity, and accuracy of 63, 83, and 74%, respectively. This initial study demonstrated the potential value of ambient ionization MS methods in intraoperative, diagnostic applications and paved the way for additional clinical studies.

The first use of a Mini MS to assess IDH genotypes of human gliomas is described in Chapter 3. Point-of-care applications necessitate the adaptation of MS methodologies to smaller devices. Miniature mass spectrometers (Mini MS) boast small footprints, simple operation, and low power consumption, noise levels, and cost, making them attractive candidates for point-of-care use. Given the success of the DESI-MS/MS assay for detecting IDH mutations and in collaboration with PurSpec, Dr. Zheng Ouyang, and a team of neurosurgeons at IU School of Medicine, we modified and translated the methodology to a Mini MS for the intraoperative determination of IDH genotype using a new ionization method and MS methodology to overcome lower sensitivities inherent to miniature devices, as described in detail in Chapter 3. Specifically, a small modification to the IDH genotyping assay was implemented in which MS/MS data is recorded simultaneously for 2HG and Glu, so as to incorporate this endogenous internal standard into the MS2 measurement rather than relying on variations in the signal of a single analyte. The ratio of the signals detected from these two analytes was then used to assess IDH genotype. A total of 25 biopsies from 13 patients were analyzed and 100% sensitivity, specificity, and accuracy are reported. The robustness of the ratiometric method was further evaluated on a benchtop instrument, where identical performance metrics were achieved. This method outperformed the previously described DESI-MS assay for the detection IDH genotypes and has been adopted for all future intraoperative applications.

Chapter 4 details efforts to develop a high-throughput DESI-MS (HT-DESI-MS) method for the rapid characterization of biological specimens, specifically tissue biopsies arranged in tissue microarrays (TMAs). As demonstrated intraoperatively, MS-based methods are capable of detecting a wide variety of molecular features, rapidly producing large quantities of information-dense data. That said, their inherent speed is rarely utilized, often due to lengthy purification and separation techniques coupled to the MS analysis. Conversely, ambient ionization, in particular DESI-MS, is well-suited for high-throughput applications due to its lack of sample preparation and purification. Over the past 10 years, we have acquired a large number of brain tissue specimens

from biobanks and patients who have participated in the intraoperative studies. Each of these samples has been molecularly characterized offline, and in some cases intraoperatively, by DESI-MS analysis of tissue sections and/or tissue smears with speeds on the order of five minutes per specimen, throughputs that preclude their analysis in a high-throughput manner. A method, such as HT-DESI-MS, that allows for the rapid analysis of a large number of samples could be a valuable tool for a wide variety of clinical and pharmaceutical applications including the generation of spectral libraries for specimen classification, the identification of biomarkers in large-scale studies, the correlation of molecular features with anatomical characteristics when coupled to digital pathology, and the assessment of drug efficacy. Using the same molecular analysis methods developed offline and applied intraoperatively in ongoing clinical studies, we developed a HT-DESI-MS method using a previously developed HT-DESI-MS system for the rapid characterization of disease state, human brain tumor type, glioma classification, and detection of IDH mutations in tissue microarrays (TMA) of banked and fresh human brain tissue biopsies. This study provided support for subsequent analyses of additional TMAs and correlation of metabolic and lipidic aberrations with patient outcomes, the focus of an ongoing collaboration with Mayo Clinic – Jacksonville. Further, the diagnostic molecular features and optimized models identified by leveraging the large data volumes that were generated using HT-DESI-MS can be used to inform and validate current intraoperative molecular diagnostic approaches.

The advanced optimization and validation of the DESI-MS platform for intraoperative glioma diagnostics has been the focus of my research for the past two years. The aforementioned DESI-MS clinical study laid the groundwork for a follow-up study in collaboration with Mayo Clinic – Jacksonville where optimization and validation of the DESI-MS platform is ongoing. To date, we have analyzed 271 biopsies from 34 patients. A modification to the IDH mutation assessment of biopsies was implemented midway through the study. Due to the observed lower intensity of low mass (metabolic) signals, including those of the second-generation product ion (MS^3) spectra of 2HG, a small modification to the IDH genotyping assay was implemented in which MS/MS data is recorded simultaneously for 2HG and Glu. Offline experiments conducted on banked human glioma biopsies and a small-scale clinical study using a Mini MS (described in Chapter 3) demonstrated the value and increased accuracy of this approach. IDH mutation assessment of 116 core biopsies from 23 patients indicated 93% sensitivity, 100% specificity, and 98% accuracy. While these results are tentative given the small number of biopsies, they are an

improvement over the diagnostic accuracy achieved in the first DESI-MS clinical study and provide support for the important contributions ambient ionization MS methods can have on the surgical and clinical fields. Validation of TCP estimates based on lipid profiles with histopathological estimates of 151 biopsies from 37 patients with primary gliomas indicated 77% sensitivity, 57% specificity, and 65% accuracy while TCP estimates based on NAA intensity indicated 83% sensitivity, 65% specificity, and 71% accuracy. A detailed description of the current state of this work, and comments on the strengths and weaknesses of the current approach, as well as future directions, can be found in Chapter 5. This DESI-MS platform will continue to provide clinicians with diagnostic and previously unavailable information that can improve patient outcomes by informing surgical decision making and adjuvant treatment strategies, complementing and not interfering with standard of care protocols.

1.6 References

1. Hayden EC. Genomics boosts brain-cancer work. Nature. 2010;463(7279):278.

2. Ogrinc N, Saudemont P, Takats Z, Salzet M, Fournier I. Cancer Surgery 2.0: Guidance by Real-Time Molecular Technologies. Trends Mol Med. 2021;27(6):602-15.

3. Louis DN, Perry A, Wesseling P, Brat DJ, Cree IA, Figarella-Branger D, et al. The 2021 WHO Classification of Tumors of the Central Nervous System: a summary. Neuro Oncol. 2021;23(8):1231-51.

4. Crick F. Central dogma of molecular biology. Nature. 1970;227(5258):561-3.

5. Wood PL. Mass spectrometry strategies for clinical metabolomics and lipidomics in psychiatry, neurology, and neuro-oncology. Neuropsychopharmacology. 2014;39(1):24-33.

6. Collins RRJ, Patel K, Putnam WC, Kapur P, Rakheja D. Oncometabolites: A New Paradigm for Oncology, Metabolism, and the Clinical Laboratory. Clin Chem. 2017;63(12):1812-20.

7. Wang R, Li B, Lam SM, Shui G. Integration of lipidomics and metabolomics for in-depth understanding of cellular mechanism and disease progression. J Genet Genomics. 2020;47(2):69-83.

8. Warburg O. On the origin of cancer cells. Science. 1956;123(3191):309-14.

9. Fiehn O. Plant Molecular Biology. 2002;48(1/2):155-71.

10. Rattray NJW, Deziel NC, Wallach JD, Khan SA, Vasiliou V, Ioannidis JPA, et al. Beyond genomics: understanding exposotypes through metabolomics. Hum Genomics. 2018;12(1):4.

11. Hamburg MA, Collins FS. The path to personalized medicine. N Engl J Med. 2010;363(4):301-4.

12. Chen R, Smith-Cohn M, Cohen AL, Colman H. Glioma Subclassifications and Their Clinical Significance. Neurotherapeutics. 2017;14(2):284-97.

13. Zhang P, Xia Q, Liu L, Li S, Dong L. Current Opinion on Molecular Characterization for GBM Classification in Guiding Clinical Diagnosis, Prognosis, and Therapy. Front Mol Biosci. 2020;7:562798.

14. Ene CI, Holland EC. Personalized medicine for gliomas. Surg Neurol Int. 2015;6(Suppl 1):S89-95.

15. Chen R, Ravindra VM, Cohen AL, Jensen RL, Salzman KL, Prescot AP, et al. Molecular features assisting in diagnosis, surgery, and treatment decision making in low-grade gliomas. Neurosurg Focus. 2015;38(3):E2.

16. Weinberg BD, Kuruva M, Shim H, Mullins ME. Clinical Applications of Magnetic Resonance Spectroscopy in Brain Tumors: From Diagnosis to Treatment. Radiol Clin North Am. 2021;59(3):349-62.

17. Mat Zin AA, Zulkarnain S. Diagnostic Accuracy of Cytology Smear and Frozen Section in Glioma. Asian Pac J Cancer Prev. 2019;20(2):321-5.

18. Zulkarnain S, Yunus N, Kandasamy R, Zun AB, Mat Zin AA. Evaluation Study of Intraoperative Cytology Smear and Frozen Section of Glioma. Asian Pac J Cancer Prev. 2020;21(10):3085-91.

19. Eberlin LS, Norton I, Dill AL, Golby AJ, Ligon KL, Santagata S, et al. Classifying human brain tumors by lipid imaging with mass spectrometry. Cancer Res. 2012;72(3):645-54.

20. Eberlin LS, Norton I, Orringer D, Dunn IF, Liu X, Ide JL, et al. Ambient mass spectrometry for the intraoperative molecular diagnosis of human brain tumors. Proc Natl Acad Sci U S A. 2013;110(5):1611-6.

21. Jarmusch AK, Pirro V, Baird Z, Hattab EM, Cohen-Gadol AA, Cooks RG. Lipid and metabolite profiles of human brain tumors by desorption electrospray ionization-MS. Proc Natl Acad Sci U S A. 2016;113(6):1486-91.

22. Pirro V, Alfaro CM, Jarmusch AK, Hattab EM, Cohen-Gadol AA, Cooks RG. Intraoperative assessment of tumor margins during glioma resection by desorption electrospray ionization-mass spectrometry. Proc Natl Acad Sci U S A. 2017;114(26):6700-5.

23. Alfaro CM, Pirro V, Keating MF, Hattab EM, Cooks RG, Cohen-Gadol AA. Intraoperative assessment of isocitrate dehydrogenase mutation status in human gliomas using desorption electrospray ionization-mass spectrometry. J Neurosurg. 2019:1-8.

24. Cooks RG, Ouyang Z, Takats Z, Wiseman JM. Ambient mass spectrometry. Science. 2006;311(5767):1566-70.

25. Takáts Z, Wiseman JM, Cooks RG. Ambient mass spectrometry using desorption electrospray ionization (DESI): instrumentation, mechanisms and applications in forensics, chemistry, and biology. J Mass Spectrom. 2005;40(10):1261-75.

26. Brown HM, Alfaro CM, Pirro V, Dey M, Hattab EM, Cohen-Gadol AA, et al. Intraoperative Mass Spectrometry Platform for IDH Mutation Status Prediction, Glioma Diagnosis, and Estimation of Tumor Cell Infiltration. J Appl Lab Med. 2021;6(4):902-16.

27. Dill AL, Ifa DR, Manicke NE, Ouyang Z, Cooks RG. Mass spectrometric imaging of lipids using desorption electrospray ionization. J Chromatogr B Analyt Technol Biomed Life Sci. 2009;877(26):2883-9.

28. Ifa DR, Eberlin LS. Ambient Ionization Mass Spectrometry for Cancer Diagnosis and Surgical Margin Evaluation. Clin Chem. 2016;62(1):111-23.

29. Kooijman PC, Nagornov KO, Kozhinov AN, Kilgour DPA, Tsybin YO, Heeren RMA, et al. Increased throughput and ultra-high mass resolution in DESI FT-ICR MS imaging through new-generation external data acquisition system and advanced data processing approaches. Sci Rep. 2019;9(1):8.

30. Wang H, Manicke NE, Yang Q, Zheng L, Shi R, Cooks RG, et al. Direct Analysis of Biological Tissue by Paper Spray Mass Spectrometry. Analytical Chemistry. 2011;83(4):1197-201.

31. Woolman M, Zarrine-Afsar A. Platforms for rapid cancer characterization by ambient mass spectrometry: advancements, challenges and opportunities for improvement towards intrasurgical use. Analyst. 2018;143(12):2717-22.

32. Jarmusch AK, Alfaro CM, Pirro V, Hattab EM, Cohen-Gadol AA, Cooks RG. Differential Lipid Profiles of Normal Human Brain Matter and Gliomas by Positive and Negative Mode Desorption Electrospray Ionization - Mass Spectrometry Imaging. PLoS One. 2016;11(9):e0163180.

33. Pu F, Alfaro CM, Pirro V, Xie Z, Ouyang Z, Cooks RG. Rapid determination of isocitrate dehydrogenase mutation status of human gliomas by extraction nanoelectrospray using a miniature mass spectrometer. Anal Bioanal Chem. 2019;411(8):1503-8.

34. Yoshimura K, Mandal MK, Hara M, Fujii H, Chen LC, Tanabe K, et al. Real-time diagnosis of chemically induced hepatocellular carcinoma using a novel mass spectrometry-based technique. Anal Biochem. 2013;441(1):32-7.

35. Alfaro CM, Jarmusch AK, Pirro V, Kerian KS, Masterson TA, Cheng L, et al. Ambient ionization mass spectrometric analysis of human surgical specimens to distinguish renal cell carcinoma from healthy renal tissue. Anal Bioanal Chem. 2016;408(20):5407-14.

36. Balog J, Sasi-Szabo L, Kinross J, Lewis MR, Muirhead LJ, Veselkov K, et al. Intraoperative tissue identification using rapid evaporative ionization mass spectrometry. Sci Transl Med. 2013;5(194):194ra93.

37. Phelps DL, Balog J, Gildea LF, Bodai Z, Savage A, El-Bahrawy MA, et al. The surgical intelligent knife distinguishes normal, borderline and malignant gynaecological tissues using rapid evaporative ionisation mass spectrometry (REIMS). Br J Cancer. 2018;118(10):1349-58.

38. Woolman M, Ferry I, Kuzan-Fischer CM, Wu M, Zou J, Kiyota T, et al. Rapid determination of medulloblastoma subgroup affiliation with mass spectrometry using a handheld picosecond infrared laser desorption probe. Chem Sci. 2017;8(9):6508-19.

39. Fatou B, Saudemont P, Leblanc E, Vinatier D, Mesdag V, Wisztorski M, et al. In vivo Real-Time Mass Spectrometry for Guided Surgery Application. Sci Rep. 2016;6:25919.

40. King ME, Zhang J, Lin JQ, Garza KY, DeHoog RJ, Feider CL, et al. Rapid diagnosis and tumor margin assessment during pancreatic cancer surgery with the MasSpec Pen technology. Proc Natl Acad Sci U S A. 2021;118(28).

41. Sans M, Zhang J, Lin JQ, Feider CL, Giese N, Breen MT, et al. Performance of the MasSpec Pen for Rapid Diagnosis of Ovarian Cancer. Clin Chem. 2019;65(5):674-83.

42. Ferreira CR, Yannell KE, Jarmusch AK, Pirro V, Ouyang Z, Cooks RG. Ambient Ionization Mass Spectrometry for Point-of-Care Diagnostics and Other Clinical Measurements. Clin Chem. 2016;62(1):99-110.

43. Jiao B, Ye H, Liu X, Bu J, Wu J, Zhang W, et al. Handheld Mass Spectrometer with Intelligent Adaptability for On-Site and Point-of-Care Analysis. Anal Chem. 2021;93(47):15607-16.

44. Brown HM, Pu F, Dey M, Miller J, Shah MV, Shapiro SA, et al. Intraoperative detection of isocitrate dehydrogenase mutations in human gliomas using a miniature mass spectrometer. Anal Bioanal Chem. 2019;411(30):7929-33.

45. Kallioniemi OP, Wagner U, Kononen J, Sauter G. Tissue microarray technology for high-throughput molecular profiling of cancer. Hum Mol Genet. 2001;10(7):657-62.

46. Gorynska PZ, Chmara K, Kupcewicz B, Gorynski K, Jaroch K, Paczkowski D, et al. Metabolomic Phenotyping of Gliomas: What Can We Get with Simplified Protocol for Intact Tissue Analysis? Cancers (Basel). 2022;14(2).

47. Wleklinski M, Loren BP, Ferreira CR, Jaman Z, Avramova L, Sobreira TJP, et al. High throughput reaction screening using desorption electrospray ionization mass spectrometry. Chem Sci. 2018;9(6):1647-53.

48. Logsdon DL, Li Y, Paschoal Sobreira TJ, Ferreira CR, Thompson DH, Cooks RG. High-Throughput Screening of Reductive Amination Reactions Using Desorption Electrospray Ionization Mass Spectrometry. Organic Process Research & Development. 2020;24(9):1647-57.

49. Jaman Z, Logsdon DL, Szilagyi B, Sobreira TJP, Aremu D, Avramova L, et al. High-Throughput Experimentation and Continuous Flow Evaluation of Nucleophilic Aromatic Substitution Reactions. ACS Comb Sci. 2020;22(4):184-96.

50. Biyani SA, Qi Q, Wu J, Moriuchi Y, Larocque EA, Sintim HO, et al. Use of High-Throughput Tools for Telescoped Continuous Flow Synthesis of an Alkynylnaphthyridine Anticancer Agent, HSN608. Organic Process Research & Development. 2020;24(10):2240-51.

51. Le MT, Morato NM, Kaerner A, Welch CJ, Cooks RG. Fragmentation of Polyfunctional Compounds Recorded Using Automated High-Throughput Desorption Electrospray Ionization. J Am Soc Mass Spectrom. 2021;32(8):2261-73.

52. Morato NM, Holden DT, Cooks RG. High-Throughput Label-Free Enzymatic Assays Using Desorption Electrospray-Ionization Mass Spectrometry. Angew Chem Int Ed Engl. 2020;59(46):20459-64.

53. Morato NM, Le MT, Holden DT, Graham Cooks R. Automated High-Throughput System Combining Small-Scale Synthesis with Bioassays and Reaction Screening. SLAS Technol. 2021;26(6):555-71.

54. Kulathunga SC, Morato NM, Zhou Q, Cooks RG, Mesecar AD. Desorption Electrospray Ionization Mass Spectrometry Assay for Label-Free Characterization of SULT2B1b Enzyme Kinetics. ChemMedChem. 2022:e202200043.

55. Szalwinski LJ, Gonzalez LE, Morato NM, Marsh BM, Cooks RG. Bacterial growth monitored by two-dimensional tandem mass spectrometry. Analyst. 2022;147(5):940-6.

CHAPTER 2. INTRAOPERATIVE MASS SPECTROMETRY PLATFORM FOR IDH MUTATION STATUS PREDICTION, GLIOMA DIAGNOSIS, AND ESTIMATION OF TUMOR CELL INFILTRATION

This chapter was adapted from the manuscript published in *The Journal of Applied Laboratory Medicine*: Brown HM, Alfaro CM, Pirro V, Dey M, Hattab EM, Cohen-Gadol AA, Cooks RG. Intraoperative mass spectrometry platform for IDH mutation status prediction, glioma diagnosis, and estimation to tumor cell infiltration. J Appl Lab Med. 2021; 6(4):902-16. DOI: 10.1093/jalm/jfaa233.

2.1 Introduction

Diffuse gliomas are high morbidity primary brain tumors. The five-year survival rate of patients with glioblastoma is less than 5%.(1) The primary treatment option for gliomas is gross total surgical resection accompanied by adjuvant chemoradiotherapy.(2-4) A central dilemma of the neurosurgeon is preservation of vital brain functions while maximizing extent of resection. Unfortunately, glioma cells are diffusely infiltrative and the high risk of neurological deficits often results in residual tumor at surgical margins, leading to progression and recurrence.(5, 6)

Accurate glioma diagnosis and prognosis increasingly relies on molecular genetic information assessed from tumor core biopsies.(2) Currently, brain tumor resections are performed without the aid of a molecular diagnosis, as these slow assays must be performed post-operatively.(7) The development of rapid intraoperative molecular diagnostics could help improve glioma patient management and the quality of surgical resection.(7-10) Notably, recent studies show that the effect of extent of resection on overall survival and malignant-free progression is significantly different between isocitrate dehydrogenase-wildtype (IDH-wt) and IDH-mutant (IDH-mut) gliomas, suggesting that surgical strategies may be impacted favorably by knowledge of the IDH mutation status at the time of surgery.(9, 10) It is important to note that even if tumor cells are found in eloquent brain areas, surgical resection of that tissue may not be indicated due to the significant harm it may cause to the patient. However, it may serve as an area to target for post-operative radiotherapy or application of local chemotherapeutics, the choice of which can be guided by information provided by rapid molecular diagnostics.

Mass spectrometry-based methods of tissue analysis may be able to provide clinical diagnostic information on brain tissue at the time of glioma resection. In particular, ambient

ionization mass spectrometry (MS) has emerged as a family of rapid methods for intraoperative tissue analysis.(11) Ambient ionization MS methods are being evaluated for their ability to assess molecular features of various cancers, as well as in assessing surgical margins for residual tumor.(12, 13) Probe-based ambient methods, such as probe electrospray ionization(14) and touch spray ionization,(15) have been demonstrated to yield pathologically relevant results on fresh surgical tissue. Rapid evaporative ionization MS has been used intraoperatively in a variety of cancers.(16, 17) Several laser ablation systems, based on picosecond-infrared and other optical regimes, have been shown to yield diagnostic MS signals with low/no tissue damage.(18, 19) The MasSpec Pen has been used *in vivo* to assess residual tumor in a minimally-invasive, non-destructive approach, recently in human ovarian cancer.(20, 21)

Desorption electrospray ionization-mass spectrometry (DESI-MS), the method utilized in this work, is an ambient ionization method in which charged microdroplets of a solvent are sprayed onto a sample surface, desorbing and ionizing molecules present in the sample and transporting them into a mass spectrometer for analysis.(11, 22) DESI is used in many laboratories for biological applications,(23, 24) including the distinction between cancerous and normal tissues in a variety of human organs.(12, 25, 26) Using banked, fresh-frozen brain tissue, we have demonstrated the capability to differentiate gliomas, meningiomas, and pituitary tumors with high accuracy,(27) along with the capability to provide glioma subtyping.(28-30) Importantly, these brain cancers could be distinguished readily from normal brain tissue.

This chapter summarizes the results from an initial proof-of-concept study that demonstrated intraoperative application of DESI-MS during glioma resection using a customized, stand-alone mass spectrometer. The findings of this study provide support for an ongoing clinical study in collaboration with Mayo Clinic – Jacksonville, the results of which are summarized in Chapter 5. Initial data from a set of 10 human patients was published early in the project to demonstrate the potential clinical utility of TCP estimation by intraoperative MS. (31) (Table 2.1). Using the same customized mass spectrometer, approximately half way through the study we developed and applied an intraoperative DESI-MS assay for the assessment of IDH-mutation status by detecting the oncometabolite 2-Hydroxyglutarate (2HG in a set of 51 glioma core biopsies obtained from 25 human patients and analyzed intrasurgically.(32) IDH mutations, specifically R132H mutations, disrupt the conversion of isocitrate to α-ketoglutarate by IDH1. Additionally, IDH1 mutations were found to result in the ability of IDH1 to catalyze the reduction of α-ketoglutarate to R(-)-2HG and,

unsurprisingly, 2HG levels have been found to be significantly higher in IDH1 mutated human gliomas.(33) Subsequently, we combined and improved our previously developed methods of tissue smear classification and analyzed tissue biopsy-smears during tumor resection in a cohort of 49 glioma patients, integrating data on new patients and re-examining data for patients whose data appear in prior publications. (Table 6 indicates the numbers of patients in each category.) As the development of an online methodology for the determination of IDH mutation status was developed midway through the study, measurement of 2HG as a predictor of IDH mutation status was collected for only 30 of the 49 recruited patients. While previous publications have analyzed the data with respect to individual tissues smears, in this work, we have elected to analyze the data with respect to biopsy in order to facilitate the understanding of the results in the context of a clinical setting. Three categories of information were acquired using DESI-MS: 1) IDH mutation status, 2) tumor cell percentage (TCP), and 3) disease status. When the DESI-MS results are considered in combination with other available data (e.g., MRI & *in vivo* brain mapping), they should allow the neurosurgeon to make better informed resection decisions

Table 2.1 Confusion matrix for assessing correlation between histopathology assessments and the DESI-MS estimates of TCP and disease status of tissue biopsies from 10 patients whose data was previously published in reference 1 (Pirro et. al. PNAS 2017).

		Histopathology[a]	
		High TCP/Glioma[b]	Low TCP/Infiltrative Margin[b]
Lipid Deconvolution TCP Estimate	High TCP/Glioma[b]	29	4
Full Scan NAA Intensity TCP Estimate		32	5
PCA-LDA Diagnosis		28	4
Lipid Deconvolution TCP Estimate	Low TCP/Infiltrative Margin[b]	6	19
Full Scan NAA Intensity TCP Estimate		3	18
PCA-LDA Diagnosis		9	17

	Lipid Deconvolution TCP Estimate	**Full Scan NAA Intensity TCP Estimate**	**PCA-LDA Diagnosis**
Sensitivity:	83%	91%	76%
Specificity:	83%	78%	81%
Accuracy:	83%	86%	78%

The results of an ongoing clinical study in collaboration with Mayo Clinic – Jacksonville are described in detail in Chapter 5. The correlation of histopathology assessments and DESI-MS estimates of TCP and disease status for this new patient cohort are summarized in Table 5.6.

2.2 Materials and Methods

2.2.1 Human Subjects

Human subjects research was performed in accordance with an Institutional Review Board approved study at the Indiana University School of Medicine (IRB #1410342262). Glioma patients undergoing craniotomy with tumor resection were prospectively enrolled after providing written informed consent and Health Insurance Portability and Accountability Act authorization. No DESI-MS results were shared with neurosurgeons during the surgical resection so as not to affect the standard of care.

2.2.2 Intraoperative DESI-MS

All experiments were performed using a modified linear ion trap mass spectrometer (Thermo LTQ) as previously described.(1, 2) For each surgery, the instrument was rolled into the operating room (OR) and turned on. During tumor resection, small stereotactic tissue biopsies (approximately 5-10 mg each) were provided by the neurosurgeon to the mass spectrometer operators for DESI-MS analysis. The number and location of the biopsies were determined according to the surgeon's best medical judgement. Samples from the tumor core (for assessing diagnostic information) as well as surgical margins (for assessing residual tumor) were provided for each case. The tissue biopsies were smeared on a glass slide and then analyzed by DESI-MS using a zig-zag raster pattern acquire representative data (Figure 5A). Two different negative ion mode DESI-MS methods were used. Using method 1, full scan lipid (*m/z* 700 - 1000) and metabolite (*m/z* 80 - 200) mass spectra and a targeted MS^2 scan for N-Acetylaspartic acid (NAA, *m/z* 174 → O), were acquired over 3.3 minutes. Using method 2, MS^2 (MS/MS) and MS^3 data were acquired specific to 2HG (*m/z* 147 → O and *m/z* 147 → *m/z* 129 → O, respectively), along with a full scan metabolite profile (*m/z* 50 - 200), all over a period of 3.3 minutes (Figure 5B & 5C). Method 1 utilized 1:1 dimethylformamide (DMF)-acetonitrile (ACN) and method 2 utilized 25:37:38 DMF-ACN-ethanol (EtOH) as solvent. A summary of the number of patients, biopsies, and smears, noting which were excluded and which were included in previous publications is depicted in Figure 5D.

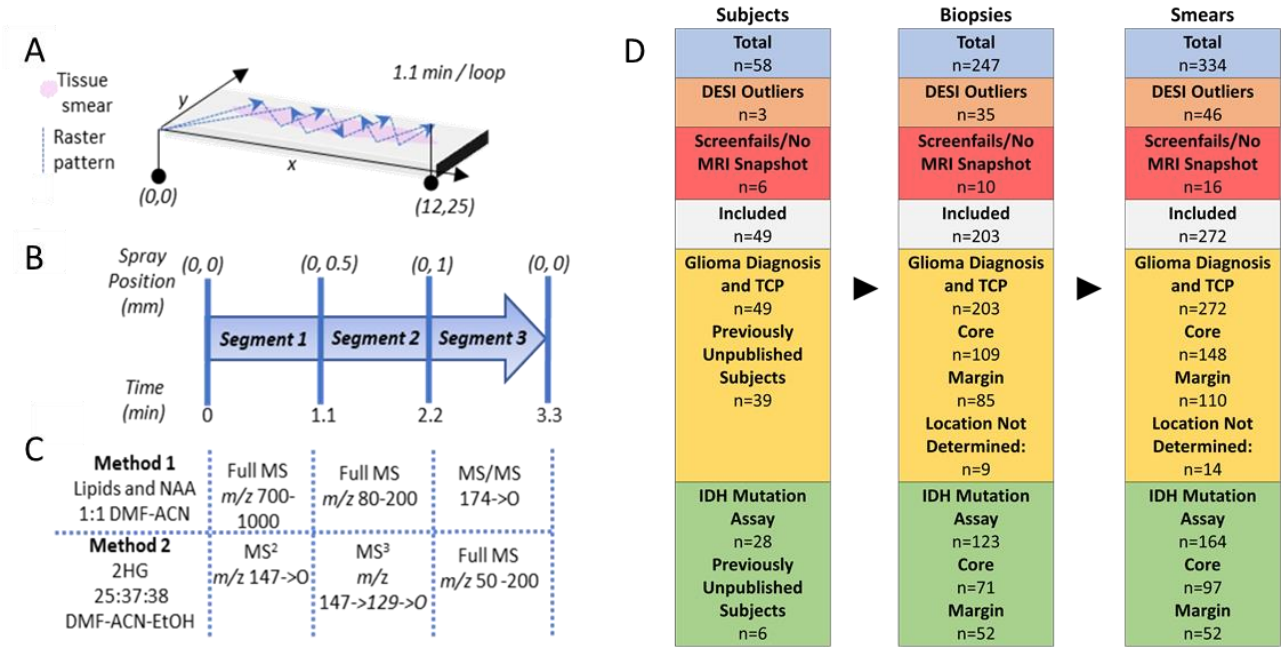

Figure 2.1 Summary of the DESI-MS method. (A) Smeared tissue (pink) is analyzed with DESI spray using a zigzag raster pattern (dotted lines, with direction noted by arrow heads), spanning 12mm in x-dimension and 25mm in y-dimension over 1.1 min; the pattern is repeated 3 times. The DESI spot is offset 0.5mm in the y-dimension after each raster loop. (B) DESI spray position and the timeline for the DESI-MS method. The (x, y) coordinates denote the starting position of the DESI spot for each raster loop. (C) Description of the 2 DESI-MS methods, shown synchronized with the position of the moving stage. A different set of MS data is collected during each method segment. Note the use of full MS, MS/MS (MS^2), and MS^3 experiments. (D) Summary of number of patients, biopsies, and smears, noting how many were excluded, and which patients are new to the study. See Supplemental Tables 2–5 for additional patient cohort data. Data from earlier patients recruited in the study were published in Reference 27 for glioma diagnosis and TCP, and in Reference 32 for IDH-mutation assessment. DESI data was considered an outlier if no lipid or metabolite profile scans were retained after data filtering due to low signal or high similarity to data collected from a blank glass slide.

2.2.3 Data Analysis

De-identified clinical data were obtained for each patient for correlation with the DESI-MS results. The DESI-MS data were analyzed in MATLAB using custom algorithms to remove background scans (e.g., signal collected from regions of the glass slide containing no tissue) and to perform statistical classifications. MS scans from areas of the glass slide containing no smeared tissue and from smears giving insufficient intensity were excluded by applying a cut-off to the absolute signal intensity. Only scans with mass spectra having the summed ion counts greater than the cutoff value were used for chemical predictions. Additionally, for each selected mass spectrum,

the full width at half maximum (FWHM) was calculated for the base peak; all spectra with resolution < 1000 were excluded.

2.2.4 Histopathological Analysis

After DESI-MS analysis, the tissue smears were moved from the surgical core to the Indiana University Health Pathology Laboratory and H&E stained. The H&E-stained smears were blindly evaluated by an expert neuropathologist (E.M.H.) and interpretations of smear diagnosis, tumor grade, TCP, and smear quality were provided (Table 10). The entire smear was evaluated and the interpretations made reflect the average state of the entire smear. Smears with significant heterogeneity (e.g., half the slide diseased and half normal) were rare (two smears out of 272 in this study).

2.3 Results and Discussion

2.3.1 Summary of Patient Cohort and Tissue Biopsies

Data was collected from 49 human patients; 203 biopsies were obtained and 272 smears were analyzed (Figure 2.1D). For some biopsies, multiple smears were created and analyzed. The patient cohort and DESI-MS results are described in detail in Tables 2.2-2.6. Table 2.2 summarizes the number of patients and the biopsies obtained, indicates whether they have been included in a previous, preliminary publication, and whether patients were excluded after recruitment; Table 2.3 provides the demographics, diagnosis, and treatment information; Table 2.4 provides additional histopathology data. The statistical predictions for disease status, TCP, and IDH mutation status for all analyzed smears are tabulated in Table 2.5. The histopathology assessments of all these DESI-MS analyzed smears are tabulated in Table 2.6. The overall patient classifications are described in detail for IDH mutation status, TCP and disease status in the following sections.

Table 2.2 Summary of patients recruited, if excluded from study or analysis, and total biopsies/smears

Patient #	Screenfail	Reason for Screenfail	Outlier	Reason for Outlier	Previously Published*	Total Biopsies	Total Smears
01	No		No	-	1	9	9
02	No		Yes	Poor DESI signal	1	0	0
03	Yes	Not glioma	No	-	1	0	0
04	No		Yes	Poor DESI signal	1	0	0
05	No		No	-	1	7	8
06	No		No	-	1	6	7
07	No		No	-	1	5	6
08	Yes (withdrawn)	Resection unsafe	No	-	1	0	0
09	No		No	-	1	7	9
10	No		No	-	1	6	7
11	No		Yes	Poor DESI signal	1	0	0
12	No		No	-	1	7	8
13	No		No	-	1	7	10
14	No		No	-	1	6	8
15	No		No	-	1	6	9
16	No		No	-	1	7	7
17	No		No	-	N	4	4
18	No		No	-	N	5	8
19	No		No	-	N	7	10
20	No		No	-	N	5	8
21	No		No	-	N	6	10
22	Yes	Not glioma	No	-	N	0	0
23	No		No	-	N	4	9
24	No		No	-	2	2	3
25	No		No	-	2	7	10

Table 2.2 continued

26	No		No	-	2	5	5
27	No		No	-	2	6	10
28	No		No	-	2	5	8
29	No		No	-	2	6	10
30	No		No	-	2	5	6
31	No		No	-	2	5	6
32	No		No	-	2	5	7
33	No		No	-	2	6	6
34	No		No	-	2	3	6
35	No		No	-	2	6	6
36	Yes	Not glioma	No	-	N	0	0
37	No		No	-	2	4	5
38	No		No	-	2	6	6
39	No		No	-	2	3	3
40	No		No	-	2	3	6
41	No		No	-	2	5	5
42	No		No	-	2	3	3
43	Yes	Not glioma	No	-	N	0	0
44	No	-	No	-	2	6	10
45	No	-	No	-	2	1	1
46	No	-	No	-	N	6	9
47	No	-	No	-	2	4	8
48	No	-	No	-	2	3	7
49	Yes	Not glioma	No	-	N	0	0
50	No	-	No	-	N	6	6
51	No	-	No	-	2	6	6
52	No	-	No	-	2	3	4
53	No	-	No	-	2	6	9
54	No	-	No	-	2	3	7

Table 2.2 continued

55	No	-	No	-	N	4	4
56	No	-	No	-	N	2	4
57	No	-	No	-	N	2	4
58	No	-	No	-	N	6	7
Total Patients Included (Excluding Screenfails and Outliers) **49**	Total Screenfails (Patient) **6**		Total Outliers (Patient) **3**	New to Glioma Diagnosis and TCP (Patient) **38**	New to IDH Mutation Assay (Patient) **6**	Total Biopsies **247**	Total Smears **334**
	Average Screenfail Rate **10.3%**		Average Outlier Rate (Patient) **6.1%**			Average Biopsies per Patient **5.0**	Average Smears per Biopsy **1.4**

**"1" and "2" indicates that data was used in SI references 1(Pirro. et al. PNAS 2017) and 2 (Alfaro. et al. J. Neurosurg. 2019), respectively. No patients included in Reference 1 were included in Reference 2. "N" indicates that the data was not utilized in a previous publication. For biopsies that were utilized in Reference 2, only the 2-HG MS^n data was utilized; lipid and metabolite profile data was collected using Method 1 (Figure 6.1), but that data was not analyzed or included in the previous publication.*

Table 2.3 Patient demographics, diagnosis, and treatment information.

Patient #	Age	Gender	Race	Ethnicity	Tumor Location	Integrated Diagnosis	Primary/ Recurrent	F	Awake	Mapping	IMRI
01	30	M	W	N.H.	Left insula	Oligodendendroglioma, IDH-M,WHO grade II	P	Y	N	Y	N
05	23	M	B	A.A.	Left frontal lobe	Dysembryoplastic neuroepithelial tumor, IDH-WT, WHO grade I	P	N	N	N	N
06	24	M	W	N.H.	Left frontal intra-axial	Astrocytoma, IDH-M, WHO grade III	P	N	N	N	N
07	65	M	W	N.H.	Right parietal lobe	GBM, IDH-WT, WHO grade IV	P	N	N	N	N
09	44	F	W	N.H.	Left parietal intra-axial	Oligodendendroglioma, IDH-M and 1p/19q codeleted, WHO grade II	P	N	N	Y	N
10	47	M	W	N.H.	Left frontotemporal	GBM, IDH-WT, WHO grade IV	R	Y	N	N	N
12	30	M	W	N.H.	Left insula	GBM, IDH-M, WHO grade IV	R	N	N	N	N
13	73	F	W	N.H.	Right temporoparietal	GBM, IDH-WT, WHO grade IV	P	Y	N	N	N
14	52	F	W	N.H.	Left parietal lobe	GBM, IDH-WT, WHO grade IV	P	Y	N	N	N
15	33	F	W	N.H.	Right parietal lobe	Oligodendendroglioma, IDH-M,WHO grade II	P	N	N	N	N
16	68	M	W	N.H.	Right frontal intra-axial	Diffuse astrocytoma, IDH-M, WHO grade II	P	N	N	N	N

Table 2.3 continued

17	38	M	W	N.H.	Left posterior frontal	Diffuse glioma, IDH-M, WHO grade II	P	N	Y	Y	N
18	25	M	M.R.	N.H.	Left frontotemporal lobe	Diffuse glioma, IDH-WT, WHO grade II	P	N	N	N	N
19	39	F	W	N.H.	Left temporal lobe	Anaplastic glioma, IDH-M, WHO grade III	R	N	N	N	N
20	53	F	W	H.	Right parietal lobe; 2 nodules	GBM, IDH-WT, WHO grade IV	P	Y	N	N	N
21	45	F	W	N.H.	Left frontal lobe	Diffuse glioma, IDH-M, WHO grade II	P	N	N	N	N
23	63	F	W	N.H.	Left parietooccipital lobe	GBM, IDH-WT, WHO grade IV	P	N	N	N	Y
24	58	M	W	N.H.	Right temporal lobe	GBM and gliosarcoma, IDH wild type, WHO grade IV	P	N	N	N	N
25	47	F	W	N.H.	Right occipital lobe	GBM, IDH-WT, WHO grade IV	P	Y	N	N	N
26	46	F	W	N.H.	Right parietal lobe	Anaplastic astrocytoma, IDH-M, WHO grade III	P	N	N	Y	N
27	52	F	W	N.H.	Left frontoparietal lobe	Complex anaplastic astrocytoma, IDH-M, WHO grade III	P	N	Y	Y	N
28	63	M	W	N.H.	Right temporal lobe	Gliosarcoma, IDH-WT, WHO grade IV	R	N	N	N	N
29	53	F	W	N.H.	Right temporal lobe	Diffuse astrocytoma, IDH-WT, WHO grade II	P	N	N	N	N

Table 2.3 continued

30	38	F	W	N.H.	Right frontal lobe	Diffuse astrocytoma, IDH-WT, WHO grade II	P	N	N	N	Y
31	68	M	W	N.H.	Right parietal lobe	GBM, IDH-WT, WHO grade IV	P	N	N	N	N
32	54	F	W	N.H.	Left parietal lobe	GBM, IDH-WT, WHO grade IV	P	Y	Y	Y	N
33	20	M	W	N.H.	Left temporal lobe	Diffuse astrocytoma, IDH-M, WHO grade II	P	N	N	N	Y
34	66	F	W	N.H.	Right temporal lobe	GBM, IDH-WT, WHO grade IV	P	N	N	N	N
35	46	M	B	A.A.	Right posterior frontal periventricular	GBM, IDH-WT, WHO grade IV	P	Y	N	N	N
37	59	M	W	N.H.	Bifrontal	GBM, IDH-WT, WHO grade IV	P	N	N	N	N
38	23	M	W	N.H.	Left frontal lobe	Anaplastic astrocytoma, IDH-mutant, WHO grade III	P	N	N	N	N
39	59	M	W	N.H.	Left temporal lobe	GBM, IDH-WT, WHO grade IV	R	N	N	N	N
40	57	F	W	N.H.	Right frontal lobe	GBM, IDH-WT, WHO grade IV	P	N	N	N	N
41	26	F	W	N.H.	Right frontal lobe	Diffuse glioma, IDH-M	P	N	N	N	N
42	35	F	W	N.H.	Right frontal lobe	GBM, IDH-mutant, WHO grade IV	P	N	N	Y	N

Table 2.3 continued

44	30	M	W	N.H.	Left temporal lobe and insula	Diffuse astrocytoma, IDH-M,WHO grade II	R	N	N	N	N
45	62	F	W	N.H.	Right frontal lobe	GBM, IDH-WT, WHO grade IV	P	N	N	N	N
46	66	F	A	N.H.	Left temporal lobe	Diffuse glioma, IDH-WT	P	N	N	N	N
47	48	M	W	N.H.	Right frontal lobe	Anaplastic astrocytoma, IDH-mutant, WHO grade III	P	N	N	Y	N
48	68	M	W	N.H.	Right frontal lobe	GBM with granular cell features, IDH-WT, WHO grade IV	P	Y	N	N	N
50	32	F	W	N.H.	Left insular and mesial temporal	Diffuse astrocytoma, IDH-M,WHO grade II	P	N	N	N	Y
51	30	F	A.A.	N.H.	Right frontal lobe	GBM, IDH-M, WHO grade IV	R	N	N	N	N
52	61	M	W	N.H.	Right temporal lobe	GBM, IDH-WT, WHO grade IV	P	Y	N	N	N
53	27	M	A	N.H.	Right temporal lobe and insula	Diffuse astrocytoma, IDH-M,WHO grade II	P	N	N	N	N
54	68	M	W	N.H.	Right parietal-occipital lobe	GBM, IDH-M, WHO grade IV	P	N	N	N	Y
55	73	M	W	N.H.	Right frontal lobe	GBM, IDH-WT, WHO grade IV	P	N	N	N	N

Table 2.3 continued

56	35	F	W	N.H.	Left parietal lobe	GBM, IDH-WT, WHO grade IV		P	N	N	N	N
57	56	F	W	N.H.	Left frontal lobe	Oligodendroglioma, IDH-M and 1p/19q codeleted,WHO grade II		R	N	N	N	N
58	26	M	W	N.H.	Right frontoparietal region	Oligodendroglioma, IDH-M and 1p/19q codeleted,WHO grade II		P	N	Y	Y	N
	Average age	Gender Distribution	Race Distribution	Ethnicity Distribution		Tumor Grade and IDH Mutation Distribution						
	47.0	Males: 25 Females: 24	W: 43 B: 3 A: 2 MR: 1	H: 1 NH: 48		Grade I: 1 Grade II: 17 Grade III: 6 Grace IV: 25	IDH-M: 23 IDH-WT: 26					

Race categories: W = White; N.H. = Non-Hispanic; B = Black; A = Asian; MR = multi-racial
GBM = Glioblastoma
Primary/Recurrent: P = Primary; R = Recurrent
F = Fluorescein
IMRI = Intraoperative MRI used (yes/no)
Mapping = Brain mapping used (yes/no)
Awake = Awake craniotomy (yes/no)

Table 2.4 Additional histopathology results for patients.

Patient #	GFAP	ATRX	P53	Ki67	1p/19q	MGMT
01	1	0	1 (20%)	1 (1%)	0	-
02	-	-	-	-	-	-
03	-	-	-	-	-	-
04	-	-	-	-	-	-
05	1	-	-	1 (1-5%)	0	-
06	1	0	1 (80%)	1 (4%)	0	-
07	1	1	1 (3%)	1 (4%)	-	0
08	-	-	-	-	-	-
09	1	1	1 (<1%)	1 (5%)	1	-
10	1	-	-	1 (20%)	0	-
11	-	-	-	-	-	-
12	1	0	1	1	0	0
13	1 (large %)	0	1	1 (30%)	-	0
14	1	-	1 (40%)	1 (30%)	-	0
15	1	1	1	1 (< 5%)	0	-
16	1	0	1 (<1%)	1 (<1%)	0	-
17	1	0	1 (40%)	1 (3%)	-	-
18	1	0	1 (15%)	1 (1-2%)	-	-
19	1	0	1 (75%)	1 (40%)	-	-
20	1	1	1 (<10%)	1 (30%)	0	1
21	0	1	1 (rare cells)	1 (10%)	-	-
22	-	-	-	-	-	-
23	1	1	1 (80%)	1 (50%)	0	1
24	1	1	1 (scattered tumor cells) & 1 (<10% spindle cell and glial component)	1 (5% spindle cell component) & 1 (40% of glial component)	-	-
25	1	1	1 (<1%)	1 (40%)	-	1
26	1	0	1 (90%)	1 (5%)	0	1
27		1	1 (<1%)	1 (10% in anaplastic gliomatous component; <5% in remaining tumor)	0	-
28	1	-	-	1 (20%)	0	0

Table 2.4 continued

29	1	1	1 (<1%)	1 (1-2%)	-	-
30	1	2	1 (15-20%)	1 (1-2%)	0	-
31	1	1	1 (<1%)	1 (approx. 50%)	-	-
32	1	1	1 (<5%)	1 (>60% in regions 1 ATRXl; as low as 10-15% in regions 0 ATRX)	-	1
33	1	2 (partial loss of staining)	1 (20%)	1 (10%)	0	-
34	1	1	1 (10%)	1 (3-5%)	0	1
35	1	1	1 (10-15%) with faint staining	1 (30%)	-	1
36	-	-	-	-	-	-
37	1	1	1 (<5%)	1 (30%)	-	-
38	1	0	1 (>75%)	1 (up to 5-10%)	0	-
39	1	-	-	-	-	-
40	1	0	1 (25%)	1 (20%)	-	1
41	1	0	1 (positive in the majority of the tumor cells)	1 (approx. 5%)	-	-
42	1	0	1 (>80%)	1 (5%)	0	Ind.
43	-	-	-	-	-	-
44	1	0	1 (>95%)	1 (approx. 3%)	0	-
45	1	0	0	1 (50-75%)	0	-
46	1	1	1 (<5%)	1 (5-10%) in most hypercellular regions	-	-
47	1	0	1 (>50%)	1 (approx. 3-5%)	0	-
48	1	1	1 (>50%)	1 (approx. 10%)	-	0
49	-	-	-	-	-	-
50	1	0	1 (40-50%)	1 (<3%)	-	-
51	1	-	1 (>80%)	-	-	1
52	1	0	1 (<1%)	1 (5-10%)	-	-
53	1	-	1 (30%)	1 (3-4%)	0	-
54	-	1	1	-	-	0
55	1	1	1 (<5%)	1 (40-50%)	-	1

Table 2.4 continued

56	1	1	1 (20%)	1 (variably immunoreactive in up to 30% of tumor cells)	0	1
57	1	-	-	-	1	-
58	1	1	-	1(1%)	1	-

This table reports IHC staining results. 1 = immunoreactive; 0 = non-immunoreactive. For Ki-67, the percentage indicates the labelling index (percentage of tumor cells that are immunoreactive).

Table 2.5 DESI-MS predictions of disease status, TCP, and IDH genotype for the smears of biopsies obtained for each patient.

Sample Information						Selected DESI-MS Scans		PCA-LDA Diagnosis	NAA (Full Scan) TCP Estimation		Lipid Deconvolution TCP Estimation		IDH Genotype from 2HG Concentration	
Patient #	**Biopsy # (Patient)**	**Core/ Margin**	**Smear # (Patient)**	**Smear # (Overall)**	**Included/ Excluded in Statistical Predictions**	**# Lipid Scans**	**# Metabolite Scans**	**Tissue Type**	**Mean TCP Value**	**TCP Category**	**Mean TCP Value**	**TCP Category**	**Normalized 2-HG Value**	**IDH Genotype**
01	1	Margin	1	1	I	62	81	G	64	High	100	High	N/A	N/A
	2	Margin	2	2	E	-	120	-	91	High	-	-	N/A	N/A
	3	Core	3	3	I	74	27	G	81	High	100	High	N/A	N/A
	4	Core	4	4	I	72	110	G	72	High	100	High	N/A	N/A
	5	Margin	5	5	I	28	63	G	82	High	98	High	N/A	N/A
	6	Core	6	6	I	64	95	G	80	High	100	High	N/A	N/A
	7	Core	7	7	I	43	112	G	70	High	100	High	N/A	N/A
	8	Core	8	8	I	55	106	G	74	High	100	High	N/A	N/A
	9	Margin	9	9	E*	58	94	G	44	Low	100	High	N/A	N/A
05	1	N/A	1	10	I	13	140	G	81	High	100	High	N/A	N/A
		N/A	2	11	I	24	115	G	72	High	100	High	N/A	N/A
	2	Margin	3	12	I	38	72	WM	55	High	32	Low	N/A	N/A
	3	Core	4	13	I	23	60	G	72	High	100	High	N/A	N/A
	4	Margin	5	14	I	29	109	WM	66	High	52	High	N/A	N/A
	5	Margin	6	15	I	40	93	WM	57	High	40	Low	N/A	N/A
	6	Margin	7	16	I	21	79	G	65	High	91	High	N/A	N/A
	7	Core	8	17	I	30	137	G	79	High	100	High	N/A	N/A

Table 2.5 continued

06	1	Core	1	18	I	40	78	WM	63	High	18	Low	N/A	N/A
	2	Core	2	19	I	65	85	G	74	High	97	High	N/A	N/A
	3	Margin	3	20	I	78	60	WM	14	Low	77	High	N/A	N/A
	4	Core	4	21	I	65	44	WM	63	High	48	Low	N/A	N/A
	5	Core	5	22	I	39	72	WM	58	High	52	High	N/A	N/A
		Core	6	23	I	87	45	WM	55	High	30	Low	N/A	N/A
	6	Core	7	24	I	99	53	WM	26	Low	0	Low	N/A	N/A
07	1	Core	1	25	I	92	121	G	65	High	64	High	N/A	N/A
	2	Margin	2	26	I	125	127	GM	6	Low	21	Low	N/A	N/A
	3	Core	3	27	I	125	120	WM	38	Low	0	Low	N/A	N/A
	4	Core	4	28	I	80	86	WM	35	Low	0	Low	N/A	N/A
	5	Margin	5	29	I	87	91	WM	14	Low	0	Low	N/A	N/A
		Margin	6	30	I	98	93	WM	5	Low	0	Low	N/A	N/A
09	1	N/A	1	31	I	9	34	G	57	High	74	High	N/A	N/A
		N/A	2	32	I	37	41	G	47	Low	78	High	N/A	N/A
	2	Core	3	33	I	124	127	WM	1	Low	0	Low	N/A	N/A
	3	Margin	4	34	I	111	120	WM	2	Low	0	Low	N/A	N/A
	4	Margin	5	35	I	92	65	WM	11	Low	0	Low	N/A	N/A
		Margin	6	36	I	105	90	WM	3	Low	0	Low	N/A	N/A
	5	Core	7	37	I	117	109	WM	27	Low	0	Low	N/A	N/A
	6	Core	8	38	I	61	84	G	58	High	99	High	N/A	N/A
	7	Core	9	39	I	72	72	WM	0	Low	0	Low	N/A	N/A
10	1	Core	1	40	I	48	109	GM	28	Low	0	Low	N/A	N/A
	2	Core	2	41	I	120	106	G	25	Low	68	High	N/A	N/A
	3	Core	3	42	I	55	93	G	49	Low	98	High	N/A	N/A
	4	Core	4	43	I	94	129	G	62	High	96	High	N/A	N/A
		Core	5	44	I	70	96	G	40	Low	74	High	N/A	N/A

Table 2.5 continued

10	5	Margin	6	45	I	48	65	G	48	Low	98	High	N/A	N/A
	6	Margin	7	46	I	104	127	WM	27	Low	38	Low	N/A	N/A
12	1	Core	1	47	I	42	83	G	76	High	100	High	N/A	N/A
		Core	2	48	I	50	121	G	78	High	100	High	N/A	N/A
	2	Core	3	49	I	52	87	G	48	Low	65	High	N/A	N/A
	3	Core	4	50	I	62	107	G	71	High	91	High	N/A	N/A
	4	N/A	5	51	I	45	92	G	48	Low	82	High	N/A	N/A
	5	N/A	6	52	I	53	93	WM	66	High	50	Low	N/A	N/A
	6	N/A	7	53	I	43	95	WM	58	High	50	Low	N/A	N/A
	7	N/A	8	54	I	47	89	WM	63	High	26	Low	N/A	N/A
13	1	Margin	1	55	I	22	20	G	76	High	83	High	N/A	N/A
		Margin	2	56	I	12	22	G	85	High	87	High	N/A	N/A
	2	Core	3	57	I	20	23	G	81	High	92	High	N/A	N/A
		Core	4	58	I	24	25	G	80	High	87	High	N/A	N/A
	3	Margin	5	59	E*	19	22	WM	78	High	47	Low	N/A	N/A
	3	Margin	6	60	I	27	23	WM	65	High	32	Low	N/A	N/A
	4	Margin	7	61	E*	12	-	-	-	-	21	Low	N/A	N/A
	5	Margin	8	62	E*	11	-	-	-	-	8	Low	N/A	N/A
	6	Margin	9	63	E	18	-	-	-	-	1	Low	N/A	N/A
	7	Margin	10	64	I	4	25	WM	49	Low	0	Low	N/A	N/A
14	1	Margin	1	65	E	-	-	-	-	-	-	-	N/A	N/A
	2	Core	2	66	E*	24	17	WM	30	Low	21	Low	N/A	N/A
	3	Margin	3	67	E	-	-	-	-	-	-	-	N/A	N/A
		Margin	4	68	E*	14	22	G	79	High	98	High	N/A	N/A
	4	Core	5	69	I	9	24	G	88	High	97	High	N/A	N/A
	5	Core	6	70	I	24	25	G	91	High	99	High	N/A	N/A
	6	Margin	7	71	I	5	24	G	88	High	100	High	N/A	N/A

Table 2.5 continued

14	6	Margin	8	72	I	15	25	G	86	High	100	High	N/A	N/A
15	1	Core	1	73	I	5	18	G	74	High	78	High	N/A	N/A
		Core	2	74	I	7	24	G	79	High	100	High	N/A	N/A
	2	Core	3	75	I	5	23	G	81	High	79	High	N/A	N/A
		Core	4	76	I	14	22	G	75	High	80	High	N/A	N/A
	3	Core	5	77	I	5	25	G	85	High	87	High	N/A	N/A
	4	Margin	6	78	I	33	21	G	40	Low	87	High	N/A	N/A
		Margin	7	79	I	43	25	WM	7	Low	3	Low	N/A	N/A
	5	Margin	8	80	I	18	23	WM	69	High	13	Low	N/A	N/A
	6	Margin	9	81	I	28	24	WM	48	Low	0	Low	N/A	N/A
16	1	Core	1	82	I	14	15	WM	1	Low	0	Low	N/A	N/A
	2	Core	2	83	I	9	22	G	21	Low	78	High	N/A	N/A
	3	Core	3	84	I	26	25	WM	43	Low	29	Low	N/A	N/A
	4	Margin	4	85	I	24	18	WM	54	High	17	Low	N/A	N/A
	5	Margin	5	86	I	28	25	WM	41	Low	17	Low	N/A	N/A
	6	Margin	6	87	I	25	21	WM	23	Low	0	Low	N/A	N/A
	7	Core	7	88	E	21	-	-	-	-	33	Low	N/A	N/A
17	1	Core	1	89	I	8	20	G	68	High	89	High	N/A	N/A
	2	Core	2	90	I	15	25	WM	71	High	54	High	N/A	N/A
	3	Core	3	91	I	32	25	WM	69	High	23	Low	N/A	N/A
	4	Margin	4	92	I	32	17	WM	52	High	28	Low	N/A	N/A
18	1	Core	1	93	E*	20	25	G	88	High	92	High	N/A	N/A
		Core	2	94	E*	23	23	G	88	High	91	High	N/A	N/A
	2	Core	3	95	I	20	25	WM	84	High	58	High	N/A	N/A
	3	Core	4	96	I	27	25	WM	89	High	68	High	N/A	N/A
	4	Margin	5	97	I	23	10	WM	11	Low	16	Low	N/A	N/A
		Margin	6	98	I	32	19	WM	26	Low	14	Low	N/A	N/A

Table 2.5 continued

18	5	Core	7	99	I	23	25	WM	80	High	33	Low	N/A	N/A
		Core	8	100	I	28	25	WM	76	High	30	Low	N/A	N/A
19	1	Core	1	101	I	27	24	G	85	High	94	High	N/A	N/A
	2	Margin	2	102	E*	24	25	WM	80	High	45	Low	N/A	N/A
	3	Core	3	103	E	-	25	-	88	High	-	-	N/A	N/A
		Core	4	104	I	23	25	G	90	High	96	High	N/A	N/A
	4	Core	5	105	I	14	25	G	89	High	92	High	N/A	N/A
	5	Margin	6	106	I	23	25	GM	26	Low	0	Low	N/A	N/A
		Margin	7	107	I	24	25	GM	26	Low	2	Low	N/A	N/A
	6	Margin	8	108	I	25	25	WM	52	High	0	Low	N/A	N/A
	7	Margin	9	109	I	13	25	WM	68	High	43	Low	N/A	N/A
		Margin	10	110	I	28	25	WM	36	High	3	Low	N/A	N/A
20	1	Margin	1	111	I	13	25	WM	72	High	40	Low	N/A	N/A
		Margin	2	112	I	30	25	WM	62	High	38	Low	N/A	N/A
	2	Margin	3	113	I	30	25	WM	70	High	59	High	N/A	N/A
		Margin	4	114	I	31	25	WM	56	High	38	Low	N/A	N/A
	3	Margin	5	115	I	32	25	WM	22	Low	0	Low	N/A	N/A
	4	Margin	6	116	I	33	25	G	72	High	83	High	N/A	N/A
	5	Margin	7	117	I	27	25	WM	31	Low	0	Low	N/A	N/A
		Margin	8	118	I	33	25	WM	12	Low	0	Low	N/A	N/A
21	1	Margin	1	119	I	8	25	G	32	Low	64	High	N/A	N/A
		Margin	2	120	I	18	25	G	24	Low	69	High	N/A	N/A
	2	Core	3	121	I	30	22	GM	17	Low	57	High	N/A	N/A
		Core	4	122	I	20	25	GM	12	Low	50	Low	N/A	N/A
22	3	N/A	5	123	I	26	25	GM	24	Low	70	High	N/A	N/A
		N/A	6	124	I	27	25	GM	25	Low	70	High	N/A	N/A
	4	Core	7	125	I	29	22	WM	32	Low	40	Low	N/A	N/A

Table 2.5 continued

22	4	Core	8	126	I	30	24	G	37	Low	68	High	N/A	N/A
	5	Margin	9	127	I	24	22	GM	18	Low	36	Low	N/A	N/A
	6	Margin	10	128	I	30	21	WM	33	Low	11	Low	N/A	N/A
23	1	Core	1	129	E*	3	25	G	71	High	83	High	N/A	N/A
	2	Core	2	130	I	2	25	WM	70	High	88	High	N/A	N/A
		Core	3	131	E*	32	25	WM	75	High	23	Low	N/A	N/A
	3	Core	4	132	I	32	25	WM	69	High	47	Low	N/A	N/A
		Core	5	133	I	32	25	WM	76	High	54	High	N/A	N/A
	1	Core	6	134	E	-	25	-	79	High	-	-	N/A	N/A
		Core	7	135	E	-	25	-	83	High	-	-	N/A	N/A
	4	Core	8	136	I	18	25	G	82	High	83	High	N/A	N/A
		Core	9	137	I	10	25	G	80	High	81	High	N/A	N/A
24	1	Margin	1	138	I	17	25	G	75	High	84	High	5.4	WT
		Margin	2	139	I	23	25	G	75	High	83	High	0	WT
	2	Core	3	140	I	26	25	G	79	High	85	High	6	WT
25	1	Margin	1	141	I	25	25	G	82	High	74	High	0	WT
	2	Margin	2	142	I	21	21	GM	63	High	52	High	N/A	N/A
	3	Margin	3	143	I	21	25	GM	67	High	59	High	N/A	N/A
	3	Margin	4	144	I	22	25	WM	58	High	19	Low	N/A	N/A
	4	Margin	5	145	E	-	25	-	79	High	-	-	N/A	N/A
	5	Margin	6	146	I	26	22	WM	33	Low	4	Low	N/A	N/A
	6	Margin	7	147	I	21	14	WM	44	Low	0	Low	N/A	N/A
	7	Margin	8	148	I	30	18	WM	39	Low	0	Low	N/A	N/A
	5	Margin	9	149	I	30	25	WM	22	Low	0	Low	0	WT
	7	Margin	10	150	I	29	16	WM	33	Low	0	Low	8.2	WT
26	1	Core	1	151	I	15	9	G	64	High	76	High	26	WT
	2	Margin	2	152	I	26	16	WM	7	Low	0	Low	61.4	WT

Table 2.5 continued

26	3	Margin	3	153	I	31	19	WM	22	Low	0	Low	70.5	Mut
	4	Margin	4	154	I	32	22	WM	16	Low	0	Low	82.5	Mut
	5	Core	5	155	I	25	11	G	52	High	71	High	62.3	WT
27	1	Core	1	156	E	-	-	-	-	-	-	-	N/A	N/A
		Core	2	157	I	2	6	G	81	High	100	High	N/A	N/A
	2	Margin	3	158	E	-	-	-	-	-	-	-	N/A	N/A
	3	Core	4	159	E	-	-	-	-	-	-	-	N/A	N/A
		Core	5	160	E	-	19	-	88	High	-	-	N/A	N/A
	4	Core	6	161	E	-	23	-	87	High	-	-	N/A	N/A
		Core	7	162	E	-	-	-	-	-	-	-	N/A	N/A
	5	Core	8	163	E	-	13	-	83	High	-	-	N/A	N/A
	6	Core	9	164	I	7	22	WM	76	High	31	Low	N/A	N/A
	5	Core	10	165	I	14	9	WM	73	High	36	Low	N/A	N/A
28	1	Core	1	166	E	-	23	-	75	High	-	-	16.9	WT
	2	Margin	2	167	E	-	-	-	-	-	-	-	0	WT
	3	Margin	3	168	I	16	20	GM	34	Low	0	Low	0	WT
		Margin	4	169	I	25	15	GM	33	Low	0	Low	61.2	WT
	4	Core	5	170	E	-	-	-	-	-	-	-	0	WT
		Core	6	171	E	-	24	-	74	High	-	-	16.4	WT
	5	N/A	7	172	I	24	25	GM	44	Low	35	Low	27.5	WT
		N/A	8	173	E	-	-	-	-	-	-	-	0	WT
29	1	Core	1	174	E	-	-	-	-	-	-	-	0	WT
		Core	2	175	E	-	-	-	-	-	-	-	0	WT
	2	Margin	3	176	E	-	-	-	-	-	-	-	0	WT
		Margin	4	177	E	-	-	-	-	-	-	-	0	WT
	3	Margin	5	178	E	-	-	-	-	-	-	-	10.5	WT
	4	Core	6	179	I	30	26	WM	24	Low	0	Low	0	WT

Table 2.5 continued

29	5	Core	7	180	I	30	25	WM	50	Low	49	Low	21.9	WT
	6	Margin	8	181	I	19	25	WM	61	High	51	High	0	WT
		Margin	9	182	I	29	25	WM	58	High	31	Low	14.1	WT
		Core	10	183	I	27	17	WM	46	Low	35	Low	0	WT
30	1	Core	1	184	I	28	26	WM	55	High	8	Low	57.1	WT
		Core	2	185	I	25	15	WM	60	High	46	Low	36.9	WT
	2	Margin	3	186	I	34	22	WM	1	Low	0	Low	12.6	WT
	3	Margin	4	187	I	36	28	WM	1	Low	0	Low	0	WT
	4	Margin	5	188	I	19	15	WM	7	Low	0	Low	56.2	WT
	5	Margin	6	189	I	18	29	GM	1	Low	0	Low	26.5	WT
31	1	Margin	1	190	I	14	29	G	79	High	72	High	0	WT
		Margin	2	191	I	22	29	GM	80	High	66	High	4.6	WT
	2	Core	3	192	E	-	-	-	-	-	-	-	0	WT
	3	Margin	4	193	I	27	29	WM	46	Low	8	Low	0	WT
	4	Core	5	194	E	-	-	-	-	-	-	-	0	WT
	5	Core	6	195	I	12	12	WM	50	Low	0	Low	0	WT
32	1	Margin	1	196	I	18	25	WM	9	Low	0	Low	0	WT
	2	Core	2	197	I	20	26	WM	44	Low	13	Low	0	WT
		Core	3	198	I	25	16	WM	31	Low	0	Low	N/A	N/A
	3	Margin	4	199	I	27	20	WM	48	Low	0	Low	N/A	N/A
	4	Margin	5	200	I	20	19	WM	44	Low	0	Low	N/A	N/A
	5	Core	6	201	I	7	13	WM	37	Low	0	Low	0	WT
		Core	7	202	I	17	8	WM	40	Low	2	Low	0	WT
33	1	Margin	1	203	I	7	21	WM	55	High	30	Low	N/A	N/A
	2	Margin	2	204	E	-	-	-	-	-	-	-	5.5	WT
	3	Margin	3	205	E	-	-	-	-	-	-	-	59.7	WT
	4	Core	4	206	I	14	27	WM	77	High	21	Low	87.6	Mut

Table 2.5 continued

33	5	Core	5	207	E	-	-	-	-	-	-	-	43.8	WT
	6	Core	6	208	E	-	-	-	-	-	-	-	71.4	Mut
34	1	Margin	1	209	I	21	19	GM	13	Low	0	Low	4.3	WT
		Margin	2	210	I	29	23	GM	17	Low	0	Low	3	WT
	2	Core	3	211	I	24	24	WM	59	High	10	Low	9.3	WT
		Core	4	212	I	16	21	WM	59	High	1	Low	0	WT
	3	Core	5	213	I	9	22	WM	57	High	0	Low	0	WT
		Core	6	214	I	13	23	WM	52	High	0	Low	10.5	WT
35	1	Core	1	215	I	23	8	WM	29	Low	0	Low	0	WT
	2	Margin	2	216	E	-	-	-	-	-	-	-	22.4	WT
	3	Margin	3	217	E	12	-	-	-	-	11	Low	0	WT
	4	Margin	4	218	E	20	-	-	-	-	0	Low	0	WT
	5	Margin	5	219	E	9	-	-	-	-	9	Low	0	WT
	6	Margin	6	220	E	-	-	-	-	-	-	-	12.9	WT
37	1	Core	1	221	I	10	16	G	84	High	71	High	0	WT
		Core	2	222	I	7	16	G	85	High	70	High	0	WT
	2	Core	3	223	I	9	22	G	85	High	99	High	0	WT
	3	Core	4	224	I	8	23	G	81	High	92	High	0	WT
	4	Core	5	225	I	12	7	G	77	High	73	High	0	WT
38	1	Core	1	226	I	6	29	G	87	High	100	High	33.5	WT
	2	Core	2	227	I	4	28	G	75	High	89	High	N/A	N/A
	3	Core	3	228	I	28	27	WM	40	Low	0	Low	101.7	Mut
	4	Margin	4	229	I	7	22	WM	65	High	56	High	N/A	N/A
	5	Margin	5	230	I	23	22	WM	78	High	36	Low	15.1	WT
	6	Core	6	231	I	22	25	WM	84	High	54	High	73.5	Mut
39	1	Margin	1	232	I	50	46	WM	17	Low	6	Low	38.3	WT
	2	Margin	2	233	I	62	64	WM	30	Low	0	Low	16.3	WT

Table 2.5 continued

39	3	Core	3	234	I	67	66	WM	38	Low	0	Low	19.7	WT
40	1	Margin	1	235	E	-	60	-	79	High	-	-	32.9	WT
		Margin	2	236	E	-	60	-	82	High	-	-	0	WT
	2	Core	3	237	I	24	62	G	76	High	93	High	15.1	WT
		Core	4	238	I	33	65	G	65	High	84	High	44.3	WT
	3	Margin	5	239	I	64	67	WM	19	Low	0	Low	65.6	WT
		Margin	6	240	I	64	65	WM	22	Low	0	Low	17.3	WT
41	1	Margin	1	241	I	49	64	WM	37	Low	22	Low	90.2	Mut
	2	Margin	2	242	I	64	61	WM	7	Low	0	Low	N/A	N/A
	3	Margin	3	243	I	53	65	G	19	Low	71	High	26.1	WT
	4	Margin	4	244	I	53	49	WM	20	Low	71	High	10.1	WT
	5	Margin	5	245	I	38	37	WM	57	High	53	High	N/A	N/A
42	1	Core	1	246	E*	21	59	G	89	High	86	High	71	Mut
	2	Core	2	247	I	20	64	WM	71	High	50	Low	180.3	Mut
	3	Core	3	248	E*	37	64	WM	74	High	39	Low	88.9	Mut
44	1	Core	1	249	I	20	64	G	95	High	94	High	70.5	Mut
		Core	2	250	I	9	64	G	91	High	91	High	91.3	Mut
		Core	3	251	I	22	63	G	96	High	88	High	97.4	Mut
	2	Core	4	252	I	39	63	G	89	High	83	High	76.4	Mut
	3	Margin	5	253	I	26	63	G	80	High	93	High	78.1	Mut
		Margin	6	254	I	18	63	G	81	High	92	High	80.7	Mut
	4	Margin	7	255	I	60	64	G	97	High	83	High	83.4	Mut
	5	Margin	8	256	I	46	65	GM	8	Low	50	Low	79.3	Mut
	6	Core	9	257	I	36	65	G	66	High	89	High	94.7	Mut
		Core	10	258	I	49	65	G	26	Low	78	High	76.7	Mut
45	1	N/A	1	259	E*	59	65	G	83	High	89	High	N/A	N/A
46	1	Core	1	260	I	36	64	G	70	High	75	High	48.5	WT

Table 2.5 continued

46		Core	2	261	I	31	64	G	62	High	85	High	69	WT
	2	Core	3	262	I	33	65	G	68	High	68	High	4.9	WT
	3	Core	4	263	I	29	65	G	61	High	87	High	15.3	WT
		Core	5	264	I	31	66	G	62	High	83	High	78.7	Mut
		Core	6	265	I	39	64	G	59	High	79	High	27.7	WT
	4	Margin	7	266	I	38	62	G	56	High	49	Low	40.6	WT
	5	Margin	8	267	I	30	64	G	59	High	68	High	29	WT
	6	Margin	9	268	I	60	65	WM	29	Low	10	Low	56.1	WT
47	1	Core	1	269	I	63	60	WM	45	Low	33	Low	41.1	WT
	1	Core	2	270	I	66	62	WM	40	Low	33	Low	53.3	WT
	2	Core	3	271	I	49	63	G	92	High	85	High	82.7	Mut
		Core	4	272	I	52	61	G	79	High	73	High	131.9	Mut
	3	Core	5	273	I	55	57	G	33	Low	56	High	91.1	Mut
		Core	6	274	I	53	59	G	37	Low	64	High	83.4	Mut
	4	Margin	7	275	I	57	61	G	57	High	38	Low	77.8	Mut
		Margin	8	276	I	62	63	WM	46	Low	28	Low	63.1	WT
48	1	Core	1	277	I	26	48	WM	43	Low	25	Low	0	WT
		Core	2	278	I	18	58	G	30	Low	71	High	16.8	WT
	2	Core	3	279	I	19	63	WM	64	High	19	Low	14.3	WT
		Core	4	280	I	2	60	WM	81	High	11	Low	46.8	WT
	3	Core	5	281	I	62	64	WM	28	Low	16	Low	28.3	WT
		Core	6	282	I	60	63	WM	30	Low	10	Low	9.6	9.6
		Core	7	283	I	63	65	WM	26	Low	6	Low	10.8	10.8
50	1	Core	1	284	I	70	75	WM	52	High	12	Low	106.7	Mut
	2	Margin	2	285	I	73	77	WM	4	Low	25	Low	62.8	WT
	3	Core	3	286	I	75	74	WM	51	High	9	Low	154.5	Mut
	4	Core	4	287	I	62	74	G	17	Low	54	High	116.9	Mut

Table 2.5 continued

50	5	Core	5	288	I	41	72	WM	84	High	36	Low	76.9	Mut
	6	Core	6	289	I	69	73	WM	54	High	32	Low	89.8	Mut
51	1	Core	1	290	I	6	71	G	100	High	72	High	393.9	Mut
	2	Margin	2	291	E*	11	73	G	82	High	75	High	466.2	Mut
	3	Margin	3	292	E*	2	72	G	83	High	89	High	631.8	Mut
	4	Core	4	293	E*	2	69	G	94	High	84	High	657.6	Mut
	5	Margin	5	294	E*	9	72	G	71	High	83	High	683.8	Mut
	6	Core	6	295	E*	15	73	G	90	High	81	High	524.1	Mut
52	1	Margin	1	296	I	50	41	GM	43	Low	27	Low	0	WT
	2	Margin	2	297	I	61	42	WM	38	Low	17	Low	28.6	WT
	3	Core	3	298	E*	23	39	G	96	High	58	High	53.2	WT
		Core	4	299	I	60	41	G	96	High	35	Low	N/A	N/A
53	1	Core	1	300	I	60	41	WM	59	High	20	Low	113.1	Mut
	2	Margin	2	301	I	54	44	WM	36	Low	25	Low	179.6	Mut
		Margin	3	302	I	68	41	WM	49	Low	16	Low	109.3	Mut
	3	Core	4	303	I	57	44	G	45	Low	55	High	95.5	Mut
		Core	5	304	I	37	44	G	46	Low	76	High	185.2	Mut
	4	Core	6	305	I	58	43	WM	65	High	20	Low	135.9	Mut
	5	Core	7	306	I	55	43	WM	65	High	26	Low	195.3	Mut
	6	Margin	8	307	I	32	40	G	67	High	63	High	43	WT
		Margin	9	308	I	40	43	G	52	High	49	Low	57.3	WT
54	1	Margin	1	309	E	-	-	-	-	-	-	-	N/A	N/A
		Margin	2	310	E	-	-	-	-	-	-	-	97.5	Mut
	2	Core	3	311	I	16	75	WM	57	High	25	Low	78.4	Mut
	2	Core	4	312	I	25	73	WM	51	High	11	Low	363	Mut
	3	Core	5	313	I	16	74	G	85	High	78	High	147.4	Mut
		Core	6	314	I	11	73	G	90	High	92	High	144.4	Mut

Table 2.5 continued

54		Core	7	315	I	15	75	G	87	High	90	High	129.8	Mut
55	1	Margin	1	316	I	25	75	G	83	High	42	Low	9.2	WT
	2	Core	2	317	I	50	60	WM	38	Low	7	Low	0	WT
	3	Core	3	318	E*	22	67	G	86	High	63	High	0	WT
	4	N/A	4	319	I	39	71	WM	72	High	27	Low	0	WT
56	1	Core	1	320	I	4	74	G	100	High	67	High	7.9	WT
	2	Core	2	321	I	9	74	G	97	High	61	High	40.2	WT
		Core	3	322	I	37	76	G	91	High	52	High	34.3	WT
		Core	4	323	I	46	74	G	83	High	60	High	63.1	WT
57	1	Core	1	324	I	5	72	G	72	High	82	High	403.1	Mut
	2	Core	2	325	I	15	74	G	57	High	76	High	588.5	Mut
		Core	3	326	I	11	72	G	62	High	86	High	597.2	Mut
		Core	4	327	I	9	73	G	77	High	91	High	367.5	Mut
58	1	Core	1	328	I	14	74	G	39	Low	87	High	644	Mut
		Core	2	329	I	7	72	G	50	Low	98	High	579.1	Mut
	2	Margin	3	330	I	5	74	WM	48	Low	51	High	453.5	Mut
	3	Margin	4	331	I	24	74	WM	11	Low	9	Low	125.1	Mut
	4	Core	5	332	I	19	74	WM	17	Low	16	Low	247.9	Mut
	5	Margin	6	333	I	33	73	WM	0	Low	5	Low	72.5	Mut
	6	Core	7	334	I	23	73	WM	21	Low	16	Low	436.4	Mut

Cells with hyphens indicate that no MS scans met the inclusion criteria and were excluded from statistical analyses.
I = Included; E = Excluded
G = glioma; WM = White matter; GM = Grey matter
For NAA predictions of TCP, the TCP categories were High ≥51% and Low ≤50%.
For lipid deconvolution TCP predictions, the TCP categories were High ≥51% and Low ≤50%.
WT = IDH-wildtype; Mut=IDH-mutant
Samples with "N/A" for the IDH assessment indicate that the smears were not analyzed with the 2-HG DESI-MS method.

Table 2.6 Pathological evaluation of tissue smears obtained from each patient.

Sample Information				Pathological Information		
Patient #	**Biopsy # (Patient)**	**Smear # (Patient)**	**Smear # (Overall)**	**Diagnosis**	**TCP-Estimate**	**Smear Quality**
01	1	1	1	G	100	-
	2	2	2	G	100	-
	3	3	3	G	100	-
	4	4	4	G	100	-
	5	5	5	G	100	-
	6	6	6	G	100	-
	7	7	7	G	100	-
	8	8	8	G	100	-
	9	9	9	IM	10	BMA
05	1	1	10	G	90	-
		2	11	G	90	-
	2	3	12	G	60	-
	3	4	13	G	80	-
	4	5	14	G	50	-
	5	6	15	G	60	-
	6	7	16	G	80	-
	7	8	17	G	80	-
06	1	1	18	G	50	-
	2	2	19	G	90	-
	3	3	20	GM	0	A
	4	4	21	G	70	-
	5	5	22	G	50	-
		6	23	IM	25	MA
	6	7	24	IM	15	-
07	1	1	25	G	90	-
	2	2	26	IM	10	-
	3	3	27	G	50	-
	4	4	28	G	50	-
	5	5	29	IM	10	-
		6	30	G	30	-
09	1	1	31	G	90	-
		2	32	G	90	-
	2	3	33	IM	30	-
	3	4	34	IM	50	-
	4	5	35	G	60	-
		6	36	IM	30	-

Table 2.6 continued

09	5	7	37	IM	15	-
	6	8	38	G	95	-
	7	9	39	IM	20	-
10	1	1	40	IM	30	-
	2	2	41	GM	0	MA
	3	3	42	G	80	-
	4	4	43	G	80	-
		5	44	G	50	-
	5	6	45	G	60	-
	6	7	46	IM	50	-
12	1	1	47	G	70	-
		2	48	G	70	-
	2	3	49	GM	0	BMA
	3	4	50	G	70	-
	4	5	51	IM	40	-
	5	6	52	G	80	-
	6	7	53	IM	50	-
	7	8	54	G	70	-
13	1	1	55	G	90	-
		2	56	G	90	-
	2	3	57	G	90	-
		4	58	G	90	-
	3	5	59	WM	0	BMA
		6	60	WM	0	MA
	4	7	61	WM	0	BMA
	5	8	62	WM	0	BMA
	6	9	63	IM	5	-
	7	10	64	IM	5	-
14	1	1	65	-	-	IA
	2	2	66	IM	30	-
	3	3	67	ACT	100	-
		4	68	ACT	100	-
	4	5	69	G	70	-
	5	6	70	G	90	-
	6	7	71	G	90	-
		8	72	G	90	-
15	1	1	73	G	75	-
		2	74	G	75	-
	2	3	75	G	75	-
		4	76	G	80	-

Table 2.6 continued

15	3	5	77	G	80	-
	4	6	78	WM	10	-
		7	79	GM	20	-
	5	8	80	WM	10	-
	6	9	81	WM	15	-
16	1	1	82	IM	30	-
	2	2	83	G	70	-
	3	3	84	G	75	MA
	4	4	85	IM	30	MA
	5	5	86	IM	30	-
	6	6	87	IM	40	-
	7	7	88	IM	40	MA
17	1	1	89	G	70	-
	2	2	90	G	80	-
	3	3	91	WM	0	A
	4	4	92	G	50	-
18	1	1	93	G	50	BMA
		2	94	G	50	IA
	2	3	95	IM	10	MA
	3	4	96	IM	10	MA
	4	5	97	IM	20	-
		6	98	IM	10	-
	5	7	99	WM	0	A
		8	100	WM	0	MA
19	1	1	101	G	90	-
	2	2	102	G	40	IA
	3	3	103	G	90	-
		4	104	G	90	-
	4	5	105	G	90	-
	5	6	106	WM	5	-
		7	107	WM	5	-
	6	8	108	WM	30	-
	7	9	109	GM	5	-
		10	110	GM	5	-
20	1	1	111	G	70	-
		2	112	G	70	-
	2	3	113	G	70	-
		4	114	G	90	MA
	3	5	115	WM	5	-
	4	6	116	G	70	-

Table 2.6 continued

20	5	7	117	WM	5	-
		8	118	WM	5	-
21	1	1	119	IM	20	MA
		2	120	G	50	-
	2	3	121	G	40	-
		4	122	G	80	A
	3	5	123	G	60	-
		6	124	G	70	MA
	4	7	125	G	40	-
		8	126	G	60	-
	5	9	127	IM	5	-
	6	10	128	IM	5	-
23	1	1	129	-	-	-
	2	2	130	G	90	-
		3	131	G	90	IA
	3	4	132	G	90	-
		5	133	G	90	-
	1	6	134	-	-	-
		7	135	-	-	-
	4	8	136	G	90	-
		9	137	G	90	-
24	1	1	138	G	70	-
		2	139	G	80	-
	2	3	140	G	80	-
25	1	1	141	G	60	-
		2	142	G	70	-
	3	3	143	G	80	-
		4	144	G	50	-
	4	5	145	G	90	-
	5	6	146	WM	5	-
	6	7	147	WM	5	-
	7	8	148	WM	5	-
	5	9	149	WM	5	-
	7	10	150	WM	5	-
26	1	1	151	G	80	-
	2	2	152	IM	10	-
	3	3	153	WM	5	-
	4	4	154	WM	10	-
	5	5	155	G	60	-
27	1	1	156	G	90	MA

Table 2.6 continued

27	1	2	157	G	90	MA
	2	3	158	G	90	MA
	3	4	159	G	90	MA
		5	160	G	90	A
	4	6	161	G	90	MA
		7	162	G	90	MA
	5	8	163	G	90	MA
	6	9	164	G	90	A
	5	10	165	G	90	A
28	1	1	166	G	90	A
	2	2	167	IM	0	MA
	3	3	168	GM	10	A
		4	169	GM	10	A
	4	5	170	G	50	MA
		6	171	G	60	MA
	5	7	172	GM	20	A
		8	173	GM	0	A
29	1	1	174	-	-	-
		2	175	G	60	MA
	2	3	176	IM	20	MA
		4	177	IM	20	BMA
	3	5	178	WM	0	BMA
	4	6	179	WM	10	MA
	5	7	180	WM	10	MA
	6	8	181	WM	10	A
		9	182	WM	10	A
		10	183	WM	10	MA
30	1	1	184	IM	30	MA
		2	185	IM	15	MA
	2	3	186	WM	5	A
	3	4	187	WM	5	A
	4	5	188	WM	5	A
	5	6	189	GM	10	A
31	1	1	190	G	90	A
		2	191	G	90	A
	2	3	192	G	90	MA
	3	4	193	WM	15	MA
	4	5	194	-	-	-
	5	6	195	G	50	MA
32	1	1	196	GM	10	A

Table 2.6 continued

32	2	2	197	GM	10	MA
		3	198	GM	10	A
	3	4	199	WM	5	A
	4	5	200	WM	5	A
	5	6	201	IM	5	MA
		7	202	IM	5	MA
33	1	1	203	GM	10	A
	2	2	204	GM	10	A
	3	3	205	G	60	MA
	4	4	206	G	60	MA
	5	5	207	G	-	IA
	6	6	208	IM	30	MA
34	1	1	209	GM	10	A
		2	210	GM	10	A
	2	3	211	G	70	A
		4	212	G	70	MA
	3	5	213	G	70	MA
		6	214	G	70	MA
35	1	1	215	WM	10	A
	2	2	216	G	90	A
	3	3	217	WM	10	A
	4	4	218	WM	10	A
	5	5	219	WM	0	MA
	6	6	220	WM	0	MA
37	1	1	221	G	90	MA
		2	222	G	70	MA
	2	3	223	G	80	A
	3	4	224	G	80	A
	4	5	225	G	80	A
38	1	1	226	G	80	MA
	2	2	227	G	80	A
	3	3	228	WM	30	A
	4	4	229	GM	20	MA
	5	5	230	WM	0	MA
	6	6	231	IM	10	MA
39	1	1	232	IM	0	A
	2	2	233	WM	0	A
	3	3	234	WM	0	A
40	1	1	235	G	100	A
		2	236	G	100	A

Table 2.6 continued

40	2	3	237	G	100	A
		4	238	G	100	A
	3	5	239	WM	20	MA
		6	240	WM	20	MA
41	1	1	241	WM	0	A
	2	2	242	WM	0	A
	3	3	243	GM	0	A
	4	4	244	IM	5	A
	5	5	245	IM	5	MA
42	1	1	246	G	0	A
	2	2	247	G	80	A
	3	3	248	-	-	IA
44	1	1	249	G	100	A
		2	250	G	100	A
		3	251	G	100	A
	2	4	252	G	100	A
	3	5	253	G	100	A
		6	254	G	100	A
	4	7	255	G	100	A
	5	8	256	GM	0	A
	6	9	257	GM	60	A
		10	258	GM	0	A
45	1	1	259	T	100	A
46	1	1	260	G	60	MA
		2	261	G	80	A
	2	3	262	G	80	A
	3	4	263	G	60	A
		5	264	G	80	A
		6	265	G	80	A
	4	7	266	G	60	A
	5	8	267	IM	0	A
	6	9	268	WM	5	A
47	1	1	269	WM	20	MA
		2	270	WM	30	A
	2	3	271	G	100	A
		4	272	G	100	A
	3	5	273	IM	50	A
		6	274	IM	50	A
	4	7	275	WM	40	A
		8	276	WM	40	A

Table 2.6 continued

48	1	1	277	GM	10	A
		2	278	GM	0	A
	2	3	279	WM	60	A
		4	280	G	50	A
	3	5	281	GM	50	MA
	5	6	282	G	50	A
		7	283	G	70	A
50	1	1	284	WM	20	MA
	2	2	285	GM	15	A
	3	3	286	WM	20	MA
	4	4	287	GM	0	A
	5	5	288	WM	50	MA
	6	6	289	WM	50	MA
51	1	1	290	G	100	A
	2	2	291	T	100	A
	3	3	292	T	100	A
	4	4	293	T	100	A
	5	5	294	T	100	A
	6	6	295	T	100	A
52	1	1	296	GM	20	MA
	2	2	297	IM	30	-
	3	3	298	WM	-	IA
		4	299	IM	40	MA
53	1	1	300	WM	10	MA
	2	2	301	GM	10	MA
		3	302	GM	10	A
	3	4	303	IM	20	A
		5	304	GM	40	A
	4	6	305	WM	30	MA
	5	7	306	WM	30	MA
	6	8	307	GM	0	MA
		9	308	GM	0	A
54	1	1	309	-	-	IA
		2	310	-	-	IA
	2	3	311	GM	10	MA
		4	312	GM	10	MA
	3	5	313	WM	40	MA
		6	314	G	60	MA
		7	315	G	70	MA
55	1	1	316	G	100	A

Table 2.6 continued

55	2	2	317	WM	10	A
	3	3	318	-	-	IA
	4	4	319	GM	30	A
56	1	1	320	G	100	MA
	2	2	321	G	100	MA
		3	322	G	100	A
		4	323	G	100	A
57	1	1	324	G	80	A
	2	2	325	G	80	A
		3	326	G	80	MA
		4	327	G	80	A
58	1	1	328	G	80	A
		2	329	G	50	MA
	2	3	330	IM	10	A
	3	4	331	WM	0	A
	4	5	332	WM	0	A
	5	6	333	WM	0	A
	6	7	334	WM	0	A

G = Glioma; WM = White matter; GM = Grey matter; IM = Infiltrative margin
A = Adequate; MA = Marginally adequate; BMA = Barely marginally adequate; IA = Inadequate
-= Information not available
Tissue smears with inadequate quality (IA) were not evaluated by EMH. The Smear Quality datapoint was not evaluated for all of the smears in the study; Smear Quality cells with hyphens indicate that smear was not evaluated for smear quality.

2.3.2 IDH Genotype Prediction from 2HG Abundance

The methodology for online determination of IDH mutation status was developed midway through the study, after off-line method development. From this point onwards, 169 smears from 30 patients were collected for the measurement of 2HG as a predictor of IDH mutation status. Three smears were excluded due to lack of location information available and/or determined, resulting in 166 smears from 30 patients being included. Of these 166 smears, 67 smears were from tumor margins and 99 smears were from tumor cores. In instances where multiple smears were made for the same tumor core biopsy, the average TIC normalized and summed 2HG product ion intensity of all smears was calculated and used to predict the IDH mutation status of that biopsy. This produced 55 margin biopsies (23 IDH-mut biopsies from 12 patients, 32 IDH-wt biopsies from 14 patients) and 68 core biopsies (36 IDH-mut biopsies from 12 patients, 32 IDH-wt biopsies from 16 patients). The measurement of 2HG is qualitative and predictions of IDH mutation status are made solely on the basis of TIC normalized and summed MS^3 intensities. Two MS^3 product ions were detected at *m/z* 85 and 101 from the sequential fragmentation of the 2HG $[M-H]^-$ precursor ion ($147 \rightarrow 129 \rightarrow O$). The intensities of the two product ions were then summed and used to predict the IDH mutation status of the tumor. While the margin biopsies from IDH-mut patients contained significantly higher levels of 2HG compared to margins from IDH-wt patients, tumor core biopsies were preferred for IDH mutation status assessment, as the concentration of 2HG is highest at the tumor core (Figure 2.2). The IDH mutation status of the patients was obtained from pathology reports and was typically the result of post-operative IDH1 R132H immunohistochemistry and, when inconclusive, PCR-based IDH1/2 sequencing analysis.

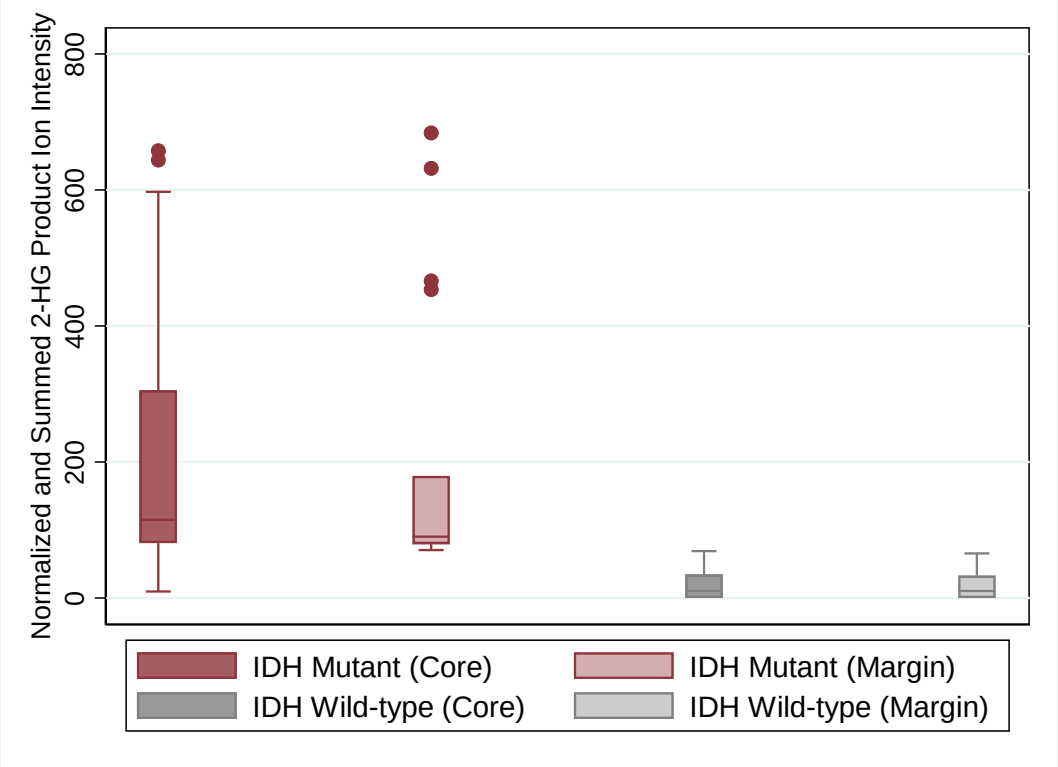

Figure 2.2 Box plots of summed 2-Hydroxyglutarate (2HG) product ion intensities, separated by isocitrate dehydrogenase (IDH) mutation status and biopsy location (core (n_{core} = 68) or margin (n_{margin} = 55). Biopsies from the tumor core and margins of IDH-mut tumors produced significantly higher 2-HG compared to the IDH-wt tumors ($p < 0.0001$ using the Tukey-HSD test for statistical significance). The IDH mutant tumors produced slightly higher 2-HG in the cores compared to margins, but the difference was not statistically significant.

The chemical structures of α-ketoglutartic acid and 2HG, its mutated form which accumulates in the presence of an IDH mutation, are shown in Figure 2.3A. A statistically significant (Wilcoxon rank-sum test $p < 0.0001$) increase in the 2HG signal of tumor core biopsies was observed in the IDH-mut patients compared to the IDH-wt patients. A receiver operating characteristic (ROC) curve model provided an area under the curve (AUC) of 0.98 using the tumor cores, as shown in Figure 2.3B. This difference is apparent in the box plots shown in Figure 2.3C. The summed and normalized 2HG product ion intensity cutoff of 62.3 (in the MS^3 spectrum) resulted in the highest overall accuracy. This normalized cutoff is instrument and method dependent and requires further interlaboratory investigation to evaluate whether a universal cutoff can be determined. Using the ROC determined cutoff, the sensitivity (correctly identifying core biopsies from IDH-mut subjects when the IDH mutation was present) and specificity (correctly

identifying core biopsies from IDH-wildtype when IDH mutation was absent) were 89% and 100%, respectively, with an overall accuracy of 94%. Further optimization of the method is part of an ongoing clinical study in collaboration with Mayo Clinic – Jacksonville, the results of which are summarized in Chapter 5.

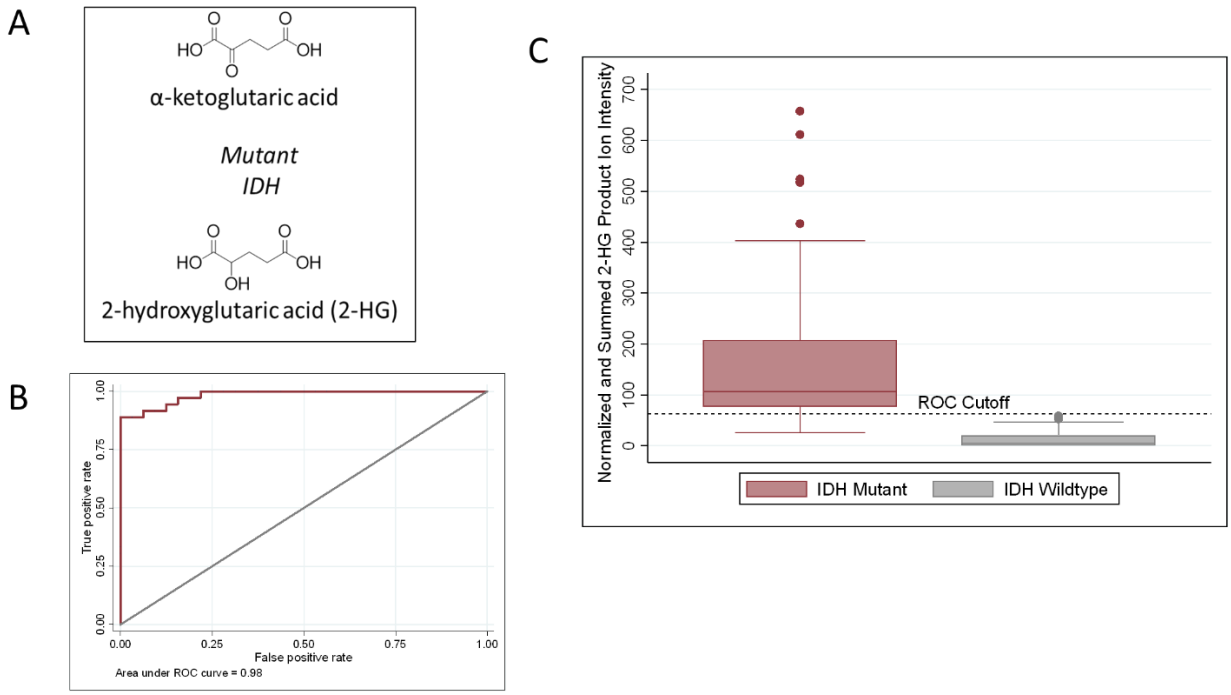

Figure 2.3 Intraoperative assessment of isocitrate dehydrogenase (IDH) mutation status from tumor cores (n_{core} = 68). (A) Chemical structure of α-ketoglutaric acid and 2-Hydroxyglutarate (2HG), the oncometabolite associated with IDH mutations. (B) ROC curve for the IDH-mutation assay using tumor core biopsies. The AUC is 0.98, indicating the high accuracy of the method. (C) Box plot showing the average summed and TIC normalized MS^3 fragment ion intensities (*m/z* 85 + *m/z* 101) produced by sequential dissociation (MS^3) of 2HG for all tumor core biopsies (n = 68 biopsies from 28 patients) by IDH mutation status. The fragment ion intensities from supplicate smears of the same biopsy were averaged to generate one value per biopsy. Error bars represent ± 1.5 times the calculated standard deviations. The black dashed horizontal decision line in (C) was calculated from ROC curve analysis and differentiates tumor core biopsies from IDH-mut patients and IDH-wt patients with the highest sensitivity and specificity.

For several biopsies included in this study ($n_{discordant}$ = 4), discordant mutation status predictions existed between core biopsies from the same patient. Due to the high degree of heterogeneity of glioma, it is likely that 2HG concentration varies within the tumor cavity, even over small distances. Additionally, cauterized or hemorrhagic tissue results in ion suppression and

provides poor diagnostic information. These problems are shared with traditional histopathology. To limit the impact of signal variation, the average the summed and TIC normalized MS^3 fragment ion intensities for all biopsies from a patient were generated and used to predict IDH mutation status. When doing so, only one patient (Patient 26) was misclassified with respect to its IDH mutation status. This patient, and patients close to the ROC cutoff value, had low grade (i.e., WHO grade II and III) astrocytomas (i.e., anaplastic astrocytomas and diffuse astrocytomas). In our experience, these lower grade tumors have lower concentrations of 2HG than higher grade gliomas, resulting in lower summed 2HG product ion intensity values. Therefore, for suspected low-grade gliomas, resampling may be necessary to increase the degree of confidence placed in measured summed 2HG product ion intensities. Biological variability within the tumor cavity is an area of active research; high powered MRI instruments are being used to probe distributions of metabolites within the tumor cavity and surrounding tissue to further understand tumor heterogeneity. As knowledge of tumor heterogeneity and its impacts on the spatial distribution of metabolites increases, this will help make further sense of discordant predictions in IDH mutation status. Additionally, IDH mutation status was only predicted for a small number of patients (i.e., 28 patients). Some degree of biological variability is expected when studying patient cohorts of this size. In circumstances in which tumor heterogeneity precludes the ability to generate an accurate IDH genotype from the averaging of data from provided biopsies, additional biopsies that produce data of sufficient diagnostic quality may be taken. While this is often impractical for standard histopathology, DESI-MS analysis takes only three minutes, so resampling from the same patient during surgery is a feasible solution.

Table 2.7 Confusion matrix assessing correlation between histopathology assessments and DESI-MS estimates of tumor cell percentage (TCP) and disease status of tissue biopsies (n = 203)

		Histopathology	
		High TCP/Glioma[a]	**Low TCP/Infiltrative Margin**
Full scan NAA Intensity TCP Estimate	**High TCP/Glioma[b]**	91	25
Lipid Deconvolution TCP Estimate		76	15
PCA-LDA Diagnosis		60	18
Full scan NAA Intensity TCP Estimate	**Low TCP/Infiltrative Margin[b]**	9	78
Lipid Deconvolution TCP Estimate		24	88
PCA-LDA Diagnosis		35	90

[a] Histopathology assessments of TCP were used for correlation with lipid deconvolution and NAA intensity classifications of TCP. Histopathology assessments of disease status were used for correlation with PCA-LDA diagnosis of the tissue smears. [b] For lipid deconvolution and NAA intensity classification, histopathology TCP categories were High ≥ 51% and Low ≤ 50%. Histopathology categories of glioma and infiltrative margin were used for correlation with PCA-LDA diagnosis of glioma and infiltrative margin. Note: The results of an ongoing clinical study in collaboration with Mayo Clinic – Jacksonville are described in detail in Chapter 5. The correlation of histopathology assessments and DESI-MS estimates of TCP and disease status for this new patient cohort are summarized in Table 5.6.

2.3.3 Estimating Tumor Cell Percentage from NAA Abundance

Two DESI-MS based methods for the rapid estimation of TCP, based on NAA and lipid abundances respectively, have been developed and tested previously on an initial set of 10 human patients.(31) Data for this original set of patients have been integrated into the complete 49 patient cohort and reexamined, with the results now discussed. Applying to the 49 patient cohort of the NAA based (first) method, the standard normal variate (SNV) normalized intensity of *m/z* 174, corresponding to NAA, measured in the full scan MS metabolite profile was used to estimate TCP, using previously published data as a training set.(27, 34) For biopsies with multiple smears, the average TCP from the corresponding smears was calculated and used to estimate TCP for the specific biopsy. This produced a collection of 203 biopsies (109 core, 85 margin, 9 undermined) from 49 patients. Biopsies that provided 50% or less glioma contribution were categorized as low TCP and samples providing 51% or more glioma contribution were categorized as high TCP. The histopathology estimates of TCP were categorized using the same decision boundary. Using these categories, an overall accuracy of correctly classifying the samples as low or high TCP was 83%, with sensitivity and specificity of 91% and 76%, respectively (Table 2.7). As shown in Figure 2.4, the full scan MS abundance of NAA (detected as *m/z* 174 in the metabolite profile scan) provided slightly higher overall accuracy than did the MS2 data (sensitivity, specificity, and overall accuracy were 79%, 85%, and 82%, respectively, for the MS2 data ($n_{NAA\ MS2} = 198$)). The targeted MS2 scan for NAA (174 → O) gave product ions at *m/z* 88, 114, 130, and 156. Box plots and ROC curves of the NAA full scan and MS2 data are shown in Figure 2.4. Principal component analysis (PCA) was performed on the metabolite profiles and the contribution of *m/z* 174 (NAA) in separating low and high TCP smears was consistent with previous reports. (27)

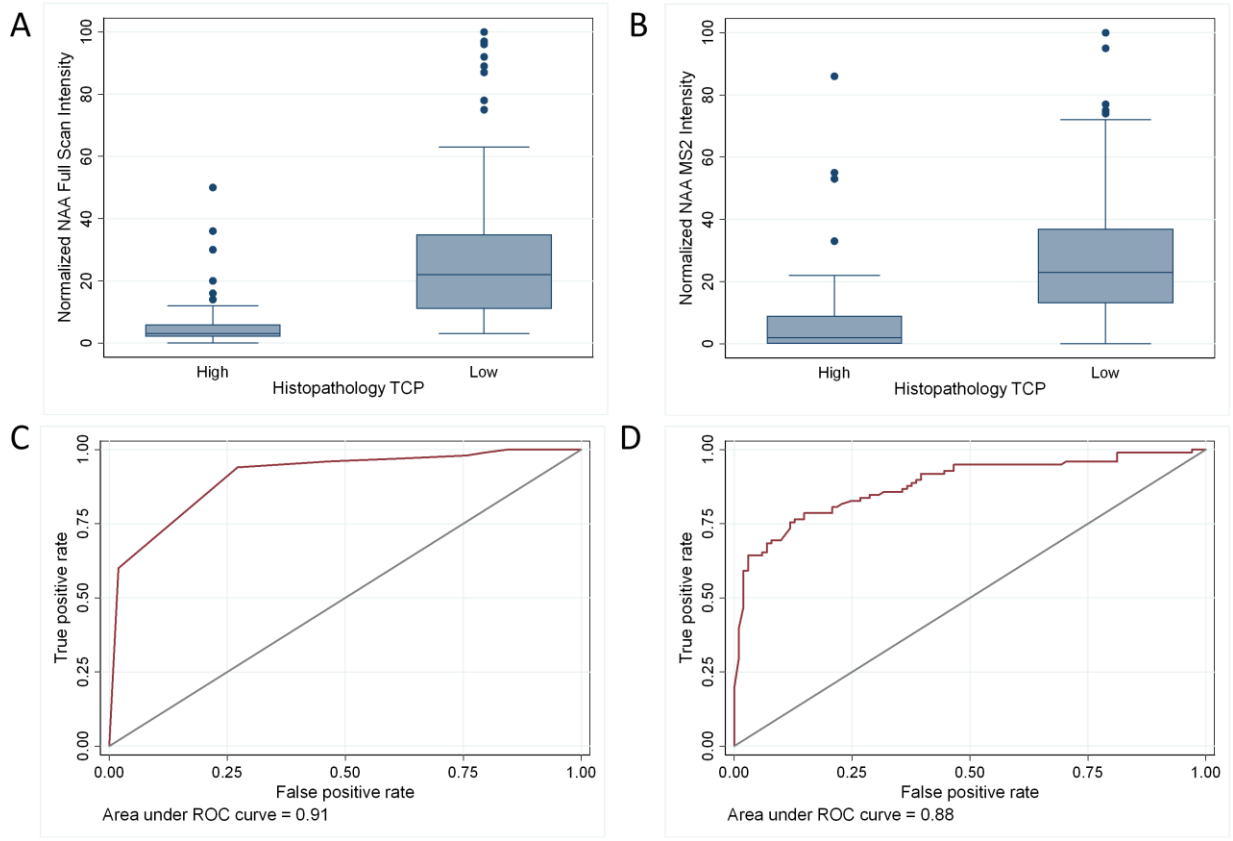

Figure 2.4 Assessment of tumor cell percentage based on N-Acetylaspartic acid (NAA) measurements. A) Box plot showing dispersion in the normalized full scan *m/z* 174 intensity (corresponding to NAA) as a function of TCP. High indicates TCP greater than or equal to 51%; Low indicates TCP less than or equal to 50% TCP. B) Box plots showing dispersion in normalized MS2 product ion intensity for NAA. C) ROC curve for A (predicting TCP high or low based on full scan NAA intensity) provided AUC of 0.91. D) ROC curve for B (predicting TCP high or low based on MS2 NAA intensity) provide AUC of 0.88.

2.3.4 Estimating Tumor Infiltration using Lipid Profile Deconvolution

The second method for estimating TCP employed a lipid profile deconvolution approach, as shown in Figure 2.5. PCA was used to calculate the percentage of white matter (WM), grey matter (GM), and glioma (G) contributing to the lipid profiles of the patient samples using a linear regression model built from data collected in a previous study.(1, 3) The model was based on the presumption that the observed lipid profile of each brain tissue biopsy is composed of a ternary mixture of WM, GM, and G. The summed percentages of these three categories are constrained to 100%. The regression model was built from data collected from DESI-MS analysis of banked glioma and normal human brain specimens. Histologically correlated mass spectra were compiled

based on histopathological assessment, compressed with PCA, and the average PC1 and PC2 scores for samples of pure WM, GM, and G were calculated. The three extremes (PC1 and PC2 scores corresponding to 100%WM, 100%GM, 100%G) were used to calculate the predicted PC1 and PC2 scores for each possible mixture. To predict the composition of new samples (n_{total} = 203), the PCA lipid profile loading matrix from the training set data(3) was used to calculate the PC scores of the new samples. The calculated PC1 and PC2 scores of the new samples were matched to predicted PC1 and PC2 scores using the original training set data; the predicted scores were each associated with a specific percentage combination of GM:WM:G (Figure 2.5). The classifications of GM and WM were recategorized as infiltrative margin (IM) to match the histopathology categories, as the nature of the underlying normal brain tissue (specifically white or grey matter) could not always be reliably determined by histopathology. The percentage of G calculated for each unknown sample was used as an estimate of the TCP. For biopsies with multiple smears, the average percentage of G from corresponding smears was calculated and used to estimate TCP for the specific biopsy. This produced data for a collection of 203 biopsies (109 core, 85 margin, 9 undermined) from 49 patients. Using 50% TCP as the delineation value as for the NAA abundance method, an overall accuracy of correctly classifying the samples as low or high TCP was 81%, with sensitivity and specificity of 76% and 85%, respectively (Table 2.7). The high TCP and low TCP smears analyzed in this study are fairly well separated in PCA space, due primarily to the ions of *m/z* 834, 794, and 888.

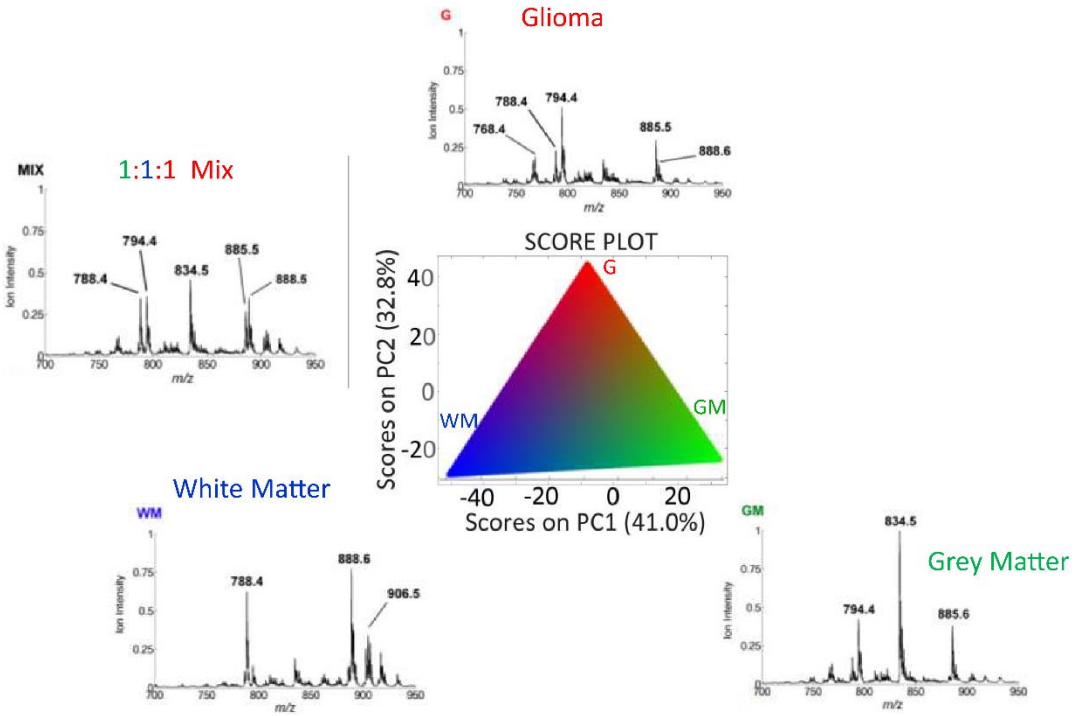

Figure 2.5 Scheme illustrating the lipid deconvolution approach. A ternary mixture model was fitted to the lipid profile PCA data obtained from a previous study. The continuous ternary mixture is indicated by the colored triangle on the PC score plot. In the illustration, RGB color coding was used to make a continuous mixture between red (glioma (G)), blue (white matter (WM)), and green (grey matter (GM)). PC1 and PC2 coordinates corresponding to each of these RGB color codes were created, such that each pair of PC1 and PC2 coordinates corresponds to a unique combination of [G GM WM]. After projection of the new samples onto this PCA space, the model was used to predict the percentages of the reference glioma, grey matter, and white matter PCA scores that best matched the unknown spectra. The average lipid profile of the pure classes along with the (PC1, PC2) coordinates are shown around the mixture model at the corresponding vertex, along with the 1:1:1 mixture G:GM:WM. For the present study, the PCA-LDA classifications of GM and WM were recategorized as infiltrative margin (IM) to match the histopathology categories.

2.3.5 Predicting Disease State from Fused Metabolite and Lipid Profiles

The final category of diagnostic information provided by DESI-MS was disease status. Using PCA-LDA on fused SNV normalized lipid and metabolite profiles obtained from DESI-MS, tissue smears were classified as either G, GM, or WM, with the latter two being recategorized as infiltrative margin (IM) to match the histopathology categories (see Table 2.7 footnote). Similar overall accuracy was observed when performing PCA-LDA cross-validation with the lipid and metabolite profiles of all 272 tissue smears (Tables 2.8 and 2.9), however, the sensitivities and

specificities were quite different, supporting the use of fused lipid and metabolite profiles for a more robust method that utilizes diagnostic features contained in both parts of a mass spectrum. For biopsies with multiple smears, the average SNV normalized lipid and metabolite profiles from corresponding smears were calculated prior to fusing to generate a representative lipid and metabolite profiles for the biopsy used to predict disease status. This produced a collection of 203 biopsies (109 core, 85 margin, 9 undermined) from 49 patients. The agreement between PCA-LDA predictions and histopathological assessment of disease status is shown in Table 1. The sensitivity, specificity, and accuracy in predicting disease status are 63%, 83%, and 74%, respectively. While the sensitivity using the fused data method was lower than either the lipid or metabolite profiles independently, the use of the fused profiles to predict TCP is likely more robust than using only one segment of the mass spectrum, as diagnostics features appear in both regions of the mass spectrum. A significant fraction of the smears classified as glioma based on histopathology ($n_{missclasified}$ smears = 43, 31%) were misclassified as either WM or GM using PCA-LDA classification. These cases likely reflect mixed tissue smears which are challenging for histopathology assessment as well for our current DESI-MS system. These types of samples were encountered both at surgical margins and at tumor cores.

Table 2.8 Confusion matrix showing correlation between histopathology and PCA-LDA cross-validation predictions of TCP category using the lipid profiles obtained from the intraoperative tissue smears (n = 272). Four principal components and five cross-validation groups were used.

		Histopathology TCP		
		Low	High	Total
PCA-LDA TCP Prediction	Low	108	13	121
	High	45	106	151
	Total	153	119	272
	Sensitivity	70.6%		
	Specificity	89.6%		
	Accuracy	78.6%		

Table 2.9 Confusion matrix showing correlation between histopathology and PCA-LDA cross-validation predictions of TCP category using the metabolite profiles obtained from the intraoperative tissue smears (n = 272). Six principal components and five cross-validation groups were used.

		Histopathology TCP		
		Low	High	Total
PCA-LDA TCP Prediction	Low	127	42	169
	High	26	77	103
	Total	153	119	272
	Sensitivity	83.0%		
	Specificity	64.7%		
	Accuracy	75.0%		

2.3.6 Evaluation of Methods for Estimating TCP and Disease State

Ultimately, we found that both methods (i.e., full scan NAA abundance and lipid deconvolution) were capable of predicting TCP with similar accuracies (83% and 80%, respectively), with the full scan NAA abundance having greater sensitivity (87% vs. 76%) and the lipid deconvolution method having greater specificity (79% vs. 84%). In instances of misclassification, it would be beneficial to compare the disease status predictions made using the fused metabolite and lipid profiles with TCP estimations using NAA and lipid deconvolution (i.e., many of the misclassified biopsies have TCP estimates indicating mixed diseased and normal tissue). Additionally, the PCA-LDA method itself may need to be adjusted to allow for the correct classification of biopsies with more mixed morphologies by adding additional classifications (i.e., rather than categorizing tissues into three rigid categories (G, WM, GM), perhaps six categories (G, G/WM, WM, WM/GM, GM, GM/G)).

While it is likely that there are many contributing factors, a possible cause of variability in TCP estimates may be that the full scan NAA abundance method predicts TCP based on the intensity of a single analyte that exists in very low concentrations within the tumor, while the lipid deconvolution method predicts TCP based on a collection of analytes in a characteristic pattern of intensities. Matrix effects are inherent in the measurements of complex samples, especially biological samples; they are an inherent component of the recorded output and, consequently, cannot be eliminated. Excepting cases where tissue is substantially different e.g., cauterized or hemorrhagic tissues, observed changes with matrix involve total signal but not relative signals, provided the same type of tissue is being analyzed. A possible exception is the analysis of a single

analyte (i.e., 2HG or NAA) where the matrix affects signal intensity but does not otherwise distort the measurement. To minimize variations in signal, the recorded mass spectra are normalized (specifically TIC and/or SNV normalized) before additional comparison or statistical analysis is performed.

There are likely many additional experimental factors that may have affected misclassification in the present study. Improvements are needed to increase the agreement between the DESI-MS predictions of disease status and TCP with histopathology, the current gold-standard method in morphology. The diagnostic sensitivity and specificity for the TCP predictions could be improved by better correlating the positions at which TCP pathology data are taken relative to DESI-MS data while the biological variation can be addressed with additional cases. The ongoing study in collaboration with Mayo Clinic – Jacksonville is exploring the impact of these factors DESI-MS measurements. The results are described in Chapter 5. There is still room for significant improvement and we have elected to focus our efforts on the advanced optimization and translation of the 2HG assay at this time and reassess other methods of estimating TCP later.

2.3.7 Assessment of Margins of Tumors of Different WHO Grades

The assessment of glioma margins is not routinely performed intraoperatively with pathologic or molecular methods. That said, glioma infiltration is significant beyond the contrast enhancement margin in MRI, especially in glioblastoma.(6) In this section, we investigate whether margins from high-grade glioma patients contain higher TCP than margins from low-grade glioma patients using our DESI-MS methods. In our study, 85 of the 203 biopsies (110 smears with some replicates) were obtained from margins (based on MRI) and provided acceptable quality for histopathology and DESI-MS analysis. WHO grade information was not available for eight margin biopsies from two patients (Patients 41 and 46) and, thus, these biopsies were excluded from this portion of the study. For low-grade gliomas (WHO grades I – III), 78% of the margin biopsies had low TCP ($n_{\text{low TCP, low grade margins}} = 35$) and 22% had high TCP based on histopathology ($n_{\text{high TCP, low grade margins}} = 10$), using 50% TCP for delineating between low and high TCP. Our accuracy with respect to agreement with histopathology assessment for the grade I-III margin samples ($n_{\text{total low grade margins}} = 45$) was 80% and 76% overall using the normalized NAA intensity and lipid deconvolution approaches, respectively (Table 2.10). For the grade IV gliomas, histopathology determined that 59% of the margin biopsies had low TCP ($n_{\text{low TCP, high grade margins}} = 19$) and 41%

had high TCP ($n_{\text{high TCP, high grade margins}} = 13$), also using the 50% TCP cutoff. Our agreement with the histopathology assessment for the margin biopsies from grade IV gliomas ($n_{\text{total high grade margins}} = 32$) was 97% and 84% overall using the normalized NAA intensities and lipid deconvolution approaches, respectively (Table 2.11).

Table 2.10 Confusion matrix comparing DESI and histopathology TCP predictions for the grade I-III margin biopsies (n = 45).

		Histopathology[a]	
		High TCP/Glioma[b]	**Low TCP/Infiltrative Margin[b]**
Full Scan NAA Intensity TCP Estimate	**High TCP/Glioma[b]**	10	9
Lipid Deconvolution TCP Estimate		5	6
Full Scan NAA Intensity TCP Estimate	**Low TCP/Infiltrative Margin[b]**	0	26
Lipid Deconvolution TCP Estimate		5	29
Full Scan NAA Intensity TCP Estimate		**Lipid Deconvolution TCP Estimate:**	
Sensitivity:	100%	*Sensitivity:*	50%
Specificity:	74%	*Specificity:*	83%
Accuracy:	80%	*Accuracy:*	76%

[a]*Histopathology assessments of TCP were used for correlation with lipid deconvolution and NAA intensity classifications of TCP.*
[b]*For lipid deconvolution and NAA intensity classification, histopathology TCP categories were High ≥51% and Low ≤50%.*

Table 2.11 Confusion matrix comparing DESI and histopathology TCP predictions for the grade IV margin biopsies (n = 32).

		Histopathology[a]	
		High TCP/Glioma[b]	**Low TCP/Infiltrative Margin[b]**
Full Scan NAA Intensity TCP Estimate	**High TCP/Glioma[b]**	12	0
Lipid Deconvolution TCP Estimate		8	0
Full Scan NAA Intensity TCP Estimate	**Low TCP/Infiltrative Margin[b]**	1	19
Lipid Deconvolution TCP Estimate		5	19
Full Scan NAA Intensity TCP Estimate		**Lipid Deconvolution TCP Estimate:**	
Sensitivity:	192%	*Sensitivity:*	62%
Specificity:	100%	*Specificity:*	100%
Accuracy:	97%	*Accuracy:*	84%

[a]*Histopathology assessments of TCP were used for correlation with lipid deconvolution and NAA intensity classifications of TCP.*
[b]*For lipid deconvolution and NAA intensity classification, histopathology TCP categories were High ≥51% and Low ≤50%.*

Literature reports suggest that high TCP may extend beyond MRI contrast enhancement, especially in grade IV glioblastomas.(6, 8, 35) We found that the margins of grade IV gliomas contained high TCP more often than the margins of grade I-III gliomas, although the difference in number of high TCP smears obtained from the margins of grade IV compared to grade I-III gliomas using nominal logistic regression and a 50% TCP cutoff to delineate between the low and high TCP categories is not statistically significant ($p = 0.0833$). In this context, a DESI-MS tool for assessment of local tumor burden must be used in combination with an independent diagnostic method such as MRI neuronavigation and/or brain mapping.

2.3.8 Simplified DESI-MS Outputs that Enable Surgical Decision Making

In this clinical study, we have demonstrated two major applications of the DESI-MS system: providing diagnostic information of two types for tumor cores (IDH mutation status and disease status) and providing surgical margin assessments of residual tumor (i.e., TCP) at discrete locations. With appropriate method validations and permissions, these predictions could be provided to the neurosurgeon in order to improve treatment strategy, including the extent of resection. Here we describe a typical example of a case in which DESI-MS would be useful. Figure 2.6A shows the biopsy locations for two stereotactic biopsies from Patient 58. Figure 2.6B-D shows the raw lipid, metabolite, and 2HG MS3 data for biopsy #328, respectively; Figure 2.6E-2G shows the same types of data but for biopsy #333. This biopsy was predicted with PCA-LDA to be glioma, by lipid deconvolution to have high TCP, and by 2HG intensity to be IDH-mut. In contrast, biopsy #333 (blue point in Figure 2.6A) was taken several millimeters outside the MRI contrast enhancing area and was predicted from PCA-LDA to be normal white matter, by lipid deconvolution to have low TCP, and by 2HG intensity to also be IDH-mut. Each of these predictions matched the histopathology assessments of the tissue smears. Thus, using the DESI-MS system, the neurosurgeon could analyze biopsies from discrete regions of the resection cavity to assess residual tumor when clinical acumen is insufficient.

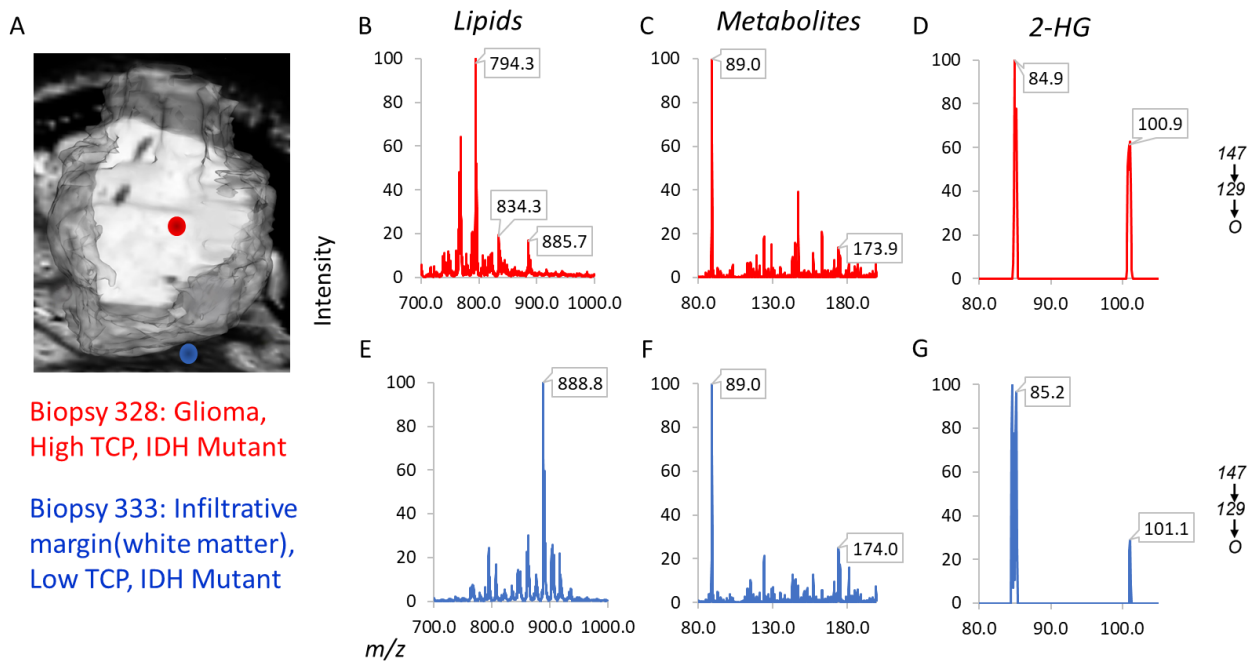

Figure 2.6 DESI-MS predictions of disease status, TCP, and IDH-genotype for a core and margin biopsy from Patient 58. (A) Reconstruction of MRI tumor volume showing the locations of the two biopsies. Biopsy 328 (red dot) is within the contrast enhancing region of the tumor; biopsy 333 (blue dot) is a few mm outside of the contrast enhancing region. (B-D) The lipid, metabolite, and 2HG MS^3 product ion scans for biopsy 328 (red dot in Figure 2.6A). (E-G) The lipid, metabolite, and 2HG MS^3 product ion scans for biopsy 333 (blue dot in Figure 2.6A). Biopsy 328 is classified as glioma, high TCP, and IDH-mut; biopsy 333 is classified as infiltrative margin (white matter), low TCP, and IDH-mut.

While the initial results presented in this paper are promising, it is important to remember that the DESI-MS system is proposed as an ancillary method to support the existing standard of care methods. Thus, when making the decision to resect, the DESI-MS assessments cannot be interpreted in isolation. In future studies, it will be worthwhile to evaluate whether DESI-MS assessment of areas at the MRI tumor borders can improve extent of resection and whether this in turn can reduce tumor recurrence and increase overall and progression-free survival. It will be worthwhile also to assess whether prediction of IDH mutation status via DESI-MS analysis can increase overall and progression-free survival by allowing for more personalized resection approaches and use of chemotherapeutic drugs targeting IDH mutations at the time of surgery.

2.4 Conclusions

DESI-MS monitoring of 2HG, along with lipid and metabolite profiling, is shown to provide utility in improving the differential diagnosis of glioma intraoperatively through the assessment of IDH mutation status and disease status. The system also provides a means of assessing surgical margins for residual tumor through lipid profile deconvolution and measurement of NAA. The clinical accuracy of the IDH mutation assay was high (94%). Implementation of a new standard of care for surgical glioma resection based on IDH mutation status would be enabled by intraoperative DESI-MS assessments in combination with pre-operative MRI detection of 2HG. Additionally, the presence of the IDH mutation in this context is 100% specific for diffuse glioma and can assist in differential diagnosis to confirm the presence of glioma.(4) The clinical accuracy of correctly predicting TCP (based on correlations with morphologic pathology evaluations) was moderate (83% and 81% for NAA and lipid profile deconvolution, respectively). Emerging evidence which suggests differences in patient outcome from maximal tumor resection based on IDH mutation status demonstrates a need for accurate and rapid intraoperative IDH mutation status assessment. Overwhelming clinical evidence showing the need to maximize extent of resection in gliomas highlights the need for methods to assess residual tumor at surgical margins. The intraoperative DESI-MS system is capable of these two applications, although they are very different with respect to data quality. Advanced development of this DESI-MS system to enable clinical diagnostic applications and rapid assessments of residual tumor could significantly improve glioma resection is being performed at Mayo Clinic – Jacksonville in an ongoing clinical study. The results are summarized in Chapter 5.

2.5 Acknowledgements

This research was supported by the National Institute of Biomedical Imaging and Bioengineering (NIH grant no. R21EB015722). Support of the Purdue Center for Cancer Research, NIH grant P30 CA023168, is gratefully acknowledged. This publication was made possible with partial support for Clint Alfaro from grant no. UL1TR001108 (to A. Shekhar, principal investigator) from the National Institutes of Health, National Center for Advancing Translational Sciences, Clinical and Translational Sciences Award. The work was performed in collaboration with a team of neurosurgeons including Dr. Mahua Dey and Dr. Aaron Cohen-Gadol and

neuropathologist Dr. Eyas Hattab at Indiana University School of Medicine. The authors thank Professor Tim Ratliff for his support; Heather Cero and Lauren Snyder for patient consent, providing clinical data, and IRB monitoring. Fan Pu, Rong Chen, Alan K. Jarmusch, and Zane Baird are thanked for their assistance with the study.

2.6 References

1. D'Amico RS, Englander ZK, Canoll P, Bruce JN. Extent of Resection in Glioma-A Review of the Cutting Edge. World Neurosurg. 2017;103:538-49.

2. Brat DJ, Verhaak RG, Aldape KD, Yung WK, Salama SR, Cooper LA, et al. Comprehensive, Integrative Genomic Analysis of Diffuse Lower-Grade Gliomas. N Engl J Med. 2015;372(26):2481-98.

3. McGirt MJ, Chaichana KL, Gathinji M, Attenello FJ, Than K, Olivi A, et al. Independent association of extent of resection with survival in patients with malignant brain astrocytoma. J Neurosurg. 2009;110(1):156-62.

4. Hervey-Jumper SL, Berger MS. Maximizing safe resection of low- and high-grade glioma. J Neurooncol. 2016;130(2):269-82.

5. Mampre D, Ehresman J, Pinilla-Monsalve G, Osorio MAG, Olivi A, Quinones-Hinojosa A, et al. Extending the resection beyond the contrast-enhancement for glioblastoma: feasibility, efficacy, and outcomes. Br J Neurosurg. 2018;32(5):528-35.

6. Eidel O, Burth S, Neumann JO, Kieslich PJ, Sahm F, Jungk C, et al. Tumor Infiltration in Enhancing and Non-Enhancing Parts of Glioblastoma: A Correlation with Histopathology. PLoS One. 2017;12(1):e0169292.

7. Chen R, Ravindra VM, Cohen AL, Jensen RL, Salzman KL, Prescot AP, et al. Molecular features assisting in diagnosis, surgery, and treatment decision making in low-grade gliomas. Neurosurg Focus. 2015;38(3):E2.

8. Claes A, Idema AJ, Wesseling P. Diffuse glioma growth: a guerilla war. Acta Neuropathol. 2007;114(5):443-58.

9. Beiko J, Suki D, Hess KR, Fox BD, Cheung V, Cabral M, et al. IDH1 mutant malignant astrocytomas are more amenable to surgical resection and have a survival benefit associated with maximal surgical resection. Neuro Oncol. 2014;16(1):81-91.

10. Patel T, Bander ED, Venn RA, Powell T, Cederquist GY, Schaefer PM, et al. The Role of Extent of Resection in IDH1 Wild-Type or Mutant Low-Grade Gliomas. Neurosurgery. 2018;82(6):808-14.

11. Takats Z, Wiseman JM, Gologan B, Cooks RG. Mass spectrometry sampling under ambient conditions with desorption electrospray ionization. Science. 2004;306(5695):471-3.

12. Ifa DR, Eberlin LS. Ambient Ionization Mass Spectrometry for Cancer Diagnosis and Surgical Margin Evaluation. Clin Chem. 2016;62(1):111-23.

13. Hanel L, Kwiatkowski M, Heikaus L, Schluter H. Mass spectrometry-based intraoperative tumor diagnostics. Future Sci OA. 2019;5(3):FSO373.

14. Yoshimura K, Mandal MK, Hara M, Fujii H, Chen LC, Tanabe K, et al. Real-time diagnosis of chemically induced hepatocellular carcinoma using a novel mass spectrometry-based technique. Anal Biochem. 2013;441(1):32-7.

15. Alfaro CM, Jarmusch AK, Pirro V, Kerian KS, Masterson TA, Cheng L, et al. Ambient ionization mass spectrometric analysis of human surgical specimens to distinguish renal cell carcinoma from healthy renal tissue. Anal Bioanal Chem. 2016;408(20):5407-14.

16. Balog J, Sasi-Szabo L, Kinross J, Lewis MR, Muirhead LJ, Veselkov K, et al. Intraoperative Tissue Identification Using Rapid Evaporative Ionization Mass Spectrometry. Science Translational Medicine. 2013;5(194):194ra93-ra93.

17. Phelps DL, Balog J, Gildea LF, Bodai Z, Savage A, El-Bahrawy MA, et al. The surgical intelligent knife distinguishes normal, borderline and malignant gynaecological tissues using rapid evaporative ionisation mass spectrometry (REIMS). Br J Cancer. 2018;118(10):1349-58.

18. Woolman M, Ferry I, Kuzan-Fischer CM, Wu M, Zou J, Kiyota T, et al. Rapid determination of medulloblastoma subgroup affiliation with mass spectrometry using a handheld picosecond infrared laser desorption probe. Chem Sci. 2017;8(9):6508-19.

19. Fatou B, Saudemont P, Leblanc E, Vinatier D, Mesdag V, Wisztorski M, et al. In vivo Real-Time Mass Spectrometry for Guided Surgery Application. Sci Rep. 2016;6:25919.

20. Zhang J, Rector J, Lin JQ, Young JH, Sans M, Katta N, et al. Nondestructive tissue analysis for ex vivo and in vivo cancer diagnosis using a handheld mass spectrometry system. Sci Transl Med. 2017;9(406).

21. Sans M, Zhang J, Lin JQ, Feider CL, Giese N, Breen MT, et al. Performance of the MasSpec Pen for Rapid Diagnosis of Ovarian Cancer. Clin Chem. 2019;65(5):674-83.

22. Swales JG, Hamm G, Clench MR, Goodwin RJA. Mass spectrometry imaging and its application in pharmaceutical research and development: A concise review. International Journal of Mass Spectrometry. 2019;437:99-112.

23. Kooijman PC, Nagornov KO, Kozhinov AN, Kilgour DPA, Tsybin YO, Heeren RMA, et al. Increased throughput and ultra-high mass resolution in DESI FT-ICR MS imaging through new-generation external data acquisition system and advanced data processing approaches. Sci Rep. 2019;9(1):8.

24. Wang H, Manicke NE, Yang Q, Zheng L, Shi R, Cooks RG, et al. Direct Analysis of Biological Tissue by Paper Spray Mass Spectrometry. Analytical Chemistry. 2011;83(4):1197-201.

25. Woolman M, Zarrine-Afsar A. Platforms for rapid cancer characterization by ambient mass spectrometry: advancements, challenges and opportunities for improvement towards intrasurgical use. Analyst. 2018;143(12):2717-22.

26. Eberlin LS, Margulis K, Planell-Mendez I, Zare RN, Tibshirani R, Longacre TA, et al. Pancreatic Cancer Surgical Resection Margins: Molecular Assessment by Mass Spectrometry Imaging. PLoS Med. 2016;13(8):e1002108.

27. Jarmusch AK, Pirro V, Baird Z, Hattab EM, Cohen-Gadol AA, Cooks RG. Lipid and metabolite profiles of human brain tumors by desorption electrospray ionization-MS. Proc Natl Acad Sci U S A. 2016;113(6):1486-91.

28. Eberlin LS, Norton I, Orringer D, Dunn IF, Liu X, Ide JL, et al. Ambient mass spectrometry for the intraoperative molecular diagnosis of human brain tumors. Proc Natl Acad Sci U S A. 2013;110(5):1611-6.

29. Eberlin LS, Norton I, Dill AL, Golby AJ, Ligon KL, Santagata S, et al. Classifying human brain tumors by lipid imaging with mass spectrometry. Cancer Res. 2012;72(3):645-54.

30. Eberlin LS, Dill AL, Golby AJ, Ligon KL, Wiseman JM, Cooks RG, et al. Discrimination of human astrocytoma subtypes by lipid analysis using desorption electrospray ionization imaging mass spectrometry. Angew Chem Int Ed Engl. 2010;49(34):5953-6.

31. Pirro V, Alfaro CM, Jarmusch AK, Hattab EM, Cohen-Gadol AA, Cooks RG. Intraoperative assessment of tumor margins during glioma resection by desorption electrospray ionization-mass spectrometry. Proc Natl Acad Sci U S A. 2017;114(26):6700-5.

32. Alfaro CM, Pirro V, Keating MF, Hattab EM, Cooks RG, Cohen-Gadol AA. Intraoperative assessment of isocitrate dehydrogenase mutation status in human gliomas using desorption electrospray ionization-mass spectrometry. J Neurosurg. 2019:1-8.

33. Dang L, White DW, Gross S, Bennett BD, Bittinger MA, Driggers EM, et al. Cancer-associated IDH1 mutations produce 2-hydroxyglutarate. Nature. 2009;462(7274):739-44.

34. Moffett JR, Ross B, Arun P, Madhavarao CN, Namboodiri AM. N-Acetylaspartate in the CNS: from neurodiagnostics to neurobiology. Prog Neurobiol. 2007;81(2):89-131.

35. Price SJ, Jena R, Burnet NG, Hutchinson PJ, Dean AF, Peña A, et al. Improved Delineation of Glioma Margins and Regions of Infiltration with the Use of Diffusion Tensor Imaging: An Image-Guided Biopsy Study. American Journal of Neuroradiology. 2006;27(9):1969-74.

36. Kim BYS, Jiang W, Beiko J, Prabhu SS, DeMonte F, Gilbert MR, et al. Diagnostic discrepancies in malignant astrocytoma due to limited small pathological tumor sample can be overcome by IDH1 testing. J Neurooncol. 2014;118(2):405-12.

CHAPTER 3. INTRAOPERATIVE MINI-MS PLATFORM FOR 2HG GENOTYPING OF HUMAN GLIOMAS

This chapter was adapted from the manuscript published in *Analytical and Bioanalytical Chemistry*: Brown HM, Pu F, Dey M, Miller J, Shah MV, Shapiro SA, Ouyang Z, Cohen-Gadol AA, Cooks RG. Intraoperative detection of isocitrate dehydrogenase mutations in human gliomas using a miniature mass spectrometer. Anal Bioanal Chem. 2019;411(30);7929-33. DOI: 10.1007/s00216-019-02198-y.

3.1 Abstract

Knowledge of the isocitrate dehydrogenase (IDH) mutation status of glioma patients could provide insights for decision-making during brain surgery. However, pathology is not able to provide such information intraoperatively. Here we describe the first application of a miniature MS to the determination of IDH mutation status in gliomas intraoperatively. The instrumentation was modified to be compatible with use in the operating room. Tandem MS was performed on the oncometabolite, 2-Hydroxyglutarate (2HG), and a reference metabolite, glutamate (Glu), which is not involved in the IDH mutation. Ratios of fragment ion intensities were measured to calculate an IDH mutation score, which was used to differentiate IDH mutant and wild-type tissues. The results of analyzing 25 biopsies from 13 patients indicate that reliable determination of IDH mutation status was achieved ($p = 0.0001$, using the Kruskal-Wallis non-parametric test). With its small footprint and low power consumption and noise level, this application of miniature mass spectrometers represents a simple and cost-effective platform for an important intraoperative measurement.

3.2 Introduction

The accurate diagnosis of gliomas relies increasingly on molecular features (1). However, the microscopic review of tissue biopsies, the principal source of intraoperative diagnostic information, does not provide any molecular or genetic information, including IDH mutation status. Conventionally, mutations in the enzyme IDH are determined using immunohistochemistry with results not available until some days after surgery (Figure 1). Knowledge of IDH mutation status at the time of surgery could improve surgical outcomes because more aggressive tumor resection of IDH-mutated gliomas is associated with increased survival.(2,3) IDH mutations alter

enzymatic pathways and lead to the accumulation of the oncometabolite 2HG.(4) While 2HG is present in very small concentrations in normal tissues, concentrations increase dramatically in tumors with mutations in IDH1 and IDH2, reaching levels up to 35 µmol per gram of tumor (5). This feature can be used to assess mutations in IDH, as has been demonstrated using magnetic resonance spectroscopy (MRS) and mass spectrometry (MS) (6,7).

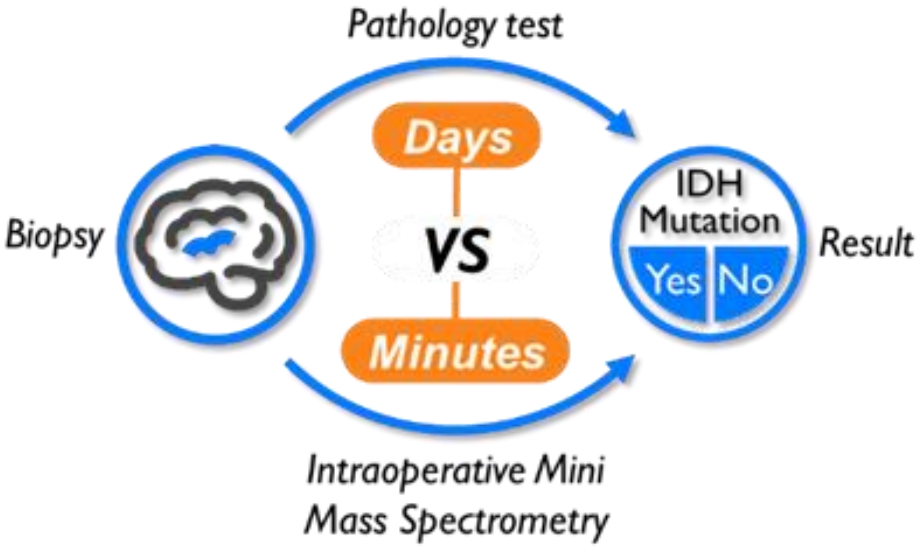

Figure 3.1 Intraoperative detection of IDH mutations with Mini MS determines mutation status in minutes as opposed to days by means of conventional genomic analysis or immunohistochemistry.

MS is a highly sensitive technique that is capable of the qualitative and quantitative analysis of complex samples, including biological tissues. This application is most accurately done in conjunction with liquid or gas chromatography but doing so requires tedious sample preparation. Matrix assisted laser desorption ionization (MALDI) is an alternative method which is important in tissue analysis (8). MALDI has been used for the detection of 2HG in frozen sections, however the required sample preparation and instrumentation makes it incompatible with intraoperative use (9). Ambient ionization allows chemical information to be obtained by MS at atmospheric pressure for a variety of matrices, including tissues, thereby eliminating purification or pretreatment steps and enabling intraoperative use. The first ambient methods were desorption electrospray ionization MS (DESI-MS) and direct analysis in real time (10,11). These experiments have provoked a re-examination of conventional tissue diagnosis and have resulted in the development of numerous

ambient ionization methods, including air flow-assisted desorption electrospray ionization, matrix assisted laser desorption electrospray ionization, liquid micro junction-surface sampling, paper spray, MasSpec Pen and rapid evaporative ionization MS (12-18).

We have previously measured the abnormal accumulation of 2HG for the intraoperative diagnosis of IDH mutation status using DESI-MS in near-real time, as described in Chapter 2 (19). However, this intraoperative application requires expensive instrumentation. By contrast, miniature MS systems have small footprints, low energy consumption, and produce little noise (20). Their use in the operating room (OR) offers the prospect of intraoperative genetic diagnosis in a cost-efficient manner. In this small-scale clinical study with 13 patients, we report the first application of a miniature mass spectrometer to determine IDH mutation status of glioma tissue intraoperatively.

3.3 Materials and Methods

3.3.1 Human Subjects

Human subjects research was performed in accordance with an Institutional Review Board approved study at the Indiana University School of Medicine (IRB #1410342262). Glioma patients undergoing craniotomy with tumor resection were prospectively enrolled after providing written informed consent and Health Insurance Portability and Accountability Act authorization. No assessments of IDH genotype were shared with neurosurgeons during the surgical resection so as not to affect the standard of care.

3.3.2 Sampling Method

Extraction nanoelectrospray ionization (nESI) is a method characterized by minimal sample preparation, was used to generate ions [21]. We have previously established this method for rapid diagnosis of IDH mutation status based-on measurement of 2-HG using banked tissue samples, so similar procedures were conducted in the OR (22). Biopsied tissue specimens from surgeon-defined positions within the tumor and at the walls of the resection cavity were collected intraoperatively. The number and location of the biopsies were determined according to the medical judgment of the attending surgeon. The biopsies were then touched with a thin strip of Whatman 1 filter paper (ca. 0.5 mm wide and 15 mm long) that was then inserted into a nanotip

(i.d. 0.86 mm, length ~4 cm) pre-filled with 20 µL methanol/water (9:1, v/v). The nanotip was subsequently placed in a custom 3D printed sample holder for MS analysis.

3.3.3 MS Analysis

The experiment used the ion trap based PurSpec Mini β, a stand-alone system that does not require external pumps or gas tanks, rendering it compatible for OR use, as shown in Figure 3.2. The Mini β which measures 55 cm × 24 cm × 31 cm (L × W × H), was placed on an aluminum cart with all equipment required for its operation. Prior to each surgery, the instrument was rolled into the OR and operated within the surgical suite for the duration of the surgery. Routine calibration was conducted for each case with a solution composed of aspartic acid, glutamate (Glu), 2-HG, and N-Acetylaspartate (NAA) using nESI in the negative ion mode, their molecular ions were found at *m/z* 132, 146, 147 and 174, respectively. Ionizing voltage (-1.5 kV) was applied to initiate nESI from a disposable acupuncture needle (diameter 0.3 mm, length 4 cm).

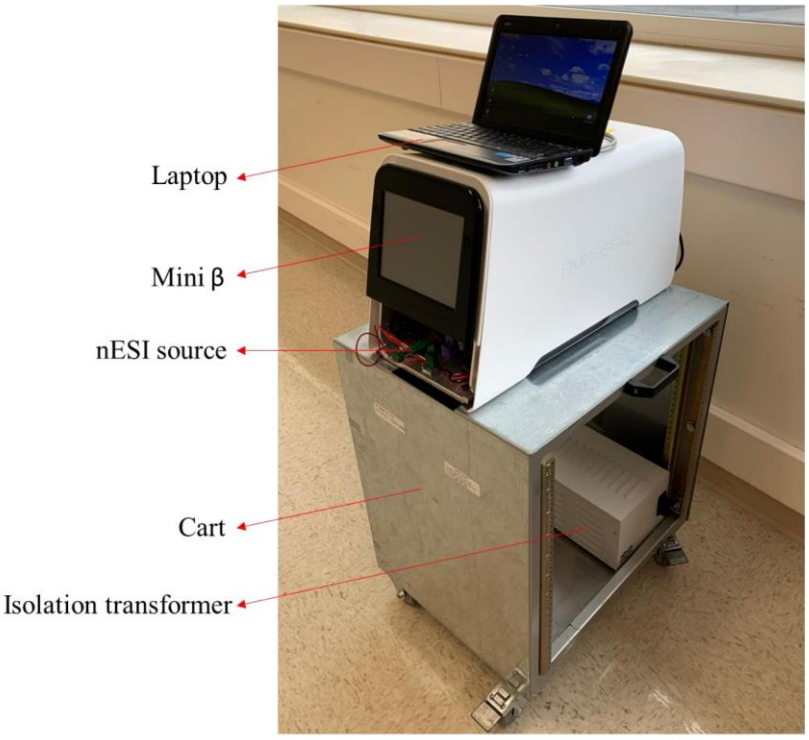

Figure 3.2 System view of intraoperative Mini MS system.

Simultaneous tandem MS analysis of 2-HG and Glu, an abundant metabolite not specifically associated with glioma serving as an endogenous internal standard, was performed in the negative ion mode. The product ion abundances for the transitions *m/z* 147 → 129 for 2-HG and *m/z* 146 → 128 for Glu provided a relative measure of the concentration of 2-HG in tissue. This is shown in the representative product ion mass spectrum of the calibration mixture shown in Figure 3.3. For each sample, at least three spectra were recorded, each recorded spectrum being the average of three scans. Each scan took ~2 s and spectra were saved manually, rendering the total data acquisition time per sample ca. 1min. To validate the intraoperative measurements made using the Mini β, postoperative analysis of the same biopsies was performed using the extraction nESI method on a Thermo TSQ. The TSQ analysis was performed using multiple reaction monitoring (MRM) mode; transitions selected were 2-HG (*m/z* 147 → 129) and Glu (*m/z* 146 → 128). With respect to each transition, optimized tube lens values of 67 and 69 V and nominal collision energies of 12 and 13 were applied.

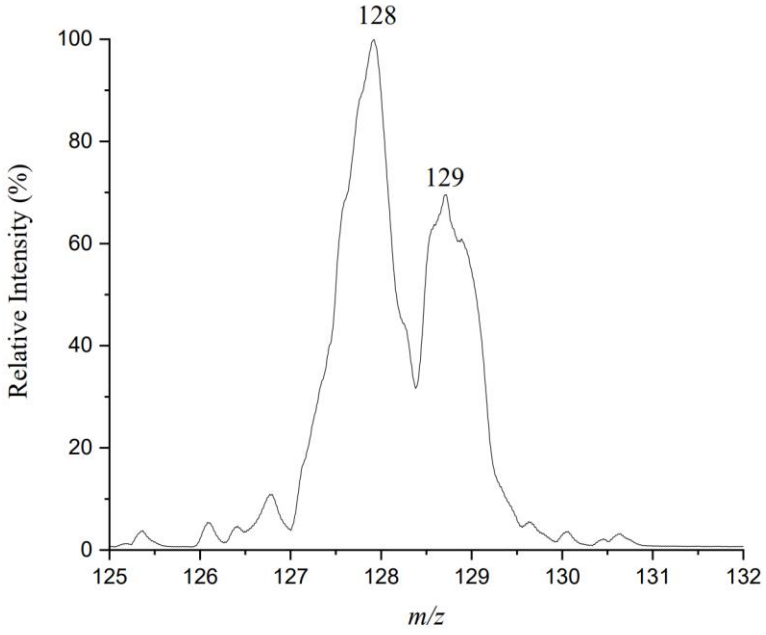

Figure 3.3 Representative product ion mass spectrum of the calibration mixture analyzed on the Mini β. The peak at *m/z* 128 is due to the fragmentation of deprotonated glutamate (*m/z* 146), which serves as an endogenous standard, while the peak at *m/z* 129 is due to the fragmentation of 2-hydroxyglutaric acid (*m/z* 147). Both precursors were isolated together prior the product ion scan being recorded.

3.3.4 Data Analysis

De-identified clinical data, consisting of patient demographics and radiology, surgical, and pathology reports were obtained for each patient for correlation with the data produced by the Mini β system. The Mini β data was analyzed in MATLAB using custom algorithms to subtract background intensities and calculate IDH mutation scores. The TSQ data was analyzed using Xcalibur. An IDH mutation score was calculated as the log ratio of the two product ion intensities after correcting for the isotopic contributions of the ^{13}C glutamate fragment ion at *m/z* 129 (Equation 1).

$$IDH\ Mutation\ Score = \log\left(\frac{I_{129}-(I_{128}\times 6.1\%)}{I_{128}}\right) \qquad (1)$$

3.4 Results and Discussion

In this preliminary clinical study, we analyzed 25 biopsies from 13 patients. The patient cohort is described in detail in Table 1. Of the 13 patients, 4 were IDH mutant (7 biopsies) and 9 were IDH wild type (18 biopsies), according to pathology reports based on immunohistochemistry. As shown in Figure 3.4 (left), the IDH wild-type tissues all had IDH mutation status scores below 0.5, whereas all IDH mutant samples had scores above 1.7. In other words, the abundance of 2HG in biopsies from IDH wild type gliomas is at or near baseline while the opposite is true for IDH mutant gliomas, where 2HG accumulates. This is illustrated in Figures 3.5 and 3.6. The box represents the interquartile range with a median line and whiskers at ± 1.5 standard deviations. The clear differentiation between IDH wild-type and mutant ($p = 0.0001$) is consistent with our previous observations on banked tissue samples, which suggests that intraoperative diagnosis of IDH mutation status can be realized with the current methodology.(22)

Table 3.1 Histopathology, IDH genotype, and IDH mutation scores of tissue biopsies assessed by Mini MS and TSQ

Patient	Biopsy	Type of Glioma	WHO Grade	IDH Genotype	IDH Mutation Score (Mini MS)	IDH Mutation Score (TSQ)
1	1	Glioblastoma	IV	Wild type	0.06	<0.01
2	1	Glioblastoma	IV	Wild type	0.02	0.02
3	1	Astrocytoma	II	Mutant	3.89	10.56
4	1	Pleomorphic xantoastrocytoma	II	Wild type	0.33	0.03
	2				0.18	0.02
	3				0.35	0.04
5	1	Glioblastoma	IV	Wild type	0.20	0.06
	2				0.24	0.06
	3				0.33	0.12
6	1	Glioblastoma	IV	Wild type	0.35	0.04
	2				0.33	0.04
7	1	Glioblastoma	IV	Wild type	0.28	0.07
	2				0.20	0.09
8	1	Anaplastic astrocytoma	III	Mutant	2.83	0.07
9	1	Glioblastoma	IV	Wild type	0.11	0.05
10	1	Glioblastoma	IV	Mutant	3.20	35.51
	2				1.73	99.33
	3				1.73	14.34
11	1	Glioblastoma	IV	Wild type		
12	1	-	III	Mutant	2.07	6.73
	2				2.30	16.93
13	1	Glioblastoma	IV	Wild type	0.25	0.04
	2				0.35	0.04
	3				0.50	0.07
	4				0.26	0.03

-= Information was not available at time of publication

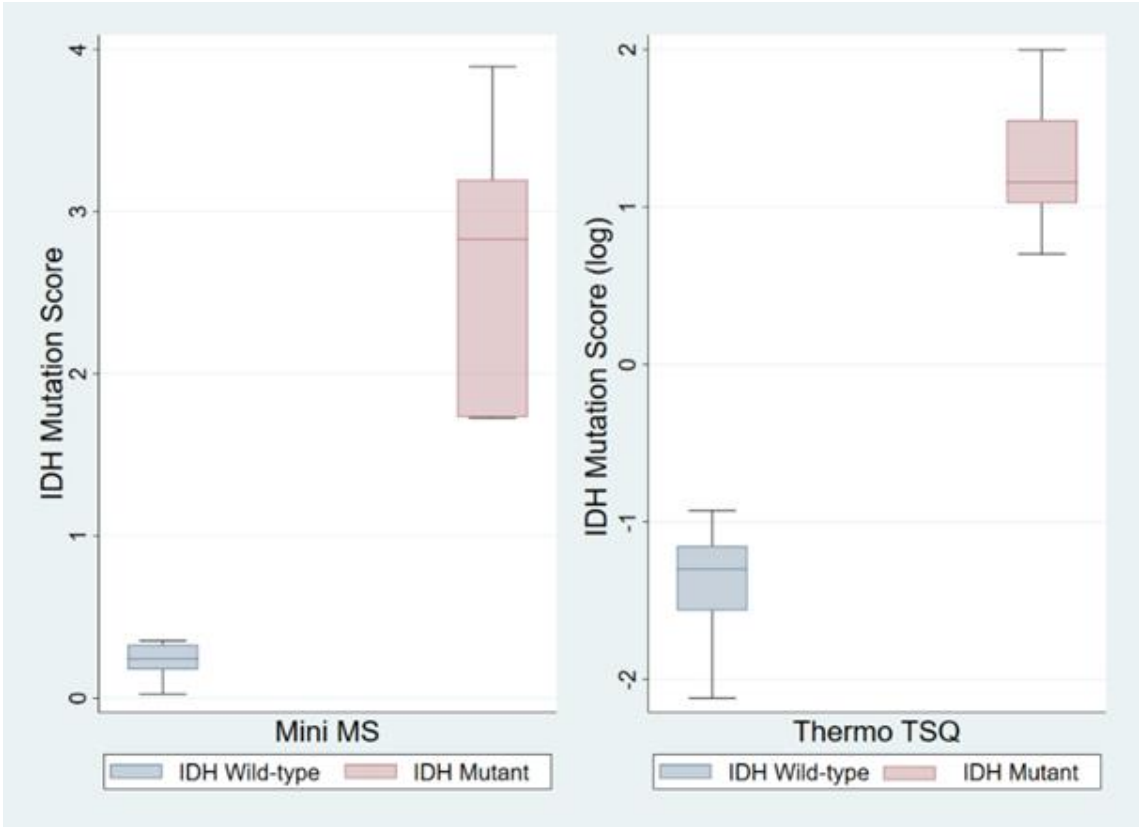

Figure 3.4 Box plot of IDH mutation scores calculated using Equation 1 of human glioma tissue specimens (n = 25) analyzed intraoperatively using a PurSpec Mini β and in the laboratory using a Thermo Triple Quadruple TSQ. (The box represents the interquartile range with a median line and whiskers at ± 1.5 SD. Population medians for IDH mutation scores for both methods were statistically different; p values for both are 0.0001, using Kruskal-Wallis non-parametric test).

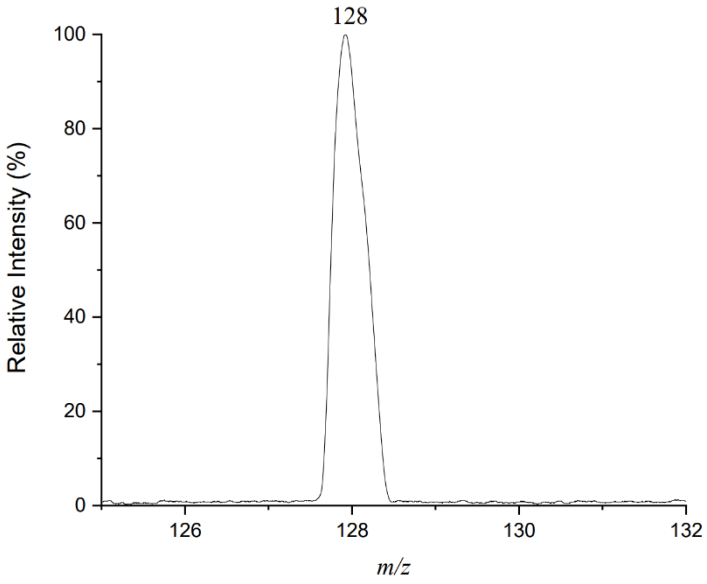

Figure 3.5 Representative MS/MS spectrum of an IDH-wild type human glioma analyzed intraoperatively using the Mini β. Note the absence of a signal for the 2HG fragment ion at *m/z* 129.

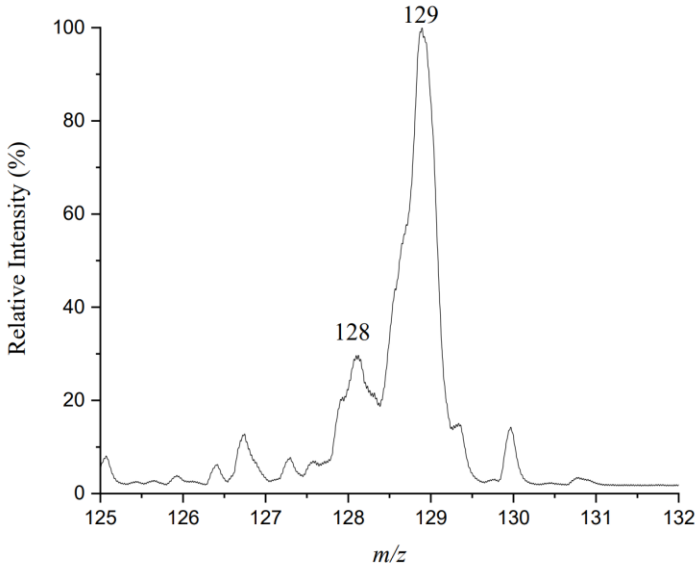

Figure 3.6 Representative MS/MS spectrum of an IDH-wild type human glioma analyzed intraoperatively using the Mini β. Note the dominant signal for the 2HG fragment ion at *m/z* 129.

The determination of IDH mutation status by measurement of 2-HG using the Mini β is a nonstandard method; as such, subsequent validation with TSQ was performed to confirm the conclusions drawn from intraoperative measurements. All IDH wild-type tissues had IDH mutation scores below 0.1 and all IDH mutant tissues had IDH mutation scores above 5.0, as shown in Figure 3.4, using this higher performance lab system The IDH mutation scores obtained from TSQ are different from those obtained using Mini β in part because the TSQ has better sensitivity. However, identical conclusions can be drawn from both sets of results, as shown in Figure 2. For both methods, the differences in population medians for the IDH mutation scores were statistically significant different ($p = 0.0001$ for both methods, using Kruskal-Wallis non-parametric test). Both instruments are capable of generating diagnostic information consistent with pathology. In this assay, the intraoperative application of a miniature mass spectrometer shows comparable performance to that of a conventional instrument.

3.5 Conclusions

We have successfully performed intraoperative diagnosis of IDH mutation using extraction nESI on Mini β. With its small footprint, low power consumption, minimal noise, and ability to generate reliable IDH mutation status predictions in near real-time, the intraoperative use of a miniature mass spectrometer represents an advance towards improved glioma patient treatment. Further studies will be conducted with protocol standardization and automation to validate these preliminary findings and reduce the barrier for broader application.

3.6 Acknowledgements

This work was made possible with funding from the Purdue University Center for Cancer Research Small Grants Program, National Institute of General Medical Sciences of the NIH under award number R44GM119584, and instrumentation support from PurSpec Technologies Inc. The work was performed in collaboration with a team of neurosurgeons including Dr. Mahua Dey, Dr. James Miller, Dr. Mitesh Shah, Dr. Scott Shapiro, and Dr. Aaron Cohen-Gadol. The authors thank clinical research nurses Lauren Snyder and Heather Cero at Goodman Campbell Brain and Spin (Indianapolis, IN) for patient consent, providing clinical data, and IRB monitoring; Clint Alfaro

and Tsdale Mehari for assistance in sample preparation; Robert Schrader for assistance with instrumentation; Zhuoer Xie for the table of contents figure.

3.7 References

1. Louis DN, Perry A, Reifenberger G, von Deimling A, Figarella-Branger D, Cavenee WK, Ohgaki H, Wiestler OD, Kleihues P, Ellison DW (2016) The 2016 World Health Organization Classification of Tumors of the Central Nervous System: a summary. Acta Neuropathol 131 (6):803-820.

2. Chen R, Ravindra VM, Cohen AL, Jensen RL, Salzman KL, Prescot AP, Colman H (2015) Molecular features assisting in diagnosis, surgery, and treatment decision making in low-grade gliomas. Neurosurg Focus 38 (3):E2.

3. Patel T, Bander ED, Venn RA, Powell T, Cederquist GY, Schaefer PM, Puchi LA, Akhmerov A, Ogilvie S, Reiner AS, Moussazadeh N, Tabar V (2018) The Role of Extent of Resection in IDH1 Wild-Type or Mutant Low-Grade Gliomas. Neurosurgery 82 (6):808-814.

4. Dang L, White DW, Gross S, Bennett BD, Bittinger MA, Driggers EM, Fantin VR, Jang HG, Jin S, Keenan MC, Marks KM, Prins RM, Ward PS, Yen KE, Liau LM, Rabinowitz JD, Cantley LC, Thompson CB, Vander Heiden MG, Su SM (2009) Cancer-associated IDH1 mutations produce 2-hydroxyglutarate. Nature 462 (7274):739-744.

5. Miller JJ, Shih HA, Andronesi OC, Cahill DP (2017) Isocitrate dehydrogenase-mutant glioma: Evolving clinical and therapeutic implications. Cancer 123 (23):4535-4546.

6. Andronesi OC, Kim GS, Gerstner E, Batchelor T, Tzika AA, Fantin VR, Vander Heiden MG, Sorensen AG (2012) Detection of 2-hydroxyglutarate in IDH-mutated glioma patients by in vivo spectral-editing and 2D correlation magnetic resonance spectroscopy. Sci Transl Med 4 (116):116ra114.

7. Santagata S, Eberlin LS, Norton I, Calligaris D, Feldman DR, Ide JL, Liu X, Wiley JS, Vestal ML, Ramkissoon SH, Orringer DA, Gill KK, Dunn IF, Dias-Santagata D, Ligon KL, Jolesz FA, Golby AJ, Cooks RG, Agar NY (2014) Intraoperative mass spectrometry mapping of an onco-metabolite to guide brain tumor surgery. Proc Natl Acad Sci U S A 111 (30):11121-11126.

8. McDonnell LA, Heeren RM (2007) Imaging mass spectrometry. Mass Spectrom Rev 26 (4):606-643.

9. Longuespee R, Wefers AK, De Vita E, Miller AK, Reuss DE, Wick W, Herold-Mende C, Kriegsmann M, Schirmacher P, von Deimling A, Pusch S (2018) Rapid detection of 2-hydroxyglutarate in frozen sections of IDH mutant tumors by MALDI-TOF mass spectrometry. Acta neuropathologica communications 6 (1):21.

10. Takats Z, Wiseman JM, Gologan B, Cooks RG (2004) Mass spectrometry sampling under ambient conditions with desorption electrospray ionization. Science 306 (5695):471-473.

11. Cody RB, Laramee JA, Durst HD (2005) Versatile new ion source for the analysis of materials in open air under ambient conditions. Anal Chem 77 (8):2297-2302.

12. Brown HM, Pirro V, Cooks RG (2018) From DESI to the MasSpec Pen: Ambient Ionization Mass Spectrometry for Tissue Analysis and Intrasurgical Cancer Diagnosis. Clin Chem 64 (4):628-630.

13. He J, Sun C, Li T, Luo Z, Huang L, Song X, Li X, Abliz Z (2018) A Sensitive and Wide Coverage Ambient Mass Spectrometry Imaging Method for Functional Metabolites Based Molecular Histology. Adv Sci (Weinh) 5 (11):1800250.

14. Robichaud G, Barry JA, Muddiman DC (2014) IR-MALDESI mass spectrometry imaging of biological tissue sections using ice as a matrix. Journal of the American Society for Mass Spectrometry 25 (3):319-328.

15. Van Berkel GJ, Kertesz V, Koeplinger KA, Vavrek M, Kong AN (2008) Liquid microjunction surface sampling probe electrospray mass spectrometry for detection of drugs and metabolites in thin tissue sections. J Mass Spectrom 43 (4):500-508.

16. Wang H, Manicke NE, Yang Q, Zheng L, Shi R, Cooks RG, Ouyang Z (2011) Direct Analysis of Biological Tissue by Paper Spray Mass Spectrometry. Analytical Chemistry 83 (4):1197-1201.

17. Zhang J, Rector J, Lin JQ, Young JH, Sans M, Katta N, Giese N, Yu W, Nagi C, Suliburk J, Liu J, Bensussan A, DeHoog RJ, Garza KY, Ludolph B, Sorace AG, Syed A, Zahedivash A, Milner TE, Eberlin LS (2017) Nondestructive tissue analysis for ex vivo and in vivo cancer diagnosis using a handheld mass spectrometry system. Sci Transl Med 9 (406).

18. Balog J, Sasi-Szabo L, Kinross J, Lewis MR, Muirhead LJ, Veselkov K, Mirnezami R, Dezso B, Damjanovich L, Darzi A, Nicholson JK, Takats Z (2013) Intraoperative Tissue Identification Using Rapid Evaporative Ionization Mass Spectrometry. Science Translational Medicine 5 (194):194ra193-194ra193.

19. Alfaro CM, Pirro V, Keating MF, Hattab EM, Cooks RG, Cohen-Gadol AA (2019) Intraoperative assessment of isocitrate dehydrogenase mutation status in human gliomas using desorption electrospray ionization-mass spectrometry. J Neurosurg:1-8.

20. Austin DE, Lammert SA (2009) Mass Analyzer Miniaturization. In: The Encyclopedia of Mass Spectrometry. vol 7, 1 edn. Elsevier.

21. Ren Y, Liu J, Li L, McLuckey MN, Ouyang Z (2013) Direct Mass Spectrometry Analysis of Untreated Samples of Ultralow Amounts Using Extraction Nano-Electrospray. Anal Methods 5 (23).

22. Pu F, Alfaro CM, Pirro V, Xie Z, Ouyang Z, Cooks RG (2019) Rapid determination of isocitrate dehydrogenase mutation status of human gliomas by extraction nanoelectrospray using a miniature mass spectrometer. Anal Bioanal Chem 411 (8):1503-1508.

CHAPTER 4. HIGH-THROUGHPUT DESI-MS PLATFORM FOR THE RAPID CHARACTERIZATION OF TISSUE BIOPSIES

This chapter summarizes the progress made in use of a high-throughput DESI-MS system for the rapid analysis of tissue biopsies arranged in a tissue microarray format. The study was designed by Dr. R. Graham Cooks, Nicolás Morato Gutiérrez, and Hannah Marie Brown. Nicolás Morato Gutiérrez and Hannah Marie Brown performed the experiments. Data analysis and statistical model optimization are ongoing. The data presented in this chapter is preliminary and meant to serve as a proof-of-concept and initial demonstration the capabilities of the instrumentation. Conclusions are tentative in view of the incomplete data analysis.

4.1 Introduction

Tissue microarrays (TMAs), arrays of up to 1000 tissue core biopsies, provide a more efficient means of tissue-based biomarker analysis by allowing for the standardized screening of biomarkers and biomarker expression using methods such as immunohistochemistry (IHC) and fluorescent in situ hybridization.(1) The use of TMAs is a preferred means to screen different tumor types, normal tissues and cells, rapidly assess the clinical significance of molecular alterations in cancer and diseases, and screen effectiveness of novel drugs, in a variety of cancers including lung, breast(2), colorectal(3), renal cell(4), and brain cancer(5). Compared to the individual examination of tissue, TMAs have multiple advantages including sequentially processing hundreds of samples using identical conditions, conserving of reagents, saving time, and decreasing the amount of tissue required for study. That said, the molecular analysis of TMAs requires the processing and staining of hundreds to thousands of slides, a labor-intensive and time-consuming task when many tumors are analyzed. Additionally, IHC and fluorescent-based methods require specific staining protocols for each biomarker investigated, precluding the ability to identify biomarkers for which a test does not already exist.

Mass spectrometry-based methods of tissue analysis can detect these molecular features of interest and rapidly generate a large amount of spectral data.(6) That said, the inherent speed of mass spectrometry, while attractive, is rarely fully utilized due to the widespread practice of using lengthy sample preparation and purification techniques prior to analysis. Ambient ionization mass spectrometry methods have emerged as a family of rapid methods for tissue analysis that do not require sample preparation or purification methods, making them well suited for high-throughput applications.(7) The method utilized in this work, desorption electrospray ionization mass

spectrometry (DESI-MS), is an ambient ionization method in which charged microdroplets of solvent are sprayed onto a sample surface, desorbing and ionizing molecules present on the sample surface and transporting them into a mass spectrometer for analysis.(7) DESI-MS has been used to analyze many complex biological samples, including different tissue types for the distinction between cancerous and normal tissue in multiple human organs, albeit in a low-throughput manner.(8-11) DESI-MS has been successfully used in a high-throughput manner to perform the rapid assessment of molecular features(12), including the screening of organic reactions(13-18), generation of mass spectral libraries(19), and biological assays(20-22) and characterization of bacteria(23), with throughputs of less than one second per sample. Given the increasingly relevant nature of the high-throughput analysis of tissue biopsies, we have expanded the capabilities of an existing high-throughput DESI-MS system to allow for the high-throughput DESI-MS characterization of complex biological samples, such as tissue biopsies.

Here we report an application of the DESI-MS high-throughput system for the molecular characterization of TMAs, as shown in Figure 4.1. In this proof-of-concept study we use brain cancer tissues sections and the methods previously developed for the intraoperative assessment of human glioma tissue biopsies. While TMAs are traditionally created by coring tissues from paraffin-embedded tissue in paraffin-embedded tissue blocks and placing them into a single paraffin block, we have modified this method to allow for the creation of TMAs of unmodified human tissue biopsies of up to 6,144 samples/array. Using high-throughput DESI-MS, we were able to assess tissue type, subtype of glioma, and IDH genotype of a collection of human brain tissue biopsies using methods previously developed for the intraoperative assessment of glioma biopsies with a throughput of 1 sample per second. We anticipate that HT-DESI-MS analysis of TMAs could become a standard tool in the generation of spectral libraries for sample classification, the identification of biomarkers through large-scale studies, and the ability to assess the effectiveness of drug candidates.

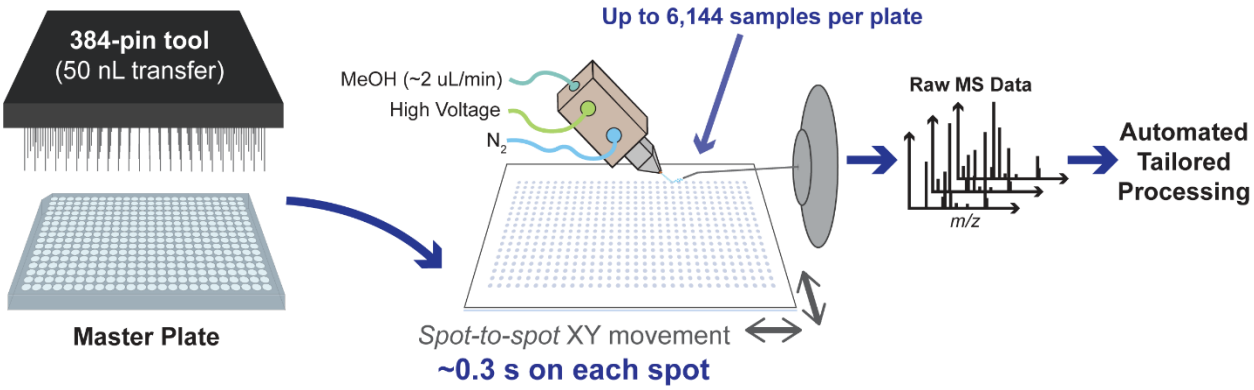

Figure 4.1 Workflow of high-throughput DESI-MS platform. Tissues are placed in one or more 384-well master plates and spotted onto a DESI analysis plate using a 384-pin tool. DESI-MS analysis is performed directly from the spotted DESI plate and the raw data is obtained and processed using custom software.

4.2 Materials and Methods

4.2.1 Samples

Two TMAs were analyzed in this study. The first tissue microarray (TMA1) was composed of a collection of 44 frozen and unmodified human brain tissue biopsies purchased by Purdue University from the Biorepository of Methodist Research Institute (Indianapolis, IN). The second tissue microarray (TMA2) was composed of 36 human brain tissue biopsies (one biopsy was divided into four aliquots prior to storage) from 11 patients undergoing tumor resection surgeries for suspected gliomas performed at Mayo Clinic – Jacksonville. The biopsies were taken from surgeon-defined positions within the tumor cavity with the sampling location (i.e., core vs. margin) was recorded by neuronavigation software. These biopsies were stored in the Biospecimen Accessioning and Processing Core at Mayo Clinic – Jacksonville and sent to Purdue University for further analysis. A complete description of the samples including information on diagnosis, IDH genotype, and tumor cell percentage is provided in Tables 4.1 and 4.2. Each biopsy was placed into a separate well of a 384-well microplate prior to high-throughput MS analysis, as shown in Figure 4.2. In situations in which the biopsy was large enough to be divided, the biopsy was divided into multiple wells to allow for replicate measurements to be made.

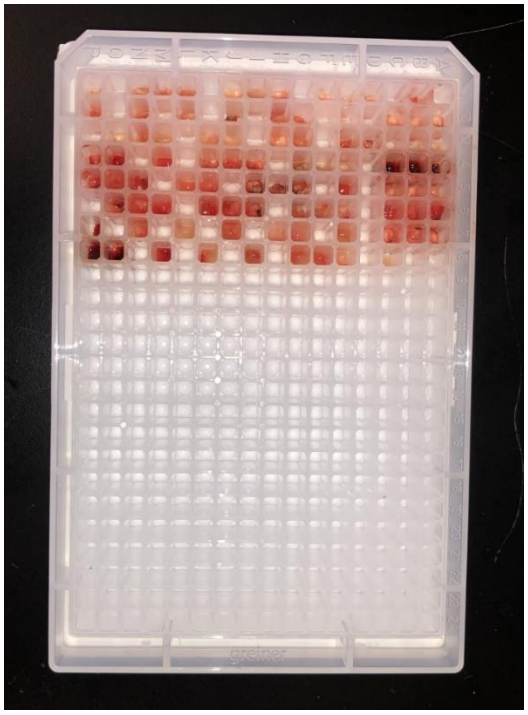

Figure 4.2 Tissue specimens arranged in separate wells in a 384-well microplate prior to HT-DESI-MS analysis For TMA1. Only 44 biopsies are included, with the rest of the table being blank.

4.2.2 Histopathological and Genetic Analysis

All tissue biopsies were subjected to pathologic evaluation prior to assessments made by HT-DESI-MS. For the banked tissue samples, tissue biopsies were cryosectioned, mounted onto glass slides, and hematoxylin and eosin (H&E) stained. For tissue samples from the ongoing intraoperative collaboration, fresh tissue biopsies were smeared onto glass slides and H&E-stained following DESI-MS analysis. Evaluation of disease state (defined simply as normal and glioma), tumor cell percentage, glioma subtype, and tumor grade of all tissue biopsies were made by senior neuropathologists in previous and ongoing collaborations. IDH genotype of all patients was confirmed by IHC and/or genetic testing of a pathologic biopsy, consistent with standard of care. All pathology information for both TMAs is included in Tables 4.1 and 4.2.

Table 4.1 Pathology information for biopsies in TMA1 including diagnosis, IDH genotype, and TCP estimate.

Sample Number	Diagnosis	IDH Genotype	TCP Estimate
1	Anaplastic astrocytoma	Mut	High
2	Normal brain	-	Low
3	Normal brain	-	Low
4	Normal brain	-	Low
5	Normal brain	-	Low
6	Normal brain	-	Low
7	Normal brain	-	Low
8	Normal brain	-	-
9	Normal brain	-	-
10	Normal brain	-	-
11	Normal brain	-	Low
12	Normal brain	-	-
13	Normal brain	-	Low
14	Normal brain	-	Low
15	Normal brain	-	-
16	Normal brain	-	Low
17	Normal brain	-	-
18	Glioblastoma	WT	-
19	Glioblastoma	WT	-
20	Glioblastoma	WT	High
21	Glioblastoma	WT	High
22	Glioblastoma	WT	Low
23	Glioblastoma	WT	High
24	Meningioma	-	-
25	Meningioma	-	-
26	Meningioma	-	-
27	Meningioma	-	-
28	Meningioma	-	-
29	Meningioma	-	-
30	Meningioma	-	-
31	Oligoastrocytoma	Mut	High
32	Oligoastrocytoma	Mut	-
33	Oligoastrocytoma	Mut	High
34	Oligoastrocytoma	Mut	High
35	Oligodendroglioma	Mut	High
36	Oligodendroglioma	WT	High
37	Oligodendroglioma	Mut	-
38	Oligodendroglioma	Mut	-
39	Oligodendroglioma	Mut	Low
40	Oligodendroglioma	WT	-
41	Pituitary	-	-
42	Pituitary	-	-
43	Pituitary	-	-
44	Pituitary	-	-

Mut= Mutant; WT= Wild type
-= Information unavailable

Table 4.2 Pathology information of biopsies in TMA2 including patient, biopsy, location, diagnosis, IDH genotype, and TCP estimate.

Sample Number	Patient	Biopsy	Location	Diagnosis	IDH Genotype	TCP Estimate
1	1	1	Core	Astrocytoma	WT	Low
2		2	Margin	Astrocytoma	WT	-
3		3	Core	Astrocytoma	WT	Low
4	2	1	Core	Astrocytoma	Mut	Low
5		2	Core	Astrocytoma	Mut	Low
6		3	Core	Astrocytoma	Mut	Low
7		4	Core	Astrocytoma	Mut	Low
8	3	1	Margin	Anaplastic astrocytoma	Mut	High
9		2	Core	Anaplastic astrocytoma	Mut	High
10		3	Core	Anaplastic astrocytoma	Mut	Low
11	4	1	Margin	Glioblastoma	WT	High
12		2	Core	Glioblastoma	WT	Low
13		3	Core	Glioblastoma	WT	-
14		4	Margin	Glioblastoma	WT	-
15	5	1	Margin	Astrocytoma	Mut	Low
16		2	Core	Astrocytoma	Mut	Low
17		3	Core	Astrocytoma	Mut	Low
18		4	Core	Astrocytoma	Mut	Low
19	6	1	Margin	Oligodendroglioma	Mut	Low
20		2	Margin	Oligodendroglioma	Mut	Low
21		3	Core	Oligodendroglioma	Mut	Low
22		4	Core	Oligodendroglioma	Mut	Low
23	7	1	Core	Glioblastoma	WT	High
24		2	Necrotic	Glioblastoma	WT	Low
25		3a	-	Glioblastoma	WT	-
26		3b	-	Glioblastoma	WT	-
27		3c	-	Glioblastoma	WT	-
28		3d	-	Glioblastoma	WT	-
29		4	Core	Glioblastoma	WT	High
30		5	Core	Glioblastoma	WT	High
31	8	1	Core	Glioblastoma	WT	Low
32		2	Core	Glioblastoma	WT	Low
33	9	1	Core	Anaplastic oligodendroglioma	Mut	High
34	10	1*	-	Astrocytoma	-	-
35		2*	-	Astrocytoma	-	-

Table 4.2 continued

36	11	1*	-	GBM	WT	-
37		2*	-	GBM	WT	-
38		3*	-	GBM	WT	-
39		4	Core	GBM	WT	Low

Mut= Mut; WT= Wild type

-= Information unavailable

**= Location information not recorded when biopsy was submitted to biobank, rendering it impossible to correlate pathological results with the biopsy*

4.2.3 High-throughput MS Analysis

High-throughput DESI-MS (HT-DESI-MS) analysis was performed using the Purdue Make It system.(12) Hardware, software, and operation of the system has been previously described. High-density tissue microarrays (up to 6,144 samples/array) were generated on DESI plates using a Beckman Biomek i7 fluid handling workstation (Beckman Coulter, Indianapolis, IN, USA) equipped with a 50-nL floating slotted 384-pin tool (V&P Scientific, San Diego, CA, USA). Minimal amounts of tissue (<500 ng) were sampled from the microplate using the pin-tool and spotted onto the slide. Up to 6,144 samples can be spotted on a single DESI plate with a center-to-center distance of ca. 1 mm at highest density. In this work, each biopsy was spotted four times, with a density of up to 1,536 samples pinned and analyzed on each plate. The DESI plates are prepared by coating custom-sized glass slides (Abrisa Technologies, Santa Paula, CA, USA) with a porous PTFE membrane (Zitex G-115, Saint-Gobain, Wayne, NJ, USA) using low VOC spray adhesive (Scotch Spray Mount, 3M, St. Paul, MN, USA). After spotting, the slide was automatically transferred to a DESI stage and analyzed in a spot-to-spot manner after calibration of sample positions using reference dye-marks on the corners of the plate. The effective sampling time was 300-400 milliseconds with a sample throughput of more than one sample per second. Data acquisition and DESI stage movement was controlled by custom hardware and Python software. In this study, we used two different mass spectrometers to conduct the two methods. Full scan analysis (in both positive and negative ion mode) was performed on a Synapt G2-Si quadrupole time-of-flight mass spectrometer using a DESI stage equipped with a high-performance XS-generation prototype sprayer and heated transfer capillary (Waters, Milford, MA, USA). In the second type of experiment, MS/MS analysis of 2HG and Glu was performed on a Finnigan LTQ linear ion trap mass spectrometer (Thermo Electron Corporation, Waltham, MA, USA) and a DESI sprayer (Waters, Milford, MA, USA) and extended ion transfer capillary.

DESI-MS was performed with ethanol as the spray solvent with a spray voltage of 0.75 kV. The solvent flow rate and nebulizing nitrogen pressure were optimized daily with values ranging between 1.5-2 μL/min and 15-20 psi, respectively. Additional source parameters are as follows: heated transfer line, 400°C; source temperature, 150 °C; sampling cone voltage, 40 V. Tissue microarrays were subjected to three sequential DESI-MS methods of acquisition. The first and second methods acquired data from *m/z* 100-1000 in the negative ion mode and positive ion

mode, respectively, and were performed on the Synapt G2-Si. The third method acquired data from a targeted tandem MS scan for the metabolites 2-Hydroxyglutarate (2HG) and glutamate (Glu) and was performed on the Finnigan LTQ.

4.2.4 Data analysis

Spectral data was processed, assigned to biopsies, and further analyzed using custom Python and MATLAB (MathWorks, Natick, MA, USA) scripts. Prior to analysis, all spectra were SNV normalized. In circumstances in which biopsies were divided into multiple wells, data from all wells from the same biopsy were averaged to produce a single, representative spectra for the three DESI-MS methods of acquisition. Data analysis of TMA2 is ongoing.

4.3 Results and Discussion

4.3.1 HT-DESI-MS Assessment of IDH Genotype

To investigate the ability of the HT-DESI-MS system to detect prognostic genetic mutations, we applied our previously published DESI-MS method of assessing IDH mutations of core biopsies intraoperatively to the high-throughput system.(24) Isocitrate dehydrogenase mutations, a common mutation in gliomas, alter enzymatic pathways and lead to the accumulation of the oncometabolite 2HG in IDH-mutant (IDH-mut) tumors. This feature can be used to detect IDH mutations by performing tandem MS on 2HG (*m/z* 147 → *m/z* 129) and Glu (*m/z* 146 → *m/z* 128), an endogenous metabolite in the brain that serves as an internal standard. Both precursors were isolated in a single scan and the ratio between the product ion abundances provided an assessment of the relative concentration of 2HG and, by extension, the IDH genotype. An IDH mutation score was obtained by calculating the log ratio of the product ion intensities, *m/z* 129 intensity divided by *m/z* 128 intensity, with isotopic corrections for contributions of the natural 13C Glu fragment ion at *m/z* 129, with a higher IDH mutation score indicating a higher relative concentration of 2HG (Equation 1).

$$IDH\ Mutation\ Score = \log\left(\frac{I_{129}-(I_{128}\times 6.1\%)}{I_{128}}\right) \quad (1)$$

As 2HG accumulated in IDH-mutated gliomas, higher intensities of 2HG are observed in IDH-mut gliomas, as compared to IDH-wild type (IDH-wt) tumors. This is shown in the

representative spectra of an IDH-wt and IDH-mut glioma, as seen in Figures 4.3 and 4.4. The tandem MS acquisition was first attempted on the Synapt G2-Si instrument but, due to significant noise present near the precursor ion masses, the experiments were conducted on the Finnigan LTQ with a throughput of six seconds per sample. Validation of IDH genotype predicted by DESI-MS were confirmed by IHC and/or genetic testing.

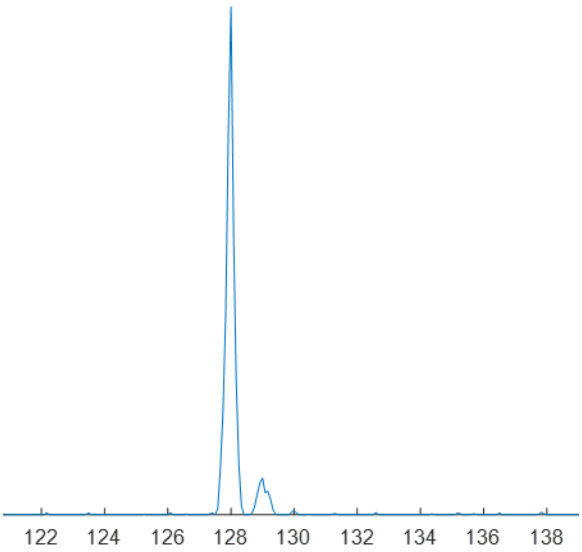

Figure 4.3 Representative MS/MS spectrum of an IDH-wt glioma performed on a Finnigan LTQ linear ion trap mass spectrometer in the negative ion mode. Note that the MS/MS signal for 2HG (*m/z* 147 → 129) is significantly smaller than the signal for Glu (*m/z* 146 → 128).

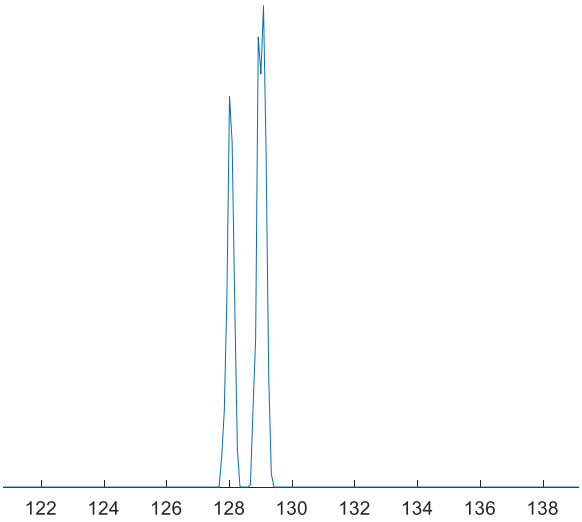

Figure 4.4 Representative MS/MS spectrum of an IDH-mut glioma performed on a Finnigan LTQ linear ion trap mass spectrometer in the negative ion mode. Note that the MS/MS signal for 2HG (*m/z* 147 → 129) is larger than the signal for Glu (*m/z* 146 → 128). This corresponds to an accumulation of 2HG within the tumor volume.

While only tumor core biopsies are used for the assessment of IDH genotype intraoperatively due to observed tumor heterogeneity, we elected to analyze all biopsies from TMA1, as location information was not available for the biopsies. When comparing predictions of IDH genotypes made by DESI-MS with those confirmed by IHC and/or genetic testing for TMA1, we report 100% accuracy, as seen by the clear separation of the 2HG:Glu MS/MS ratios for normal brain (n_{TMA1} = 15), IDH-wt (n = 6), and IDH-mut (n = 6) shown in Figure 4.5. The high accuracy of DESI-MS-determined IDH genotype observed suggests the ability of the high-throughput DESI-MS method to validate similar molecular diagnostic approaches using large, banked sample sets. Analysis of TMA2 is ongoing.

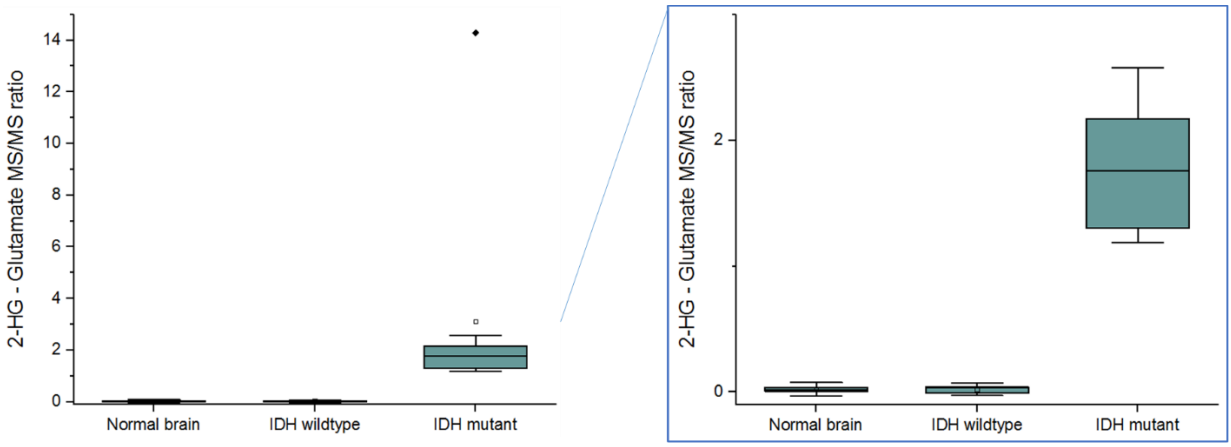

Figure 4.5 Box plot of 2HG:Glu MS/MS ratios for normal brain, IDH-wt, and IDH-mut glioma biopsies in TMA1 (n = 33). We report 100% accuracy in determining IDH genotype of tissue biopsies in TMA1.

4.3.2 HT-DESI-MS Characterization of Biopsies by Disease State and Tumor Type

To assess the ability of the HT-DESI-MS system to assess disease state (i.e. normal vs. glioma) and tumor type (i.e. glioma, meningioma, pituitary), the molecular differences between brain parenchyma and different brain tumors were compared using the molecular information obtained in their MS profiles and evaluated for their ability to differentiate disease state and tumor type, with the intention of replicating our previous performance of DESI-MS analysis on tissue sections and smears. Full scan analysis (*m/z* 100-1000) was performed on a Synapt G2-Si quadrupole time-of-flight mass spectrometer in the negative ion mode produced high-quality spectral data capable of identifying tissue type for both TMAs, although the metabolite profile (*m/z* 100-400) was found to be less informative than the fatty acids and lipid profiles (*m/z* 400-1000),

largely due to significant noise being present at low masses. To assess disease state, we elected to look at the difference between brain parenchyma and glioma, as our previous offline and intraoperative experience is largely focused on assessing tumor infiltration at surgical margins.(25-27) The demonstration of this technique could be applied to the detection of surgical margins in other cancer types.

Principal component analysis (PCA) was performed on full scan negative MS lipid profiles of biopsies of brain parenchyma (n = 16) and glioma (n = 17) in TMA1, as shown in Figure 4.6. Biopsies of brain parenchyma were well-separated from glioma in PCA space, suggesting that high-throughput DESI-MS analysis can readily distinguish diseased and healthy tissue in a TMA using molecular features in the range *m/z* 400-1000 in the negative ion mode. The few glioma biopsies molecularly similar to the cluster of brain parenchyma biopsies illustrate the disease spectrum and the complexity in classifying disease state in the presence of contributions of signals from both background parenchyma and tumor infiltration. This tissue heterogeneity, especially near surgical margins, is a phenomenon that has been previously observed both online and offline. Machine learning models were generated using the principal components generated from the PCA as inputs, resulting in the training and evaluation of 25 models. The two best performing models are summarized in Table 4.4. As can be seen, both models demonstrate good classification of the tissue biopsies by disease state. Data analysis of TMA2 and the further development of a classification model by machine learning models is ongoing.

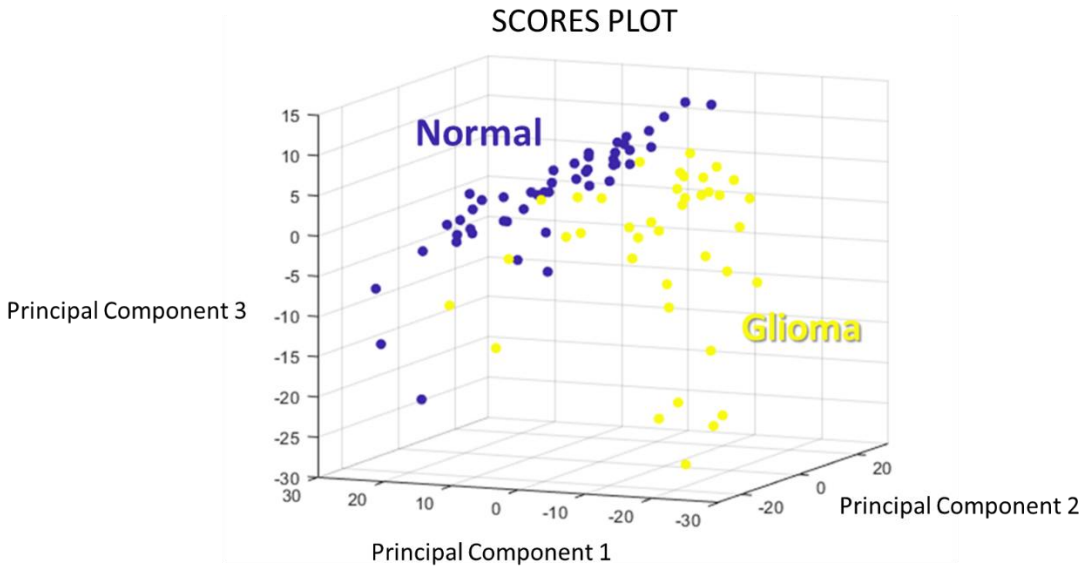

Figure 4.6 PCA of normal brain parenchyma (n = 16) and glioma (n = 17) biopsies in TMA1. Full scan analysis (*m/z* 100-1000) was performed on a Synapt G2-Si quadrupole time-of-flight mass spectrometer in the negative ion mode. Separation between normal brain parenchyma and diseased tissue is observed.

Table 4.3 Diagnostic performance of the two best performing machine learning models for the classification of biopsies by disease state (e.g., normal (n = 16) vs. glioma (n = 17)).

	Model 1 (LASSO)		**Model 2**	
Normal vs. glioma	100%	97%	100%	92%
	Sensitivity	*Specificity*	*Sensitivity*	*Specificity*

Meningiomas and pituitary tumors also represent a large proportion of all brain tumors and exhibit differences in their lipid profiles, as shown in previous studies.(3, 5) Using previously analyzed banked tissue biopsies (TMA1), we investigated if the same characterization of tumor type could be accomplished using the high-throughput DESI-MS system. Full scan analysis (*m/z* 100-1000) was performed on a Synapt G2-Si quadrupole time-of-flight mass spectrometer in the negative ion mode. As shown in Figure 4.7, PCA performed on biopsies of glioma (n = 17), meningioma (n = 7), and pituitary (n = 4) tumors using molecular features from *m/z* 400-1000 in the negative ion mode provided good separation between all tumor types, consistent with previous analyses of the same biopsies.(3) This is to be expected as the cells and tissues from which the differing tumors arise are distinct (e.g. glia vs. meninges). The results of the three best performing machine learning models for the classification of tissue biopsies are summarized in Table 4.4. All

three models demonstrate high sensitivity and specificity in their ability to characterize the different tumor types. These results suggest a biopsy from any of these three tumor types could be chemically recognized and rapidly classified using the high-throughput DESI-MS system.

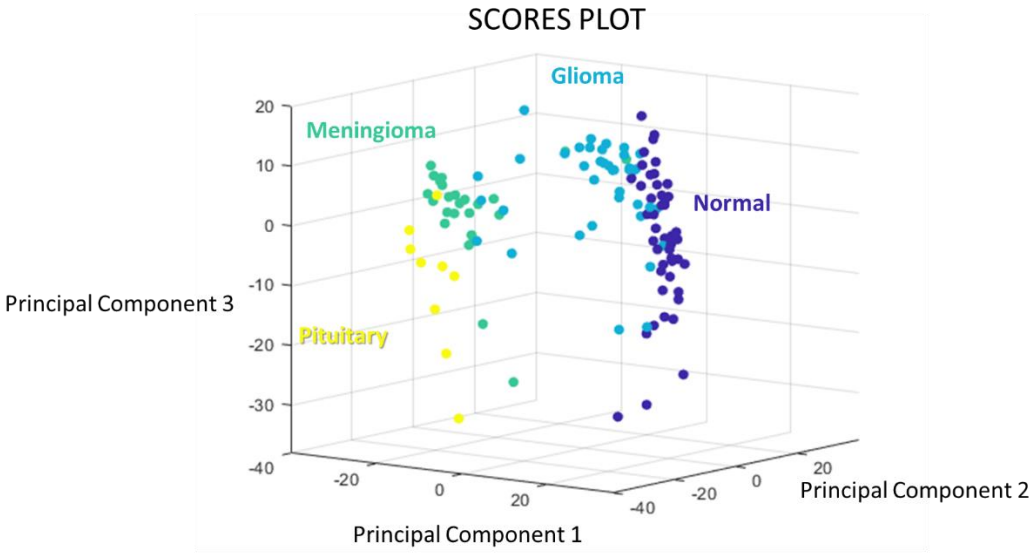

Figure 4.7 PCA of normal brain parenchyma (n = 16) and the different tumor types (i.e. meningioma (n = 7), pituitary (n = 4), and glioma (n = 17)) in TMA1. Full scan analysis (*m/z* 100-1000) was performed on a Synapt G2-Si quadrupole time-of-flight mass spectrometer in the negative ion mode. Separation between the normal brain parenchyma and different tumor types is noted.

Table 4.4 Diagnostic performance of the three best performing machine learning models for the classification of biopsies by tumor type (e.g. normal (n = 16) vs. glioma (n = 17) vs. meningioma (n = 7) vs. pituitary (n = 4)).

	Model 1		**Model 2**		**Model 3**	
Normal	100%	97%	100%	96%	98%	96%
Glioma	92%	99%	92%	98%	90%	97%
Meningioma	96%	99%	100%	100%	92%	99%
Pituitary	100%	100%	100%	100%	100%	100%
	Sensitivity	*Specificity*	*Sensitivity*	*Specificity*	*Sensitivity*	*Specificity*

4.3.3 Glioma Classification by HT-DESI-MS

A likely contribution to the observed variability in the glioma biopsies, as shown in Figures 4.7 and 4.8, is the presence of glioma subtypes (e.g., astrocytoma, oligodendroglioma, glioblastoma), whose names and types are derived from the glial cells from which the cancer is

derived. Knowledge of the subtype of glioma is important. The majority the therapies that have demonstrated significant survival benefit for glioma patients are based on nonspecific targeting of proliferating cells.(30) However, the histologic-based glioma classification is increasingly composed of multiple different molecular subtypes with distinct biology, molecular features, potential drug targets, and molecular features. Consequently, the World Health Organization has recently updated their classification of gliomas to incorporate more of these molecular features into the glioma subtyping framework.(31) While not currently part of our intraoperative DESI-MS workflow, discrimination of sections of glioma biopsies into histologic-based subclassifications (specifically oligodendrogliomas, astrocytomas, and oligodendrogliomas, now a defunct classification) by DESI-MS has been previously studied in an offline experiment, although the sample set did not contain samples from patients with glioblastoma and classification of tissue was made using previous WHO guidelines, including a now defunct glioma subclassification, oligoastrocytoma.(32) The throughput of previous glioma subclassification by DESI-MS precludes the generation of a new data set to identify molecular features that could allow for the accurate classification of glioma by current WHO guidelines. That said, the inherent speed of high-throughput DESI-MS analysis overcomes this bottleneck and allows for the generation of a large amount of spectral data containing new diagnostic molecular features.

Diagnostic features identified by high-throughput DESI-MS could be translated to the existing intraoperative workflow and enhance the diagnostic information available to surgeons at the time of surgery, allowing for personalized treatment approaches. To assess this possibility, full scan MS data were recorded for biopsies in TMA1 with a mass range of *m/z* 100-1000 using a Synapt G2-Si quadrupole time-of-flight mass spectrometer in the negative ion mode. Similar to the disease state and tumor type analyses, the metabolite profile (*m/z* 100-400) was found to be less informative than the fatty acids and lipid profiles (*m/z* 400-1000). The average mass spectra for the different glioma subclassifications were not as visually different as were those observed for normal parenchyma and the various tumor types (i.e., meningioma, pituitary, and glioma). This is to be expected because, rather than the different tumor types arising from different cells and tissue types, glioma subtypes arise from the same type of cells (i.e., glial cells). As can be seen in Figure 4.8, biopsies of astrocytoma (n = 1), oligodendroglioma (n = 6), and glioblastoma (n = 6) were well-separated from one another in PCA space. It is worth noting that the classification oligoastrocytoma is defunct and, under the 2021 WHO guidelines, these tumors would be further

classified as either oligodendrogliomas or astrocytomas.(33) This accounts for the observed similarities of the molecular features of these biopsies with those from patients with oligodendrogliomas and astrocytomas. Machine learning models for the classification of glioma tissue biopsies by glioma type were generated used the principal components from the PCA with the diagnostic performance of the best model summarized in Table 4.6. The analysis of additional TMAs is necessary in the future to validate the method and establish diagnostic accuracy, especially for astrocytomas, for which we have only one biopsy in TMA1. This task will be made significantly easier and faster by the high-throughput DESI-MS system. Data analysis of TMA2 and the generation of a classification model by machine learning models is ongoing.

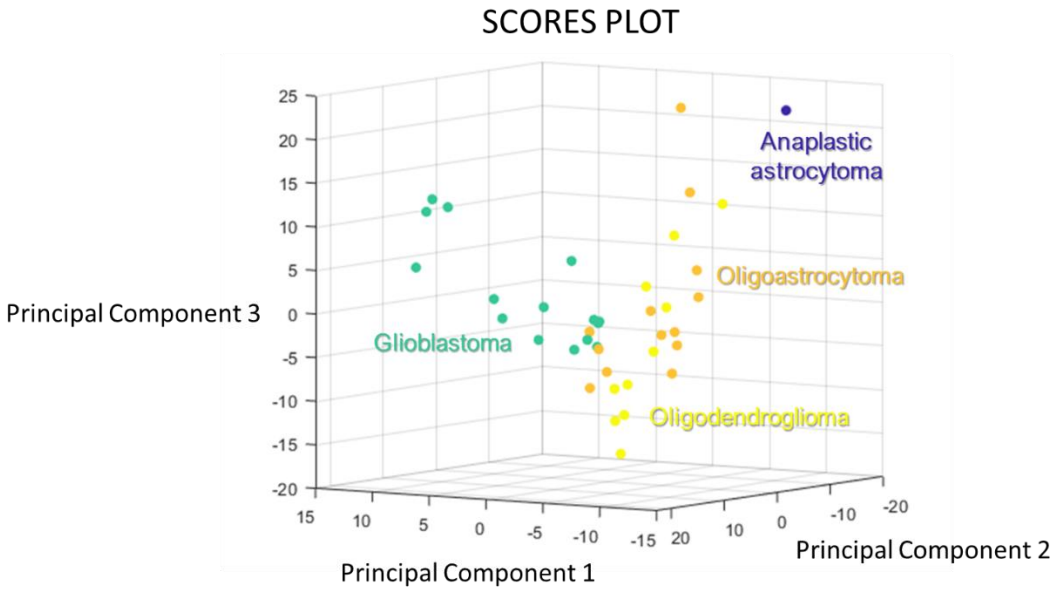

Figure 4.8 PCA of normal brain parenchyma and the different glioma classifications (i.e. astrocytoma (n = 1), oligoastrocytoma (n = 4), oligodendroglioma (n = 6), and glioblastoma (n = 6)) in TMA1. Separation between the different glioma subtypes is noted. Note that the classification of oligoastrocytoma is defunct; these tumors are now classified as either astrocytomas or oligodendrogliomas.

Table 4.5 Diagnostic performance of the three best performing machine learning models for the classification of biopsies by glioma type (e.g. astrocytoma (n = 1) vs. glioblastoma (n = 6) vs. oligoastrocytoma (n = 4) vs. oligodendroglioma (n = 6)).

	Model 1	
Astrocytoma	0%	100%
Glioblastoma	100%	89%
Oligoastrocytoma	85%	93%
Oligodendroglioma	60%	94%
	Sensitivity	*Specificity*

4.4 Conclusions

Here we present the first application of the DESI-MS high-throughput methodology to molecular characterize tissue microarrays. A novel method was developed for the creation of TMAs of fresh, unmodified human tissue biopsies of up to 6,144 samples/array. Using DESI-MS, we were able to assess IDH genotypes with 100% accuracy of human brain tissue biopsies with a throughput of greater than one sample per second. Additionally, preliminary results of TMA1 indicate the ability of HT-DESI-MS to differentiate tissue biopsies by tissue type and subtype of glioma. Spectral data showed high signal/noise ratios and results consistent with those made in previous publications and intraoperatively. Further, the relevant features and optimized models identified by leveraging the large data volumes that are generated using the high-throughput approach can be used to validate molecular diagnostic approaches used intraoperatively. With its minimal sample preparation, small volume of sample required, and rapid throughput, DESI-MS could become standard tool for the generation of spectral libraries for sample classification, the identification of biomarkers through large-scale studies, and the testing for biochemical activity or drug distribution in tissue.

4.5 Acknowledgements

This research is supported in part by the Innovative Molecular Analysis Technologies (IMAT) Program of the National Cancer Institute of the National Institutes of Health (R33CA240181-01A1) and Waters Corporation. Biospecimens in TMA2 were collected as part of an ongoing collaboration with a clinical team at Mayo Clinic – Jacksonville including neurosurgeons Dr. Kaisorn Chaichana and Dr. Alfredo Quiñones-Hinojosa, neuropathologist Dr. Mark Jentoft, neuroradiologist Dr. Erik Middlebrooks, and research fellow Dr. Diogo Garcia.

Rong Chen is acknowledged for her contributions to the ongoing clinical study. Thanks to neuropathologist Dr. Eyas Hattab for providing expert readings of the biospecimens in TMA1.

4.6 References

1. Kallioniemi OP, Wagner U, Kononen J, Sauter G. Tissue microarray technology for high-throughput molecular profiling of cancer. Hum Mol Genet. 2001;10(7):657-62.

2. Fredholm H, Magnusson K, Lindstrom LS, Garmo H, Falt SE, Lindman H, et al. Long-term outcome in young women with breast cancer: a population-based study. Breast Cancer Res Treat. 2016;160(1):131-43.

3. Magnusson K, de Wit M, Brennan DJ, Johnson LB, McGee SF, Lundberg E, et al. SATB2 in combination with cytokeratin 20 identifies over 95% of all colorectal carcinomas. Am J Surg Pathol. 2011;35(7):937-48.

4. Gremel G, Djureinovic D, Niinivirta M, Laird A, Ljungqvist O, Johannesson H, et al. A systematic search strategy identifies cubilin as independent prognostic marker for renal cell carcinoma. BMC Cancer. 2017;17(1):9.

5. Ikota H, Kinjo S, Yokoo H, Nakazato Y. Systematic immunohistochemical profiling of 378 brain tumors with 37 antibodies using tissue microarray technology. Acta Neuropathol. 2006;111(5):475-82.

6. Gorynska PZ, Chmara K, Kupcewicz B, Gorynski K, Jaroch K, Paczkowski D, et al. Metabolomic Phenotyping of Gliomas: What Can We Get with Simplified Protocol for Intact Tissue Analysis? Cancers (Basel). 2022;14(2).

7. Takáts Z, Wiseman JM, Cooks RG. Ambient mass spectrometry using desorption electrospray ionization (DESI): instrumentation, mechanisms and applications in forensics, chemistry, and biology. J Mass Spectrom. 2005;40(10):1261-75.

8. Wood PL. Mass spectrometry strategies for clinical metabolomics and lipidomics in psychiatry, neurology, and neuro-oncology. Neuropsychopharmacology. 2014;39(1):24-33.

9. Collins RRJ, Patel K, Putnam WC, Kapur P, Rakheja D. Oncometabolites: A New Paradigm for Oncology, Metabolism, and the Clinical Laboratory. Clin Chem. 2017;63(12):1812-20.

10. Wang R, Li B, Lam SM, Shui G. Integration of lipidomics and metabolomics for in-depth understanding of cellular mechanism and disease progression. J Genet Genomics. 2020;47(2):69-83.

11. Warburg O. On the origin of cancer cells. Science. 1956;123(3191):309-14.

12. Wleklinski M, Loren BP, Ferreira CR, Jaman Z, Avramova L, Sobreira TJP, et al. High throughput reaction screening using desorption electrospray ionization mass spectrometry. Chem Sci. 2018;9(6):1647-53.

13. Logsdon DL, Li Y, Paschoal Sobreira TJ, Ferreira CR, Thompson DH, Cooks RG. High-Throughput Screening of Reductive Amination Reactions Using Desorption Electrospray Ionization Mass Spectrometry. Organic Process Research & Development. 2020;24(9):1647-57.

14. Jaman Z, Logsdon DL, Szilagyi B, Sobreira TJP, Aremu D, Avramova L, et al. High-Throughput Experimentation and Continuous Flow Evaluation of Nucleophilic Aromatic Substitution Reactions. ACS Comb Sci. 2020;22(4):184-96.

15. Jaman Z, Sobreira TJP, Mufti A, Ferreira CR, Cooks RG, Thompson DH. Rapid On-Demand Synthesis of Lomustine under Continuous Flow Conditions. Organic Process Research & Development. 2019;23(3):334-41.

16. Fedick PW, Iyer K, Wei Z, Avramova L, Capek GO, Cooks RG. Screening of the Suzuki Cross-Coupling Reaction Using Desorption Electrospray Ionization in High-Throughput and in Leidenfrost Droplet Experiments. J Am Soc Mass Spectrom. 2019;30(10):2144-51.

17. Biyani SA, Qi Q, Wu J, Moriuchi Y, Larocque EA, Sintim HO, et al. Use of High-Throughput Tools for Telescoped Continuous Flow Synthesis of an Alkynylnaphthyridine Anticancer Agent, HSN608. Organic Process Research & Development. 2020;24(10):2240-51.

18. Ewan HS, Biyani SA, DiDomenico J, Logsdon D, Sobreira TJP, Avramova L, et al. Aldol Reactions of Biorenewable Triacetic Acid Lactone Precursor Evaluated Using Desorption Electrospray Ionization Mass Spectrometry High-Throughput Experimentation and Validated by Continuous Flow Synthesis. ACS Comb Sci. 2020;22(12):796-803.

19. Le MT, Morato NM, Kaerner A, Welch CJ, Cooks RG. Fragmentation of Polyfunctional Compounds Recorded Using Automated High-Throughput Desorption Electrospray Ionization. J Am Soc Mass Spectrom. 2021;32(8):2261-73.

20. Morato NM, Holden DT, Cooks RG. High-Throughput Label-Free Enzymatic Assays Using Desorption Electrospray-Ionization Mass Spectrometry. Angew Chem Int Ed Engl. 2020;59(46):20459-64.

21. Morato NM, Le MT, Holden DT, Graham Cooks R. Automated High-Throughput System Combining Small-Scale Synthesis with Bioassays and Reaction Screening. SLAS Technol. 2021;26(6):555-71.

22. Kulathunga SC, Morato NM, Zhou Q, Cooks RG, Mesecar AD. Desorption Electrospray Ionization Mass Spectrometry Assay for Label-Free Characterization of SULT2B1b Enzyme Kinetics. ChemMedChem. 2022:e202200043.

23. Szalwinski LJ, Gonzalez LE, Morato NM, Marsh BM, Cooks RG. Bacterial growth monitored by two-dimensional tandem mass spectrometry. Analyst. 2022;147(5):940-6.

24. Brown HM, Pu F, Dey M, Miller J, Shah MV, Shapiro SA, et al. Intraoperative detection of isocitrate dehydrogenase mutations in human gliomas using a miniature mass spectrometer. Anal Bioanal Chem. 2019;411(30):7929-33.

25. Jarmusch AK, Alfaro CM, Pirro V, Hattab EM, Cohen-Gadol AA, Cooks RG. Differential Lipid Profiles of Normal Human Brain Matter and Gliomas by Positive and Negative Mode Desorption Electrospray Ionization - Mass Spectrometry Imaging. PLoS One. 2016;11(9):e0163180.

26. Pirro V, Alfaro CM, Jarmusch AK, Hattab EM, Cohen-Gadol AA, Cooks RG. Intraoperative assessment of tumor margins during glioma resection by desorption electrospray ionization-mass spectrometry. Proc Natl Acad Sci U S A. 2017;114(26):6700-5.

27. Brown HM, Alfaro CM, Pirro V, Dey M, Hattab EM, Cohen-Gadol AA, et al. Intraoperative Mass Spectrometry Platform for IDH Mutation Status Prediction, Glioma Diagnosis, and Estimation of Tumor Cell Infiltration. J Appl Lab Med. 2021;6(4):902-16.

28. Calligaris D, Feldman DR, Norton I, Brastianos PK, Dunn IF, Santagata S, et al. Molecular typing of Meningiomas by Desorption Electrospray Ionization Mass Spectrometry Imaging for Surgical Decision-Making. Int J Mass Spectrom. 2015;377:690-8.

29. Jarmusch AK, Pirro V, Baird Z, Hattab EM, Cohen-Gadol AA, Cooks RG. Lipid and metabolite profiles of human brain tumors by desorption electrospray ionization-MS. Proc Natl Acad Sci U S A. 2016;113(6):1486-91.

30. Bush NA, Chang SM, Berger MS. Current and future strategies for treatment of glioma. Neurosurg Rev. 2017;40(1):1-14.

31. Louis DN, Perry A, Wesseling P, Brat DJ, Cree IA, Figarella-Branger D, et al. The 2021 WHO Classification of Tumors of the Central Nervous System: a summary. Neuro Oncol. 2021;23(8):1231-51.

32. Eberlin LS, Norton I, Dill AL, Golby AJ, Ligon KL, Santagata S, et al. Classifying human brain tumors by lipid imaging with mass spectrometry. Cancer Res. 2012;72(3):645-54.

33. Sahm F, Reuss D, Koelsche C, Capper D, Schittenhelm J, Heim S, et al. Farewell to oligoastrocytoma: in situ molecular genetics favor classification as either oligodendroglioma or astrocytoma. Acta Neuropathol. 2014;128(4):551-9.

CHAPTER 5. ADVANCED OPTIMIZATION OF INTRAOPERATIVE DESI-MS PLATFORM FOR THE MOLECULAR ANALYSIS OF BRAIN TISSUE BIOPSIES

This chapter summarizes the progress made in an intraoperative and collaborative study with Mayo Clinic – Jacksonville. Patient recruitment, intraoperative data collection, and analysis and correlation of DESI-MS data with histopathologic assessments of IDH genotype and TCP are ongoing. The data presented in this chapter is current as of 04/11/2022 and analysis and conclusions are tentative.

5.1 Introduction

The use of molecular diagnostics has the potential to improve the intraoperative diagnosis of gliomas from pathology biopsies.(1, 2) While our understanding of the molecular diversity of glioma has greatly expanded in the past three decades, the available treatments for glioma patients remain mostly unchanged. The established therapeutic approach is surgical resection followed by adjuvant radiation and chemotherapy, specifically temozolomide.(3) That said, there is an increasing understanding and desire to tailor treatment regimens to the molecular features of a patient's specific tumor. However, the principal source of intraoperative diagnostic information, the histological review of frozen tissue sections, in addition to being time consuming, does not provide molecular or genetic information, including information regarding prognostic mutations such as isocitrate dehydrogenase (IDH) mutations.(4, 5)

Knowledge of IDH mutations intraoperatively is important for three key reasons: diagnosis, prognosis, and treatment approach (both intraoperatively and postoperatively).(6) IDH mutations play an essential role in the algorithm for determining glioma classification. Until recently, the diagnosis of gliomas was based solely on morphological features. However, in 2016, the WHO Classification of Tumors of the Central Nervous System introduced the inclusion of specific molecular features in the official diagnostic system, including IDH genotype.(7) Now, gliomas are divided into IDH-wild type (IDH-wt) and IDH-mutant (IDH-mut) categories in addition to grade (I-IV) and glioma type (e.g. astrocytoma, oligodendroglioma, glioblastoma) as the standard of care diagnostic approach.(2) Further, IDH mutations have prognostic value in the sense that longer patient survival rates are observed for patients with IDH-mut gliomas than for patients with IDH-wt gliomas of the same grade receiving the same treatment.(8-12) With respect to patient treatment

plans, knowledge of a tumor's IDH genotype at the time of surgery can inform treatment approach, as demonstrated by the finding that surgical benefit differs with IDH genotype, with patients with IDH mutant tumors having longer survival rates those with IDH wildtype tumors.(13-15) Finally, IDH-targeting drugs offer a promising new avenue for personalized medicine as they link cellular metabolism to epigenetic dysregulation responsible for cellular differentiation and oncogenesis.(16) Specifically, IDH mutations alter enzymatic pathways and lead to the accumulation of the oncometabolite 2-Hydroxyglutarate (2HG) in IDH-mutant tumors, as shown in Figure 6.1. This discovery has led several investigators to try to develop strategies that either restore normal IDH function or block the production or downstream effects of the accumulation of 2HG.(17, 18) While none of these IDH-targeting drugs are FDA approved, several candidates are in Phase II and Phase III clinical trials. Currently, IDH genotypes are determined by immunohistochemistry (IHC) and/or genetic testing, with results available days after surgery. Measuring the amount of 2HG relative to glutamate (Glu), an endogenous metabolite in the brain that serves as an internal standard, provides an assessment of the relative concentration of 2HG and, by extension, the IDH genotype.(19, 20)

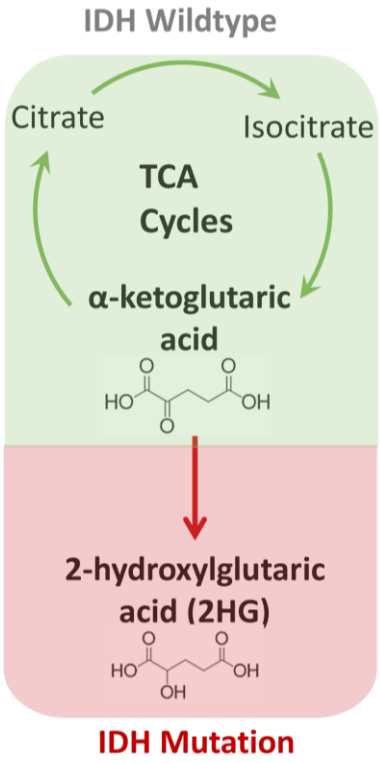

Figure 5.1 Metabolic reprogramming in IDH-mutated gliomas. Acquisition of an IDH mutation results in significant metabolic aberrations. Specifically, α-ketoglutaric acid is reduced to 2HG, thereby leading to an accumulation of the oncometabolite in IDH-mutated tumors.

Maximal surgical resection that avoids non-infiltrated tissue is associated with the highest survival benefit in patients with gliomas.(21, 22) While the infiltrative nature of gliomas and their morphological and genetic diversity demand the use of an integrated imaging and diagnostic approach during surgery to personalize decision making and guide the extent of resection,(23) estimation of tumor cell percentage (TCP) of pathology biopsies is not routinely performed intraoperatively. (4, 5) Rapid molecular assessment of tumor infiltration in biopsied tissue near surgical resection margins could help improve resection and better inform patient management strategies, including postoperative radiotherapy.

We address these unmet needs by using desorption electrospray ionization mass spectrometry (DESI-MS) for the expeditious molecular assessment of biopsies, both at the tumor core and near surgical margins. Mass spectrometry is the gold standard technique for the accurate identification and quantitation of molecules in complex samples. DESI allows for the direct and rapid examination of tissue smears with no sample preparation other than smearing the tissues and,

consequently, lends itself to point-of-care testing. Further, DESI is the ambient ionization method that is least susceptible to capillary blockage and most tolerant of salts present in complex mixtures. The DESI analysis is nondestructive when using morphologically-friendly solvents to extract molecules from the tissue surface, allowing for post-hoc histopathology to be performed on the same tissue analyzed by DESI-MS and the correlation of molecular and morphological features.(24) A DESI-MS system was previously developed and tested in a 49-patient intraoperative study conducted at Indiana University School of Medicine.(25-27) Building on the success of this preliminary study, we modified and optimized the DESI-MS system and are performing and validating the methodology in an ongoing collaboration with Mayo Clinic – Jacksonville. Stereotactic biopsies from surgeon defined positions within the tumor cavity are smeared on a glass substrate and analyzed by DESI-MS. Two categories of information are acquired using DESI-MS: 1) IDH mutation status and 2) tumor cell percentage (TCP). Augmented with other data available intraoperatively (e.g., histopathology analysis of frozen tissue biopsies, magnetic resonance imaging (MRI), *in vivo* brain mapping), molecular information provided by DESI-MS can assist clinicians in making informed intraoperative and postoperative treatment plans that improve patient prognosis.

5.2 Materials and Methods

5.2.1 Human Subjects

Human subjects research is performed in accordance with an Institutional Review Board approved study at Mayo Clinic – Jacksonville (IRB #19-010725). Patients with glioma undergoing craniotomy with tumor resection are prospectively enrolled after providing written informed consent and Health Insurance Portability and Accountability Act authorization. No DESI-MS results are shared with the participating neurosurgeons intraoperatively so as not to affect the standard of care.

5.2.2 Intraoperative DESI-MS

All experiments are conducted using the same DESI-MS system using a modified linear ion trap mass spectrometer (Thermo LTQ) as previously described.(25-27) Prior to installation at Mayo Clinic – Jacksonville, the instrument was minimally modified to include additional sound-proofing materials lining the instrument cart to reduce the noise generated by the vacuum pumps.

The instrument was subsequently moved from Purdue University to Mayo Clinic – Jacksonville and installed in a hallway directly adjacent to the intraoperative MRI operating room. At the beginning of each case, the instrument is turned on and the performance is tested using a series of quality controls, specifically a tissue smear of IDH-mut and IDH-wt gliomas for the IDH genotype assay and a smear of human brain tissue to assess the mass accuracy and signal intensity of the detection of lipids and diagnostic metabolites for TCP estimation. Small stereotactic biopsies (ca. 5-10 mg, each) are provided by a neurosurgeon to the mass spectrometry operators during tumor resection surgery. The number and location of the biopsies are decided at the surgeon's discretion, with the intention of providing eight to ten biopsies from both the tumor core (for assessing IDH genotype) and surgical margins (for assessing tumor infiltration). The locations of these biopsies are recorded using the

"Snapshot" feature of the neuronavigation system. The tissue biopsies are smeared on a glass slide, allowed to dry, and rastered underneath the DESI-MS spray in a serpentine pattern in order to obtain representative DESI-MS data. Two different negative ion mode DESI-MS methods are used. In Method 1, full scan lipid (*m/z* 700 - 1000) and metabolite (*m/z* 80 - 200) mass spectra and a targeted MS2 scan for N-Acetylaspartic acid (NAA, 174 → O), are acquired over 3.3 minutes. In Method 2, simultaneous tandem MS (MS/MS) analysis of 2HG (*m/z* 147) and Glu (*m/z* 146) and MS3 analysis of 2HG are acquired (*m/z* 147 → *m/z* 129 → O, respectively), along with a full scan metabolite profile (*m/z* 50 - 200), all over a period of 3.3 minutes. The chemistry of the spray solvents has been modified to achieve the best ionization of the analytes of interest for each method, with Method 1 using a spray solvent of 1:1 dimethylformamide (DMF)-acetonitrile (ACN) and Method 2 using 25:37:38 DMF-ACN-ethanol (EtOH).

5.2.3 Data Analysis

Deidentified clinical data is provided for each patient for correlation with DESI-MS results and is summarized in Table 5.2. DESI-MS data is analyzed in MATLAB using custom algorithms to remove background scans and to perform statistical, as described in Chapter 2. The collected lipid data are filtered using standard deviation thresholds of the summed absolute intensities of important peaks, including *m/z* 768, 788, 794, 834, 885, and 888, compared to background spectra collected from a blank glass slide. Lipid scans with the summed signal three-standard deviations

greater than the blank are retained and averaged to generate a representative lipid profile for the sample. The metabolite profiles are filtered in a similar way, with the calculated intensities to be *m/z* 89 + *m/z* 175 - *m/z* 120 - *m/z* 143 - *m/z* 157 - *m/z* 171. The peaks of *m/z* 89 and 175 are characteristic of brain tissue while peaks of *m/z* 120, 143, 157, and 171 are dominant in the background spectra. Metabolite profiles with the calculated intensities three-standard deviation higher than the blank glass slide are retained. The additional filtering criterion for metabolite profiles lies in peak resolution to alleviate influences from space charging. The full width at half maximum (FWHM) is calculated for the base peak and only scans with peak resolution greater than 250 are retained and further averaged to generate a representative metabolite profile for the sample. The lipid profile scans that are retained are normalized using standard normal variate (SNV) transformation prior to PCA to correct for baseline shifts and fluctuations in total ion count (TIC). The retained metabolite profiles are directly normalized by TIC to correct for fluctuations in their absolute intensities.

For some tissue smears, no scans are selected after using these data filtering criteria due to low DESI-MS signal or noisy background signal. To fully extract molecular features from these tissue smears, a customized cut-off of the calculated intensities is applied for both lipid profiles and metabolite profiles. The filtered and averaged spectra normally show limited absolute signal, but their relative profiles are still diagnostic of tumor concentrations in the smeared tissue. Smears for which no scans are selected in either the lipid or metabolite profile are excluded from further statistical analysis. The smears that provided poor signal and were excluded tended to contain acellular tissue, have sparse smear cell density, be smears with overall low cellularity, or had significant air-drying artifacts, as noted by an expert senior neuropathologist.

5.2.4 Histopathological Analysis

Upon completion of DESI-MS analysis, the tissue smears are taken to the surgical pathology facility and H&E stained. The H&E-stained smears are blindly evaluated by an expert neuropathologist, Dr. Mark E. Jentoft, and interpretations of smear diagnosis, TCP, and smear quality are provided. This information is summarized in Table 5.4.

5.3 Results and Discussion

5.3.1 Summary of Patient Cohort and Tissue Samples

To date, we have recruited 44 patients, with seven of these patients being clinical screen fails (e.g., patient withdrew consent, presence of tumor other than glioma confirmed, tumor not large enough to provide biopsies for research, patient expired, etc.). In total, we have analyzed 295 biopsies from 37 patents, accounting for 74% of the planned 50-patient cohort. It is worth noting that a modification to the DESI-MS assay to assess IDH genotypes was implemented after the initiation of the study, beginning with Patient 15. Thus, only 116 biopsies from 23 patients have been analyzed using the modified method, representing 46% of the planned 50-patient cohort. The patient cohort and DESI-MS results are summarized in tables 5.1-5.4. A summary of patients recruited, whether a patient was included or excluded from analysis, which biopsies were analyzed offline, and the total number of biopsies analyzed intraoperatively and offline is provided in Table 5.1. Patient demographics, diagnosis, and treatment information is described in Table 5.2. The results of DESI-MS assessment of TCP and IDH genotype for all analyzed biopsies are included in Table 5.3. Histopathology assessments of all smeared tissue biopsies previously analyzed by DESI-MS are listed in Table 5.4.

Table 5.1 Summary of patients recruited, if excluded from study or analysis, if biopsies were subsequently analyzed offline, total biopsies analyzed intraoperatively, and number of biopsies analyzed offline.

Patient #	Screenfail	Analyzed offline	Total Biopsies Analyzed	Biopsies Analyzed Offline
01	No	No	10	0
02	No	No	7	0
03	No	No	8	0
04	No	No	8	0
05	No	No	8	0
06	Yes	-	-	-
07	No	No	8	0
08	No	No	8	0
09	No	No	8	0
10	No	No	8	0
11	No	No	8	0
12	No	No	8	0
13	No	No	6	0
14	No	No	8	0
15	No	No	8	0
16	No	No	8	0
17	No	No	8	0
18	No	No	8	0
19	No	No	8	0
20	No	No	8	0
21	No	No	8	0
22	No	No	8	0
23	No	No	8	0
24	Yes	-	-	-
25	No	No	8	0
26	No	No	8	0
27	Yes	-	-	-
28	No	Yes	8	5
29	No	Yes	8	5
30	No	Yes	8	5
31	No	Yes	8	5
32	No	No	8	0
33	No	No	8	4
34	No	Yes	8	5
35	No	Yes	8	4
36	No	Yes	8	3
37	No	Yes	8	2
38	Yes	-	-	-

Table 5.1 continued

39	Yes	-	-	-
40	Yes	-	-	-
41	Yes	-	-	-
42	No	Yes	8	1
43	No	Yes	8	1
44	No	No	8	0

-= Information is irrelevant, as the patient was a screen fail

Table 5.2 Patient demographics, diagnosis, recurrency, and IDH genotype.

Patient #	Age	Gender	Race	Ethnicity	Glioma Classification	WHO Grade	Primary/ Recurrent	IDH Genotype
01	51	F	W	N.H.	Glioblastoma	IV	R	WT
03	53	M	W	N.H.	Glioblastoma	IV	P	WT
04	38	F	-	N.H.	Anaplastic oligodendroglioma	III	P	Mut
05	48	M	W	N.H.	Oligodendroglioma	II	R	Mut
06	18	M	W	-	Infiltrating glioma	II	P	Mut
07	58	F	W	N.H.	Glioblastoma	IV	P	WT
08	41	F	W	N.H.	Glioblastoma	IV	R	Mut
09	64	M	W	N.H.	Glioblastoma	IV	P	WT
10	26	F	W	N.H.	Anaplastic astrocytoma	III	R	Mut
11	27	M	W	N.H.	Glioblastoma	IV	R	Mut
12	71	F	W	N.H.	Glioblastoma	IV	P	WT
13	75	M	W	N.H.	Anaplastic astrocytoma	III	R	WT
14	67	F	W	-	Glioblastoma	IV	P	WT
15	64	M	W	N.H.	Glioblastoma	IV	R	WT
16	46	F	W	H	Glioblastoma	IV	P	WT
17	59	M	W	N.H.	Glioblastoma	IV	P	WT
18	66	M	-	-	Glioblastoma	IV	P	WT
19	44	M	W	N.H.	Oligodendroglioma	II	-	Mut
20	46	M	W	N.H.	Glioblastoma	IV	R	WT
21	70	M	W	N.H.	Glioblastoma	IV	P	WT
22	47	M	W	N.H.	Glioblastoma	IV	R	Mut
23	-	M	-	-	Glioblastoma	IV	-	WT
25	53	F	W	N.H.	Glioblastoma	IV	R	WT
26	51	M	W	N.H.	Glioblastoma	IV	P	WT
27	55	M	W	N.H.	Oligodendroglioma	II	R	Mut
28	72	M	W	N.H.	Astrocytoma	II	P	WT
29	20	F	W	N.H.	Astrocytoma	II	P	Mut
30	26	M	B	N.H.	Anaplastic astrocytoma	III	P	Mut
31	49	F	W	N.H.	Astrocytoma	II	P	Pending
32	71	M	W	N.H.	Glioblastoma	IV	R	WT
33	51	M	W	N.H.	Glioblastoma	IV	P	WT
34	37	F	A.I.	N.H.	Oligodendroglioma	II	P	Mut
35	60	F	W	N.H.	Glioblastoma	IV	P	WT
36	63	F	W	N.H.	Glioblastoma	IV	P	WT

Table 5.2 continued

37	71	M	W	N.H.	Anaplastic oligodendroglioma	III	P	Mut
42	81	M	W	N.H.	Glioblastoma	IV	P	WT
43	58	M	W	N.H.	Glioblastoma	IV	P	WT
44	39	M	W	N.H.	Astrocytoma	II	P	Mut
	Average Age:	**Gender Distribution:**	**Race Distribution:**	**Ethnicity Distribution:**		**Tumor Grade Distribution:**	**Recurrency Distribution:**	**IDH Genotype Distribution:**
	52.3	M: 24 F: 14	W: 33 B: 1 A.I.: 1 Unknown: 3	H: 1 N.H.: 33 Unknown: 1		Grade I: 0 Grade II: 9 Grade III: 5 Grade IV: 24	Primary: 24 Recurrent: 12 Unknown: 2	WT: 23 Mut: 14 Pending: 1

M= Male; F= Female
W= White; A.I.= Asian Indian; B= Black
H= Hispanic; N.H.= Not Hispanic
P= Primary; R= Recurrent
Mut= Mutant; WT= Wild type
-= information not provided/available

Table 5.3 DESI-MS predictions of TCP and IDH genotype for the biopsies obtained from each patient.

Sample Info					Selected DESI-MS Scans		NAA (Full Scan) TCP Estimation		Lipid Deconvolution TCP Estimation		IDH Genotype from 2HG:Glu Ratio	
Patient #	**Biopsy #**	**Location**	**Included/Excluded from Statistical Predictions of TCP**	**Included/Excluded from IDH Genotype Assessment**	**# Lipid Scans**	**# Metabolite Scans**	**Mean TCP Value**	**TCP Category**	**Mean TCP Value**	**TCP Category**	**2HG:Glu Ratio (log)**	**IDH Genotype**
01	1	Margin	E*	N/A	28	25	0	Low	28	High	N/A	N/A
	2	Margin	I	N/A	60	33	16	High	63	High	N/A	N/A
	3	Core	E**	N/A	66	57	4	Low	44	High	N/A	N/A
	4	Core	E**	N/A	21	11	65	High	64	High	N/A	N/A
	5	Margin	I	N/A	67	48	0	Low	48	High	N/A	N/A
	6	Margin	I	N/A	44	37	0	Low	47	High	N/A	N/A
	7	Margin	I	N/A	49	47	0	Low	33	High	N/A	N/A
	8	Margin	I	N/A	61	51	0	Low	48	High	N/A	N/A
	9	Margin	I	N/A	62	64	0	Low	47	High	N/A	N/A
	10	Margin	I	N/A	29	14	8	High	50	High	N/A	N/A
02	1	Margin	I	N/A	64	78	0	Low	9	Low	N/A	N/A
	2	Core	I	N/A	64	75	0	Low	9	Low	N/A	N/A
	3	Margin	E*	N/A	67	77	8	High	14	Low	N/A	N/A
	4	Margin	E*	N/A	68	67	0	Low	11	Low	N/A	N/A
	5	Margin	E**	N/A	65	74	9	High	11	Low	N/A	N/A
	6	Core	I	N/A	61	78	31	High	18	Low	N/A	N/A
	7	Margin	I	N/A	61	67	31	High	39	High	N/A	N/A
03	1	Core	E**	N/A	61	78	1	Low	8	Low	N/A	N/A

Table 5.3 continued

03	2	Margin	I	N/A	51	77	24	High	8	Low	N/A	N/A
	3	Margin	I	N/A	53	73	7	High	8	Low	N/A	N/A
	4	Margin	I	N/A	35	60	38	High	7	Low	N/A	N/A
	5	Core	I	N/A	53	79	0	Low	7	Low	N/A	N/A
	6	Margin	I	N/A	56	80	19	High	8	Low	N/A	N/A
	7	Core	E*	N/A	21	21	35	High	18	Low	N/A	N/A
	8	Core	I	N/A	20	17	39	High	15	Low	N/A	N/A
04	1	-	I***	N/A	71	81	0	Low	43	High	N/A	N/A
	2	-	I***	N/A	70	79	0	Low	46	High	N/A	N/A
	3	-	I***	N/A	72	81	0	Low	42	High	N/A	N/A
	4	-	I***	N/A	57	75	0	Low	40	High	N/A	N/A
	5	-	I***	N/A	65	79	0	Low	42	High	N/A	N/A
	6	-	I***	N/A	68	77	0	Low	36	High	N/A	N/A
	7	-	I***	N/A	62	78	1	Low	40	High	N/A	N/A
	8	-	I***	N/A	73	81	0	Low	26	High	N/A	N/A
05	1	Margin	I	N/A	69	82	0	Low	40	High	N/A	N/A
	2	Core	I	N/A	73	82	0	Low	39	High	N/A	N/A
	3	Margin	I	N/A	66	80	0	Low	62	High	N/A	N/A
	4	Margin	I	N/A	72	82	0	Low	27	High	N/A	N/A
	5	Core	I	N/A	70	81	0	Low	34	High	N/A	N/A
	6	Margin	I	N/A	73	82	0	Low	32	High	N/A	N/A
	7	Core	I	N/A	70	77	1	Low	57	High	N/A	N/A
	8	Core	I	N/A	70	78	2	Low	64	High	N/A	N/A
07	1	Margin	I	N/A	68	81	2	Low	20	Low	N/A	N/A
	2	Margin	I	N/A	73	82	20	High	33	High	N/A	N/A

Table 5.3 continued

07	3	Core	I	N/A	70	82	14	High	28	High	N/A	N/A
	4	Core	I	N/A	71	82	17	High	34	High	N/A	N/A
	5	Core	I	N/A	70	82	21	High	35	High	N/A	N/A
	6	Margin	I	N/A	72	82	32	High	47	High	N/A	N/A
	7	Core	I	N/A	73	82	32	High	37	High	N/A	N/A
	8	Margin	I	N/A	72	82	43	High	36	High	N/A	N/A
08	1	Margin	I	N/A	73	81	0	Low	27	High	N/A	N/A
	2	Margin	I	N/A	73	82	0	Low	20	Low	N/A	N/A
	3	Core	I	N/A	69	82	0	Low	40	High	N/A	N/A
	4	Margin	I	N/A	72	82	0	Low	20	Low	N/A	N/A
	5	Core	I	N/A	53	82	32	High	12	Low	N/A	N/A
	6	Core	I	N/A	51	81	9	High	10	Low	N/A	N/A
	7	Margin	I	N/A	60	82	29	High	15	Low	N/A	N/A
	8	Margin	I	N/A	65	82	14	High	13	Low	N/A	N/A
09	1	Margin	I	N/A	64	82	0	Low	53	High	N/A	N/A
	2	Margin	I	N/A	43	78	46	High	53	High	N/A	N/A
	3	Margin	I	N/A	73	82	0	Low	21	Low	N/A	N/A
	4	Core	I	N/A	54	82	13	High	25	High	N/A	N/A
	5	Margin	I	N/A	64	81	29	High	62	High	N/A	N/A
	6	Core	I	N/A	55	81	55	High	64	High	N/A	N/A
	7	Margin	I	N/A	63	82	29	High	48	High	N/A	N/A
	8	Core	I	N/A	14	79	46	High	62	High	N/A	N/A
10	1	Margin	I	N/A	68	82	0	Low	39	High	N/A	N/A
	2	Margin	I	N/A	66	81	0	Low	33	High	N/A	N/A
	3	Margin	I	N/A	68	75	0	Low	46	High	N/A	N/A

Table 5.3 continued

10	4	Margin	I	N/A	73	78	0	Low	46	High	N/A	N/A
	5	Core	I	N/A	26	73	11	High	60	High	N/A	N/A
	6	Core	I	N/A	18	64	61	High	67	High	N/A	N/A
	7	Core	I	N/A	26	65	61	High	77	High	N/A	N/A
	8	Core	I	N/A	28	74	29	High	61	High	N/A	N/A
11	1	Margin	E*	N/A	67	72	0	Low	55	High	N/A	N/A
	2	Margin	I	N/A	71	82	0	Low	25	High	N/A	N/A
	3	Margin	I	N/A	70	82	0	Low	18	Low	N/A	N/A
	4	Margin	I	N/A	68	81	0	Low	30	High	N/A	N/A
	5	Core	I	N/A	40	82	0	Low	30	High	N/A	N/A
	6	Margin	I	N/A	64	82	0	Low	17	Low	N/A	N/A
	7	Core	I	N/A	55	82	15	High	34	High	N/A	N/A
	8	Core	I	N/A	29	82	0	Low	19	Low	N/A	N/A
12	1	Margin	I	N/A	73	82	0	Low	21	Low	N/A	N/A
	2	Margin	I	N/A	73	82	0	Low	36	High	N/A	N/A
	3	Margin	E**	N/A	27	74	50	High	78	High	N/A	N/A
	4	Core	E**	N/A	17	73	65	High	78	High	N/A	N/A
	5	Margin	E**	N/A	6	76	42	High	69	High	N/A	N/A
	6	Core	I	N/A	34	78	48	High	74	High	N/A	N/A
	7	Core	I	N/A	27	72	31	High	65	High	N/A	N/A
	8	Margin	I	N/A	15	81	38	High	65	High	N/A	N/A
13	1	Margin	I	N/A	73	82	0	Low	19	Low	N/A	N/A
	2	Margin	E*	N/A	64	82	0	Low	8	Low	N/A	N/A
	3	Core	E*	N/A	73	82	0	Low	6	Low	N/A	N/A
	4	Margin	I	N/A	72	82	0	Low	4	Low	N/A	N/A

Table 5.3 continued

13	5	Margin	I	N/A	72	82	0	Low	4	Low	N/A	N/A
	6	Margin	I	N/A	72	77	0	Low	26	High	N/A	N/A
14	1	Margin	E*	N/A	30	50	39	High	69	High	N/A	N/A
	2	Margin	E*	N/A	32	62	75	High	72	High	N/A	N/A
	3	Core	I	N/A	45	70	73	High	66	High	N/A	N/A
	4	Core	I	N/A	20	59	70	High	72	High	N/A	N/A
	5	Core	I	N/A	41	69	69	High	74	High	N/A	N/A
	6	Margin	I	N/A	70	81	40	High	41	High	N/A	N/A
	7	Core	I	N/A	29	27	51	High	72	High	N/A	N/A
	8	Margin	I	N/A	50	50	59	High	64	High	N/A	N/A
15	1	Margin	I	E	66	77	16	High	21	Low	-1.06	WT
	2	Core	E*	I	68	82	24	High	12	Low	-0.66	WT
	3	Core	I	I	64	81	19	High	16	Low	-0.79	WT
	4	Core	I	I	66	82	11	High	18	Low	-1.04	WT
	5	Core	I	I	64	82	9	High	18	Low	-0.93	WT
	6	Core	I	I	67	76	0	Low	19	Low	-0.95	WT
	7	Core	E*	I	72	82	13	High	13	Low	-0.79	WT
	8	Core	I	I	64	82	9	High	17	Low	-0.79	WT
16	1	Margin	I	E	66	82	1	Low	14	Low	-1.05	WT
	2	Core	E*	I	40	69	54	High	18	Low	-0.59	WT
	3	Margin	I	E	70	78	5	Low	11	Low	-1.00	WT
	4	Core	I	I	57	78	22	High	15	Low	-0.86	WT
	5	Core	I	I	65	78	30	High	32	High	-0.68	WT
	6	Core	I	I	60	76	21	High	24	High	-0.85	WT
	7	Core	I	I	42	50	52	High	69	High	-0.75	WT

Table 5.3 continued

16	8	Core	I	I	63	70	52	High	63	High	-0.96	WT
17	1	Core	I	I	73	82	0	Low	14	Low	-1.36	WT
	2	Core	I	I	69	82	0	Low	27	High	-1.24	WT
	3	Core	I	I	73	82	0	Low	13	Low	-1.32	WT
	4	Core	I	I	70	75	21	High	44	High	-1.12	WT
	5	Core	I	I	71	74	25	High	36	High	-1.31	WT
	6	Margin	I	E	73	82	0	Low	22	High	-1.61	WT
	7	Core	I	I	69	67	29	High	62	High	-1.18	WT
	8	Core	I	I	68	81	26	High	57	High	-1.13	WT
18	1	Core	E*	I	56	73	68	High	66	High	-0.78	WT
	2	Core	I	I	70	82	0	Low	14	Low	-0.98	WT
	3	Core	E**	I	66	73	54	High	50	High	-0.82	WT
	4	Core	I	I	65	82	29	High	36	High	-1.05	WT
	5	Core	E**	I	52	74	48	High	60	High	-0.92	WT
	6	Core	I	I	68	82	2	Low	33	High	-0.91	WT
	7	Core	E**	I	47	66	48	High	58	High	-0.81	WT
	8	Core	I	I	71	82	29	High	33	High	-1.12	WT
19	1	Margin	I	E	73	82	0	Low	16	Low	0.14	Mut
	2	Margin	I	E	73	82	0	Low	7	Low	-0.02	Mut
	3	Core	I	I	73	82	15	High	24	High	1.39	Mut
	4	Core	I	I	73	82	0	Low	3	Low	0.17	Mut
	5	Core	I	I	73	82	21	High	23	High	1.48	Mut
	6	Core	I	I	73	82	8	High	19	Low	1.45	Mut
	7	Margin	I	E	71	82	0	Low	10	Low	0.08	Mut
	8	Margin	E**	E	68	82	2	Low	10	Low	0.75	Mut

Table 5.3 continued

20	1	Margin	I	E	64	78	64	High	66	High	-0.85	WT
	2	Margin	I	E	66	78	61	High	59	High	-0.83	WT
	3	Margin	I	E	62	82	44	High	14	Low	-0.87	WT
	4	Margin	I	E	53	82	20	High	7	Low	-0.80	WT
	5	Core	I	I	55	79	42	High	8	Low	-0.83	WT
	6	Core	I	I	54	79	40	High	11	Low	-0.97	WT
	7	Core	I	I	60	80	27	High	9	Low	-1.10	WT
	8	Core	I	I	71	82	0	Low	2	Low	-1.25	WT
21	1	Core	I	I	60	79	6	High	26	High	-1.00	WT
	2	Core	I	I	67	82	7	High	9	Low	-0.67	WT
	3	Core	I	I	64	82	0	Low	7	Low	-1.05	WT
	4	Core	I	I	69	82	0	Low	9	Low	-0.97	WT
	5	Margin	I	E	73	82	0	Low	0	Low	-1.33	WT
	6	Core	I	I	69	82	9	High	32	High	-0.87	WT
	7	Core	I	I	62	79	40	High	33	High	-0.85	WT
	8	Core	I	I	61	80	0	Low	18	Low	-1.02	WT
22	1	Margin	I	E	63	82	37	High	18	Low	1.34	Mut
	2	Margin	I	E	73	78	83	High	40	High	1.77	Mut
	3	Margin	I	E	61	80	64	High	39	High	1.34	Mut
	4	Margin	I	E	69	81	73	High	41	High	1.72	Mut
	5	Core	I	I	63	82	53	High	22	High	1.32	Mut
	6	Margin	E**	E	67	82	0	Low	5	Low	0.58	Mut
	7	Margin	I	E	68	80	62	High	36	High	1.76	Mut
	8	Core	I	I	69	82	19	High	10	Low	0.99	Mut
23	1	Margin	I	E	71	82	0	Low	7	Low	-1.21	WT

Table 5.3 continued

23	2	Margin	I	E	63	78	0	Low	14	Low	-1.59	WT
	3	Core	I	I	73	82	0	Low	12	Low	-1.45	WT
	4	Margin	I	E	73	82	0	Low	14	Low	-1.52	WT
	5	Core	I	I	69	82	35	High	46	High	-0.81	WT
	6	Core	I	I	60	79	32	High	28	High	-1.05	WT
	7	Core	E*	I	36	54	37	High	68	High	-0.63	WT
	8	Core	I	I	71	82	0	Low	7	Low	-1.11	WT
25	1	Core	I	I	73	82	0	Low	12	Low	-1.47	WT
	2	Core	I	I	65	82	0	Low	7	Low	-1.11	WT
	3	Margin	I	E	73	82	0	Low	5	Low	-1.33	WT
	4	Core	I	I	68	82	12	High	12	Low	-1.06	WT
	5	Core	I	I	59	81	40	High	41	High	-0.93	WT
	6	Core	I	I	44	53	34	High	48	High	-0.72	WT
	7	Core	I	I	68	82	13	High	7	Low	-0.94	WT
	8	Core	I	I	68	82	2	Low	8	Low	-1.25	WT
26	1	Margin	I	E	65	82	0	Low	8	Low	-0.90	WT
	2	Margin	I	E	74	82	0	Low	6	Low	-1.09	WT
	3	Core	E**	I	58	69	42	High	35	High	-1.26	WT
	4	Core	I	I	46	74	54	High	48	High	-0.95	WT
	5	Core	E**	I	54	77	46	High	23	High	-1.06	WT
	6	Core	E**	I	53	72	56	High	46	High	-0.78	WT
	7	Core	E*	I	39	70	45	High	52	High	-1.13	WT
	8	Core	E*	I	27	39	49	High	61	High	-0.68	WT
28	1	Margin	I	E	73	82	0	Low	2	Low	-1.23	WT
	2	Margin	I	E	72	82	0	Low	4	Low	-1.13	WT

Table 5.3 continued

28	3	Margin	I	E	73	82	0	Low	2	Low	-1.28	WT
	4	Core	I	I	73	82	0	Low	5	Low	-0.92	WT
	5	Core	I	I	69	82	0	Low	9	Low	-1.12	WT
	6	Margin	E*	E	73	82	0	Low	5	Low	-1.09	WT
	7	Margin	I	E	73	82	0	Low	5	Low	-1.13	WT
	8	Core	I	I	64	82	0	Low	6	Low	-0.81	WT
29	1	Margin	I	E	55	62	53	High	29	High	1.40	Mut
	2	Margin	I	E	56	42	66	High	69	High	1.88	Mut
	3	Core	I	I	63	63	39	High	63	High	1.69	Mut
	4	Core	I	I	49	75	63	High	71	High	1.87	Mut
	5	Core	I	I	57	53	35	High	57	High	1.84	Mut
	6	Core	I	I	50	34	75	High	74	High	1.93	Mut
	7	Core	I	I	42	38	62	High	77	High	2.00	Mut
	8	Core	I	I	60	67	30	High	34	High	1.56	Mut
30	1	Margin	I	E	59	78	19	High	33	High	0.90	Mut
	2	Margin	I	E	66	79	8	High	22	High	0.56	Mut
	3	Margin	I	E	66	62	61	High	67	High	1.11	Mut
	4	Core	I	I	68	37	31	High	56	High	1.00	Mut
	5	Core	I	I	70	72	31	High	52	High	0.96	Mut
	6	Core	I	I	73	82	0	Low	7	Low	0.33	Mut
	7	Core	I	I	70	82	0	Low	5	Low	0.41	Mut
	8	Core	I	I	73	82	0	Low	3	Low	-0.83	WT
31	1	Margin	I	E	65	81	4	Low	9	Low	1.10	Mut
	2	Margin	I	E	72	81	0	Low	5	Low	0.67	Mut
	3	Margin	I	E	74	82	1	Low	9	Low	1.00	Mut

Table 5.3 continued

31	4	Margin	I	E	72	81	0	Low	9	Low	1.07	Mut
	5	Core	I	I	73	82	0	Low	7	Low	0.82	Mut
	6	Core	I	I	71	78	0	Low	25	High	0.82	Mut
	7	Core	I	I	73	82	0	Low	5	Low	0.62	Mut
	8	Margin	I	E	73	81	0	Low	4	Low	-0.01	Mut
32	1	Margin	I	E	65	82	33	High	17	Low	-1.19	WT
	2	Margin	I	E	71	82	0	Low	6	Low	-1.08	WT
	3	Margin	I	E	67	82	0	Low	9	Low	-1.23	WT
	4	Core	I	I	37	50	45	High	37	High	-1.23	WT
	5	Core	E*	I	56	20	52	High	59	High	-0.88	WT
	6	Core	E*	I	67	13	61	High	59	High	-0.46	WT
	7	Core	E*	I	50	57	48	High	59	High	-1.22	WT
	8	Core	E*	I	53	75	51	High	27	High	-1.05	WT
33	1	Margin	I	E	63	78	19	High	40	High	-0.87	WT
	2	Margin	I	E	67	78	0	Low	28	High	-0.89	WT
	3	Margin	I	E	64	82	22	High	22	High	-0.81	WT
	4	Margin	I	E	57	75	60	High	37	High	-0.77	WT
	5	Core	I	I	73	75	0	Low	25	High	-1.03	WT
	6	Core	E*	I	40	64	39	High	57	High	-0.71	WT
	7	Core	E*	I	63	72	9	High	25	High	-0.68	WT
	8	Margin	E*	E	58	41	25	High	61	High	-0.85	WT
34	1	Margin	I	E	67	82	0	Low	14	Low	-0.17	Mut
	2	Margin	I	E	58	80	15	High	38	High	0.33	Mut
	3	Margin	I	E	68	82	0	Low	8	Low	-0.51	WT
	4	Margin	I	E	73	82	0	Low	6	Low	-0.92	WT

Table 5.3 continued

34	5	Core	I	I	73	82	0	Low	3	Low	-0.93	WT
	6	Core	I	I	63	81	18	High	50	High	0.44	Mut
	7	Core	I	I	71	82	0	Low	13	Low	0.15	Mut
	8	Core	I	I	71	69	0	Low	55	High	0.51	Mut
35	1	Core	I	I	70	82	51	High	31	High	-1.15	WT
	2	Core	I	I	65	82	7	High	23	High	-1.18	WT
	3	Necrotic	I	E*	54	81	51	High	47	High	-1.12	WT
	4	Core	E*	I	40	51	25	High	70	High	-0.81	WT
	5	Core	I	I	62	76	44	High	48	High	-1.03	WT
	6	Core	I	I	42	77	50	High	51	High	-0.99	WT
	7	Core	I	I	65	82	17	High	32	High	-1.28	WT
	8	Core	I	I	57	82	7	High	12	Low	-1.62	WT
36	1	Margin	E*	E	72	81	0	Low	4	Low	-1.26	WT
	2	Core	I	I	73	80	0	Low	1	Low	-1.16	WT
	3	Core	I	I	67	82	0	Low	4	Low	-1.05	WT
	4	Core	I	I	60	81	29	High	13	Low	-0.84	WT
	5	Core	I	I	70	59	58	High	56	High	-0.31	WT
	6	Core	I	I	62	54	55	High	66	High	-0.49	WT
	7	Core	I	I	49	77	38	High	21	Low	-0.83	WT
	8	Core	I	I	61	71	3	Low	38	High	-1.03	WT
37	1	Margin	I	E	64	45	25	High	77	High	0.44	Mut
	2	Margin	I	E	66	82	7	High	55	High	0.89	Mut
	3	Margin	I	E	65	66	21	High	64	High	0.65	Mut
	4	Margin	I	E	67	82	9	High	46	High	0.99	Mut
	5	Margin	I	E	66	81	11	High	59	High	0.80	Mut

Table 5.3 continued

37	6	Margin	I	E	70	80	0	Low	41	High	0.55	Mut
	7	Core	I	I	71	82	13	High	36	High	0.81	Mut
	8	Core	E**	I	67	77	6	High	42	High	0.63	Mut
42	1	-	I***	E***	72	82	0	Low	10	Low	-1.43	WT
	2	-	I***	E***	64	82	1	Low	9	Low	-1.00	WT
	3	-	I***	E***	62	82	16	High	17	Low	-1.12	WT
	4	-	I***	E***	66	78	52	High	45	High	-1.19	WT
	5	-	I***	E***	67	80	64	High	36	High	-1.33	WT
	6	-	I***	E***	65	78	6	High	31	High	-0.98	WT
	7	-	I***	E***	65	82	18	High	18	Low	-0.93	WT
	8	-	I***	E***	64	77	8	High	32	High	-0.80	WT
43	1	Margin	I	E	70	82	0	Low	14	Low	-1.38	WT
	2	Margin	I	E	67	80	0	Low	8	Low	-1.39	WT
	3	Core	I	I	73	82	0	Low	6	Low	-1.39	WT
	4	Margin	I	E	67	82	0	Low	7	Low	-1.03	WT
	5	Core	I	I	63	82	7	High	11	Low	-1.02	WT
	6	Core	I	I	71	82	0	Low	20	Low	-1.33	WT
	7	Core	I	I	60	81	0	Low	15	Low	-1.41	WT
	8	Margin	I	E	73	82	0	Low	12	Low	-1.27	WT
44	1	Margin	I	E	65	82	0	Low	8	Low	-1.07	WT
	2	Margin	I	E	61	82	0	Low	9	Low	-1.33	WT
	3	Margin	I	E	68	70	65	High	74	High	1.07	Mut
	4	Core	I	I	66	75	13	High	55	High	0.68	Mut
	5	Margin	I	E	66	67	61	High	77	High	1.37	Mut
	6	Core	I	I	64	66	73	High	76	High	1.37	Mut

Table 5.3 continued

44	7	Core	I	I	68	63	75	High	75	High	1.26	Mut
	8	Core	I	I	65	58	63	High	64	High	0.81	Mut

I= included; E= excluded
= Tissue is non-diagnostic, predominantly blood, or necrosis; **= Poor smear quality; *= Location not recorded; biopsy is included for TCP study, but excluded from location comparisons and IDH study*
N/A= Not assessed.
Mut= Mutant; WT= Wild type
Note: IDH assessment based on 2HG intensity began after the commencement of the study, starting with Patient 15.

Table 5.4 Histopathological evaluation and TCP assessment tissue smears

Patient #	Biopsy #	Tissue Type	TCP Estimate	Smear Quality
01	1	Non-diagnostic	N/A	N/A
	2	Glioma	High	A
	3	Glioma	High	I
	4	Glioma	High	I
	5	Glioma	Low	MA
	6	Glioma	Low	MA
	7	Glioma	Low	MA
	8	Glioma	Low	MA
	9	Glioma	Low	MA
	10	Glioma	Low	MA
02	1	Glioma	Low	A
	2	Glioma	Low	MA
	3	Brain tissue	N/A	N/A
	4	Glioma	N/A	N/A
	5	Glioma	Low	I
	6	Glioma	Low	MA
	7	Glioma	Low	A
03	1	Glioma	Low	I
	2	Glioma	Low	MA
	3	Glioma	Low	MA
	4	Glioma	Low	A
	5	Glioma	Low	A
	6	Glioma	Low	A
	7	Necrotic debris	N/A	N/A
	8	Astrocytoma	High	A
04	1	Glioma	High	A
	2	Glioma	Low	A
	3	Glioma	Low	A
	4	Glioma	Low	A
	5	Glioma	Low	MA
	6	Glioma	Low	A
	7	Glioma	Low	A

Table 5.4 continued

04	8	Glioma	Low	A
05	1	Glioma	Low	A
	2	Glioma	Low	A
	3	Glioma	Low	A
	4	Glioma	Low	A
	5	Glioma	Low	A
	6	Glioma	Low	A
	7	Glioma	High	A
	8	Glioma	High	A
07	1	Glioblastoma	Low	A
	2	Glioblastoma	High	A
	3	Glioblastoma	High	A
	4	Glioblastoma	High	A
	5	Glioblastoma	High	A
	6	Glioblastoma	High	A
	7	Glioblastoma	High	A
	8	Glioblastoma	High	A
08	1	Glioblastoma	Low	A
	2	Glioblastoma	Low	A
	3	Glioblastoma	Low	A
	4	Glioblastoma	Low	A
	5	Glioblastoma	Low	A
	6	Glioblastoma	Low	A
	7	Glioblastoma	Low	A
	8	Glioblastoma	High	A
09	1	Glioblastoma	High	A
	2	Glioblastoma	High	A
	3	Glioblastoma	High	MA
	4	Glioblastoma	High	A
	5	Glioblastoma	High	A
	6	Glioblastoma	High	A
	7	Glioblastoma	High	A
	8	Glioblastoma	High	A
10	1	Anaplastic astrocytoma	Low	A
	2	Anaplastic astrocytoma	High	A

Table 5.4 continued

10	3	Anaplastic astrocytoma	Low	A
	4	Anaplastic astrocytoma	High	A
	5	Anaplastic astrocytoma	Low	A
	6	Anaplastic astrocytoma	High	A
	7	Anaplastic astrocytoma	High	A
	8	Anaplastic astrocytoma	Low	A
11	1	Negative	N/A	N/A
	2	Glioma	Low	A
	3	Glioma	Low	A
	4	Glioma	Low	A
	5	Glioma	Low	A
	6	Glioma	Low	MA
	7	Glioma	Low	I
	8	Glioma	Low	A
12	1	Glioma	Low	A
	2	Glioma	Low	A
	3	Glioma	High	I
	4	Glioma	Low	I
	5	Glioma	High	I
	6	Glioma	High	A
	7	Glioma	High	A
	8	Glioma	High	MA
13	1	Glioma	Low	A
	2	Negative	N/A	N/A
	3	Negative	N/A	N/A
	4	Glioma	Low	A
	5	Glioma	Low	A
	6	Glioma	Low	A
14	1	Necrotic debris/tumor	N/A	N/A
	2	Necrotic debris/tumor	N/A	N/A
	3	Necrotic debris/tumor	High	A
	4	Necrotic debris/tumor	High	A
	5	Necrotic debris/tumor	High	A
	6	Viable glioma	High	A
	7	Necrotic debris/tumor	High	A

Table 5.4 continued

14	8	Approximately half tumor and have necrosis	High	A
15	1	Glioma	Low	A
	2	Necrotic debris/tumor	N/A	N/A
	3	Glioma	Low	A
	4	Glioma	High	A
	5	Glioma	High	A
	6	Glioma	High	A
	7	Necrotic tumor	N/A	N/A
	8	Glioma	High	A
16	1	Glioma	High	A
	2	Necrosis	N/A	N/A
	3	Glioma	Low	A
	4	Glioma	High	A
	5	Glioma	High	A
	6	Glioma	High	A
	7	Glioma	High	I
	8	Glioma	High	A
17	1	Glioma	Low	A
	2	Glioma	Low	A
	3	Glioma	Low	A
	4	Glioma	High	A
	5	Glioma	High	A
	6	Glioma	Low	A
	7	Glioma	High	A
	8	Glioma	High	A
18	1	Necrosis	N/A	N/A
	2	Glioma	High	A
	3	Glioma	High	I
	4	Glioma	High	A
	5	Glioma	High	I
	6	Glioma	High	A
	7	Glioma	N/A	I
	8	Glioma	High	A
19	1	Glioma	High	A
	2	Glioma	Low	A

Table 5.4 continued

19	3	Glioma	High	A
	4	Glioma	Low	A
	5	Glioma	High	A
	6	Glioma	Low	A
	7	Glioma	Low	A
	8	Glioma	Low	I
20	1	Glioma	High	A
	2	Glioma	High	A
	3	Glioma	High	A
	4	Glioma	High	A
	5	Glioma	High	A
	6	Glioma	High	A
	7	Glioma	Low	A
	8	Glioma	Low	A
21	1	Glioma	High	A
	2	Glioma	High	A
	3	Glioma	Low	A
	4	Glioma	High	A
	5	Glioma	High	A
	6	Glioma	High	A
	7	Glioma	High	A
	8	Glioma	High	A
22	1	Glioma	Low	A
	2	Glioma	High	A
	3	Glioma	High	A
	4	Glioma	High	A
	5	Glioma	High	A
	6	Glioma	Low	I
	7	Glioma	High	A
	8	Glioma	Low	A
23	1	Glioma	Low	A
	2	Glioma	Low	A
	3	Glioma	Low	A
	4	Glioma	Low	A
	5	Glioma	Low	A

Table 5.4 continued

23	6	Glioma	Low	A
	7	N/A	N/A	N/A
	8	Glioma	Low	A
25	1	Glioma	Low	A
	2	Glioma	Low	A
	3	Glioma	Low	A
	4	Glioma	Low	A
	5	Glioma	Low	A
	6	Glioma	High	A
	7	Glioma	Low	A
	8	Glioma	Low	A
26	1	Glioma	Low	A
	2	Glioma	Low	A
	3	Glioma	Low	I
	4	Blood	NA	A
	5	Glioma	Low	I
	6	Glioma	NA	I
	7	Blood	NA	I
	8	Blood	NA	I
28	1	Glioma	Low	A
	2	Glioma	Low	A
	3	Glioma	Low	A
	4	Brain tissue	Low	A
	5	Glioma	Low	A
	6	Brain tissue	N/A	N/A
	7	Glioma	Low	A
	8	Glioma	Low	A
29	1	Glioma	Low	A
	2	Glioma	Low	MA
	3	Glioma	Low	MA
	4	Glioma	Low	MA
	5	Glioma	Low	MA
	6	Glioma	Low	MA
	7	Glioma	Low	MA
	8	Glioma	Low	MA

Table 5.4 continued

30	1	Glioma	High	A
	2	Glioma	High	A
	3	Glioma	High	A
	4	Glioma	High	A
	5	Glioma	Low	A
	6	Glioma	Low	A
	7	Glioma	Low	A
	8	Glioma	Low	A
31	1	Glioma	Low	MA
	2	Glioma	Low	A
	3	Glioma	Low	MA
	4	Glioma	Low	A
	5	Glioma	Low	A
	6	Glioma	Low	A
	7	Glioma	Low	A
	8	Glioma	Low	A
32	1	Glioma	Low	A
	2	Glioma	Low	A
	3	Glioma	Low	A
	4	Glioma	Low	A
	5	N/a	N/A	I
	6	N/a	N/A	I
	7	N/a	N/A	I
	8	N/a	N/A	I
33	1	Glioma	High	A
	2	Glioma	High	A
	3	Glioma	High	MA
	4	Glioma	High	A
	5	Glioma	Low	A
	6	Blood	N/A	N/A
	7	Predominantly blood and some small clumps of glioma	N/A	N/A
	8	Blood	N/A	N/A
34	1	Glioma	Low	A
	2	Glioma	Low	A
	3	Glioma	Low	A

Table 5.4 continued

34	4	Glioma	Low	A
	5	Glioma	Low	A
	6	Glioma	Low	A
	7	Glioma	Low	A
	8	Glioma	Low	A
35	1	Glioma	High	A
	2	Glioma	High	A
	3	Glioma	Low	A
	4	Predominantly blood	N/A	N/A
	5	Glioma	High	A
	6	Glioma	High	A
	7	Glioma	Low	A
	8	Predominantly blood and some small clumps of glioma	High	A
36	1	Brain tissue	N/A	N/A
	2	Glioma	Low	A
	3	Glioma	Low	A
	4	Glioma	Low	A
	5	Glioma	Low	A
	6	Glioma	Low	A
	7	Glioma	Low	A
	8	Glioma	Low	A
37	1	Glioma	Low	A
	2	Glioma	Low	A
	3	Glioma	Low	A
	4	Glioma	High	A
	5	Glioma	Low	A
	6	Glioma	Low	A
	7	Glioma	Low	A
	8	Glioma	High	I
42	1	Glioma	Low	A
	2	Glioma	Low	A
	3	Glioma	Low	A
	4	Glioma	High	A
	5	Glioma	Low	A
	6	Glioma	Low	A

Table 5.4 continued

42	7	Glioma	High	A
	8	Glioma	Low	A
43	1	Glioma	Low	A
	2	Glioma	Low	A
	3	Glioma	Low	A
	4	Glioma	Low	A
	5	Glioma	Low	A
	6	Glioma	Low	A
	7	Glioma	Low	A
	8	Glioma	Low	A
44	1	Glioma	Low	A
	2	Glioma	Low	A
	3	Glioma	Low	A
	4	Glioma	High	A
	5	Glioma	High	A
	6	Glioma	High	A
	7	Glioma	Low	A
	8	Glioma	Low	A

A= adequate; MA= marginally adequate; I= inadequate
N/A= not assessed

5.3.2 IDH Genotyping by Measurement of Relative 2HG Abundance

The methodology for the determination of IDH genotype by DESI-MS was modified midway through the study, in response to the poor signal intensity of low mass ions (e.g. metabolites), including those of the MS3 analysis of 2HG, detected by DESI-MS. Simultaneous MS/MS analysis of 2HG and Glu, an abundant molecule in the brain not associated with IDH mutations, is performed, thereby incorporating this endogenous internal standard into the MS/MS measurement. The ratio of the signals detected from these two analytes is used to assess IDH genotype. Offline experiments conducted on banked human glioma biopsies(19) and validated intraoperatively in a small-scale clinical study using a Mini MS (described in Chapter 3)(20) demonstrated the value and increased robustness and accuracy of this approach. To date, we have analyzed 184 biopsies (116 core, 67 margin, 1 necrotic) from 23 patients. Consistent with the approach taken in the previous study at IU School of Medicine, we elected to only use core biopsies for the assessment of IDH genotype, as we have noticed some variability in the concentration throughout the tumor volume, especially near surgical margins.(27) Assessments of IDH genotypes by DESI-MS were confirmed by immunochemistry and/or genetic testing.

IDH mutation assessment of 116 core biopsies from 23 patients indicate 93% sensitivity, 100% specificity, and 98% accuracy (Table 5.5). A statistically significant (Wilcoxon rank-sum test $p < 0.0001$) increase in the 2HG signal relative to the signal from Glu in tumor core biopsies is observed in patients with IDH-mut gliomas compared with patients with IDH-wt gliomas. This difference is apparent in the box plots shown in Figure 5.2. A receiver operating characteristic (ROC) curve model provides an area under the curve (AUC) of 0.98 using the tumor cores and the ROC-determined cutoff of the log of the 2HG:Glu ratio is -0.31, represented as a horizontal dashed black line as seen Figure 6.2. This cutoff is instrument and method dependent and requires further optimization to determine whether it can be applied universally.

Table 5.5 Confusion matrix correlation between IHC and/or genetic testing and DESI-MS assessments of IDH genotype from 116 core biopsies from 23 patients.

		IHC and/or Genetic Testing		
		IDH-mut	IDH-wt	Total
DESI-MS	IDH-mut	28	0	28
	IDH-wt	2	86	88
	Total	30	86	116
	Sensitivity	93%		
	Specificity	100%		
	Accuracy	98%		

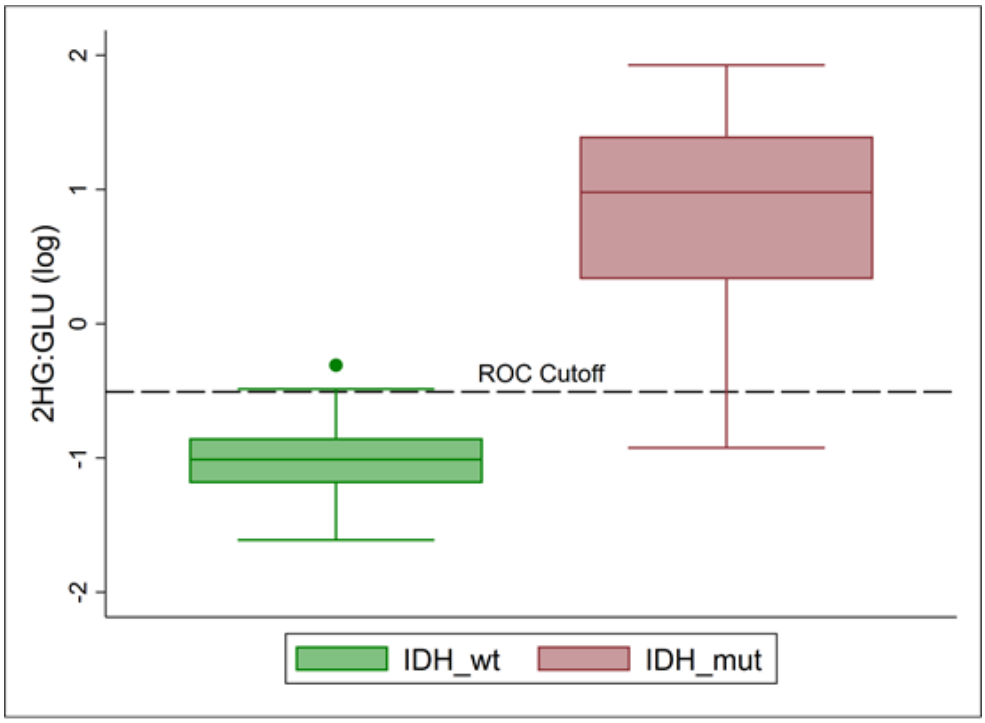

Figure 5.2 Intraoperative assessment of IDH genotype from tumor cores. Box plot of the log of IDH mutation scores in human glioma tissue biopsies (n = 116) analyzed intraoperatively by DESI-MS/MS in the negative ion mode. Error bars represent ± 1.5 times the calculated standard deviations. The black dashed horizontal decision line was calculated from ROC curve analysis and differentiates tumor core biopsies from IDH-mut patients and IDH-wt patients with the highest sensitivity and specificity.

A small number of biopsies (n = 2 of 116) are misclassified intraoperatively with respect their confirmed IDH genotype. Varying relative concentrations of 2HG were observed in different biopsies, even from locations close in proximity to one another. This is to be expected due to the high degree of heterogeneity of glioma, an observation also noted in Chapter 2.(27) This is also an

area of active research in the field of magnetic resonance spectroscopy.(28) As we learn more about heterogeneity in gliomas and its impact on the spatial distribution of molecules, we may be able to better explain the underlying reasons for the observed variability. Adopting a similar employed in the previous study, when averaging the 2HG:Glu ratios for all core biopsies from the same patient and using the averaged ratio to predict IDH mutation status, none of the patients are misclassified. This reiterates the heterogenous nature of gliomas and the importance of sampling multiple locations when attempting to molecularly characterize the tumor, an approach which is made possible by the rapid speed of DESI-MS analysis.

To assess the robustness of the DESI-MS/MS ratiometric method, a small selection of biopsies (n = 50) was sent back to Purdue University. where the same method used intraoperatively was performed on a laboratory Thermo LTQ. The comparison between the online and offline assessments of IDH genotypes of the same 50 biopsies is summarized in Figure 5.3. As can be seen, similar diagnostic performance is achieved for both the online and offline measurements of both core and margin biopsies, with poorer performance noted in margin biopsies due to the heterogeneity in concentration of 2HG in the tumor volume. These data further support the robustness of the method. Given the accurate and robust nature of the assay, efforts to commercialize the technology in preparation for a clinical trial and widespread clinical translation are ongoing.

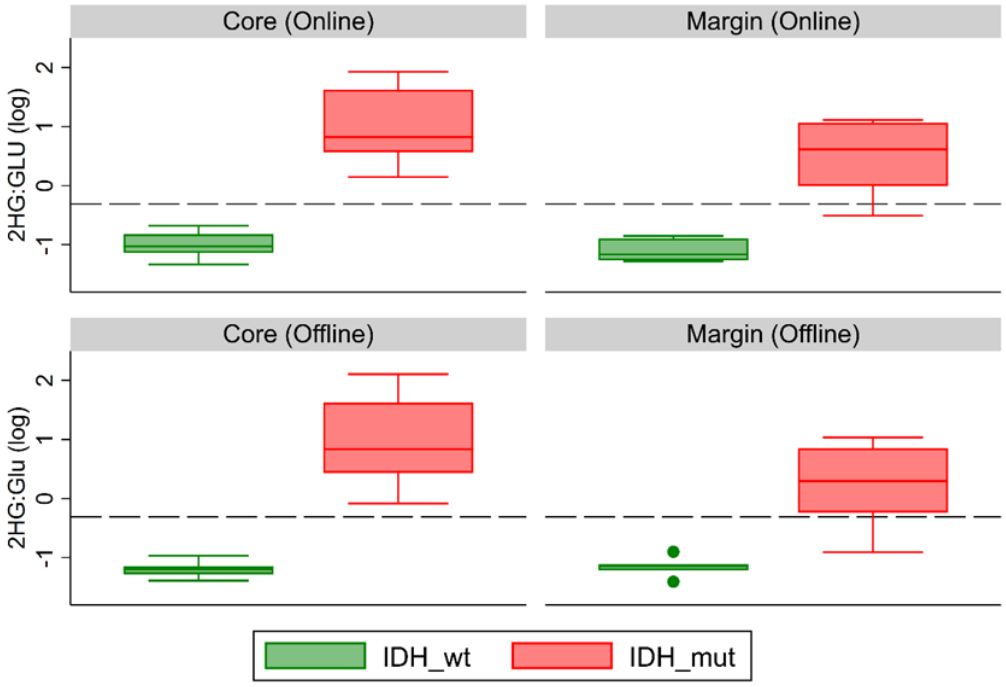

Figure 5.3 Comparison of the intraoperative and postoperative assessment of IDH genotype from tumor core and surgical margin biopsies. Box plot of the log of IDH mutation scores in human glioma tissue specimens (n = 50) analyzed intraoperatively by DESI-MS/MS. Error bars represent ± 1.5 times the calculated standard deviations. The black dashed horizontal decision line is the same as that determined from the ROC curve analysis of the intraoperative data and represents the cutoff with the highest sensitivity and specificity.

5.3.3 Assessment of TCP by NAA Intensity and Lipid Profile Deconvolution

The advanced development of two methods for the assessment of tumor infiltration at surgical margins was performed, based on NAA and lipid abundances, respectively. A total of 295 biopsies from 37 patients (153 core, 125 margin, 1 necrotic, 16 missing location information) has been analyzed. Histopathology estimates of TCP from the same slides analyzed intraoperatively are categorized as low or high TCP and an assessment of the tissue composition and smear quality has been assessed. Of the 295 biopsies analyzed, 251 biopsies from 37 patients have good or moderate smear quality with enough tumor cell present on the slide to allow for the visual estimation of TCP by the expert neuropathologist. The remaining 44 biopsies have been excluded from this portion of the study for not been assessed by the neurosurgeon, not having tumor present (e.g., necrosis, predominantly blood, etc.), having poor smear quality, or a combination of the three.

With respect to the first method, the TIC-normalized full scan intensity of NAA (*m/z* 174) is used to estimate TCP as a percentage, using previously published data as a training set.(25, 27) ROC curve analysis (AUC = 0.82) has been performed to determine the optimized TCP cutoff of 7%. Using the optimized ROC-optimized TCP cutoff, an overall accuracy of correctly classifying biopsies (both core and margin) as low or high TCP of 72%, with 83% sensitivity and 65% specificity, has been achieved, as shown in Table 5.6.

The second method for the estimation of TCP uses a lipid profile deconvolution approach, as previously described.(25, 27) Briefly, principal component analysis (PCA) is used to calculate the percentage of white matter (WM), grey matter (GM), and glioma (G) contributing to the lipid profiles of the new samples using the least squares regression model built from data collected in a previous study. The model is based on the presumption that the observed lipid profile for the glioma samples is composed of a ternary mixture of white-matter, grey-matter, and glioma. The summed percentage of these three categories is 100%. The regression model is built from data collected from DESI-MS imaging of banked glioma and normal human brain specimens. Histologically correlated mass spectra are compiled based on histopathological assessment, compressed with PCA, and the PC1 and PC2 scores for samples of pure WM, GM, and G are estimated. The three extremes (PC1 and PC2 scores corresponding to 100%WM, 100%GM, 100%G) are used to define a triangle model and to further calculate the relative compositions for each possible mixture. The PCA lipid profile loading matrix from the previous study is used to calculate the scores of a new sample, where the PC1 and PC2 scores reveal its position inside the triangle. Relative distances between the spot, representing the new sample, and three tips of the triangle model are used to predict the specific percentages of GM, WM, and G for the new sample. GM and WM are categorized as infiltrative margins (IM) to correspond with histopathological categorization. The percentage of G calculated for each unknown sample is used as an estimate of the TCP. ROC curve analysis (AUC = 0.68) has been performed to determine the optimized TCP cutoff of 23%. Using the optimized ROC-optimized TCP cutoff, an overall accuracy of correctly classifying biopsies (both core and margin) as low or high TCP of 65%, with 77% sensitivity and 57% specificity, has been achieved, as shown in Table 5.6.

Table 5.6 Confusion matrix showing the correlation of histopathology assessments with DESI-MS estimates of TCP in 251 biopsies from 37 patients.

		Histopathology	
		High TCP	**Low TCP**
Full Scan NAA Intensity TCP Estimate	**High TCP**	77	55
Lipid Deconvolution TCP Estimate		72	68
Full Scan NAA Intensity TCP Estimate	**Low TCP**	16	103
Lipid Deconvolution TCP Estimate		21	90
Full Scan NAA Intensity TCP Estimate		**Lipid Deconvolution TCP Estimate:**	
Sensitivity:	83%	*Sensitivity:*	77%
Specificity:	65%	*Specificity:*	57%
Accuracy:	72%	*Accuracy:*	65%

5.3.4 Comments on Decreased Accuracy in TCP Assessment

Decreased diagnostic performance with respect to the previous intraoperative study was observed for the assessment of tumor infiltration as TCP by DESI-MS. A multitude of factors may contribute to the discrepancy. One possible explanation is that the observed differences in NAA or lipid intensities are too small, or the number of ions used to assess tumor infiltration are two few. We have identified additional metabolites in offline experiments and developed DESI-MS methods that could be integrated with the current intraoperative workflow to improve diagnostic accuracy.(29) That said, there are several other sources of error that are independent of the DESI method and do not have straightforward solutions. Glioma surgical margins are incredibly difficult to discern and heterogenous due to the infiltrative nature of glioma.(23) Further, the assessment of infiltration by a pathology is a nonstandard, subjective assessment with a level of intrinsic bias and error.(30) In other words, there is a level of uncertainty in the validation of the assessment of tumor infiltration as TCP. Another approach is the use of image recognition algorithms for automated tumor annotation and percentage tumor nuclei measurements using digital pathology images. These methods have been found to have more accurate concordance than estimation by eye when

compared with manually counted tumor cells, specifically in the case of lung cancer.(31) Correlating TCP estimates made by DESI-MS with those made by automated image analyses may help eliminate some of the observed inter- and intra-observer variability and improve the diagnostic accuracy of the method. All said, we believe that the impact of these biases and error can minimized by choosing to target molecular features with validation methods that have objective, binary outputs (e.g., genotypes that are mutant/wild type) with known uncertainties.

5.4 Conclusions and Future Directions

The molecular characterization of tissue biopsies by ambient ionization, specifically DESI-MS, can provide valuable information on prognostic genotypes and tumor infiltration. In an ongoing clinical study with Mayo Clinic-Jacksonville, we have analyzed 295 glioma tissue biopsies from 37 patients by DESI-MS for the intraoperative assessment of IDH genotypes and TCP. The characterization of the IDH genotypes of gliomas, which was initiated midway through the study, is accomplished by the measurement of the concentration of 2HG relative to the endogenous internal standard Glu. To date, 116 biopsies from 22 patients have been analyzed. The clinical performance of the IDH mutation assay was excellent, with 93% sensitivity, 100% specificity, and 98% accuracy observed.

In addition to the assessment of IDH genotype, the DESI-MS system was also able to assess tumor infiltration at surgical margins by measurement of NAA and lipid abundances, although with lower diagnostic accuracy. The diagnostic performance of the methods for TCP (validated by comparison with estimations made by the review of the same tissue smears by a senior pathologist) was significantly lower than the previous clinical study (83%, 65%, and 72% sensitivity specificity, and accuracy from the measurement of NAA abundance and 77%, 57%, and 65% from the deconvolution of lipid profiles). Thus, we have elected to forgo further optimization of the method after the completion of the current clinical study. Patient recruitment is ongoing and the results interpreted herein are tentative in light of the incomplete dataset. Given the excellent diagnostic accuracy, we are particularly interested in taking actions leading to the acceptance of the DESI-MS measurement of IDH mutations on core biopsies as complementary diagnostic modality capable of assisting physicians and improving patient outcomes by providing prognostic molecular information that can inform diagnosis, prognosis, and treatment approaches.

5.5 Acknowledgements

This research is supported by the Innovative Molecular Analysis Technologies (IMAT) Program of the National Cancer Institute of the National Institutes of Health (R33CA240181-01A1) and Waters Corporation. Support from the Purdue University COVID-19 Research Disruption Fund is gratefully acknowledged. This work was performed in collaboration with a clinical team at Mayo Clinic – Jacksonville including neurosurgeons Dr. Kaisorn Chaichana and Dr. Alfredo Quiñones-Hinojosa, neuropathologist Dr. Mark Jentoft, neuroradiologist Dr. Erik Middlebrooks, and research fellow Dr. Diogo Garcia. We thank Rob Schneider for assistance in 3D-printing and Lucas Szalwinski for assistance with instrument modification and installation. Thanks to Aleeshba Basil for her efforts in patient consent and IRB monitoring.

5.6 References

1. Ogrinc N, Saudemont P, Takats Z, Salzet M, Fournier I. Cancer Surgery 2.0: Guidance by Real-Time Molecular Technologies. Trends Mol Med. 2021;27(6):602-15.

2. Louis DN, Perry A, Wesseling P, Brat DJ, Cree IA, Figarella-Branger D, et al. The 2021 WHO Classification of Tumors of the Central Nervous System: a summary. Neuro Oncol. 2021;23(8):1231-51.

3. Sengupta S, Marrinan J, Frishman C, Sampath P. Impact of temozolomide on immune response during malignant glioma chemotherapy. Clin Dev Immunol. 2012;2012:831090.

4. Mat Zin AA, Zulkarnain S. Diagnostic Accuracy of Cytology Smear and Frozen Section in Glioma. Asian Pac J Cancer Prev. 2019;20(2):321-5.

5. Zulkarnain S, Yunus N, Kandasamy R, Zun AB, Mat Zin AA. Evaluation Study of Intraoperative Cytology Smear and Frozen Section of Glioma. Asian Pac J Cancer Prev. 2020;21(10):3085-91.

6. Huse JT, Aldape KD. The evolving role of molecular markers in the diagnosis and management of diffuse glioma. Clin Cancer Res. 2014;20(22):5601-11.

7. Louis DN, Perry A, Reifenberger G, von Deimling A, Figarella-Branger D, Cavenee WK, et al. The 2016 World Health Organization Classification of Tumors of the Central Nervous System: a summary. Acta Neuropathol. 2016;131(6):803-20.

8. Nobusawa S, Watanabe T, Kleihues P, Ohgaki H. IDH1 mutations as molecular signature and predictive factor of secondary glioblastomas. Clin Cancer Res. 2009;15(19):6002-7.

9. Qi ST, Yu L, Lu YT, Ou YH, Li ZY, Wu LX, et al. IDH mutations occur frequently in Chinese glioma patients and predict longer survival but not response to concomitant chemoradiotherapy in anaplastic gliomas. Oncol Rep. 2011;26(6):1479-85.

10. Juratli TA, Kirsch M, Geiger K, Klink B, Leipnitz E, Pinzer T, et al. The prognostic value of IDH mutations and MGMT promoter status in secondary high-grade gliomas. J Neurooncol. 2012;110(3):325-33.

11. Sturm D, Witt H, Hovestadt V, Khuong-Quang DA, Jones DT, Konermann C, et al. Hotspot mutations in H3F3A and IDH1 define distinct epigenetic and biological subgroups of glioblastoma. Cancer Cell. 2012;22(4):425-37.

12. Sun H, Yin L, Li S, Han S, Song G, Liu N, et al. Prognostic significance of IDH mutation in adult low-grade gliomas: a meta-analysis. J Neurooncol. 2013;113(2):277-84.

13. Beiko J, Suki D, Hess KR, Fox BD, Cheung V, Cabral M, et al. IDH1 mutant malignant astrocytomas are more amenable to surgical resection and have a survival benefit associated with maximal surgical resection. Neuro Oncol. 2014;16(1):81-91.

14. Patel T, Bander ED, Venn RA, Powell T, Cederquist GY, Schaefer PM, et al. The Role of Extent of Resection in IDH1 Wild-Type or Mutant Low-Grade Gliomas. Neurosurgery. 2018;82(6):808-14.

15. Patel SH, Bansal AG, Young EB, Batchala PP, Patrie JT, Lopes MB, et al. Extent of Surgical Resection in Lower-Grade Gliomas: Differential Impact Based on Molecular Subtype. AJNR Am J Neuroradiol. 2019;40(7):1149-55.

16. Molenaar RJ, Maciejewski JP, Wilmink JW, van Noorden CJF. Wild-type and mutated IDH1/2 enzymes and therapy responses. Oncogene. 2018;37(15):1949-60.

17. Golub D, Iyengar N, Dogra S, Wong T, Bready D, Tang K, et al. Mutant Isocitrate Dehydrogenase Inhibitors as Targeted Cancer Therapeutics. Front Oncol. 2019;9:417.

18. Karpel-Massler G, Nguyen TTT, Shang E, Siegelin MD. Novel IDH1-Targeted Glioma Therapies. CNS Drugs. 2019;33(12):1155-66.

19. Pu F, Alfaro CM, Pirro V, Xie Z, Ouyang Z, Cooks RG. Rapid determination of isocitrate dehydrogenase mutation status of human gliomas by extraction nanoelectrospray using a miniature mass spectrometer. Anal Bioanal Chem. 2019;411(8):1503-8.

20. Brown HM, Pu F, Dey M, Miller J, Shah MV, Shapiro SA, et al. Intraoperative detection of isocitrate dehydrogenase mutations in human gliomas using a miniature mass spectrometer. Anal Bioanal Chem. 2019;411(30):7929-33.

21. Chaichana KL, Cabrera-Aldana EE, Jusue-Torres I, Wijesekera O, Olivi A, Rahman M, et al. When gross total resection of a glioblastoma is possible, how much resection should be achieved? World Neurosurg. 2014;82(1-2):e257-65.

22. Mampre D, Ehresman J, Pinilla-Monsalve G, Osorio MAG, Olivi A, Quinones-Hinojosa A, et al. Extending the resection beyond the contrast-enhancement for glioblastoma: feasibility, efficacy, and outcomes. Br J Neurosurg. 2018;32(5):528-35.

23. Hu LS, Hawkins-Daarud A, Wang L, Li J, Swanson KR. Imaging of intratumoral heterogeneity in high-grade glioma. Cancer Lett. 2020;477:97-106.

24. Takáts Z, Wiseman JM, Cooks RG. Ambient mass spectrometry using desorption electrospray ionization (DESI): instrumentation, mechanisms and applications in forensics, chemistry, and biology. J Mass Spectrom. 2005;40(10):1261-75.

25. Pirro V, Alfaro CM, Jarmusch AK, Hattab EM, Cohen-Gadol AA, Cooks RG. Intraoperative assessment of tumor margins during glioma resection by desorption electrospray ionization-mass spectrometry. Proc Natl Acad Sci U S A. 2017;114(26):6700-5.

26. Alfaro CM, Pirro V, Keating MF, Hattab EM, Cooks RG, Cohen-Gadol AA. Intraoperative assessment of isocitrate dehydrogenase mutation status in human gliomas using desorption electrospray ionization-mass spectrometry. J Neurosurg. 2019:1-8.

27. Brown HM, Alfaro CM, Pirro V, Dey M, Hattab EM, Cohen-Gadol AA, et al. Intraoperative Mass Spectrometry Platform for IDH Mutation Status Prediction, Glioma Diagnosis, and Estimation of Tumor Cell Infiltration. J Appl Lab Med. 2021;6(4):902-16.

28. Leather T, Jenkinson MD, Das K, Poptani H. Magnetic Resonance Spectroscopy for Detection of 2-Hydroxyglutarate as a Biomarker for IDH Mutation in Gliomas. Metabolites. 2017;7(2).

29. Chen R, Brown HM, Cooks RG. Metabolic profiles of human brain parenchyma and glioma for rapid tissue diagnosis by targeted desorption electrospray ionization mass spectrometry. Anal Bioanal Chem. 2021.

30. Smits AJ, Kummer JA, de Bruin PC, Bol M, van den Tweel JG, Seldenrijk KA, et al. The estimation of tumor cell percentage for molecular testing by pathologists is not accurate. Mod Pathol. 2014;27(2):168-74.

31. Hamilton PW, Wang Y, Boyd C, James JA, Loughrey MB, Hougton JP, et al. Automated tumor analysis for molecular profiling in lung cancer. Oncotarget. 2015;6(29):27938-52.

CHAPTER 6. FUTURE PERSPECTIVES ON THE APPLICATION OF AMBIENT IONIZATION MASS SPECTROMETRY FOR BRAIN CANCER DIAGNOSTICS

6.1 Conclusions and Perspectives

Since its first application for the analysis of tissue samples in 2005, ambient ionization MS has made significant progress and reshaped the landscape of POC molecular diagnostics.(1) The enthusiasm and acceptance of these methods by the clinical community emphasizes the value and promise these methods hold to positively impact patient outcomes. While the progress made is substantial, there are many areas where improvement is needed to realize the full potential of ambient ionization to POC applications.

As demonstrated in the assessment of tumor infiltration at tumor core and surgical margins in Chapters 2 and 6, there is still substantial work to be down in improving the agreement of DESI-MS predictions with those made by pathological review of the tissue. There are likely many sources of potential error. In offline experiments, we have identified additional metabolites and developed DESI-MS methods that could be added to existing intraoperative workflow to improve accuracy.(2) That said, there are additional sources of error that are outside the scope of the DESI-MS method. Due to the infiltrative nature of glioma, surgical margins are heterogenous in nature(3) and difficult to discern(4, 5). Additionally, the assessment of tumor infiltration is a nonstandard, subjective assessment with a level of bias and error inherent to the assessments.(6) Consequently, there is a level of uncertainty in the validation that is unavoidable. For that reason, we believe that the most successful clinical applications of ambient ionization MS will be those that provide assessments that can be evaluated in a binary nature (e.g., genotypes characterized as mutant/wild type) and that are confirmed by methods with known diagnostic errors. Image recognition algorithms for automated tumor annotation and percentage tumor nuclei measurements using digital pathology images, such as those developed by Hamilton et al., have been found to have more accurate concordance than estimation by eye when compared with manually counted tumor cells.(7) Validating the TCP estimates made by DESI-MS with these automated image analyses may help eliminate some of the high inter- and intra-observer variability and improve diagnostic accuracy.

The DESI-MS assay for IDH genotyping of gliomas described in Chapters 2, 3, and 5 is such an example and is well suited for point-of-care (POC) application. The ratiometric approach using an endogenous internal standard as reference, as opposed to the intensity of a single analyte, has proven an accurate and robust method, with similar diagnostic performance observed when analyzing the sample tissue biopsies using different instruments. The ability to provide information on highly prognostic molecular cancer features intraoperatively has the potential to significantly improve patient outcomes. The DESI-MS IDH assay is one such example. Additionally, as IDH-targeting personalized medicine drugs currently in FDA clinical trials are made available, the value of this intraoperative assessment is likely to increase. The translation of this method to a commercial triple quadrupole mass spectrometer that will allow for increased sensitivity of the measurement in preparation for a clinical trial is ongoing.

The finding and development of additional diagnostic methods that are capable of detecting other key molecular cancer markers used to diagnosis and inform treatments, such as 1p19q co-deletions in gliomas, could follow a similar approach to translation as that for the aforementioned DESI-MS assay for IDH genotyping. 1p19q codeletions are key factors in the diagnosis and prognosis of gliomas, although, similar to IDH genotyping, results are not available until days after surgery. Specifically, 1p19q codeletions define a distinct glioma entity and are characteristic of oligodendrogliomas.(8, 9) Further, almost all 1p19q co-deleted gliomas are IDH-mut.(9, 10) Thus, knowledge of 1p19q co-deletion can assist in distinguishing oligodendrogliomas that are IDH-mut and 1p19q co-deleted from tumors that are IDH-mut but follow an astrocytic lineage, a distinction which could assist in the personalization of patient treatment plans.(8) A recent study by Branzoli et al. found selective accumulation of the metabolite cystathione in 1p19q co-deleted gliomas.(11) A similar MS approach as that of the IDH assay could be used to measure cystathione in glioma tissue as a means of providing this unavailable information intraoperatively.

The role of miniature mass spectrometers in POC applications has gained much interest in the past few years due to their small size and affordability.(12) Numerous instrumentation companies are working on producing and improving new mini-MS systems that are smaller and easier to use, while also boasting higher resolutions and analytical sensitivity (i.e. lower limits of detection).(13) All of these advances support their continued translation into clinical applications. Dr. Ouyang's group continues to work to improve the robustness of these devices in preparation for clinical

translation.(14) A continued concern is whether the limit of detections and decrease sensitivity inherent to miniature instruments can satisfy analytical and clinical standards for clinical use.

The success of the high-throughput desorption electrospray ionization mass spectrometry (HT-DESI-MS) method for the molecular assessment of tissue microarrays (TMAs) described in Chapter 4 is also an exciting extension of the previous capabilities of the DESI-MS method to the molecular characterization of tissue.(15) The new method should be of particular interest to those in the molecular oncology, pathology, and pharmaceutical fields. Additionally, it enables the full utilization of the strengths of ambient ionization MS, specifically HT-DESI-MS, for the rapid generation of spectral libraries from tissue specimens. The technology can either be used in a discovery phase, enabling the rapid generation of molecular data for metabolomic and lipidomic studies, or in a screening phase, for specific biomarkers in a sample population. Of particular interest to the ongoing clinical study is the ability to screen metabolic and lipid profiles of tumor biopsies to identify biomarkers associated with clinical outcomes as indicators of disease progression and treatment response.

To date, our experience conducting DESI-MS analysis of tissue specimens has been confined to unmodified, snap frozen tissue biopsies. However, since the 19th century, the most widely used method of tissue fixation and preservation has been formalin-fixed, paraffin-embedded (FFPE) tissue preservation, where a tissue block is frozen in formaldehyde and embedded in paraffin wax. Given the prevalence of the method, a significant number of FFPE tissue sections are generated and stored in hospitals around the world, representing a very large sample bank. Very recently, new ambient ionization MS methods have enabled the detection of molecules from FFPE tissues, including matrix assisted laser desorption ionization mass spectrometry aided by the application of a copper adhesive tape attached to the reverse side of a glass slide.(16) When voltage is applied to the conductive tape, an electrical field drive is generated that drives molecules to the surface of the tissue section and allows for the detection of previously inaccessible proteins and peptides. The detection of metabolites and lipids by DESI-MS using a similar approach to apply an electric field to the glass slide and drive metabolites and lipids to the surface of the tissue section. If successful, this method would greatly expand the potential applications of the current DESI-MS system.

It is evident that the future of cancer diagnostics will be increasingly molecular. We believe the inherent strengths of ambient ionization mass spectrometry and improvements to the methodology that have allowed for its increased clinical translation make it well-suited to serve as

a complementary diagnostic modality capable of providing information on key molecular features of cancer that are unavailable intraoperatively using conventional methods, complementing and not interfering with standard of care protocols. I look forward to a future in which ambient ionization MS methods will play a significant role in the diagnosis and treatment of cancers.

6.2 References

1. Ferreira CR, Yannell KE, Jarmusch AK, Pirro V, Ouyang Z, Cooks RG. Ambient Ionization Mass Spectrometry for Point-of-Care Diagnostics and Other Clinical Measurements. Clin Chem. 2016;62(1):99-110.

2. Chen R, Brown HM, Cooks RG. Metabolic profiles of human brain parenchyma and glioma for rapid tissue diagnosis by targeted desorption electrospray ionization mass spectrometry. Anal Bioanal Chem. 2021.

3. Hu LS, Hawkins-Daarud A, Wang L, Li J, Swanson KR. Imaging of intratumoral heterogeneity in high-grade glioma. Cancer Lett. 2020;477:97-106.

4. Orringer D, Lau D, Khatri S, Zamora-Berridi GJ, Zhang K, Wu C, et al. Extent of resection in patients with glioblastoma: limiting factors, perception of resectability, and effect on survival. J Neurosurg. 2012;117(5):851-9.

5. Chaichana KL, Cabrera-Aldana EE, Jusue-Torres I, Wijesekera O, Olivi A, Rahman M, et al. When gross total resection of a glioblastoma is possible, how much resection should be achieved? World Neurosurg. 2014;82(1-2):e257-65.

6. Smits AJ, Kummer JA, de Bruin PC, Bol M, van den Tweel JG, Seldenrijk KA, et al. The estimation of tumor cell percentage for molecular testing by pathologists is not accurate. Mod Pathol. 2014;27(2):168-74.

7. Hamilton PW, Wang Y, Boyd C, James JA, Loughrey MB, Hougton JP, et al. Automated tumor analysis for molecular profiling in lung cancer. Oncotarget. 2015;6(29):27938-52.

8. Louis DN, Perry A, Wesseling P, Brat DJ, Cree IA, Figarella-Branger D, et al. The 2021 WHO Classification of Tumors of the Central Nervous System: a summary. Neuro Oncol. 2021;23(8):1231-51.

9. Cancer Genome Atlas Research N, Brat DJ, Verhaak RG, Aldape KD, Yung WK, Salama SR, et al. Comprehensive, Integrative Genomic Analysis of Diffuse Lower-Grade Gliomas. N Engl J Med. 2015;372(26):2481-98.

10. Sanson M, Marie Y, Paris S, Idbaih A, Laffaire J, Ducray F, et al. Isocitrate dehydrogenase 1 codon 132 mutation is an important prognostic biomarker in gliomas. J Clin Oncol. 2009;27(25):4150-4.

11. Branzoli F, Pontoizeau C, Tchara L, Di Stefano AL, Kamoun A, Deelchand DK, et al. Cystathionine as a marker for 1p/19q codeleted gliomas by in vivo magnetic resonance spectroscopy. Neuro Oncol. 2019;21(6):765-74.

12. Zhang W, Wang X, Xia Y, Ouyang Z. Ambient Ionization and Miniature Mass Spectrometry Systems for Disease Diagnosis and Therapeutic Monitoring. Theranostics. 2017;7(12):2968-81.

13. Snyder DT, Pulliam CJ, Ouyang Z, Cooks RG. Miniature and Fieldable Mass Spectrometers: Recent Advances. Anal Chem. 2016;88(1):2-29.

14. Jiao B, Ye H, Liu X, Bu J, Wu J, Zhang W, et al. Handheld Mass Spectrometer with Intelligent Adaptability for On-Site and Point-of-Care Analysis. Anal Chem. 2021;93(47):15607-16.

15. Morato NM, Cooks RG. Inter-platform assessment of performance of high-throughput desorption electrospray ionization mass spectrometry. Talanta Open. 2021;4.

16. Wu R, Qin L, Chen L, Ma R, Chen D, Liu H, et al. Copper adhesive tape attached to the reverse side of a non-conductive glass slide to achieve protein MALDI-imaging in FFPE-tissue sections. Chem Commun (Camb). 2021;57(82):10707-10.

VITA

Hannah Marie Brown was born in Baltimore, MD to Heidi Marie Wahlstrom Brown and Daniel Rufus Brown. She attended Dover-Eyota High School in Eyota, Minnesota, where she graduated as Valedictorian in 2013. When contemplating what she wanted to pursue as her vocation, she recalled a quote from one of her favorite childhood movies, *Robots*: "See a need, fill a need!" At the time, Hannah was interested in politics and saw a need for passionate policy makers that she intended to fill. In 2013, she was accepted to St. Olaf College in Northfield, MN to study political science. In her first year, she attended a course in forensic science as one of her science electives. It was during this course that she fell in love with chemistry and saw the many problems (i.e., needs) that chemistry could be used to address (i.e., fill). In her remaining three years, she studied chemistry in conjunction with political science, earning her B.A. with distinction in Chemistry and Political Science. Hannah participated in undergraduate research for two years under the advisement of Dr. Douglas Beussman. Her projects used isotope ratio mass spectrometry to characterize fibers of different compositions as well as to explore the effect of environmental factors, specifically blood, on these isotope ratios. In recognition of her work, she was awarded the 2017 Undergraduate Award in Analytical Chemistry by the American Chemical Society Division of Analytical Chemistry.

In 2017, Hannah was accepted to Purdue University in West Lafayette, Indiana to pursue a Ph.D. in Analytical Chemistry. Her research focused on the development, application, and translation of ambient ionization mass spectrometry (MS)-based platforms in clinical and surgical settings, specifically in the area of brain cancer diagnostics. While conducting this research, she was fortunate to collaborate with clinicians at Indiana University School of Medicine in Indianapolis, Indiana and Mayo Clinic – Jacksonville in Jacksonville, Florida and witness firsthand the impact chemistry, specifically mass spectrometry, can have on patient lives.

In July 2022, she will join the Department of Pathology and Immunology in the Division of Laboratory and Genomic Medicine at Washington University in St. Louis School of Medicine in St. Louis, Missouri as a Clinical Fellow in Clinical Chemistry. She is extremely excited to continue to fill the needs of clinicians and patients in the field of clinical chemistry and molecular pathology while conducting research to advance molecular diagnostics using mass spectrometry.

LIST OF PUBLICATIONS

1. Chen R, **Brown HM**, Cooks, RG. Metabolic Profiles of Human Brain Parenchyma and Glioma for Rapid Tissue Diagnosis by Desorption Electrospray Ionization Mass Spectrometry. Anal Bioanal Chem. 2021. DOI: 10.1007/s00216-021-03593-0.

2. **Brown HM**, Alfaro CM, Pirro V, Dey M, Hattab EM, Cohen-Gadol AA, et al. Intraoperative Mass Spectrometry Platform for IDH Mutation Status Prediction, Glioma Diagnosis, and Estimation of Tumor Cell Infiltration. J Appl Lab Med. 2021;6(4):902-16. DOI: 10.1093/jalm/jfaa233.

3. **Brown HM**, Pu F, Dey M, Miller J, Shah MV, Shapiro SA, et al. Intraoperative detection of isocitrate dehydrogenase mutations in human gliomas using a miniature mass spectrometer. Anal Bioanal Chem. 2019. DOI: 10.1007/s00216-019-02198-y.

4. **Brown HM**, Pirro V, Cooks RG. From DESI to the MasSpec Pen: Ambient Ionization Mass Spectrometry for Tissue Analysis and Intrasurgical Cancer Diagnosis. Clin Chem. 2018;64(4):628-30. DOI: 10.1373/clinchem.2017.281923.

Analytical and Bioanalytical Chemistry (2021) 413:6213–6224
https://doi.org/10.1007/s00216-021-03593-0

PAPER IN FOREFRONT

Metabolic profiles of human brain parenchyma and glioma for rapid tissue diagnosis by targeted desorption electrospray ionization mass spectrometry

Rong Chen[1] · Hannah Marie Brown[1] · R. Graham Cooks[1]

Received: 8 June 2021 / Revised: 23 July 2021 / Accepted: 30 July 2021 / Published online: 9 August 2021

Abstract
Desorption electrospray ionization mass spectrometry (DESI-MS) is well suited for intraoperative tissue analysis since it requires little sample preparation and offers rapid and sensitive molecular diagnostics. Currently, intraoperative assessment of the tumor cell percentage of glioma biopsies can be made by measuring a single metabolite, N-acetylaspartate (NAA). The inclusion of additional biomarkers will likely improve the accuracy when distinguishing brain parenchyma from glioma by DESI-MS. To explore this possibility, mass spectra were recorded for extracts from 32 unmodified human brain samples with known pathology. Statistical analysis of data obtained from full-scan and multiple reaction monitoring (MRM) profiles identified discriminatory metabolites, namely gamma-aminobutyric acid (GABA), creatine, glutamic acid, carnitine, and hexane-1,2,3,4,5,6-hexol (abbreviated as hexol), as well as the established biomarker NAA. Brain parenchyma was readily differentiated from glioma based on these metabolites as measured both in full-scan mass spectra and by the intensities of their characteristic MRM transitions. New DESI-MS methods (5 min acquisition using full scans and MS/MS), developed to measure ion abundance ratios among these metabolites, were tested using smears of 29 brain samples. Ion abundance ratios based on signals for GABA, creatine, carnitine, and hexol all had sensitivities > 90%, specificities > 80%, and accuracies > 85%. Prospectively, the implementation of diagnostic ion abundance ratios should strengthen the discriminatory power of individual biomarkers and enhance method robustness against signal fluctuations, resulting in an improved DESI-MS method of glioma diagnosis.

Keywords Metabolomics · Biomarker · Glioma · Ambient ionization · Multiple reaction monitoring · Tandem mass spectrometry

Introduction

Glioma is the most common intracranial tumor and it accounts for more than 50% of all primary brain tumors [1]. Gross total tumor resection is considered to be the most effective treatment for glioma patients, despite not often being achieved clinically [2]. Glioma cells are diffusely infiltrative and often result in residual tumor at surgical margins that may lead to disease progression and tumor reoccurrence. Currently, neurosurgeries are guided by magnetic resonance imaging (MRI), which is not sufficiently sensitive to gauge the infiltration of glioma, especially in regions with low tumor cell density [3]. Moreover, spatial registration between a patient's brain and the preoperative MR images may be compromised as brain shift is common during craniotomies [4]. Consequently, intraoperative tissue diagnosis increasingly relies on molecular features assessed from tumor biopsies [5] to locate the tumor boundary with a higher sensitivity and to provide additional pathological information, like tumor grade and genetic mutation [6]. Ultimately, this should allow surgeons to maximize tumor resection and personalize adjunctive therapies.

Several molecular diagnostic techniques have been applied clinically, including magnetic resonance spectroscopy (MRS) and fluorescence imaging [7]. MRS is conducted preoperatively to assess tumor type and aggressiveness, but it is not well suited for intrasurgical tissue analysis. 5-Aminolevulinic acid–induced fluorescence guidance has been used as a surgical guide to improve glioma resection by identifying tumor location [8] although it has limited value in accurate tissue diagnosis [9]. Techniques that rapidly and quantitatively interrogate molecular features of tissue are currently being

✉ R. Graham Cooks
cooks@purdue.edu

[1] Department of Chemistry, Purdue University, 560 Oval Drive, West Lafayette, IN 47907-2084, USA

developed. One such technique, Raman spectroscopy, is capable of providing label-free and molecular-specific information of tissue [10]. Raman spectroscopy can be conducted either in vivo, with a handheld Raman probe placed directly on the tissue surface for data acquisition [3], or ex vivo to analyze brain biopsies with little sample preparation, automatic data acquisition and analysis, and near-immediate feedback [11]. Additionally, ambient ionization mass spectrometry (MS) has been identified as a potential method for intraoperative tissue diagnosis [5, 12], given its capability of sensitive and rapid metabolite characterization. MS-based techniques use various approaches of rapid and simple tissue sampling. For example, the MasSpec Pen relies on water extraction to sample analytes from tissue non-destructively [13, 14], picosecond infrared laser mass spectrometry (PIRL-MS) utilizes laser ablation to vaporize molecules from the irradiated tissue [15, 16], SpiderMass uses water as an endogenous matrix to assist in laser desorption of analytes in tissue [17], and rapid evaporative ionization mass spectrometry (REIMS) analyzes electrosurgical vapors [18]. The molecular information offered by MS is typically characterized using relative ion signals of analytes, without attempting to convert ion abundances into their concentrations in tissue.

Desorption electrospray ionization mass spectrometry (DESI-MS), the technique utilized in this work, uses charged solvent droplets to rapidly extract analytes, including metabolites, from the tissue surface [19]. The metabolic profile recorded by MS allows differentiation between cancerous tissue and normal tissue [20, 21] and identification of tumor grade and subtype [22]. While still an experimental modality, DESI-MS has been used to distinguish between cancerous and normal tissue in a variety of human cancers including pancreatic [23], breast [24], brain [25–27], ovarian [21, 28], and gastric cancers [29]. To facilitate its potential intraoperative application, morphologically friendly spray solvents have been used so that the same specimen can be subjected to histopathologic analysis following MS measurement [30]. Intraoperatively, fresh tissue smears are used for DESI-MS analysis, which simplifies sample preparation and facilitates the formation of a homogeneous layer of tissue so that rapid profiling can capture its overall chemical features [31].

Metabolic (and lipidic) fingerprints, which are unique to different tissue types, are the fundamental basis of all the diagnostic methods mentioned above. The altered cellular metabolism of tumors [32–34] has been explored both by in vivo methods, including metabolic imaging (e.g., MRS) and isotope-labeled metabolite tracing (using ^{13}C-labeled analogs) [35], as well as by ex vivo methods including MS and nuclear magnetic resonance spectroscopy [36]. Several metabolites involved in various biosynthetic pathways have been reported to differentiate glioma and other cancer cells from normal cells. For example, D-2-hydroxyglutarate (D-2HG) is a well-established biomarker for isocitrate dehydrogenase (IDH) mutations [35, 37], since the mutated IDH exclusively converts α-ketoglutarate to D-2HG. Increased lactic acid production has been reported for several cancer types, including glioma [38, 39], kidney [40], prostate [41], and ovarian cancer [14], because cancerous cells generally require anaerobic glycolysis to sustain energy production in hypoxia [42]. NAA is synthesized in neuronal mitochondria and hydrolyzed to supply acetate for acetyl coenzyme A (CoA) synthesis [43, 44]. Its decreased level in glioma [25] may be explained by a lower neuron density [42] or accelerated utilization of CoA for increased gene transcription and energy metabolism in glioma cells [35, 44]. Glutamate is the most abundant neurotransmitter, and its extracellular concentration is maintained at low levels by excitatory amino acid transporters (EAAT) to prevent excitotoxicity [45]. However, glioma cells lose the ability to absorb glutamate since EAAT is under-expressed, causing a local downregulation of glutamate [45]. Creatine is involved in the creatine/creatine kinase (CK)/phosphocreatine system for adenosine triphosphate (ATP) regeneration [46, 47]. Several studies have reported lower creatine concentrations in malignant glioma [47–49] and oral [50] and bladder cancer [51], possibly due to adapted ATP production and increased phosphocreatine consumption for tumor bioenergetics [47, 52]. Gamma-aminobutyric acid (GABA) signaling has been reported to lead to membrane depolarization and to result in cell growth attenuation [53]. Fast-growing glioma tumors downregulate the GABA signaling pathway, causing the depletion of GABA [53]. Carnitine facilitates the transport of fatty acids into mitochondria for energy metabolism [54]; therefore, its increased level offers an additional energy source to promote tumor progression [55]. Mannitol, widely used to control brain edema in patients by creating an osmotic gradient across the blood-brain barrier (BBB) [56], is upregulated in glioma due to the tumor's defective BBB. Our DESI-MS method for intraoperative assessment of glioma [26, 27, 37] presently uses the measurement of a single oncometabolite, NAA, for estimating tumor cell percentage (TCP) and another, 2HG, for assessing IDH mutation status. The inclusion of additional glioma biomarkers is worth investigation as it has the potential to improve differentiation of brain parenchyma from glioma and so increase diagnostic accuracy.

Here, we report a study which used rapid, comprehensive metabolic profiling to discover diagnostic metabolites capable of distinguishing normal human brain and glioma tissue. First, mass spectra of extracts from 32 human brain samples were recorded using nanoESI (nESI) for biomarker discovery. To mine more metabolic information, multiple reaction monitoring (MRM) profiling, which offers a higher sensitivity and specificity [57], was applied. The diagnostic metabolites uncovered—GABA, creatine, glutamic acid, carnitine, and hexane-1,2,3,4,5,6-hexol (abbreviated as hexol)—were integrated into a new DESI-MS method and used to analyze 29 brain smears, mimicking the intraoperative workflow. In parallel,

ion abundance ratios of these diagnostic metabolites were tested for their discriminatory power using known pathologic information. Their prediction sensitivity (> 90%), specificity (> 80%), and accuracy (> 85%) show promise for improving the current DESI-MS method for intraoperative glioma diagnosis.

Materials and methods

Specimens

A set of 32 frozen and unmodified human brain tissue was purchased by Purdue University from the Biorepository of Methodist Research Institute. Extracts were prepared from these specimens by keeping the aqueous phase of the Bligh and Dyer extraction [58]. Separately, 29 specimens from this tissue collection were smeared on glass microscope slides for DESI-MS analysis using the new multi-metabolite method (illustrated in Supplementary information Fig. S1).

Pathology

Pathologic evaluations of specimens in the tissue collection were made in our previous work and are summarized in Supplementary information Table S1 [25]. Cryo-sectioned tissue was mounted onto glass slides and hematoxylin and eosin (H&E) stained following the standard protocol. The stained slides were blindly evaluated by an expert pathologist to provide pathological information including tissue type (i.e., brain or subtypes of glioma), tumor grade, and estimated TCP.

MS analysis

MS analysis of brain extracts was performed using a triple quadrupole mass spectrometer (TSQ Quantum Access MAX, Thermo Fisher Scientific) by nESI. The orifice of glass tips was optimized at 8 μm and the spray voltage was optimized at 1.4 kV for a stable spray. In full-scan MS profiling, the mass range was set at m/z 50–350 and three replicas were acquired for one sample in both ion modes. In the discovery phase of MRM profiling, precursor and neutral loss scans from the scan library (summarized in Supplementary information Table S2) were applied to the pooled healthy brain and glioma extracts to discover informative transitions with abundant and stable signals. In the subsequent screening phase, individual brain extracts were interrogated for these selected transitions in both ion polarities. To identify diagnostic molecules, their exact masses were measured using a high-resolution mass spectrometer (Q Exactive Orbitrap, Thermo Fisher Scientific) and product ion scans were acquired using the TSQ. DESI-MS analysis of brain smears was performed with a linear ion-trap mass spectrometer (Finnigan LTQ, Thermo Fisher Scientific). Methanol was used as the spray solvent with a flow rate of 3 μL/min, nitrogen was the nebulizing gas at a pressure of 150 psi, and the spray voltage was 5 kV. The position of the DESI sprayer was optimized at a sprayer-to-surface distance of 2 mm, a sprayer-to-inlet distance of 4 mm, and a spray impact angle of 54°. To support rapid tissue analysis, brain smears were rastered under the DESI spray to capture average data from various locations on the tissue surface. The developed multiple-metabolite DESI method for positive-ion mode was composed of five segments: full scan over the range of m/z 50–350, MS/MS of m/z 104, MS/MS of m/z 132, MS/MS of m/z 162, and MS/MS of m/z 170. Each segment took 1 min, making the overall analysis time of a smear approximately 5 min. The negative-ion DESI method shared a similar configuration, covering five segments: a scan over the range of m/z 50–350, MS/MS of m/z 146, MS/MS of m/z 174, MS/MS of m/z 217, and MS/MS of m/z 271. Note that all data discussed in this study was recorded explicitly for this purpose; no data was re-purposed.

Statistical analysis

In both profiling methods, the raw MS data was normalized, filtered, and averaged before principal component analysis (PCA) to show the separation between the two tissue types. The optimal separating hyperplane in the score plot was determined by the method of soft-margin support vector machine. The support vectors were identified using the MATLAB function "fitcsvm" to maximize the soft margin between the separating hyperplane and data points. The most discriminatory spectral features were discovered by t tests based on their p values. For ion abundance ratios in DESI-MS, discriminatory cutoffs were optimized for maximum area-under-curve (AUC) in the receiver operating characteristic (ROC) curves. Sensitivity, specificity, and accuracy at the optimal cutoff were calculated to assess diagnostic performances of these ion abundance ratios.

Results and discussion

Spectral features discovered by full-scan MS profiling

As a straightforward and efficient method of discovering biomarkers, full-scan mass spectra were acquired using nESI for all brain extracts in the two groups established by pathology as healthy or glioma. After normalization and filtering (see Supplementary information section entitled "Experimental Details"), PCA was applied to the mass spectral data. In the PCA score plot based on positive-mode spectra (Fig. 1b), the points representing 14 glioma samples separate well from those representing the 18 healthy samples. The observation of two misclassified samples may be because the assumed glioma tissue is likely to contain significant healthy tissue and therefore have mixed morphology. Spectral features

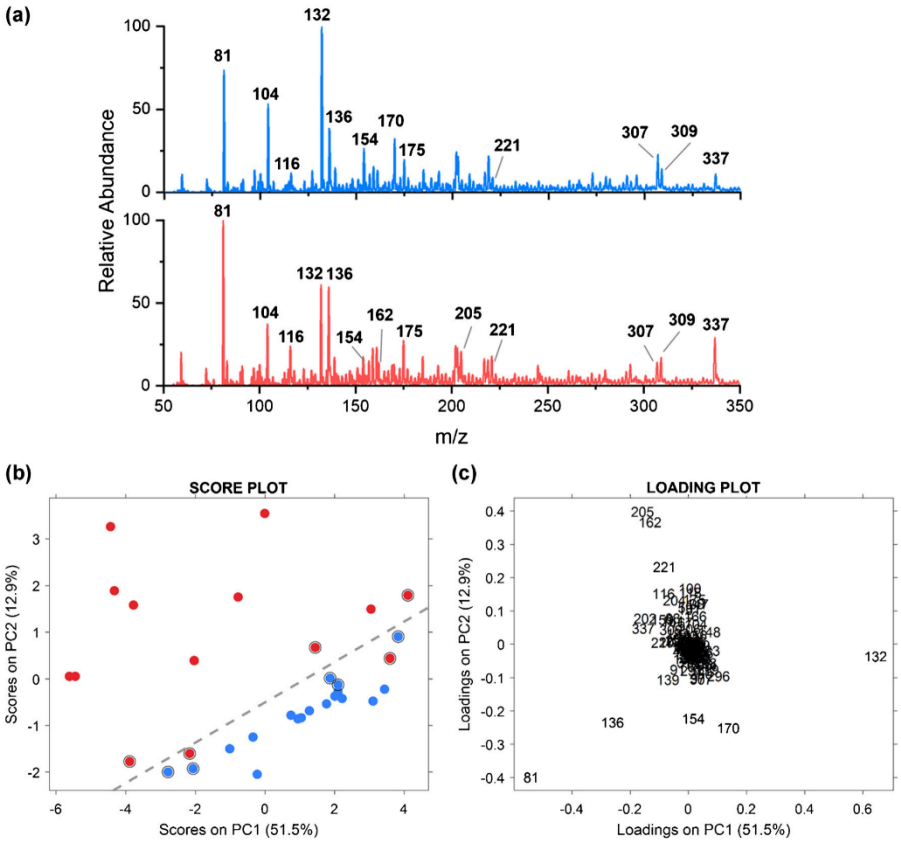

Fig. 1 Full-scan profiling of brain extracts in the positive-ion mode. **a** Representative mass spectra of healthy brain (blue) and glioma extracts (red) recorded by nESI. **b** PCA score plot of the 18 healthy and 14 glioma brain extracts using abundant positive-mode spectral features. The separating hyperplane (gray dotted line) was optimized by the soft-margin support vector machine using the circled data as support vectors. **c** PCA loading plot showing spectral features which contribute most to the separation

contributing to the separation are shown in the loading plot (Fig. 1c), where metabolites indicated by *m/z* 132, 154, and 170 are characteristic of healthy brain tissue. As expected, signal intensities of these metabolites are lower in glioma samples, as shown in the representative full-scan spectra (Fig. 1a) and in their box plots (Supplementary information Fig. S2a). Conversely, metabolites indicated by *m/z* 162, 205, and 211 are characteristic of glioma tissue and exhibit higher signal intensities in glioma samples (Fig. 1a and Supplementary information Fig. S2b). Based on their measured exact masses and fragmentation patterns in tandem MS (MS/MS) spectra, the spectral features most representative of healthy tissue were identified as protonated creatine (*m/z* 132), its sodium adduct (*m/z* 154), and its potassium adduct (*m/z* 170), while the most characteristic features for glioma tissue are protonated carnitine (*m/z* 162), the potassium adduct of hexol (*m/z* 221), and an unknown compound (*m/z* 205). A complete list of the 20 most discriminatory features in the positive-ion mode, as well as their identities, is summarized in Supplementary information Table S3.

After applying PCA to mass spectral profiles acquired in the negative-ion mode, similar separation between the two groups was observed in the score plot (Fig. 2b). The loading plot (Fig. 2c) revealed that healthy brain samples are primarily differentiated by *m/z* 146 and 174, while glioma samples are differentiated by *m/z* 147, 181, 217, 219, and 271. Signal variations of these features can be visualized in the representative mass spectra (Fig. 2a) and their box plots (Supplementary information Fig. S3). After structural identification by exact mass measurement and MS/MS, these discriminatory features were identified as glutamate (*m/z* 146), 2HG (*m/z* 147), NAA (*m/z* 174), deprotonated hexol ($[M-H]^-$, *m/z* 181), its chloride adducts

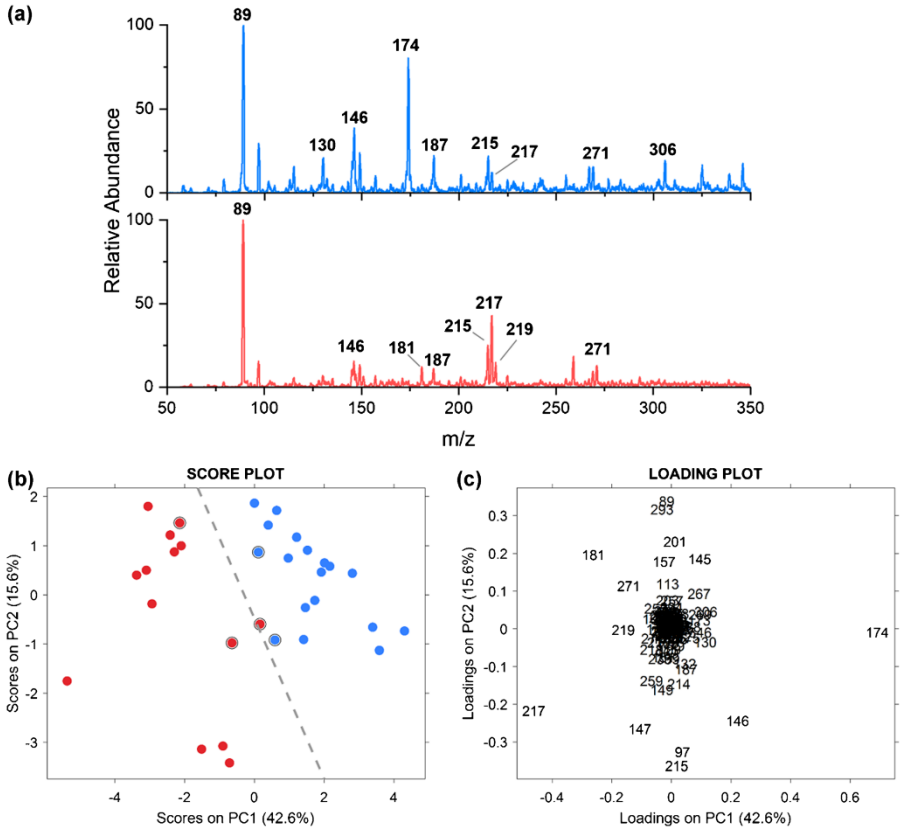

Fig. 2 Full-scan profiling of brain extracts in the negative-ion mode. **a** Representative mass spectra of healthy brain (blue) and glioma extracts (red) recorded by nESI. **b** PCA score plot of the 18 healthy and 14 glioma brain extracts using abundant negative-mode spectral features. The separating hyperplane (gray dotted line) was optimized by the soft-margin support vector machine using circled data as support vectors. **c** PCA loading plot showing significant spectral features which contribute to the separation

($[M{\cdot}^{35}Cl]^-$, *m/z* 217; $[M{\cdot}^{37}Cl]^-$, *m/z* 219), and the lactate adduct ($[M{\cdot}C_3H_5O_3]^-$, *m/z* 271). Considering that all stereoisomers in the family of hexols (e.g., mannitol and sorbitol) share the same exact masses and fragmentation pathways, a more specific identification was not possible in this case. The observed down-regulation of NAA and upregulation of 2HG in glioma samples are consistent with previous reports [25, 37] and confirm the feasibility of the current DESI-MS method for glioma tissue diagnosis [26, 27, 37]. A complete list of the 20 most discriminatory features in the negative-ion mode is provided in Supplementary information Table S4.

Fragmentation features discovered by MRM profiling

Brain extract is a complex biosample with high concentrations of salts, whose interference can attenuate MS signals. The increased specificity of tandem MS was exploited by applying MRM profiling to identify additional diagnostic metabolites not seen in the full-scan spectra. MRM profiling is a two-stage exploratory technique to perform rapid metabolomics and lipidomics based on chemical functionalities of small molecules [57]. First, in the discovery stage, precursor and neutral loss (NL) scans targeting common functional groups were applied to representative samples to discover informative precursor-product transitions (viz. MRMs). The library of precursor and NL scans used in this study can be found in Supplementary information Table S2. In total, 953 transitions (573 in the positive-ion mode and 380 in the negative-ion mode) passed the thresholds set for signal intensity and stability. Second, in the screening phase, abundances of all informative transitions were recorded for each of the 32 tissue extracts and statistical analysis was performed to identify the most discriminatory transitions.

After applying PCA to data for the informative transitions in both polarities, the resulting score plots (Fig. 3a, b) displayed good separations between the two groups. A few misclassified samples were also observed; they were determined by pathology to have low to medium tumor density, which explains the similarities of their profiles to healthy tissue. Transitions with the highest discriminatory power (lowest p values) were identified by t tests and summarized in Supplementary information Tables S5 and S6. In the positive-ion mode, the 20 most diagnostic transitions include those associated with GABA, creatine (protonated and potassium adduct), glutamic acid, homocarnosine, and inosine. The box plots shown in Fig. 3c exhibit the good discriminatory power of GABA, glutamic acid, and creatine. The discovery of diagnostic transitions not only will benefit targeted analysis using benchtop mass spectrometers, but should also promote point-of-care analysis using portable instruments where low-resolution and noisy full-scan spectra are common [59]. Comparing results of the two profiling methods, a few metabolites such as creatine and inosine were identified by both.

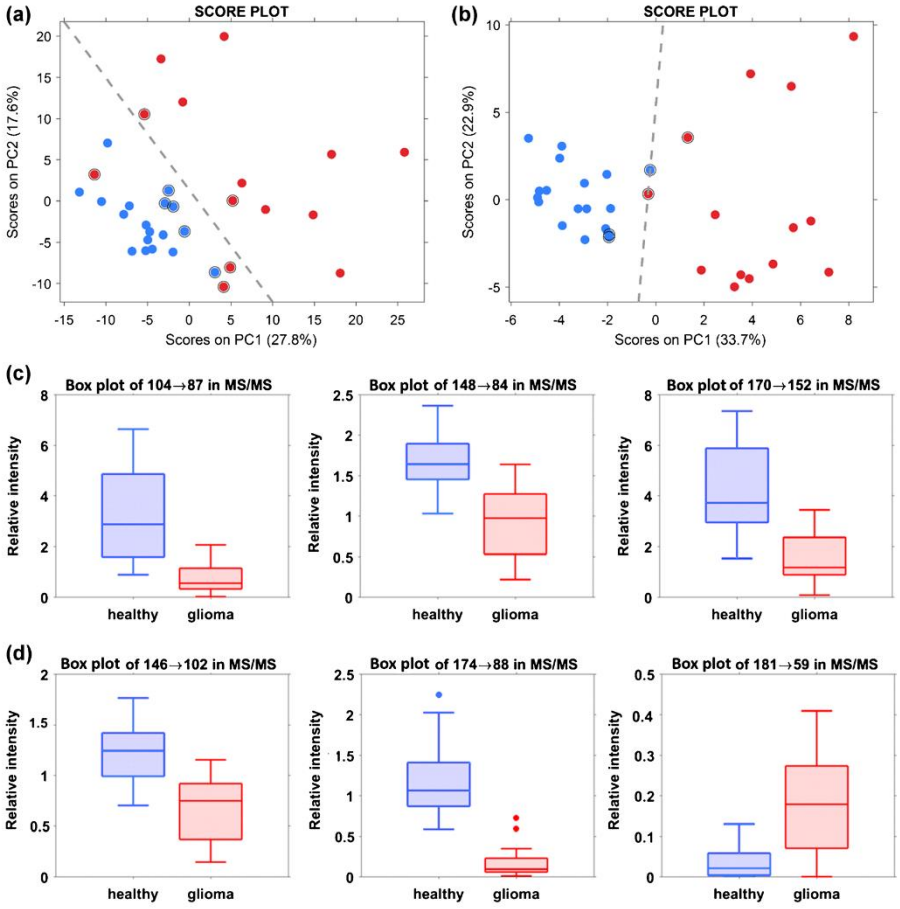

Fig. 3 **a** PCA score plot using informative transitions in the positive-ion mode where blue points represent healthy extracts and red points represent glioma extracts. The separating hyperplane (gray dotted line) was optimized by the soft-margin support vector machine using the circled data as support vectors. **b** PCA score plot using informative transitions in the negative-ion mode. **c** Box plots of transitions associated with diagnostic metabolites in the positive-ion mode, including GABA (104 → 87), glutamic acid (148 → 84), and creatine (potassium adduct: 170 → 152). The y-axis of box plots refers to transition intensities normalized to that of the internal standard transition (glutamic acid-d_3: 151 → 133). The box represents the interquartile range with a median line, and the maximal length of whiskers is 1.5 times the interquartile range. **d** Box plots of transitions associated with diagnostic metabolites in the negative-ion mode, including glutamate (146 → 102), NAA (174 → 88), and deprotonated hexol (181 → 59). The internal standard transition in negative polarity was glutamate-d_3: 149 → 105

MRM profiling expanded the number of diagnostic metabolites to include GABA, whose full-scan spectral intensity was not reliable given the presence of an isobaric ion namely choline. In the negative-ion mode, the 20 most diagnostic transitions included those associated with glutamate, NAA, hexol, inosine, and N-acetylaspartylglutamate, which are consistent with the full-scan profiling results. Box plots of the characteristic transitions of glutamate, NAA, and deprotonated hexol demonstrated good separation between the glioma and healthy groups (Fig. 3d).

The integration of data from full-scan profiling and MRM profiling represents a comprehensive screening of potential glioma biomarkers. Full-scan profiling is easier to conduct and has a relatively impartial coverage of molecules that ionize well. Conversely, MRM profiling relies on the scan library to target common functional groups, potentially biasing against molecules with unusual structures or those that ionize to form adducts. That said, MRM profiling can facilitate more sensitive and specific measurements, benefiting from its operation in the MS/MS mode. This also makes MRM profiling less vulnerable to matrix effects and better able to distinguish isobaric ions. Taken together, full-scan and MRM profiling unveiled several diagnostic metabolites, including GABA, creatine, glutamic acid, carnitine, hexol, inosine, and N-acetylaspartylglutamate, in addition to the established 2HG and NAA. Given that the extraction occurring during DESI-MS is nearly instantaneous and presumably less efficient than Bligh and Dyer extraction, only the most abundant features observed in brain extracts could be interrogated further by DESI-MS. These are GABA, creatine (protonated and potassium adduct), and carnitine in the positive-ion mode, and glutamate, NAA, and hexol (deprotonated and chloride/lactate adducts) in the negative-ion mode.

Translation to DESI-MS analysis

The discriminatory power of the metabolites selected in the previous section was further tested using smeared brain tissue to mimic a multi-metabolite-based extension of intraoperative DESI-MS analysis [26, 27, 37]. Methanol was selected as the spray solvent of DESI due to its morphologically friendly nature and the ability to provide rich metabolic information with minimal background noise. More detailed information on the DESI instrumentation and optimized parameters is included in the "Experimental Details" section of the Supplementary information. Supplementary information Fig. S1 is a schematic illustration of rapid DESI-MS analysis, showing the smearing of brain tissue (ca. 30 s operation time) and rastering of smears under the DESI spray (5 min data-acquisition time). Unlike DESI-MS imaging, this experiment records the average chemical features of the entire sample rather than being used to provide spatially resolved information.

DESI-MS is a semi-quantitative technique unless internal standards are used [60]. In order to deploy the diagnostic power of identified markers in DESI-MS without the use of an internal standard, we used ion abundance ratios, rather than absolute peak intensities, to enhance the method's robustness against signal fluctuations or background noise. Additionally, by using abundance ratios, the discriminating power can be strengthened when the numerator and denominator of the ratio show opposite variations. For example, in the positive-ion mode (Figs. 1 and 3), carnitine is upregulated in glioma samples while creatine is downregulated, making the ratio between neighboring peaks of m/z 162 (protonated carnitine) and m/z 170 (potassium adduct of creatine) highly diagnostic of the tissue disease state. This was experimentally confirmed by the representative DESI-MS spectra recorded in the positive mode (Fig. 4a) and by the box plot of this ratio (Fig. 4c). Further, the peak at m/z 175, identified as protonated arginine, displayed weak if any discrimination based on its intensity in the full-scan mass spectra (Supplementary information Fig. S4a) or its MRM transitions (Supplementary information Fig. S4b). Therefore, arginine can be treated as an endogenous internal standard for creatine, causing the signal ratio m/z 170:175 to decrease in glioma samples. Protonated GABA has an isobaric ion, choline, whose presence makes the full-scan intensity data unreliable. However, the isobars give different fragment ions in the MS/MS mode. The transition associated with choline shows a relatively constant level (Supplementary information Fig. S4c), making it an endogenous standard for GABA. In other words, when fragmenting the peak of m/z 104 (Fig. 4b), choline (MS/MS: $104 \rightarrow 60$) and protonated GABA (MS/MS: $104 \rightarrow 87$) each produce their respective fragments simultaneously making the fragment ratio m/z 87:60 diagnostic. Figure 4c–e show box plots of these three ion abundance ratios with good separation between the two tissue types. The marked cutoff in the plots was optimized for a maximum area under the curve (AUC) in the receiver operating characteristic (ROC) curve. Based on the optimal cutoff, values for sensitivity, specificity, and accuracy were calculated. The three ion abundance ratios all display sensitivities > 90%, specificities > 80%, and accuracies > 85%. Wilcoxon rank-sum tests were also applied for these ratios; all ratios display p values < 0.001. Based on these statistical results (summarized in Supplementary information Table S7), the three ion abundance ratios are sufficiently powerful to discriminate between the healthy and glioma samples. Note that two are determined from the single-stage MS while the third is an MS/MS measurement.

In the negative-ion mode, the ratio between downregulated NAA and upregulated hexol in glioma tissue was investigated. Representative full-scan spectra (Fig. 5a) show that hexol is detected by DESI-MS primarily as its chloride adducts ($[M\cdot^{35}Cl]^-$, m/z 217; $[M\cdot^{37}Cl]^-$, m/z 219) and its lactate adduct ($[M\cdot C_3H_5O_3]^-$, m/z 271), rather than as the deprotonated

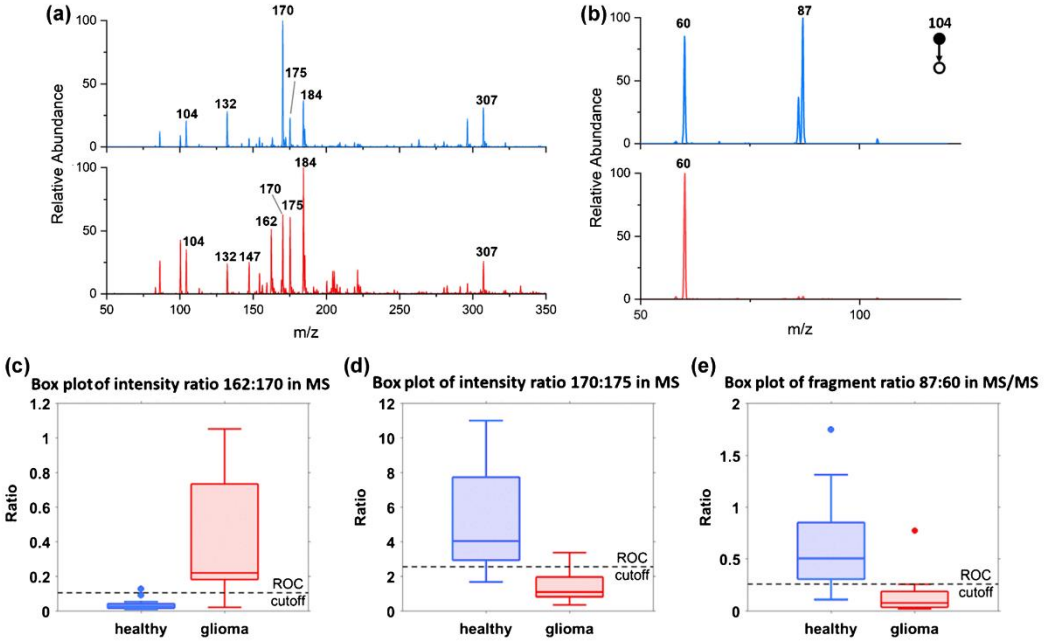

Fig. 4 **a** Positive-mode DESI-MS mass spectra for a representative healthy (blue) and glioma (red) tissue smear. **b** Product ion scans of *m/z* 104 for a representative healthy and glioma tissue smear. The choline-associated transition (104 → 60) is used as the endogenous standard for the GABA-associated transition (104 → 87). **c** Box plot using MS abundance ratio *m/z* 162:170 as a discriminator: *m/z* 162 indicates protonated carnitine and *m/z* 170 indicates creatine K^+. The ROC cutoff was optimized at 0.11, with a sensitivity, specificity, and accuracy of 92, 94, and 93%, respectively. Wilcoxon rank-sum test indicated a statistically significant variation between the two groups (p value < 0.001). **d** Box plot using MS abundance ratio *m/z* 170:175 as a discriminator: *m/z* 170 indicates creatine K^+ and *m/z* 175 indicates protonated arginine. The ROC cutoff was optimized at 2.56, with a sensitivity, specificity, and accuracy of 92, 81, and 86%, respectively. Wilcoxon rank-sum test indicated a statistically significant result (p value < 0.001). **e** Box plot using the fragment ion ratio *m/z* 87:60 as a discriminator, comparing the GABA-associated transition to that of choline. The ROC cutoff was optimized at 0.26, with a sensitivity, specificity, and accuracy of 92, 88, and 90%, respectively. Wilcoxon rank-sum test indicated a statistically significant result (p value < 0.001)

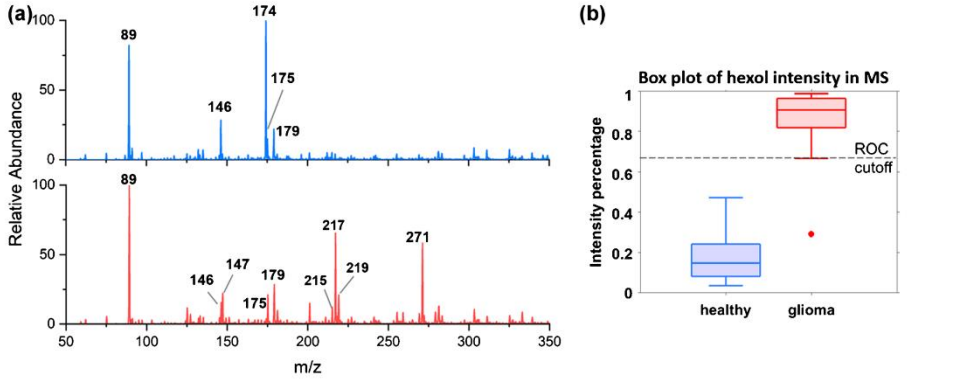

Fig. 5 **a** Negative-mode DESI-MS mass spectra for a representative healthy (blue) and glioma (red) tissue smear. **b** Box plot using the intensity percentage of hexol (as defined in Eq. 1) as a discriminator. The ROC cutoff was optimized at 0.67, with a sensitivity, specificity, and accuracy of 92, 100, and 97%, respectively. Wilcoxon rank-sum test indicated a statistically significant result (p value < 0.001)

molecule ($[M-H]^-$, m/z 181). To better characterize the abundance ratio between all hexol-related species and NAA, the intensity percentage of hexol is used. (1)

$$\%\text{Intensity}_{\text{hexol}} = \frac{I_{\text{total hexol}}}{I_{\text{NAA}} + I_{\text{total hexol}}} \quad (1)$$

$$= \frac{I_{181} + I_{217} + I_{219} + I_{271}}{(I_{174}) + (I_{181} + I_{217} + I_{219} + I_{271})} * 100\%$$

Figure 5b shows the box plot of this intensity percentage with good separation between the two tissue types. Similarly, the optimal cutoff was determined based on ROC, yielding a sensitivity, specificity, and accuracy of 92, 100, and 97%, respectively. Wilcoxon rank-sum test showed that hexol-related species were significantly upregulated in glioma samples (p value < 0.001). NAA intensities were also calculated to allow comparison with the performance of the current intraoperative DESI method. Illustrated in Supplementary information Fig. S5, NAA alone is powerful enough to distinguish glioma from normal tissue with sensitivity, specificity, and accuracy values of 100, 88, and 93%. The improved diagnostic accuracy obtained by characterizing hexol intensity percentage (96%), compared to NAA measurement (93%), suggests that the inclusion of an inversely related metabolite can increase diagnostic power over that for a single biomarker. While the three diagnostic ratios in the positive-ion mode have comparable accuracies to the existing NAA measurement (93, 86, 90%, respectively), their inclusion in the new method offers multiple diagnosis channels to ensure a robust prediction. This expectation remains to be tested on a large number of samples and in an intraoperative setting where a wider range of tissue types is likely to be encountered.

Conclusions

The inclusion of additional biomarkers in a DESI-MS method will likely improve the diagnostic accuracy and method robustness of distinguishing brain parenchyma from glioma. In this study, metabolic biomarkers of healthy brain tissue and glioma have been discovered by both full-scan MS profiling and MRM profiling using nESI. The most diagnostic and abundant are GABA, creatine, glutamic acid, carnitine, and hexol. Good separation between the two tissue types has been observed in PCA score plots and box plots. With the goal of using these metabolites for rapid tissue diagnosis, new DESI-MS methods (taking 5 min) have been developed and tested using brain smears. Several diagnostic ion abundance ratios, generated both from intact ions in full-scan mass spectra and from fragment ions in MS/MS spectra, have been identified. The positive-mode abundance ratios (full-scan MS and MS/MS) related to GABA, carnitine, and creatine all display > 90% sensitivities, > 80% specificities, and > 85% accuracies for tissue diagnosis at their optimized ROC cutoffs. Further, the negative-mode abundance ratio of hexol shows good discrimination, with a sensitivity, specificity, and accuracy of 92, 100, and 97%, respectively. We envision that integrating these discriminatory metabolites into the current intraoperative DESI-MS methodology will provide a more sensitive detection of glioma near infiltrative margins and ultimately assist the achievement of gross total tumor resection during surgeries.

Supplementary Information The online version contains supplementary material available at https://doi.org/10.1007/s00216-021-03593-0.

Acknowledgements The authors thank Dr. Eyas M. Hattab for providing evaluation of brain samples used in this and previous work. We thank Clint M. Alfaro for his assistance in writing custom MATLAB codes for data processing and Christina R. Ferreira for providing the scan library used in multiple reaction monitoring (MRM) profiling.

Code availability The custom MATLAB codes used for data processing are available from the corresponding author upon request.

Author contribution R. Chen and R.G. Cooks designed the research; R. Chen performed the research; R. Chen and H.M. Brown analyzed the data; R. Chen, H.M. Brown, and R.G. Cooks wrote the paper.

Funding This work was funded by National Cancer Institute (IR33CA240181-01A1) and Waters Inc. (Grant #40002775).

Data availability All data analyzed during this study are included in this published article and its electronic supplementary information.

Declarations

Ethics approval Not applicable.

Consent to participate Not applicable.

Consent for publication Not applicable.

Conflict of interest The authors declare no competing interests.

References

1. Minniti G, Muni R, Lanzetta G, Marchetti P, Enrici RM. Chemotherapy for glioblastoma: current treatment and future perspectives for cytotoxic and targeted agents. Anticancer Res. 2009;29(12):5171–84.
2. Chaichana KL, Cabrera-Aldana EE, Jusue-Torres I, Wijesekera O, Olivi A, Rahman M, et al. When gross total resection of a glioblastoma is possible, how much resection should be achieved? World Neurosurg. 2014;82(1-2):e257–65 Available from. https://doi.org/10.1016/j.wneu.2014.01.019.
3. Jermyn M, Mok K, Mercier J, Desroches J, Pichette J, Saint-Arnaud K, et al. Intraoperative brain cancer detection with Raman spectroscopy in humans. Sci Transl Med. 2015;7(274):274ra19 Available from. https://doi.org/10.1126/scitranslmed.aaa2384.

4. Reinges MH, Nguyen HH, Krings T, Hutter BO, Rohde V, Gilsbach JM. Course of brain shift during microsurgical resection of supratentorial cerebral lesions: limits of conventional neuronavigation. Acta Neurochir. 2004;146(4):369–77; discussion 77. Available from. https://doi.org/10.1007/s00701-003-0204-1.
5. Ogrinc N, Saudemont P, Takats Z, Salzet M, Fournier I. Cancer surgery 2.0: guidance by real-time molecular technologies. Trends Mol Med. 2021;27(6):602–15. Available from. https://doi.org/10.1016/j.molmed.2021.04.001.
6. Brat DJ, Verhaak RG, Aldape KD, Yung WK, Salama SR, Cooper LA, et al. Comprehensive, integrative genomic analysis of diffuse lower-grade gliomas. N Engl J Med. 2015;372(26):2481–98. Available from. https://doi.org/10.1056/NEJMoa1402121.
7. Stummer W, Koch R, Valle RD, Roberts DW, Sanai N, Kalkanis S, et al. Intraoperative fluorescence diagnosis in the brain: a systematic review and suggestions for future standards on reporting diagnostic accuracy and clinical utility. Acta Neurochir. 2019;161(10):2083–98. Available from. https://doi.org/10.1007/s00701-019-04007-y.
8. Stummer W, Pichlmeier U, Meinel T, Wiestler OD, Zanella F, Reulen H-J. Fluorescence-guided surgery with 5-aminolevulinic acid for resection of malignant glioma: a randomised controlled multicentre phase III trial. The Lancet Oncology. 2006;7(5):392–401. Available from. https://doi.org/10.1016/s1470-2045(06)70665-9.
9. Valdes PA, Juvekar P, Agar NYR, Gioux S, Golby AJ. Quantitative wide-field imaging techniques for fluorescence guided neurosurgery. Front Surg. 2019;6:31. Available from. https://doi.org/10.3389/fsurg.2019.00031.
10. Hollon T, Lewis S, Freudiger CW, Sunney Xie X, Orringer DA. Improving the accuracy of brain tumor surgery via Raman-based technology. Neurosurg Focus. 2016;40(3):E9. Available from. https://doi.org/10.3171/2015.12.FOCUS15557.
11. Hollon TC, Pandian B, Adapa AR, Urias E, Save AV, Khalsa SSS, et al. Near real-time intraoperative brain tumor diagnosis using stimulated Raman histology and deep neural networks. Nat Med. 2020;26(1):52–8. Available from. https://doi.org/10.1038/s41591-019-0715-9.
12. Hänel L, Kwiatkowski M, Heikaus L, Schluter H. Mass spectrometry-based intraoperative tumor diagnostics. Future Sci OA. 2019;5(3):FSO373. Available from. https://doi.org/10.4155/fsoa-2018-0087.
13. Zhang J, Rector J, Lin JQ, Young JH, Sans M, et al. Nondestructive tissue analysis for ex vivo and in vivo cancer diagnosis using a handheld mass spectrometry system. Sci Transl Med. 2017;9(406). Available from. https://doi.org/10.1126/scitranslmed.aan3968
14. Sans M, Zhang J, Lin JQ, Feider CL, Giese N, Breen MT, et al. Performance of the MasSpec pen for rapid diagnosis of ovarian cancer. Clin Chem. 2019;65(5):674–83. Available from. https://doi.org/10.1373/clinchem.2018.299289.
15. Woolman M, Kuzan-Fischer CM, Ferry I, Kiyota T, Luu B, Wu M, et al. Picosecond infrared laser desorption mass spectrometry identifies medulloblastoma subgroups on intrasurgical timescales. Cancer Res. 2019;79(9):2426–34. Available from. https://doi.org/10.1158/0008-5472.CAN-18-3411.
16. Woolman M, Qiu J, Kuzan-Fischer CM, Ferry I, Dara D, Katz L, et al. In situ tissue pathology from spatially encoded mass spectrometry classifiers visualized in real time through augmented reality. Chem Sci. 2020;11(33):8723–35. Available from. https://doi.org/10.1039/d0sc02241a.
17. Ogrinc N, Saudemont P, Balog J, Robin YM, Gimeno JP, Pascal Q, et al. Water-assisted laser desorption/ionization mass spectrometry for minimally invasive in vivo and real-time surface analysis using SpiderMass. Nat Protoc. 2019;14(11):3162–82. Available from. https://doi.org/10.1038/s41596-019-0217-8.
18. Vaysse PM, Kooreman LFS, Engelen SME, Kremer B, Olde Damink SWM, Heeren RMA, et al. Stromal vapors for real-time molecular guidance of breast-conserving surgery. Sci Rep. 2020;10(1):20109. Available from. https://doi.org/10.1038/s41598-020-77102-1.
19. Takáts Z, Wiseman JM, Gologan B, Cooks RG. Mass spectrometry sampling under ambient conditions with desorption electrospray ionization. Science. 2004;306(5695):471–3. Available from. https://doi.org/10.1126/science.1104404.
20. Jarmusch AK, Alfaro CM, Pirro V, Hattab EM, Cohen-Gadol AA, Cooks RG. Differential lipid profiles of normal human brain matter and gliomas by positive and negative mode desorption electrospray ionization - mass spectrometry imaging. PLoS One. 2016;11(9):e0163180. Available from. https://doi.org/10.1371/journal.pone.0163180.
21. Akbari Lakeh M, Tu A, Muddiman DC, Abdollahi H. Discriminating normal regions within cancerous hen ovarian tissue using multivariate hyperspectral image analysis. Rapid Commun Mass Spectrom. 2019;33(4):381–91. Available from. https://doi.org/10.1002/rcm.8362.
22. Eberlin LS, Dill AL, Golby AJ, Ligon KL, Wiseman JM, Cooks RG, et al. Discrimination of human astrocytoma subtypes by lipid analysis using desorption electrospray ionization imaging mass spectrometry. Angew Chem Int Ed Eng. 2010;49(34):5953–6. Available from. https://doi.org/10.1002/anie.201001452.
23. Eberlin LS, Margulis K, Planell-Mendez I, Zare RN, Tibshirani R, Longacre TA, et al. Pancreatic cancer surgical resection margins: molecular assessment by mass spectrometry imaging. PLoS Med. 2016;13(8):e1002108. Available from. https://doi.org/10.1371/journal.pmed.1002108.
24. Santoro AL, Drummond RD, Silva IT, Ferreira SS, Juliano L, Vendramini PH, et al. In situ DESI-MSI lipidomic profiles of breast cancer molecular subtypes and precursor lesions. Cancer Res. 2020;80(6):1246–57. Available from. https://doi.org/10.1158/0008-5472.CAN-18-3574.
25. Jarmusch AK, Pirro V, Baird Z, Hattab EM, Cohen-Gadol AA, Cooks RG. Lipid and metabolite profiles of human brain tumors by desorption electrospray ionization-MS. Proc Natl Acad Sci U S A. 2016;113(6):1486–91. Available from. https://doi.org/10.1073/pnas.1523306113.
26. Pirro V, Alfaro CM, Jarmusch AK, Hattab EM, Cohen-Gadol AA, Cooks RG. Intraoperative assessment of tumor margins during glioma resection by desorption electrospray ionization-mass spectrometry. Proc Natl Acad Sci U S A. 2017;114(26):6700–5. Available from. https://doi.org/10.1073/pnas.1706459114.
27. Brown HM, Alfaro CM, Pirro V, Dey M, Hattab EM, Cohen-Gadol AA, et al. Intraoperative mass spectrometry platform for IDH mutation status prediction, glioma diagnosis, and estimation of tumor cell infiltration. J Appl Lab Med. 2021;6(4):902–16. Available from. https://doi.org/10.1093/jalm/jfaa233.
28. Cordeiro FB, Jarmusch AK, Leon M, Ferreira CR, Pirro V, Eberlin LS, et al. Mammalian ovarian lipid distributions by desorption electrospray ionization-mass spectrometry (DESI-MS) imaging. Anal Bioanal Chem. 2020;412(6):1251–62. Available from. https://doi.org/10.1007/s00216-019-02352-6.
29. Eberlin LS, Tibshirani RJ, Zhang J, Longacre TA, Berry GJ, Bingham DB, et al. Molecular assessment of surgical-resection margins of gastric cancer by mass-spectrometric imaging. Proc Natl Acad Sci U S A. 2014;111(7):2436–41. Available from. https://doi.org/10.1073/pnas.1400274111.
30. Eberlin LS, Ferreira CR, Dill AL, Ifa DR, Cooks RG. Desorption electrospray ionization mass spectrometry for lipid characterization and biological tissue imaging. Biochim Biophys Acta. 2011;1811(11):946–60. Available from. https://doi.org/10.1016/j.bbalip.2011.05.006.

31. Pirro V, Jarmusch AK, Alfaro CM, Hattab EM, Cohen-Gadol AA, Cooks RG. Utility of neurological smears for intrasurgical brain cancer diagnostics and tumour cell percentage by DESI-MS. Analyst. 2017;142(3):449–54. Available from. https://doi.org/10.1039/c6an02645a.
32. Tousignant KD, Rockstroh A, Poad BLJ, Talebi A, Young RSE, Taherian Fard A, et al. Therapy-induced lipid uptake and remodeling underpin ferroptosis hypersensitivity in prostate cancer. Cancer Metab. 2020;8:11. Available from. https://doi.org/10.1186/s40170-020-00217-6.
33. Young RSE, Bowman AP, Williams ED, Tousignant KD, Bidgood CL, Narreddula VR, et al. Apocryphal FADS2 activity promotes fatty acid diversification in cancer. h. 2021;34(6):108738. Available from. https://doi.org/10.1016/j.celrep.2021.108738.
34. Andersen MK, Høiem TS, Claes BSR, Balluff B, Martin-Lorenzo M, Richardsen E, et al. Spatial differentiation of metabolism in prostate cancer tissue by MALDI-TOF MSI. Cancer Metab. 2021;9(1):9. Available from. https://doi.org/10.1186/s40170-021-00242-z.
35. Bi J, Chowdhry S, Wu S, Zhang W, Masui K, Mischel PS. Altered cellular metabolism in gliomas - an emerging landscape of actionable co-dependency targets. Nat Rev Cancer. 2020;20(1):57–70. Available from. https://doi.org/10.1038/s41568-019-0226-5.
36. Pandey R, Caflisch L, Lodi A, Brenner AJ, Tiziani S. Metabolomic signature of brain cancer. Mol Carcinog. 2017;56(11):2355–71. Available from. https://doi.org/10.1002/mc.22694.
37. Alfaro CM, Pirro V, Keating MF, Hattab EM, Cooks RG, Cohen-Gadol AA. Intraoperative assessment of isocitrate dehydrogenase mutation status in human gliomas using desorption electrospray ionization-mass spectrometry. J Neurosurg. 2019:1–8. Available from. https://doi.org/10.3171/2018.8.JNS181207.
38. Nakamizo S, Sasayama T, Shinohara M, Irino Y, Nishiumi S, Nishihara M, et al. GC/MS-based metabolomic analysis of cerebrospinal fluid (CSF) from glioma patients. J Neuro-Oncol. 2013;113(1):65–74. Available from. https://doi.org/10.1007/s11060-013-1090-x.
39. Kampa JM, Kellner U, Marsching C, Ramallo Guevara C, Knappe UJ, Sahin M, et al. Glioblastoma multiforme: metabolic differences to peritumoral tissue and IDH-mutated gliomas revealed by mass spectrometry imaging. Neuropathology. 2020;40(6):546–58. Available from. https://doi.org/10.1111/neup.12671.
40. Yan X, Zhao X, Zhou Z, McKay A, Brunet A, Zare RN. Cell-type-specific metabolic profiling achieved by combining desorption electrospray ionization mass spectrometry imaging and immunofluorescence staining. Anal Chem. 2020;92(19):13281–9. Available from. https://doi.org/10.1021/acs.analchem.0c02519.
41. Banerjee S, Zare RN, Tibshirani RJ, Kunder CA, Nolley R, Fan R, et al. Diagnosis of prostate cancer by desorption electrospray ionization mass spectrometric imaging of small metabolites and lipids. Proc Natl Acad Sci U S A. 2017;114(13):3334–9. Available from. https://doi.org/10.1073/pnas.1700677114.
42. Bulik M, Jancalek R, Vanicek J, Skoch A, Mechl M. Potential of MR spectroscopy for assessment of glioma grading. Clin Neurol Neurosurg. 2013;115(2):146-53. Available from: https://doi.org/10.1016/j.clineuro.2012.11.002.
43. Long PM, Moffett JR, Namboodiri AMA, Viapiano MS, Lawler SE, Jaworski DM. N-acetylaspartate (NAA) and N-acetylaspartylglutamate (NAAG) promote growth and inhibit differentiation of glioma stem-like cells. J Biol Chem. 2013;288(36):26188–200. Available from. https://doi.org/10.1074/jbc.M113.487553.
44. Moffett JR, Arun P, Ariyannur PS, Namboodiri AM. N-Acetylaspartate reductions in brain injury: impact on post-injury neuroenergetics, lipid synthesis, and protein acetylation. Front Neuroenerg. 2013;5:11. Available from. https://doi.org/10.3389/fnene.2013.00011.
45. Robert SM, Sontheimer H. Glutamate transporters in the biology of malignant gliomas. Cell Mol Life Sci. 2014;71(10):1839–54. Available from. https://doi.org/10.1007/s00018-013-1521-z.
46. Rackayova V, Cudalbu C, Pouwels PJW, Braissant O. Creatine in the central nervous system: from magnetic resonance spectroscopy to creatine deficiencies. Anal Biochem. 2017;529:144–57. Available from. https://doi.org/10.1016/j.ab.2016.11.007.
47. Jothi J, Janardhanam VA, Krishnaswamy R. Metabolic variations between low-grade and high-grade gliomas-profiling by (1)H NMR spectroscopy. J Proteome Res. 2020;19(6):2483-2490. Available from: https://doi.org/10.1021/acs.jproteome.0c00243.
48. Cai K, Tain RW, Zhou XJ, Damen FC, Scotti AM, Hariharan H, et al. Creatine CEST MRI for differentiating gliomas with different degrees of aggressiveness. Mol Imaging Biol. 2017;19(2):225–32. Available from. https://doi.org/10.1007/s11307-016-0995-0.
49. Shao W, Gu J, Huang C, Liu D, Huang H, Huang Z, et al. Malignancy-associated metabolic profiling of human glioma cell lines using 1H NMR spectroscopy. Mol Cancer. 2014;13:197. Available from. https://doi.org/10.1186/1476-4598-13-197.
50. Song X, Yang X, Narayanan R, Shankar V, Ethiraj S, Wang X, et al. Oral squamous cell carcinoma diagnosed from saliva metabolic profiling. Proc Natl Acad Sci U S A. 2020;117(28):16167–73. Available from. https://doi.org/10.1073/pnas.2001395117.
51. Wittmann BM, Stirdivant SM, Mitchell MW, Wulff JE, McDunn JE, Li Z, et al. Bladder cancer biomarker discovery using global metabolomic profiling of urine. PLoS One. 2014;9(12):e115870. Available from. https://doi.org/10.1371/journal.pone.0115870.
52. Patra S, Ghosh A, Roy SS, Bera S, Das M, Talukdar D, et al. A short review on creatine-creatine kinase system in relation to cancer and some experimental results on creatine as adjuvant in cancer therapy. Amino Acids. 2012;42(6):2319–30. Available from. https://doi.org/10.1007/s00726-011-0974-3.
53. Jung E, Alfonso J, Osswald M, Monyer H, Wick W, Winkler F. Emerging intersections between neuroscience and glioma biology. Nat Neurosci. 2019;22(12):1951–60. Available from. https://doi.org/10.1038/s41593-019-0540-y.
54. Fink MA, Paland H, Herzog S, Grube M, Vogelgesang S, Weitmann K, et al. L-carnitine-mediated tumor cell protection and poor patient survival associated with OCTN2 overexpression in glioblastoma multiforme. Clin Cancer Res. 2019;25(9):2874–86. Available from. https://doi.org/10.1158/1078-0432.CCR-18-2380.
55. Melone MAB, Valentino A, Margarucci S, Galderisi U, Giordano A, Peluso G. The carnitine system and cancer metabolic plasticity. Cell Death Dis. 2018;9(2):228. Available from. https://doi.org/10.1038/s41419-018-0313-7.
56. Harder BG, Blomquist MR, Wang J, Kim AJ, Woodworth GF, Winkles JA, et al. Developments in blood-brain barrier penetrance and drug repurposing for improved treatment of glioblastoma. Front Oncol. 2018;8:462. Available from. https://doi.org/10.3389/fonc.2018.00462.
57. Xie Z, Ferreira CR, Virequ AA, Cooks RG. Multiple reaction monitoring profiling (MRM profiling): small molecule exploratory analysis guided by chemical functionality. Chem Phys Lipids. 2021;235:105048. Available from. https://doi.org/10.1016/j.chemphyslip.2021.105048.
58. Sündermann A, Eggers LF, Schwudke D. Liquid extraction: Bligh and Dyer. In: Wenk MR, editor. Encyclopedia of lipidomics. Dordrecht: Springer Netherlands; 2016. p. 1–4.
59. Brown HM, Pu F, Dey M, Miller J, Shah MV, Shapiro SA, et al. Intraoperative detection of isocitrate dehydrogenase mutations in human gliomas using a miniature mass spectrometer. Anal Bioanal Chem. 2019. Available from. https://doi.org/10.1007/s00216-019-02198-y.

60. Manicke NE, Kistler T, Ifa DR, Cooks RG, Ouyang Z. High-throughput quantitative analysis by desorption electrospray ionization mass spectrometry. J Am Soc Mass Spectrom. 2009;20(2):321–5. Available from. https://doi.org/10.1016/j.jasms.2008.10.011.

Rong Chen is a Ph.D. candidate in analytical chemistry under the supervision of Prof. Graham Cooks of Purdue University. Her research interest lies in the discovery and measurement of molecular biomarkers for rapid tissue diagnosis by mass spectrometry.

Hannah Marie Brown is a graduate researcher in Dr. R. Graham Cooks' laboratory in the Department of Chemistry of Purdue University. Her research focuses on developments of ambient ionization mass spectrometry for intraoperative and high-throughput brain cancer diagnostics.

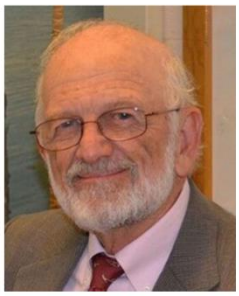

R. Graham Cooks is Henry Bohn Hass Distinguished Professor of Chemistry of Purdue University. His career has been devoted to realizing new concepts in mass spectrometry through instrumentation and their real-world applications. After early work in desorption ionization and tandem mass spectrometry, he has focused on accelerated reactions in droplets, high-throughput analysis, and synthesis using molecular ions. The use of desorption electrospray ionization (DESI) in cancer diagnosis is a current interest.

ARTICLE

Intraoperative Mass Spectrometry Platform for IDH Mutation Status Prediction, Glioma Diagnosis, and Estimation of Tumor Cell Infiltration

Hannah Marie Brown,[a,‡] Clint M. Alfaro,[a,‡] Valentina Pirro,[a,‡] Mahua Dey,[b,†] Eyas M. Hattab,[c] Aaron A. Cohen-Gadol,[b] and R. Graham Cooks[a,*]

Background: Surgical tumor resection is the primary treatment option for diffuse glioma, the most common malignant brain cancer. The intraoperative diagnosis of gliomas from tumor core samples can be improved by use of molecular diagnostics. Further, residual tumor at surgical margins is a primary cause of tumor recurrence and malignant progression. This study evaluates a desorption electrospray ionization mass spectrometry (DESI-MS) system for intraoperative isocitrate dehydrogenase (IDH) mutation assessment, estimation of tumor cell infiltration as tumor cell percentage (TCP), and disease status. This information could be used to enhance the extent of safe resection and so potentially improve patient outcomes.

Methods: A mobile DESI-MS instrument was modified and used in neurosurgical operating rooms (ORs) on a cohort of 49 human subjects undergoing craniotomy with tumor resection for suspected diffuse glioma. Small tissue biopsies ($n_{total} = 203$) from the tumor core and surgical margins were analyzed by DESI-MS in the OR and classified using univariate and multivariate statistical methods.

Results: Assessment of IDH mutation status using DESI-MS/MS to measure 2-hydroxyglutarate (2-HG) ion intensities from tumor cores yielded a sensitivity, specificity, and overall diagnostic accuracy of 89, 100, and 94%, respectively ($n_{core} = 71$). Assessment of TCP (categorized as low or high) in tumor margin and core biopsies using N-acetyl-aspartic acid (NAA) intensity provided a sensitivity, specificity, and accuracy of 91, 76, and 83%, respectively ($n_{total} = 203$). TCP assessment using lipid profile deconvolution provided sensitivity, specificity, and accuracy of 76, 85, and 81%, respectively ($n_{total} = 203$). Combining the experimental data and using PCA-LDA predictions of disease status, the sensitivity, specificity, and accuracy in predicting disease status are 63%, 83%, and 74%, respectively ($n_{total} = 203$).

Conclusions: The DESI-MS system allowed for identification of IDH mutation status, glioma diagnosis, and estimation of tumor cell infiltration intraoperatively in a large human glioma cohort. This methodology should be further refined for clinical diagnostic applications.

[a]Department of Chemistry, Purdue University, West Lafayette, IN, USA; [b]Department of Neurological Surgery, Indiana University School of Medicine, Goodman Campbell Brain and Spine, Indianapolis, IN, USA; [c]Department of Pathology and Laboratory Medicine, University of Louisville, KY, USA.
*Address correspondence to this author at: 560 Oval Drive, Department of Chemistry, Purdue University, West Lafayette, IN 47907-1393, USA. Fax 765-494-0239; e-mail cooks@purdue.edu.
[†]Present address: Department of Neurological Surgery, University of Wisconsin Medical School, Medical School, Madison, WI, USA
[‡]Authors contributed equally
Previous presentations: Oral presentation at MSACL 2019 US conference.
Received September 11, 2020; accepted November 23, 2020.
DOI: 10.1093/jalm/jfaa233

IMPACT STATEMENT

The intraoperative diagnosis of gliomas from tumor core samples can be improved using molecular diagnostics. Residual tumor at surgical margins is a primary contributor to tumor recurrence and malignant progression. Additionally, knowledge of prognostic genetic mutations at the time of surgery can better inform patient management strategies. DESI-MS can be used as a tool to aid intraoperative decision-making during glioma resection, specifically by allowing for the intraoperative assessment of IDH mutations, estimation of tumor cell infiltration, and disease status. Consequently, intraoperative DESI-MS has the potential to increase survival of glioma patients if available at the time of surgical resection.

INTRODUCTION

Diffuse gliomas are high morbidity primary brain tumors. The 5-year survival rate of patients with glioblastoma is less than 5% (1). The primary treatment option for gliomas is gross total surgical resection, accompanied by adjuvant chemoradiotherapy (2–4). A central dilemma of the neurosurgeon is preservation of vital brain functions while maximizing extent of resection. Unfortunately, glioma cells are diffusely infiltrative and the high risk of neurological deficits often results in residual tumor at surgical margins, leading to progression and recurrence (5, 6).

Accurate glioma diagnosis and prognosis increasingly relies on molecular and genetic information assessed from tumor core biopsies (2). Currently, brain tumor resections are performed without the aid of a molecular diagnosis, as these slow assays must be performed postoperatively (7). The development of rapid intraoperative molecular diagnostics could help improve glioma patient management and the quality of surgical resection (7–10). Notably, recent studies show that the effect of extent of resection on overall survival and malignant-free progression is significantly different between isocitrate dehydrogenase-wildtype (IDH-wt) and IDH-mutant (IDH-mut) gliomas, suggesting that surgical strategies may be impacted favorably by knowledge of the IDH mutation status at the time of surgery (9, 10). It is important to note that even if tumor cells are found in eloquent brain areas, surgical resection of that tissue may not be performed due to the significant harm it may cause to the patient. However, it may serve as an area to target for postoperative radiotherapy or application of local chemotherapeutics, the choice of which can be guided by information provided by rapid molecular diagnostics.

Mass spectrometry-based methods of tissue analysis may be able to provide clinical diagnostic information on brain tissue at the time of glioma resection. In particular, ambient ionization mass spectrometry (MS) has emerged as a family of rapid methods for intraoperative tissue analysis (11). Ambient ionization MS methods are being evaluated for their ability to assess molecular features of various cancers, as well as in assessing surgical margins for residual tumor (12, 13). Probe-based ambient methods, such as probe electrospray ionization (14) and touch spray ionization (15), have yielded pathologically relevant results on fresh surgical tissue. Rapid evaporative ionization MS has been used intraoperatively in a variety of cancers (16, 17). Several laser ablation systems, based on picosecond-infrared and other

optical regimes, have byielded diagnostic MS signals with low/no tissue damage (18, 19). The MassSpec Pen has been used in vivo to assess residual tumor in a minimally invasive, nondestructive approach, recently in human ovarian cancer (20, 21).

Desorption electrospray ionization-mass spectrometry (DESI-MS), the method utilized in this work, is an ambient ionization method in which charged microdroplets of a solvent are sprayed onto a sample surface, desorbing and ionizing molecules present in the sample and transporting them into a mass spectrometer for analysis (11, 22). DESI is used in many laboratories for biological applications (23, 24), including the distinction between cancerous and normal tissues in a variety of human organs (12, 25, 26). In some studies, such as the one described herein, DESI is not used as an imaging modality but as a diagnostic method. Using banked, fresh-frozen brain tissue, we have demonstrated the capability to differentiate gliomas, meningiomas, and pituitary tumors with high accuracy (27), along with the capability to provide glioma subtyping (28–30). Importantly, these brain cancers could be distinguished readily from normal brain tissue.

This study represents the completion of a project which demonstrated intraoperative application of DESI-MS during glioma resection using a customized, stand-alone mass spectrometer. Initial data from a set of 10 human subjects was published early in the project to highlight the potential clinical utility of TCP estimation by intraoperative MS (31) (Supplemental Table 1). Using the same customized mass spectrometer, approximately half way through the study we developed and applied an intraoperative DESI-MS assay for the assessment of IDH-mutation status by detecting the oncometabolite 2-hydroxyglutarate (2-HG), a key glioma prognostic marker, in a set of 51 glioma core biopsies obtained from 25 human subjects and analyzed intrasurgically (32). IDH mutations, specifically R132H mutations, disrupt the conversion of isocitrate to α-ketoglutarate. Additionally, IDH1 mutations result in the ability of IDH1 to catalyze the reduction of α-ketoglutarate to R(-)-2-HG. Consequently, 2-HG levels have been found to be significantly higher in IDH1 mutated human gliomas (33).

In this report, we have combined and improved our previously developed methods of tissue smear classification and analyzed tissue biopsy-smears during tumor resection in a cohort of 49 glioma patients, integrating data on new subjects, and re-examining data for subjects whose data appear in the aforementioned publications. (Supplemental Table 2 indicates the numbers of subjects in each category.) As the development of an online methodology for the determination of IDH mutation status was completed midway through the study, measurement of 2-HG as a predictor of IDH mutation status was possible for only 30 of the 49 recruited patients. While previous publications have analyzed the data with respect to individual tissues smears, in this work, we have elected to analyze the data with respect to biopsy in order to facilitate the understanding of the results in the context of a clinical setting. Three categories of information were acquired using DESI-MS: 1) IDH mutation status, 2) tumor cell percentage (TCP), and 3) disease status. When the DESI-MS results are considered in combination with other available data (e.g., MRI and in vivo brain mapping), they should allow the neurosurgeon to make better informed resection decisions.

MATERIALS AND METHODS

Human Subjects

Human subjects research was performed in accordance with an Institutional Review Board approved study at the Indiana University School of Medicine (IRB #1410342262). Glioma patients

undergoing craniotomy with tumor resection were prospectively enrolled after providing written informed consent and Health Insurance Portability and Accountability Act authorization. No DESI-MS results were shared with neurosurgeons during the surgical resection, so as not to affect the standard of care.

Intraoperative DESI-MS

All experiments were performed using a modified linear ion trap mass spectrometer (Thermo LTQ) as previously described (31, 32). For each surgery, the instrument was rolled into the operating room (OR) and turned on. During tumor resection, small stereotactic tissue biopsies (approximately 5–10 mg each) were provided by the neurosurgeon to the mass spectrometer operators for DESI-MS analysis. The number and location of the biopsies were determined according to the surgeon's best medical judgement. Samples from the tumor core (for assessing diagnostic information) as well as surgical margins (for assessing residual tumor) were provided for each case. The tissue biopsies were smeared on glass slides and then analyzed by DESI-MS using a zigzag raster pattern acquire representative data (Fig. 1, A). Two different negative ion mode DESI-MS methods were used. Using method 1, full-scan lipid (*m/z* 700—1000) and metabolite (*m/z* 80—200) mass spectra and a targeted MS^2 scan for N-acetyl-aspartic acid (NAA, 174 -> O), were acquired over 3.3 minutes. Using method 2, MS^2 (MS/MS) and MS^3 data were acquired specific to 2-HG (147 -> O and 147 -> 129 -> O, respectively), along with a full-scan metabolite profile (*m/z* 50 - 200), all over a period of 3.3 minutes (Fig. 1, B and C). Method 1 utilized 1:1 dimethylformamide (DMF)-acetonitrile (ACN) and method 2 utilized 25:37:38 DMF-ACN-ethanol (EtOH) as solvent. Additional details of the MS methods and conditions are given in the Supplemental Information.

Data Analysis

De-identified clinical data were obtained for each subject for correlation with the DESI-MS results (Supplemental Tables 3–6). The DESI-MS data were analyzed in MATLAB using custom algorithms to remove background scans (e.g., signal collected from regions of the glass slide containing no tissue) and to perform statistical classifications. MS scans from areas of the glass slide containing no smeared tissue and from smears giving insufficient intensity were excluded by applying a cut-off to the absolute signal intensity. Only scans with mass spectra having the summed ion counts greater than the cutoff value were used for chemical predictions. Additionally, for each selected mass spectrum, the full width at half maximum (FWHM) was calculated for the base peak; all spectra with resolution < 1000 were excluded. Additional information on the filtering and statistical methods used is included in the Supplemental Information (Data Analysis).

Histopathological Analysis

After DESI-MS analysis, the tissue smears were moved from the surgical core to the Indiana University Health Pathology Laboratory and were stained with H&E. The stained smears were then blindly evaluated by an expert neuropathologist (E.M.H.) and interpretations of smear diagnosis, tumor grade, TCP, and smear quality were provided (Supplemental Table 6). The entire smear was evaluated and the interpretations made reflect the average state of the entire smear. Smears with significant heterogeneity (e.g., half the slide diseased and half normal) were rare (2 smears out of 272 in this study).

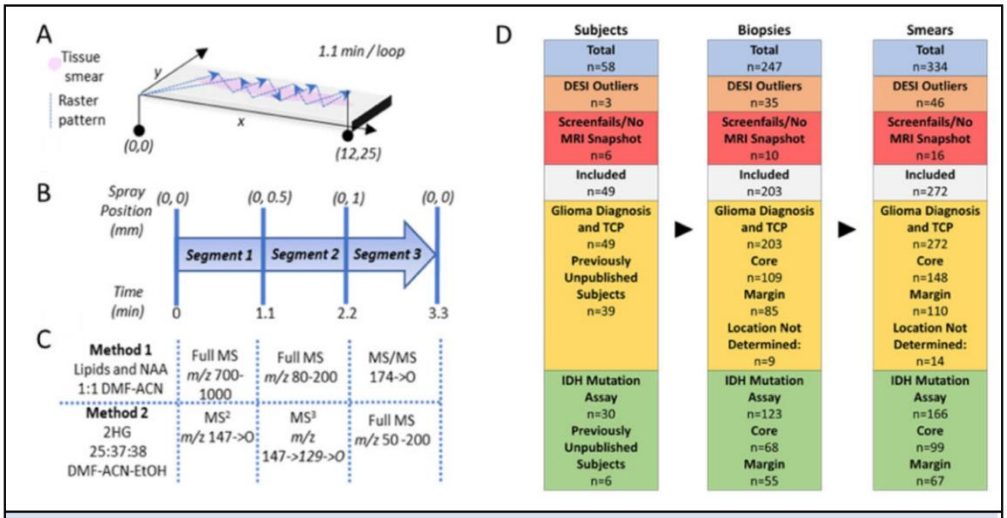

Fig. 1. Summary of the DESI-MS method. (A) Smeared tissue (pink) is analyzed with DESI spray using a zigzag raster pattern (dotted lines, with direction noted by arrow heads), spanning 12 mm in x-dimension and 25 mm in y-dimension over 1.1 min; the pattern is repeated 3 times. The DESI spot is offset 0.5 mm in the y-dimension after each raster loop. (B) DESI spray position and the timeline for the DESI-MS method. The (*x, y*) coordinates denote the starting position of the DESI spot for each raster loop. (C) Description of the 2 DESI-MS methods, shown synchronized with the position of the moving stage. A different set of MS data is collected during each method segment. Note the use of full MS, MS/MS (MS^2), and MS^3 experiments. (D) Summary of number of patients, biopsies, and smears, noting how many were excluded, and which subjects are new to the study. See Supplemental Tables 2–5 for additional patient cohort data. Data from earlier subjects recruited in the study were published in Reference 27 for glioma diagnosis and TCP, and in Reference 32 for IDH-mutation assessment. DESI data was considered an outlier if no lipid or metabolite profile scans were retained after data filtering due to low signal or high similarity to data collected from a blank glass slide (see Supplemental Methods for data filtering methods).

RESULTS AND DISCUSSION

Summary of Patient Cohort and Tissue Samples

Data were collected from 49 human subjects; 203 biopsies were obtained and 272 smears were analyzed (Fig. 1, D). For some biopsies, multiple smears were created and analyzed. The subject cohort and DESI-MS results are described in detail in the Supplemental Information and in Supplemental Tables 2–6. Supplemental Table 2 summarizes the number of patients and the biopsies obtained, indicates whether they have been included in a previous, preliminary publication, and whether subjects were excluded after recruitment; Supplemental Table 3 provides the demographics, diagnosis, and treatment information; Supplemental Table 4 provides additional histopathology data. The statistical predictions for disease status, TCP, and IDH mutation status for all analyzed smears are tabulated in Supplemental Table 5. The histopathology assessments of all these

DESI-MS analyzed smears are tabulated in Supplemental Table 6. The overall subject classifications are described in detail for IDH mutation status, TCP, and disease status in the following sections.

IDH Mutation Status Prediction from 2-HG Abundance

The methodology for online determination of IDH mutation status was developed midway through the study, after off-line method development. From this point onwards, 169 smears from 30 subjects were collected for the measurement of 2-HG as a predictor of IDH mutation status. Three smears were excluded due to lack of location information available and/or determined, resulting in 166 smears from 30 subjects being included. Of these 166 smears, 67 smears were from tumor margins and 99 smears were from tumor cores. In instances where multiple smears were made for the same tumor core biopsy, the average TIC normalized and summed 2-HG product ion intensity of all smears was calculated and used to predict the IDH mutation status of that biopsy. This produced 55 margin biopsies (23 IDH-mut biopsies from 12 subjects, 32 IDH-wt biopsies from 14 subjects), and 68 core biopsies (36 IDH-mut biopsies from 12 subjects, 32 IDH-wt biopsies from 16 subjects). The measurement of 2-HG is qualitative and predictions of IDH mutation status are made solely on the basis of TIC normalized and summed MS^3 intensities. Two MS^3 product ions were detected at *m/z* 85 and 101 from the sequential fragmentation of the 2-HG $[M\text{-}H]^-$ precursor ion (147 -> 129 -> O). The intensities of the two product ions were then summed and used to predict the IDH mutation status of the tumor. While the margin biopsies from IDH-mut subjects contained significantly higher levels of 2-HG compared to margins from IDH-wt subjects (ROC AUC = 0.96, Wilcoxon rank-sum test $P < 0.0001$), tumor core biopsies were preferred for IDH mutation status assessment, as the concentration of 2-HG is highest at the tumor core (Supplemental Fig. 1). The IDH mutation status of the subjects was obtained from pathology reports and was typically the result of postoperative IDH1 R132H immunohistochemistry and, when inconclusive, PCR-based IDH1/2 sequencing analysis.

The chemical structures of α-ketoglutartic acid and 2-HG, its mutated form which accumulates in the presence of an IDH mutation, are shown in Fig. 2, A. A statistically significant (Wilcoxon rank-sum test $P < 0.0001$) increase in the 2-HG signal of tumor core biopsies was observed in the IDH-mut subjects compared to the IDH-wt subjects. A receiver operating characteristic (ROC) curve model provided an area under the curve (AUC) of 0.98 using the tumor cores, as shown in Fig. 2, B. This difference is apparent in the box-plots shown in Fig. 2, C. The summed and normalized 2-HG product ion intensity cutoff of 62.3 (in the MS^3 spectrum) resulted in the highest overall accuracy. This normalized cutoff is instrument- and method-dependent and requires further interlaboratory investigation to evaluate whether a universal cutoff can be determined. Using the ROC determined cutoff, the sensitivity (correctly identifying core biopsies from IDH-mut subjects when the IDH mutation was present) and specificity (correctly identifying core biopsies from IDH-wildtype when IDH mutation was absent) were 89% and 100%, respectively, with an overall accuracy of 94%.

For several biopsies included in this study ($n_{discordant} = 4$), discordant mutation status predictions exist between core biopsies from the same subject. Due to the high degree of heterogeneity of glioma, it is likely that 2-HG concentration varies within the tumor cavity, even over small distances. Additionally, cauterized or hemorrhagic tissue results in ion suppression and provides poor diagnostic information. These problems are shared with traditional histopathology. The solution for both methods is to take additional biopsies that are of sufficient diagnostic quality. While this is impractical for histopathology, DESI-MS analysis

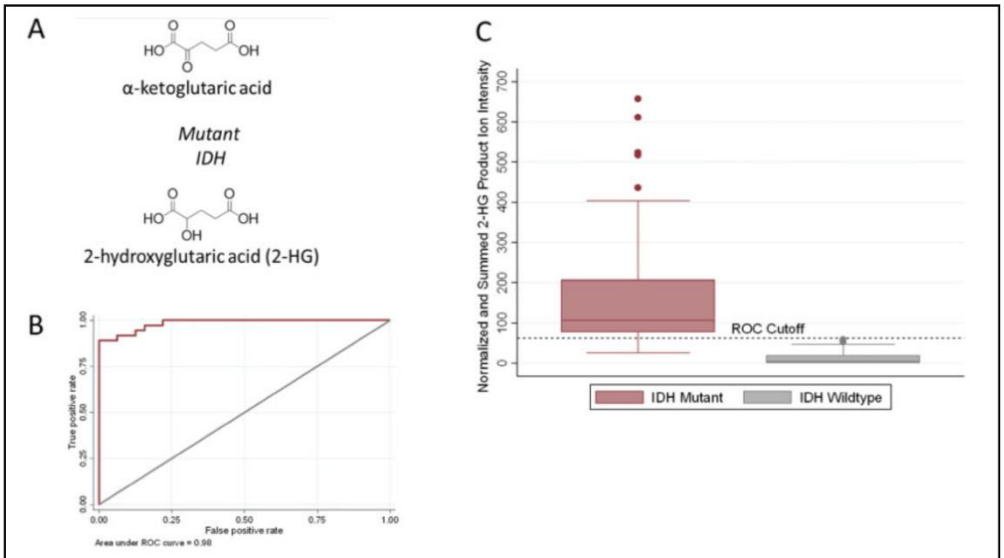

Fig. 2. Intraoperative assessment of IDH-mutation status from tumor cores. (A) Chemical structure of α-ketoglutaric acid and 2-hydroxyglutarate (2-HG), the oncometabolite associated with IDH mutations. (B) ROC curve for the IDH-mutation assay using the tumor core biopsies. The area under the curve is 0.98, indicating the high accuracy of the method. (C) Box-plot showing the average summed and TIC normalized MS^3 fragment ion intensities (*m/z* 85 + *m/z* 101) produced by sequential dissociation (MS^3) of 2-HG for all tumor core biopsies (*n* = 68 biopsies from 28 subjects) by IDH mutation status. The fragment ion intensities from duplicate smears of the same biopsy were averaged to generate one value per biopsy. Error bars represent ± 1.5 times the calculated standard deviations. The black dashed horizontal decision line was calculated from ROC curve analysis and differentiates tumor core biopsies from IDH-mut subjects and IDH-wt subjects with the highest sensitivity and specificity.

takes only 3 min, so resampling from the same patient during surgery is a feasible solution. To further limit the impact of signal variation, the average of the normalized 2-HG intensity for all biopsies from a subject was generated and used to predict IDH mutation status. When doing so, only 1 subject (Subject 26) was misclassified with respect to its IDH mutation status. This subject, and subjects close to the ROC cutoff value, had low grade (i.e., WHO grade II and III) astrocytomas (i.e., anaplastic astrocytomas and diffuse astrocytomas). In our experience, these lower grade tumors have lower concentrations of 2-HG than higher grade gliomas, resulting in lower summed 2-HG product ion intensity values. Therefore, for suspected low-grade gliomas, resampling may be necessary to increase the degree of confidence placed in measured summed 2-HG product ion intensities. Biological variability within the tumor cavity is an area of active research; MRI instruments are being used to probe distributions of metabolites within the tumor cavity and surrounding tissue to further understand tumor heterogeneity. As knowledge of tumor heterogeneity and

its impacts on the spatial distribution of metabolites increases, so too will our understanding of discordant predictions in IDH mutation status.

Estimating Tumor Cell Percentage from N-Acetyl-Aspartic Acid (NAA) Abundance

Two DESI-MS-based methods for the rapid estimation of TCP, based on NAA and lipid abundances, respectively, have been developed and tested previously on an initial set of 10 human subjects (31). Data for this original set of subjects have been integrated into the complete 49 patient cohort and reexamined, with the results now discussed. In the first method, the standard normal variate (SNV) normalized intensity of *m/z* 174, corresponding to NAA, measured in the full-scan MS metabolite profile was used to estimate TCP, using previously published data as a training set (27, 34). For biopsies with multiple smears, the average TCP from the corresponding smears was calculated and used to estimate TCP for the specific biopsy. This produced a collection of 203 biopsies (109 core, 85 margin, 9 undermined) from 49 subjects. Biopsies that provided 50% or less glioma contribution were categorized as low TCP and samples providing 51% or more glioma were categorized as high TCP. The histopathology estimates of TCP were categorized using the same decision boundary. Using these categories, an overall accuracy of correctly classifying the biopsies as low or high TCP was 83%, with sensitivity and specificity of 91% and 76%, respectively (Table 1). The full-scan MS abundance of NAA (detected as *m/z* 174 in the metabolite profile scan) provided slightly higher overall accuracy than did the MS^2 data (sensitivity, specificity, and overall accuracy were 79%, 85%, and 82%, respectively, for the MS^2 data ($n_{NAA\ MS2} = 198$).) The targeted MS^2 scan for NAA (174 -> O) gave product ions at *m/z* 88, 114, 130, and 156. See the Supplemental Information Data Analysis section for details. Box plots and ROC curves of the NAA full-scan and MS^2 data are shown in Supplemental Fig. 2. Principal component analysis (PCA) was performed on the metabolite profiles and the contribution of *m/z* 174 (NAA) in separating low and high TCP smears was consistent with previous reports (27).

Estimating Glioma Content (Relative Tumor Burden) Using Lipid Profile Deconvolution

The second method for estimating TCP employed a lipid profile deconvolution approach: PCA was used to calculate the percentage of white matter (WM), gray matter (GM), and glioma (G) contributing to the lipid profiles of the subject samples using a linear regression model built from data collected in a previous study (27, 31). The model was based on the presumption that the observed lipid profile of each brain tissue biopsy is composed of a ternary mixture of WM, GM, and G. The summed percentages of these 3 categories are constrained to 100%. The regression model was built from data collected from DESI-MS analysis of banked glioma and normal human brain specimens. Histologically correlated mass spectra were compiled based on histopathological assessment, compressed with PCA, and the average PC1 and PC2 scores for samples of pure WM, GM, and G were calculated. The three extremes (PC1 and PC2 scores corresponding to 100% WM, 100% GM, 100% G) were used to calculate the predicted PC1 and PC2 scores for each possible mixture (Supplemental Fig. 3). To predict the composition of new samples ($n_{total} = 203$), the PCA lipid profile loading matrix from the training set data (27) was used to calculate the PC scores of the new samples. The calculated PC1 and PC2 scores of the new samples were matched to predicted PC1 and PC2 scores using the original training set data; the predicted scores were each associated with a specific percentage combination of GM: WM: G (Supplemental Fig. 3).

The classifications of GM and WM were recategorized as infiltrative margin (IM) to match the histopathology categories, as the nature of the underlying normal brain tissue (specifically white

Table 1. Confusion matrix for assessing correlation between histopathology assessments and the DESI-MS estimates of TCP and disease status of tissue biopsies

		Histopathology[a] High TCP/Glioma[b]	Low TCP/Infiltrative Margin[b]
Full-scan NAA Intensity TCP Estimate	High TCP/Glioma[b]	91	25
Lipid Deconvolution TCP Estimate		76	15
PCA-LDA Diagnosis		60	18
Full-scan NAA Intensity TCP Estimate	Low TCP/Infiltrative Margin[b]	9	78
Lipid Deconvolution TCP Estimate		24	88
PCA-LDA Diagnosis		35	91

[a] Histopathology assessments of TCP were used for correlation with lipid deconvolution and NAA intensity classifications of TCP. Histopathology assessments of disease status were used for correlation with PCA-LDA diagnosis of the tissue smears.
[b] For lipid deconvolution and NAA intensity classification, histopathology TCP categories were High =51% and Low =50%. Histopathology categories of glioma and infiltrative margin were used for correlation with PCA-LDA diagnosis of glioma and infiltrative margin.

or gray matter) could not always be reliably determined by histopathology. The percentage of G calculated for each unknown sample was used as an estimate of the TCP. See Supplemental Information for additional details. For biopsies with multiple smears, the average percentage of G from corresponding smears was calculated and used to estimate TCP for the specific biopsy. This produced data for a collection of 203 biopsies (109 core, 85 margin, 9 undermined) from 49 subjects. Using 50% TCP delineation value as for the NAA abundance method, an overall accuracy of correctly classifying the biopsies as low or high TCP was 81%, with sensitivity and specificity of 76% and 85%, respectively (Table 1). The low TCP and high TCP smears analyzed in this study are fairly well separated in PCA space, due primarily to the ions of *m/z* 834, 794, and 888.

Predicting Disease Status from Fused Metabolite and Lipid Profiles

The final category of diagnostic information provided by DESI-MS was disease status. Using PCA-LDA on fused SNV normalized lipid and metabolite profiles obtained from DESI-MS, tissue smears were classified as either G, GM, or WM, with the latter two being recategorized as infiltrative margin (IM) to match the histopathology categories (see Table 1 footnote). Similar overall accuracy was observed when performing PCA-LDA cross-validation with the lipid and metabolite profiles of all 272 tissue smears (Supplemental Tables 7 and 8), however, the sensitivities and specificities were quite different, supporting the use of fused lipid and metabolite profiles for a more robust method that utilizes diagnostic features contained in both parts of a mass spectrum. For biopsies with multiple smears, the average SNV normalized lipid and metabolite profiles from corresponding smears were calculated prior to fusing to generate a representative lipid and metabolite profiles for the biopsy used to predict disease status. This produced a collection of 203 biopsies (109 core, 85 margin, 9 undermined) from 49 subjects. The agreement between PCA-LDA predictions and histopathological assessment of disease status of tissue biopsies is shown in Table 1. The sensitivity, specificity, and accuracy in predicting disease status are 63%, 83%, and 74%, respectively.

While the sensitivity using the fused data method was lower than either the lipid or metabolite profiles independently, the use of the fused profiles to predict TCP is likely more robust than using only one segment of the mass spectrum, as diagnostics features appear in both regions of the mass spectrum. A significant fraction of the smears classified as glioma based on histopathology ($n_{missclasified\ smears}$ = 43%) were misclassified as either WM or GM using PCA-LDA classification. These cases likely reflect mixed tissue smears which are challenging for histopathology assessment as well for our current DESI-MS system. These types of samples were encountered both at surgical margins and at tumor cores.

Evaluation of Methods for Estimating TCP and Disease Status

Ultimately, we found that both methods (i.e., full-scan NAA abundance and lipid deconvolution) were capable of predicting TCP with similar accuracies (83% and 80%, respectively), with the full-scan NAA abundance having greater sensitivity (87% vs. 76%) and the lipid deconvolution method having greater specificity (79% vs. 84%). In instances of misclassification, it would be beneficial to compare the disease status predictions made using the fused metabolite and lipid profiles with TCP estimations using NAA and lipid deconvolution (i.e., many of the misclassified biopsies have TCP estimates indicating mixed diseased and normal tissue). Additionally, the PCA-LDA method itself may need to be adjusted in the future to improve classification of biopsies with mixed morphologies by using additional categories (i.e., rather than categorizing tissues into 3 rigid categories (G, WM, GM), perhaps 6 categories (G, G/WM, WM, WM/GM, GM, GM/G)).

While it is likely that there are many contributing factors, a possible cause of variability in TCP estimates may be that the full-scan NAA abundance method predicts TCP based on the intensity of a single analyte that exists in very low concentrations within the tumor, while the lipid deconvolution method predicts TCP based on a collection of analytes in a characteristic pattern of intensities. Matrix effects are inherent in the measurements of complex samples, especially biological samples; they are an intrinsic component of the material being analyzed and, consequently, cannot be eliminated. Excepting cases where tissue is substantially different (e.g., cauterized or hemorrhagic tissues), observed changes with matrix should involve total signal but not relative signals, provided the same type of tissue is being analyzed. That said, the measurement of a single analyte (i.e., 2-HG or NAA) is a situation where the matrix effects on signal intensity are of most concern. To minimize variations in signal, the recorded mass spectra are normalized (specifically TIC and/or SNV normalized) before additional comparison or statistical analysis is performed.

There are likely additional experimental factors that may have affected classification in the present study. Improvements are needed to increase the agreement between the DESI-MS predictions of disease status and TCP with histopathology, the current gold-standard method in morphology. The diagnostic sensitivity and specificity for the TCP predictions could be improved by better correlating the positions at which TCP pathology data are taken relative to DESI-MS data, while the biological variation can be addressed with additional cases. To explore the impact of these factors, a new 50 patient study for the optimization of the DESI-MS platform has commenced in which the above factors will be rigorously controlled.

Assessment of Margins of Tumors of Different WHO Grades

The assessment of glioma margins is not routinely performed intraoperatively with pathologic or molecular methods. That said, glioma infiltration is often significant beyond contrast enhancement in MRI, especially in glioblastoma (6). In this section, using our DESI-MS methods, we investigate whether margins from high-grade glioma patients contain higher TCP than margins from

low-grade glioma patients. In our study, 85 of the 203 biopsies (110 smears with some replicates) were obtained from margins (based on MRI) and provided acceptable quality for histopathology and DESI-MS analysis. WHO grade information was not available for eight margin biopsies from two subjects (Subjects 41 and 46) and, thus, these biopsies were excluded from this portion of the study.

For low-grade gliomas (WHO grades I–III), 78% of the margin biopsies had low TCP ($n_{\text{low TCP, low grade margins}} = 35$) and 22% had high TCP based on histopathology ($n_{\text{high TCP, low grade margins}} = 10$), using 50% TCP for delineating between low and high TCP. Our accuracy with respect to agreement with histopathology assessment for the grade I–III margin samples ($n_{\text{total low grade margins}} = 45$) was 80% and 76% overall using the normalized NAA intensity and lipid deconvolution approaches, respectively (Supplemental Table 9). For the grade IV gliomas, histopathology determined that 59% of the margin biopsies had low TCP ($n_{\text{low TCP, high grade margins}} = 19$) and 41% had high TCP ($n_{\text{high TCP, high grade margins}} = 13$), also using the 50% TCP cutoff. Our agreement with the histopathology assessment for the margin biopsies from grade IV gliomas ($n_{\text{total high grade margins}} = 32$) was 97% and 84% overall using the normalized NAA intensities and lipid deconvolution approaches, respectively (Supplemental Table 10).

Literature reports suggest that high TCP may extend beyond MRI contrast enhancement, especially in grade IV glioblastomas (6, 8, 35). We found that the margins of grade IV gliomas contained high TCP more often than the margins of grade I–III gliomas, although the difference in number of high TCP smears obtained from the margins of grade IV compared to grade I–III gliomas using nominal logistic regression and a 50% TCP cutoff to delineate between the low and high TCP categories is not statistically significant ($P = 0.0833$). In this context, a DESI-MS tool for assessment of local tumor burden must be used in combination with an independent diagnostic method such as MRI neuronavigation and/or brain mapping.

Simplified DESI-MS Outputs That Enable Surgical Decision Making

In this study, we have demonstrated two major applications of the DESI-MS system: providing diagnostic information of two types for tumor cores (IDH mutation status and disease status) and providing surgical margin assessments of residual tumor (i.e., TCP) at discrete locations. With appropriate method validations and permissions, these predictions could be provided to the neurosurgeon in order to improve treatment strategy, including the extent of resection. Here we describe a typical example of a case in which DESI-MS would be useful. Figure 3, A shows the biopsy locations for two stereotactic biopsies from Subject 58. Figure 3, B–D shows the raw lipid, metabolite, and 2-HG MS^3 data for biopsy #328, respectively; Fig. 3, E–G shows the same types of data but for biopsy #333. This biopsy was predicted with PCA-LDA to be glioma, by lipid deconvolution to have high TCP, and by 2-HG intensity to be IDH-mut. In contrast, biopsy #333 (blue point in Fig. 3, A) was taken several millimeters outside the MRI contrast enhancing area and was predicted from PCA-LDA to be normal white matter, by lipid deconvolution to have low TCP, and by 2-HG intensity to also be IDH-mut. Each of these predictions matched the histopathology assessments of the tissue smears. Thus, using the DESI-MS system, the neurosurgeon could analyze biopsies from discrete regions of the resection cavity to assess residual tumor when clinical acumen is insufficient.

While the initial results presented in this article are promising, it is important to remember that the DESI-MS system is proposed as an ancillary method to support the existing standard of care. Thus, when making the decision to resect, the DESI-MS assessments cannot be interpreted in isolation. In future studies, it will be worthwhile to

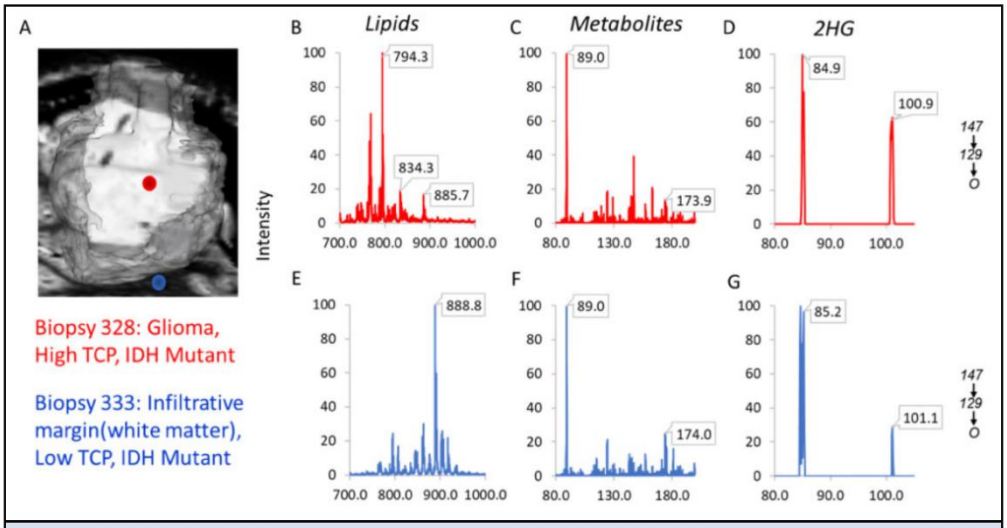

Fig. 3. DESI-MS predictions of disease status, TCP, and IDH-mutation status for a core and margin biopsy from Subject 58. (A) Reconstruction of MRI tumor volume showing location of the two biopsies. Biopsy 328 (red dot) is within the contrast enhancing region of the tumor; biopsy 333 (blue dot) is a few mm outside of the contrast enhancing region. (B–D) The lipid, metabolite, and 2-HG MS^3 product ion scans for biopsy 328 (red dot in Fig. 2, A). (E–G) The lipid, metabolite, and 2-HG MS^3 product ion scan for biopsy 333 (blue dot in Fig. 2, A). Biopsy 328 was classified as glioma, high TCP, and IDH-mut; biopsy 333 was infiltrative margin (white matter), low TCP, and IDH-mut.

evaluate whether DESI-MS assessment of areas at the MRI tumor borders can improve extent of resection and whether this in turn can reduce tumor recurrence and increase overall and progression-free survival. It will be worthwhile also to assess whether prediction of IDH mutation status via DESI-MS analysis can increase overall and progression-free survival by allowing for more personalized resection approaches and use of chemotherapeutic drugs targeting IDH mutations at the time of surgery.

CONCLUSIONS

DESI-MS monitoring of 2-HG, along with lipid and metabolite profiling, can improve the differential diagnosis of glioma intraoperatively through the assessment of IDH mutation status and disease status. The system also provides a means of assessing surgical margins for residual tumor through lipid profile deconvolution and measurement of NAA. The clinical accuracy of the IDH mutation assay was high (94%). Implementation of a new standard of care for surgical glioma resection based on IDH mutation status would be enabled by intraoperative DESI-MS assessments in combination with preoperative MRI detection of 2-HG. Additionally, the presence of the IDH mutation in this context is 100% specific for diffuse glioma and can assist in differential diagnosis to confirm the presence of glioma (36). The clinical accuracy of correctly predicting TCP (based on correlations with morphologic pathology evaluations) was moderate

(83% and 81% for NAA and lipid profile deconvolution, respectively). Emerging evidence which suggests differences in patient outcome from maximal tumor resection based on IDH mutation status demonstrates a need for accurate and rapid intraoperative IDH mutation status assessment. Overwhelming clinical evidence showing the need to maximize extent of resection in gliomas highlights the need for methods to assess residual tumor at surgical margins. The intraoperative DESI-MS system is capable of these two applications. Advanced development of this DESI-MS system to enable clinical diagnostic applications and rapid assessments of residual tumor could significantly improve glioma resection.

SUPPLEMENTAL MATERIAL

Supplemental material is available at *The Journal of Applied Laboratory Medicine* online.

Nonstandard Abbreviations: ACN, acetonitrile; AUC, area under curve; DESI-MS, desorption electrospray ionization-mass spectrometry; DMF, dimethylformamide; FWHM, full width at half maximum; G, glioma; GM, gray matter; 2-HG, 2-hydroxyglutarate; IDH, isocitrate dehydrogenase; IM, infiltrative margin; NAA, N-acetyl-aspartic acid; PCA, principal component analysis; ROC, receiver operating curve; SNV, standard normal variate; TCP, tumor cell percentage; WM, white matter.

Author Contributions: *All authors confirmed they have contributed to the intellectual content of this paper and have met the following 4 requirements: (a) significant contributions to the conception and design, acquisition of data, or analysis and interpretation of data; (b) drafting or revising the article for intellectual content; (c) final approval of the published article; and (d) agreement to be accountable for all aspects of the article thus ensuring that questions related to the accuracy or integrity of any part of the article are appropriately investigated and resolved.*

H.M. Brown, statistical analysis.

Authors' Disclosures or Potential Conflicts of Interest: *Upon manuscript submission, all authors completed the author disclosure form. Disclosures and/or potential conflicts of interest*. **Employment or Leadership:** None declared. **Consultant or Advisory Role:** None declared. **Stock Ownership:** None declared. **Honoraria:** None declared. **Research Funding:** This research was supported by the National Institute of Biomedical Imaging and Bioengineering (NIH grant no. R21EB015722). Support of the Purdue Center for Cancer Research, NIH grant P30 CA023168, is gratefully acknowledged. This publication was made possible with partial support for Clint Alfaro from grant no. UL1TR001108 (to A. Shekhar, principal investigator) from the National Institutes of Health, National Center for Advancing Translational Sciences, Clinical and Translational Sciences Award. **Expert Testimony:** None declared. **Patents:** R.G. Cooks, 7,335,897.

Role of Sponsor: The funding organizations played a direct role in the design of study, review, and interpretation of data, preparation of manuscript, and final approval of manuscript. The funding organizations played no role in the choice of enrolled patients.

Acknowledgments: We thank Professor Tim Ratliff for his support; Heather Cero and Lauren Snyder for patient consent, providing clinical data, and IRB monitoring. Fan Pu, Rong Chen, Alan K. Jarmusch, and Zane Baird are thanked for their assistance with the study.

REFERENCES

1. D'Amico RS, Englander ZK, Canoll P, Bruce JN. Extent of resection in glioma-a review of the cutting edge. World Neurosurg 2017;103:538–49.
2. Brat DJ, Verhaak RGW, Aldape KD, Yung WKA, Salama SR, Cooper LAD; Cancer Genome Atlas Research Network, et al. Comprehensive, integrative genomic analysis of diffuse lower-grade gliomas. N Engl J Med 2015;372:2481–98.
3. McGirt MJ, Chaichana KL, Gathinji M, Attenello FJ, Than K, Olivi A, et al. Independent association of extent of resection with survival in patients with malignant brain astrocytoma. J Neurosurg 2009;110:156–62.
4. Hervey-Jumper SL, Berger MS. Maximizing safe resection of low- and high-grade glioma. J Neurooncol 2016;130:269–82.
5. Mampre D, Ehresman J, Pinilla-Monsalve G, Osorio MAG, Olivi A, Quinones-Hinojosa A, et al. Extending the resection beyond the contrast-enhancement for glioblastoma: feasibility, efficacy, and outcomes. Br J Neurosurg 2018;32:528–35.

6. Eidel O, Burth S, Neumann JO, Kieslich PJ, Sahm F, Jungk C, et al. Tumor infiltration in enhancing and non-enhancing parts of glioblastoma: a correlation with histopathology. PLoS One 2017;12:e0169292.
7. Chen R, Ravindra VM, Cohen AL, Jensen RL, Salzman KL, Prescot AP, et al. Molecular features assisting in diagnosis, surgery, and treatment decision making in low-grade gliomas. Neurosurg Focus 2015;38:E2.
8. Claes A, Idema AJ, Wesseling P. Diffuse glioma growth: a guerilla war. Acta Neuropathol 2007;114: 443–58.
9. Beiko J, Suki D, Hess KR, Fox BD, Cheung V, Cabral M, et al. IDH1 mutant malignant astrocytomas are more amenable to surgical resection and have a survival benefit associated with maximal surgical resection. Neuro Oncol 2014;16:81–91.
10. Patel T, Bander ED, Venn RA, Powell T, Cederquist GY, Schaefer PM, et al. The role of extent of resection in IDH1 wild-type or mutant low-grade gliomas. Neurosurgery 2018;82:808–14.
11. Takats Z, Wiseman JM, Gologan B, Cooks RG. Mass spectrometry sampling under ambient conditions with desorption electrospray ionization. Science 2004;306: 471–3.
12. Ifa DR, Eberlin LS. Ambient ionization mass spectrometry for cancer diagnosis and surgical margin evaluation. Clin Chem 2016;62:111–23.
13. Hanel L, Kwiatkowski M, Heikaus L, Schluter H. Mass spectrometry-based intraoperative tumor diagnostics. Future Sci OA 2019;5:FSO373.
14. Yoshimura K, Mandal MK, Hara M, Fujii H, Chen LC, Tanabe K, et al. Real-time diagnosis of chemically induced hepatocellular carcinoma using a novel mass spectrometry-based technique. Anal Biochem 2013;441: 32–7.
15. Alfaro CM, Jarmusch AK, Pirro V, Kerian KS, Masterson TA, Cheng L, et al. Ambient ionization mass spectrometric analysis of human surgical specimens to distinguish renal cell carcinoma from healthy renal tissue. Anal Bioanal Chem 2016;408:5407–14.
16. Balog J, Sasi-Szabo L, Kinross J, Lewis MR, Muirhead LJ, Veselkov K, et al. Intraoperative tissue identification using rapid evaporative ionization mass spectrometry. Sci Transl Med 2013;5:194ra93.
17. Phelps DL, Balog J, Gildea LF, Bodai Z, Savage A, El-Bahrawy MA, et al. The surgical intelligent knife distinguishes normal, borderline and malignant gynaecological tissues using rapid evaporative ionisation mass spectrometry (REIMS). Br J Cancer 2018;118: 1349–58.
18. Woolman M, Ferry I, Kuzan-Fischer CM, Wu M, Zou J, Kiyota T, et al. Rapid determination of medulloblastoma subgroup affiliation with mass spectrometry using a handheld picosecond infrared laser desorption probe. Chem Sci 2017;8:6508–19.
19. Fatou B, Saudemont P, Leblanc E, Vinatier D, Mesdag V, Wisztorski M, et al. In vivo real-time mass spectrometry for guided surgery application. Sci Rep 2016;6:25919.
20. Zhang J, Rector J, Lin JQ, Young JH, Sans M, Katta N, et al. Nondestructive tissue analysis for ex vivo and in vivo cancer diagnosis using a handheld mass spectrometry system. Sci Transl Med 2017;9:eaan3968.
21. Sans M, Zhang J, Lin JQ, Feider CL, Giese N, Breen MT, et al. Performance of the MasSpec pen for rapid diagnosis of ovarian cancer. Clin Chem 2019;65:674–83.
22. Swales JG, Hamm G, Clench MR, Goodwin RJA. Mass spectrometry imaging and its application in pharmaceutical research and development: A concise review. Int J Mass Spectrometry 2019;437:99–112.
23. Kooijman PC, Nagornov KO, Kozhinov AN, Kilgour DPA, Tsybin YO, Heeren RMA, et al. Increased throughput and ultra-high mass resolution in DESI FT-ICR MS imaging through new-generation external data acquisition system and advanced data processing approaches. Sci Rep 2019;9:8.
24. Wang H, Manicke NE, Yang Q, Zheng L, Shi R, Cooks RG, et al. Direct analysis of biological tissue by paper spray mass spectrometry. Anal Chem 2011;83:1197–201.
25. Woolman M, Zarrine-Afsar A. Platforms for rapid cancer characterization by ambient mass spectrometry: advancements, challenges and opportunities for improvement towards intrasurgical use. Analyst 2018; 143:2717–22.
26. Eberlin LS, Margulis K, Planell-Mendez I, Zare RN, Tibshirani R, Longacre TA, et al. Pancreatic cancer surgical resection margins: molecular assessment by mass spectrometry imaging. PLoS Med 2016;13: e1002108.
27. Jarmusch AK, Pirro V, Baird Z, Hattab EM, Cohen-Gadol AA, Cooks RG. Lipid and metabolite profiles of human brain tumors by desorption electrospray ionization-MS. Proc Natl Acad Sci Usa USA 2016;113:1486–91.
28. Eberlin LS, Norton I, Orringer D, Dunn IF, Liu X, Ide JL, et al. Ambient mass spectrometry for the intraoperative molecular diagnosis of human brain tumors. Proc Natl Acad Sci USA 2013;110:1611–6.
29. Eberlin LS, Norton I, Dill AL, Golby AJ, Ligon KL, Santagata S, et al. Classifying human brain tumors by lipid imaging with mass spectrometry. Cancer Res 2012;72:645–54.
30. Eberlin LS, Dill AL, Golby AJ, Ligon KL, Wiseman JM, Cooks RG, et al. Discrimination of human astrocytoma subtypes by lipid analysis using desorption electrospray ionization imaging mass spectrometry. Angew Chem Int Ed Engl 2010;49:5953–6.
31. Pirro V, Alfaro CM, Jarmusch AK, Hattab EM, Cohen-Gadol AA, Cooks RG. Intraoperative assessment of tumor margins during glioma resection by desorption electrospray ionization-mass spectrometry. Proc Natl Acad Sci USA 2017;114:6700–5.
32. Alfaro CM, Pirro V, Keating MF, Hattab EM, Cooks RG, Cohen-Gadol AA. Intraoperative assessment of isocitrate dehydrogenase mutation status in human gliomas using desorption electrospray ionization-mass spectrometry. J Neurosurg 2019;132:1–8.
33. Dang L, White DW, Gross S, Bennett BD, Bittinger MA, Driggers EM, et al. Cancer-associated IDH1 mutations produce 2-hydroxyglutarate. Nature 2009;462:739–44.

34. Moffett JR, Ross B, Arun P, Madhavarao CN, Namboodiri AM. N-Acetylaspartate in the CNS: from neurodiagnostics to neurobiology. Prog Neurobiol 2007; 81:89–131.
35. Price SJ, Jena R, Burnet NG, Hutchinson PJ, Dean AF, Peña A, et al. Improved delineation of glioma margins and regions of infiltration with the use of diffusion tensor imaging: an image-guided biopsy study. AJNR Am J Neuroradiol 2006;27:1969–74.
36. Kim BYS, Jiang W, Beiko J, Prabhu SS, DeMonte F, Gilbert MR, et al. Diagnostic discrepancies in malignant astrocytoma due to limited small pathological tumor sample can be overcome by IDH1 testing. J Neurooncol 2014;118:405–12.

Analytical and Bioanalytical Chemistry (2019) 411:7929–7933
https://doi.org/10.1007/s00216-019-02198-y

COMMUNICATION

Intraoperative detection of isocitrate dehydrogenase mutations in human gliomas using a miniature mass spectrometer

Hannah Marie Brown[1] · Fan Pu[1] · Mahua Dey[2] · James Miller[2] · Mitesh V. Shah[2] · Scott A. Shapiro[2] · Zheng Ouyang[1,3] · Aaron A. Cohen-Gadol[2] · R. Graham Cooks[1]

Received: 4 September 2019 / Revised: 26 September 2019 / Accepted: 7 October 2019 / Published online: 21 November 2019

Abstract

Knowledge of the isocitrate dehydrogenase (IDH) mutation status of glioma patients could provide insights for decision-making during brain surgery. However, pathology is not able to provide such information intraoperatively. Here we describe the first application of a miniature mass spectrometer (MS) to the determination of IDH mutation status in gliomas intraoperatively. The instrumentation was modified to be compatible with use in the operating room. Tandem MS was performed on the oncometabolite, 2-hydroxyglutarate, and a reference metabolite, glutamate, which is not involved in the IDH mutation. Ratios of fragment ion intensities were measured to calculate an IDH mutation score, which was used to differentiate IDH mutant and wild-type tissues. The results of analyzing 25 biopsies from 13 patients indicate that reliable determination of IDH mutation status was achieved ($p = 0.0001$, using the Kruskal-Wallis non-parametric test). With its small footprint and low power consumption and noise level, this application of miniature mass spectrometers represents a simple and cost-effective platform for an important intraoperative measurement.

Keywords Molecular cancer diagnostics · Ambient ionization mass spectrometry · Isocitrate dehydrogenase mutation · Miniature mass spectrometry · Point-of-care diagnostics

Introduction

The accurate diagnosis of gliomas relies increasingly on molecular features [1]. However, the microscopic review of tissue biopsies, the principal source of intraoperative diagnostic information, does not provide any molecular or genetic information, including information on isocitrate dehydrogenase (IDH) mutation status. Conventionally, mutations in the enzyme IDH are determined using immunohistochemistry with results not available until some days after surgery (Fig. 1). Knowledge of IDH mutation status at the time of surgery could improve surgical outcomes because more aggressive tumor resection of IDH-mutated gliomas is associated with increased survival [2, 3]. IDH mutations alter enzymatic pathways and lead to the accumulation of the oncometabolite 2-hydroxyglutarate (2-HG) [4]. While 2-HG is present in very small concentrations in normal tissues, concentrations increase dramatically in tumors with mutations in IDH1 and IDH2, reaching levels up to 35 μmol per gram of tumor [5]. This feature can be used to assess mutations in IDH, as has been demonstrated using magnetic resonance spectroscopy and mass spectrometry (MS) [6, 7].

MS is a highly sensitive technique that is capable of the qualitative and quantitative analysis of complex samples, including biological tissues. This application is most accurately done in conjunction with liquid or gas chromatography but doing so requires tedious sample preparation. Matrix-assisted laser desorption ionization (MALDI) is an alternative method which is important in tissue analysis [8]. MALDI has been used for the detection of 2-HG in frozen sections;

Hannah Marie Brown and Fan Pu contributed equally to this work.

Electronic supplementary material The online version of this article (https://doi.org/10.1007/s00216-019-02198-y) contains supplementary material, which is available to authorized users.

✉ R. Graham Cooks
cooks@purdue.edu

[1] Department of Chemistry and Bindley Biosciences Center, Purdue University, 560 Oval Drive, West Lafayette, IN 47907-1393, USA

[2] Department of Neurological Surgery, Goodman Campbell Brain and Spine, Indiana University School of Medicine, Indianapolis, IN 46202, USA

[3] Department of Precision Instrument, Tsinghua University, Beijing 100084, China

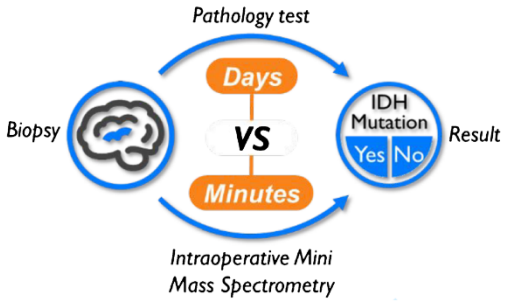

Fig. 1 Intraoperative detection of IDH mutations with Mini MS determines mutation status in minutes as opposed to days by means of conventional genomic analysis or immunohistochemistry

however, the required sample preparation and instrumentation make it incompatible with use in the operating room (OR) [9]. By contrast, ambient ionization is well suited for intraoperative use, as it allows chemical information to be obtained by MS at atmospheric pressure for a variety of matrices, including tissues, thereby eliminating sample pretreatment steps and making possible analysis in the OR. The first ambient methods were desorption electrospray ionization mass spectrometry (DESI-MS) and direct analysis in real time [10, 11]. These experiments have stimulated the development of numerous ambient ionization methods, including air flow–assisted desorption electrospray ionization, matrix-assisted laser desorption electrospray ionization, liquid micro junction-surface sampling, paper spray, MasSpec Pen, and rapid evaporative ionization MS [12–18]. They have also prompted a re-examination of conventional tissue diagnosis.

We have previously measured the abnormal accumulation of 2-HG for the intraoperative diagnosis of IDH mutation status using DESI-MS in near real time [19]. However, this intraoperative application requires expensive instrumentation. By contrast, miniature MS systems have small footprints, have low energy consumption, and produce little noise [20]. Their use in the OR offers the prospect of intraoperative genetic diagnosis in a cost-efficient manner. In an earlier study, we established the fact that a miniature mass spectrometer can be used to determine IDH mutation status in banked brain tissue samples [21]. In this small-scale clinical study with 13 subjects, we report the first application of a miniature mass spectrometer to determine IDH mutation status of glioma tissue intraoperatively, building on prior laboratory-based work [21, 22].

Experimental

Sampling method

Extraction nanoelectrospray ionization (nESI), a method characterized by minimal sample preparation, was used to generate ions [23]. We have previously established this method for rapid diagnosis of IDH mutation status based on measurement of 2-HG using banked tissue samples [21], so similar procedures were carried out in the OR. Biopsied tissue specimens from surgeon-defined positions within the tumor and at the walls of the resection cavity were collected intraoperatively. The number and location of the biopsies were determined according to the medical judgment of the attending surgeon. The biopsies were touched with a thin strip of Whatman 1 filter paper (ca. 0.5 mm wide and 15 mm long) that was then inserted into a nanotip (i.d. 0.86 mm, length ~ 4 cm) pre-filled with 20 μL methanol/water (9:1, *v/v*). The nanotip was subsequently placed in a custom 3D printed sample holder for MS analysis.

MS analysis

The experiment used the ion trap based PURSPEC Mini β, a stand-alone system that does not require external pumps or gas tanks. The Mini β, which measures 55 cm × 24 cm × 31 cm ($L \times W \times H$), was placed on an aluminum cart with all equipment required for its operation in the OR (Fig. S1, see Electronic Supplementary Material, ESM). An enclosed volume was employed to minimize any material transfer from the instrument. Prior to each surgery, the instrument was rolled into the OR and operated within the surgical suite for the duration of the surgery. The method is not quantitative, but we carried out calibration of the instrument before and after every surgical case to establish mass accuracy. This was done using a solution composed of aspartic acid, glutamate (GLU), 2-HG, and N-acetylaspartate using nESI in the negative ion mode; their molecular ions were found at *m/z* 132, 146, 147, and 174, respectively (Fig. S2, ESM). Ionizing voltage (− 1.5 kV) was applied to initiate nESI from a disposable acupuncture needle (diameter 0.3 mm, length 4 cm).

Tandem MS analysis of 2-HG was performed in the negative ion mode with GLU, an abundant metabolite not specifically associated with glioma, serving as an internal standard. The product ion abundances for the transitions *m/z* 147 → 129 for 2-HG and *m/z* 146 → 128 for GLU provided a relative measure of the concentration of 2-HG in tissue. The precursor ions were selected using a 2-Th-wide mass window. For each sample, at least three product ion spectra were recorded, each recorded spectrum being the average of three scans. Each scan took ~ 2 s and spectra were saved manually, making the total data acquisition time per sample ca. 1 min and the total analysis time including sample manipulation ca. 3 min. Postoperative analysis of the same biopsies was performed using the extraction nESI method on a Thermo TSQ to confirm intraoperative IDH mutation predictions. The TSQ analysis was performed using multiple reaction monitoring (MRM) mode; transitions selected were 2-HG (*m/z* 147 → 129) and GLU (*m/z* 146 → 128) (Figs. S3 and S4, ESM). With respect to each transition, optimized tube lens values of 67 and 69 V and nominal collision energies of 12 and 13 were applied.

Table 1 IDH mutation scores of tissue biopsies

Subject	Biopsy	Type of glioma	WHO grade	IDH mutation status	IDH mutation score (Mini MS)	IDH mutation score (TSQ)
1	1	Glioblastoma	IV	Wild-type	0.06	< 0.01
2	1	Glioblastoma	IV	Wild-type	0.02	0.02
3	1	Astrocytoma	II	Mutant	3.89	10.56
4	1	Pleomorphic xantoastrocytoma	II	Wild-type	0.33	0.03
	2				0.18	0.02
	3				0.35	0.07
5	1	Glioblastoma	IV	Wild-type	0.20	0.06
	2				0.24	0.06
	3				0.33	0.12
6	1	Glioblastoma	IV	Wild-type	0.35	0.04
	2				0.33	0.04
7	1	Glioblastoma	IV	Wild-type	0.28	0.07
	2				0.20	0.09
8	1	Anaplastic astrocytoma	III	Mutant	2.83	5.01
9	1	Glioblastoma	IV	Wild-type	0.11	0.05
10	1	Glioblastoma	IV	Mutant	3.20	35.51
	2				1.73	99.33
	3				1.73	14.34
11	1	Glioblastoma	IV	Wild-type	0.12	0.06
12	1		III	Mutant	2.07	6.73
	2				2.30	16.93
13	1	Glioblastoma	IV	Wild-type	0.25	0.04
	2				0.35	0.04
	3				0.50	0.07
	4				0.26	0.03

Data analysis

De-identified clinical data, consisting of patient demographics and radiology, surgical, and pathology reports, were obtained for each patient for correlation with the data produced by the Mini β system. The Mini β data were analyzed within 30 s postoperatively in MATLAB using a custom program to subtract background intensities and to calculate IDH mutation scores. This calculation can be done intraoperatively. The TSQ data were analyzed using Xcalibur. An IDH mutation score was calculated as the ratio of the two product ion intensities after correcting for the isotopic contributions of the ^{13}C glutamate fragment ion at *m/z* 129 (Eq. 1).

$$IDH \text{ mutation score} = \frac{I_{129} - (I_{128} \times 6.1\%)}{I_{128}} \quad (1)$$

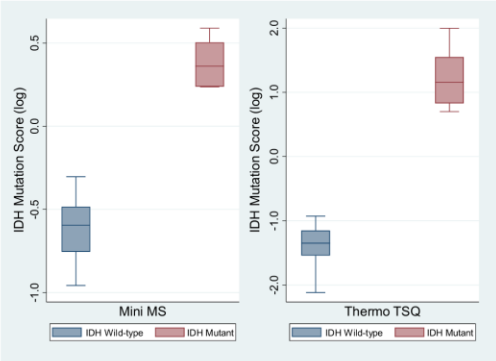

Fig. 2 Box-and-whisker plot of IDH mutation scores in human glioma tissue specimens (n = 25) analyzed intraoperatively using a PURSPEC Mini β and in the laboratory using a Thermo Triple Quadruple TSQ. (The box represents the interquartile range with a median line and whiskers at ± 1.5 SD. Two outliers (IDH wild-type) with IDH mutation scores below 1.5 SD were excluded in the Mini MS plot. Population medians for IDH mutation scores for both methods were statistically different; p values for both are 0.0001, using the Kruskal-Wallis non-parametric test.)

Results and discussion

In this preliminary clinical study, we analyzed 25 biopsies from 13 subjects. The patient cohort is described in detail in Table 1. Of the 13 subjects, 4 were IDH mutant (7 biopsies) and 9 were IDH wild-type (18 biopsies), according to postoperative pathology reports based on immunohistochemistry. Representative product ion mass spectra from an IDH wild-type and an IDH mutant glioma are included in the ESM (Figs. S5 and S6). As shown in Fig. 2 (left), the IDH wild-type tissues all had IDH mutation status scores below 0.5, whereas all IDH mutant samples had scores above 1.7. The box represents the interquartile range with a median line and whiskers at ± 1.5 standard deviations. The clear differentiation between IDH wild-type and mutant (p = 0.0001) is consistent

with our previous observations on banked tissue samples [21], which suggests that intraoperative diagnosis of IDH mutation status can be realized with the current methodology.

Postoperative analysis of the same biopsies was performed using extraction nESI on a Thermo TSQ. All IDH wild-type tissues had IDH mutation scores below 0.1 and all IDH mutant tissues had IDH mutation scores above 5.0 (Fig. 2, right) using this higher performance lab system. The higher sensitivity of the Thermo TSQ results in less noise and hence an increase in the absolute differences of the mutation scores. Identical conclusions can be drawn from both sets of results, as shown in Fig. 2. For both methods, the differences in population medians for the IDH mutation scores were statistically significant different (p values both 0.0001, using Kruskal-Wallis nonparametric test). Both instruments are capable of generating diagnostic information consistent with pathology. In this assay, the intraoperative application of a miniature mass spectrometer shows comparable performance with that of a conventional instrument.

Conclusion

We have successfully performed intraoperative diagnosis of IDH mutation using extraction nESI on Mini β. The instrumentation was modified to be compatible with use in the operating room. With its small footprint, low power consumption, minimal noise, and ability to generate reliable IDH mutation status predictions in near real time, the intraoperative use of a miniature mass spectrometer represents an advance towards improved glioma patient treatment. Further studies will be carried out with protocol standardization and automation to validate these preliminary findings and reduce the barrier for broader application.

Acknowledgments The authors thank clinical research nurses Lauren Snyder and Heather Cero at Goodman Campbell Brain and Spin (Indianapolis, IN) for patient consent, providing clinical data, and IRB monitoring; Clint Alfaro and Tsdale Mehari for assistance in sample preparation; Robert Schrader for assistance with instrumentation; Zhuoer Xie for the table of contents figure; and PURSPEC Technologies Inc. for instrumentation support.

Funding information This study received funding from the Purdue University Center for Cancer Research Small Grants Program; from National Institute of General Medical Sciences of the NIH under award number R44GM119584.

Compliance with ethical standards Biopsies for tissue analysis were obtained from human subjects undergoing tumor resection for suspected glioma at IU Health Methodist Hospital, after they had provided written informed consent to participate in the research study, following an IUSM IRB approved protocol (IRB No. 1410342262). No results were shared with the neurosurgeons during the surgical resection so as not to affect the standard of care.

Conflict of interest Zheng Ouyang is the founder of PURSPEC Technologies Inc. All other authors declare that they have no conflict of interest.

References

1. Louis DN, Perry A, Reifenberger G, von Deimling A, Figarella-Branger D, Cavenee WK, et al. The 2016 World Health Organization Classification of Tumors of the Central Nervous System: a summary. Acta Neuropathol. 2016;131(6):803–20. https://doi.org/10.1007/s00401-016-1545-1.
2. Chen R, Ravindra VM, Cohen AL, Jensen RL, Salzman KL, Prescot AP, et al. Molecular features assisting in diagnosis, surgery, and treatment decision making in low-grade gliomas. Neurosurg Focus. 2015;38(3):E2. https://doi.org/10.3171/2015.1.FOCUS14745.
3. Patel T, Bander ED, Venn RA, Powell T, Cederquist GY, Schaefer PM, et al. The Role of Extent of Resection in IDH1 Wild-Type or Mutant Low-Grade Gliomas. Neurosurgery. 2018;82(6):808–14. https://doi.org/10.1093/neuros/nyx265.
4. Dang L, White DW, Gross S, Bennett BD, Bittinger MA, Driggers EM, et al. Cancer-associated IDH1 mutations produce 2-hydroxyglutarate. Nature. 2009;462(7274):739–44. https://doi.org/10.1038/nature08617.
5. Miller JJ, Shih HA, Andronesi OC, Cahill DP. Isocitrate dehydrogenase-mutant glioma: Evolving clinical and therapeutic implications. Cancer. 2017;123(23):4535–46. https://doi.org/10.1002/cncr.31039.
6. Andronesi OC, Kim GS, Gerstner E, Batchelor T, Tzika AA, Fantin VR, et al. Detection of 2-hydroxyglutarate in IDH-mutated glioma patients by in vivo spectral-editing and 2D correlation magnetic resonance spectroscopy. Sci Transl Med. 2012;4(116):116ra114. https://doi.org/10.1126/scitranslmed.3002693.
7. Santagata S, Eberlin LS, Norton I, Calligaris D, Feldman DR, Ide JL, et al. Intraoperative mass spectrometry mapping of an onco-metabolite to guide brain tumor surgery. Proc Natl Acad Sci U S A. 2014;111(30):11121–6. https://doi.org/10.1073/pnas.1404724111.
8. McDonnell LA, Heeren RM. Imaging mass spectrometry. Mass Spectrom Rev. 2007;26(4):606–43. https://doi.org/10.1002/mas.20124.
9. Longuespee R, Wefers AK, De Vita E, Miller AK, Reuss DE, Wick W, et al. Rapid detection of 2-hydroxyglutarate in frozen sections of IDH mutant tumors by MALDI-TOF mass spectrometry. Acta Neuropathol Commun. 2018;6(1):21. https://doi.org/10.1186/s40478-018-0523-3.
10. Takats Z, Wiseman JM, Gologan B, Cooks RG. Mass spectrometry sampling under ambient conditions with desorption electrospray ionization. Science. 2004;306(5695):471–3. https://doi.org/10.1126/science.1104404.
11. Cody RB, Laramee JA, Durst HD. Versatile new ion source for the analysis of materials in open air under ambient conditions. Anal Chem. 2005;77(8):2297–302. https://doi.org/10.1021/ac050162j.
12. Brown HM, Pirro V, Cooks RG. From DESI to the MasSpec Pen: Ambient Ionization Mass Spectrometry for Tissue Analysis and Intrasurgical Cancer Diagnosis. Clin Chem. 2018;64(4):628–30. https://doi.org/10.1373/clinchem.2017.281923.
13. He J, Sun C, Li T, Luo Z, Huang L, Song X, et al. A Sensitive and Wide Coverage Ambient Mass Spectrometry Imaging Method for Functional Metabolites Based Molecular Histology. Adv Sci. 2018;5(11):1800250. https://doi.org/10.1002/advs.201800250.
14. Robichaud G, Barry JA, Muddiman DC. IR-MALDESI mass spectrometry imaging of biological tissue sections using ice as a matrix. J Am Soc Mass Spectrom. 2014;25(3):319–28. https://doi.org/10.1007/s13361-013-0787-6.

15. Van Berkel GJ, Kertesz V, Koeplinger KA, Vavrek M, Kong AN. Liquid microjunction surface sampling probe electrospray mass spectrometry for detection of drugs and metabolites in thin tissue sections. J Mass Spectrom. 2008;43(4):500–8. https://doi.org/10.1002/jms.1340.
16. Wang H, Manicke NE, Yang Q, Zheng L, Shi R, Cooks RG, et al. Direct Analysis of Biological Tissue by Paper Spray Mass Spectrometry. Anal Chem. 2011;83(4):1197–201. https://doi.org/10.1021/ac103150a.
17. Zhang J, Rector J, Lin JQ, Young JH, Sans M, Katta N, et al. Nondestructive tissue analysis for ex vivo and in vivo cancer diagnosis using a handheld mass spectrometry system. Sci Transl Med. 2017;9(406). https://doi.org/10.1126/scitranslmed.aan3968.
18. Balog J, Sasi-Szabo L, Kinross J, Lewis MR, Muirhead LJ, Veselkov K, et al. Intraoperative Tissue Identification Using Rapid Evaporative Ionization Mass Spectrometry. Sci Transl Med. 2013;5(194):194ra193. https://doi.org/10.1126/scitranslmed.3005623.
19. Alfaro CM, Pirro V, Keating MF, Hattab EM, Cooks RG, Cohen-Gadol AA. Intraoperative assessment of isocitrate dehydrogenase mutation status in human gliomas using desorption electrospray ionization-mass spectrometry. J Neurosurg. 2019:1–8. https://doi.org/10.3171/2018.8.JNS181207.
20. Austin DE, Lammert SA. Mass Analyzer Miniaturization. In: The Encyclopedia of Mass Spectrometry, vol. 7. 1st ed: Elsevier; 2009.
21. Pu F, Alfaro CM, Pirro V, Xie Z, Ouyang Z, Cooks RG. Rapid determination of isocitrate dehydrogenase mutation status of human gliomas by extraction nanoelectrospray using a miniature mass spectrometer. Anal Bioanal Chem. 2019;411(8):1503–8. https://doi.org/10.1007/s00216-019-01632-5.
22. Zou R, Cao W, Chong L, Hua W, Xu H, Mao Y, et al. Point-of-Care Tissue Analysis Using Miniature Mass Spectrometer. Anal Chem. 2019;91(1):1157–63. https://doi.org/10.1021/acs.analchem.8b04935.
23. Ren Y, Liu J, Li L, McLuckey MN, Ouyang Z. Direct Mass Spectrometry Analysis of Untreated Samples of Ultralow Amounts Using Extraction Nano-Electrospray. Anal Methods. 2013;5(23). https://doi.org/10.1039/C3AY41149D.

Clinical Chemistry 64:4
628–630 (2018)

Perspective

From DESI to the MasSpec Pen: Ambient Ionization Mass Spectrometry for Tissue Analysis and Intrasurgical Cancer Diagnosis

Hannah Marie Brown,[1] Valentina Pirro,[1,2] and R. Graham Cooks[1,2*]

With the increasing prevalence of cancer, there is strong motivation to accurately assess and diagnose tissue during cancer surgery. Assessment of the negative margin for the maximum possible tumor excision is critical for achieving remission and improving overall patient survival. To that end, the MasSpec Pen is the latest iteration of ambient ionization mass spectrometry (MS)[3] for the purposes of tissue diagnosis that allows direct, real-time tissue sampling and molecular analysis *(1)*. This development occurs at a time when molecular analysis is rapidly emerging as an important aspect of cancer tissue diagnosis and substantial efforts are made to develop technology that is automated, biocompatible, nondestructive, handheld, and available at the bedside. While the gold standard for cancer diagnosis continues to be histopathology augmented by immunohistochemistry, molecular analysis holds great promise for several reasons: (*a*) small molecules provide information on the phenotype that may be unavailable from examination of the genotype; (*b*) complex and dynamic interactions between biomolecules influence biological functions and so signify the health state of an entity; and (*c*) rapid and accurate pattern recognition of tissue types is possible with multiple spectroscopic/spectrometric methods. With pathology providing a gold standard reference, it has become clear that both MS and Raman spectroscopy have potential value for cancer diagnostics. A minimum requirement for surgical relevance is that a technique provides reliable molecular data very rapidly while using unprocessed samples. Ambient ionization MS is a suite of methods that does exactly that, allowing chemical information to be obtained for a variety of analytes at atmospheric pressure, thereby eliminating the usual requirement for ionization to be performed under suction or for prior sample purification and pretreatment.

The first tissue measurements completed with ambient ionization, reported in 2005, were based on phospholipid distributions, and they served to demarcate tissue type and disease state. That work used the imaging method of desorption electrospray ionization (DESI), a label-free method in which a spray of charged solvent impacts a tissue surface and desorbs secondary droplets containing analytes that are sampled by the mass spectrometer (Fig. 1). DESI is an offline ex vivo method that has been followed by others, e.g., swab touch spray, coated blade spray, probe ESI. In these cases, tissue samples are transferred onto a stage or substrate from which desorption/extraction and ionization are performed. This line of research ultimately led to the MasSpec Pen, a tool for localized, online in vivo tissue analysis *(1)*.

In its short 12-year history, molecular tissue analysis by means of ambient ionization MS has provoked a reexamination of conventional methodologies of tissue diagnosis. DESI itself has evolved into a nondestructive technology in which MS spectra are recorded with morphologically friendly solvent sprays, allowing accurate verification through comparison of molecular and morphological signatures from the same tissue sample. Detailed diagnostic information, including tumor cell percentage in diseased tissue, is represented at the molecular level in the DESI mass spectra obtained from biopsied tissue sections or smears *(2)*. Distinctive DESI lipid profiles are observed from cancerous and adjacent normal tissue, enabling demarcation of cancerous borders on the basis of molecular information.

Given the strong concordance between the results of molecular measurements and those of pathology, considerable efforts have been made to extend the role of ambient ionization methods from the research laboratory to the operating room. While DESI has been used intrasurgically on an experimental basis, for example for brain cancer diagnostics *(2)*, true in vivo intraoperative use is out of reach. This capability has been sought with rapid evaporative ionization mass spectrometry (REIMS), a high throughput platform for the rapid and accurate identification of cancerous biomarkers that requires no preparative steps *(3)*. REIMS is based chiefly on lipid profiles that are recorded by direct online analysis of surgical smoke, i.e., electrosurgical aerosols that release cellular contents into the gas phase upon cutting or coagu-

[1] Department of Chemistry, Purdue University, West Lafayette, IN; [2] Center for Analytical Instrumentation Development, Purdue University, West Lafayette, IN.
* Address correspondence to this author at: 560 Oval Drive, West Lafayette, IN 47907. Fax 765-494-0239; e-mail cooks@purdue.edu.
Received November 8, 2017; accepted January 16, 2018.
Previously published online at DOI: 10.1373/clinchem.2017.281923

[3] Nonstandard abbreviations: MS, mass spectrometry; DESI, desorption electrospray ionization; REIMS, rapid evaporative ionization mass spectrometry; LMJ, liquid microjunction.

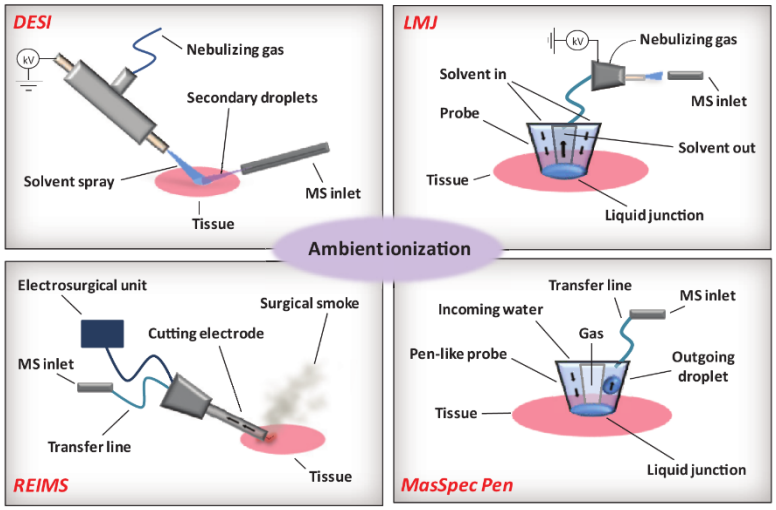

Fig. 1. Four related ambient ionization methods that have been used to characterize tissue by mass spectrometry of desorbed or dissolved molecules.
Drawings are not to scale.

lating tissue (Fig. 1). This methodology, while being capable of rapid in vivo analysis, is limited insofar as it requires electrosurgery, is destructive, and allows only indirect cross-comparisons with pathology.

The MasSpec Pen provides localized molecular information from tissue samples by a nondestructive liquid-solid extraction process and subsequent ionization. This is achieved by contacting the tissue sample with the tip of the pen-like probe by way of a discrete water droplet. The system itself consists of a syringe pump programed to deliver solvent to the sampling probe, tubing conduits integrated with a fast two-way pinch valve to control solvent transport to and from the tissue, and a three-dimensional printed probe for direct sampling from the tissue *(1)*. The tip of the probe contains 3 ports: an incoming port that delivers a solitary water droplet to the tissue surface, a central port for the delivery of a gas, and an outgoing port to transport the molecular analytes in the water droplet from the tissue to the mass spectrometer (Fig. 1). The gas prevents the collapse of the system due to the use of suction and assists in the transport of individual water droplets to the mass spectrometer. The third port is directly connected to a mass spectrometer, such that the negative pressure of the suction system drives the droplet from the tip of the pen to the mass spectrometer for ionization and subsequent high-resolution MS analysis. This process decreases the number of operational steps and allows ambient ionization MS to be performed at high speed. Of interest are the signals obtained from lipids that collectively serve as cancer biomarker. Multivariate statistical analysis of spectral patterns is used to expedite tissue diagnosis and is ultimately meant to be automated. Through comparison with pathology, mass spectra collected with the MasSpec Pen preliminarily showed high sensitivity, specificity, and accuracy for tissue diagnosis of different types of cancer, including breast, ovarian, and thyroid cancer *(1)*.

While the preliminary results of the MasSpec Pen are undeniably promising, questions remain regarding the mechanism of operation. It is likely that molecules are extracted from the surface not solely by dissolution, given that the solvent of choice is water. It is possible that the molecular information is transported in the form of small tissue particles that move in the solution. There are parallels between the processes in the MasSpec Pen, nanospray DESI *(4)*, and liquid microjunction (LMJ) MS interface *(5)*, also used for tissue analysis. Unlike the original DESI experiment, sampling in nanospray DESI is performed by subjecting the tissue to a continuous stream of solvent by means of 2 small glass capillaries that form a liquid microjunction without pneumatic assistance. When the solvent touches the tissue sample, the material on the substrate is dissolved. The second capillary transports the dissolved analytes and releases them as

ions by ESI, which are then analyzed by MS. The LMJ MS interface pumps the extraction solvent to the tissue surface through the annular space between 2 coaxial tubes at the sampling end of the probe and pulls it into and through the inner tube to the ionization source via a self-aspirating ESI or atmospheric pressure chemical ionization emitter (Fig. 1). In these methods, various solvents can be used to target different analyte species, except for in vivo tissue analysis with the MasSpec Pen, which demands the use of sterile water or surgical irrigation (e.g., saline) solutions.

Given the vast academic and clinical interest in in vivo methods of molecular cancer diagnosis, it is likely that the application of MS diagnostic methods based on phospholipids and oncometabolites will grow rapidly in the near future. Clinical trials to explore the intraoperative application of ambient ionization MS are on the horizon. Development of intrasurgical MS technology, such as that of the MasSpec Pen, proves the possibility for ambient ionization methods of overcoming barriers like in vivo and nondestructive molecular tissue analysis. Commercialization and automation will be ways to ease accessibility to intrasurgical MS technologies, which thereby will contribute to fostering the advance of molecular pathology. The implementation of consensus protocols for method development and clinical performance assessment will follow.

Lastly, we envision that the integration of lipidomics and metabolomics will add breadth and depth to cancer diagnostics and will play a role that can extend beyond surgical tumor resection. After all, altered metabolism is one of the hallmarks of cancer, and it has been speculated that metabolic disorders can initiate tumorigenesis, in contrast with the traditional concept that mutations in oncogenes are the direct causes of cancer and lead to metabolic deregulation. In this manner, intrasurgical MS technologies can further strengthen the molecular basis for classifying tumors (currently mostly based on genomic information) and help to develop personalized medicine therapies.

Author Contributions: *All authors confirmed they have contributed to the intellectual content of this paper and have met the following 3 requirements: (a) significant contributions to the conception and design, acquisition of data, or analysis and interpretation of data; (b) drafting or revising the article for intellectual content; and (c) final approval of the published article.*

Authors' Disclosures or Potential Conflicts of Interest: *No authors declared any potential conflicts of interest.*

References

1. Zhang J, Rector J, Lin JQ, Young JH, Sans M, Katta N, et al. Nondestructive tissue analysis for ex vivo and in vivo cancer diagnosis using a handheld mass spectrometry system. Sci Transl Med 2017;9:eaan3968.
2. Pirro V, Alfaro CM, Jarmusch AK, Hattab EM, Cohen-Gadol AA, Cooks RG. Intraoperative assessment of tumor margins during glioma resection by desorption electrospray ionization-mass spectrometry. Proc Natl Acad Sci USA 2017;114:6700–5.
3. Laskin J, Heath BS, Roach PJ, Cazares L, Semmes OJ. Tissue imaging using nanospray desorption electrospray ionization mass spectrometry. Anal Chem 2012;84:141–8.
4. Balog J, Sasi-Szabó L, Kinross J, Lewis MR, Muirhead LJ, Veselkov K, et al. Intraoperative tissue identification using rapid evaporative ionization mass spectrometry. Sci Transl Med 2013;5:194ra93.
5. Kertesz V, Ford MJ, Van Berkel GJ. Automation of a surface sampling probe/electrospray mass spectrometry system. Anal Chem 77;2005:7183–9.